NEUP Final Report

Project Title: **Multilayer Composite Fuel Cladding and Core Internals for LWR Performance Enhancement and Severe Accident Tolerance**

Technical Workscope: **FC-2.1, Advanced Nuclear Fuel, Cladding, and Core Components**

NEUP Application Number: 15-8347

Federal Grant Number: DE-NE0008413

Project Start Date: 10/1/2015

Original End Date: 9/30/2018

Final End Date with No-Cost Extension: 6/30/2019

PI: Michael Short (Massachusetts Institute of Technology)

Co-PIs: Jinsuo Zhang (orig. Ohio State University, now Virginia Tech)

Michael Tonks (orig. Penn State, now University of Florida at Gainesville)

International Partners: Ulla Ehrnstén (VTT Technical Research Centre, Finland)

Project Overall Summary and Status: Accident tolerance of LWR fuels and structures is of paramount importance, as highlighted by the accident at the Fukushima Daiichi nuclear power station. The ability of fuel cladding and core internals to resist runaway oxidation during a beyond design basis accident (BDBA), as well as to minimize corrosion during steady state operation and design basis accidents (DBAs), determines its degree of accident tolerance. A gap was identified in the accident tolerant fuel (ATF) concepts under consideration, as most consisted either of coatings which may not hold their integrity under prolonged operation, or different materials altogether which incur significant neutronic penalties. A compromise was therefore sought – by minimizing the amount of coating material while ensuring a strong microstructural bond, it was thought that a Zircaloy-steel layered composite would achieve the best of both approaches.

The goal of this NEUP project was to develop a ***multi-metallic layered composite (MMLC)*** tailored to addressing accident tolerance of LWR fuel cladding and core internal structures using an innovative fabrication technology. The MMLC developed in this program is expected to enhance the accident tolerance of LWRs, thereby reducing the cost by recovering lost operating margins and/or increasing operating windows of peak cladding temperature, peak linear power, reducing steady-state corrosion, and enhancing severe accident tolerance.

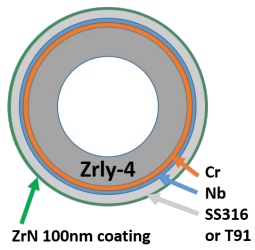

Figure 1: Original diagram of the proposed MMLC fuel cladding. Similar layers will be simply weld-overlaid onto Zircaloy core internal structures in addition.

As of this final report the concept has been fully vetted on the laboratory scale, but work at the industrial scale is ongoing due to unforeseen setbacks in the full-sized extrusion billet fabrication process. The original layer structure (see Figure 1) has changed from its initial conception based on the tests carried out in this project. The Nb layer originally believed to serve as a barrier layer between Cr and the steel on the outside (which it did) also led to deadhesion of the layers during fabrication, thus a new V-4Ti-4Cr layer was substituted upon slightly relaxing neutronics design constraints. This new four layer MMLC billet is still under industrial-scale fabrication, expected to finish by the end of the 2019 calendar year. Full scale fabrication of a three layer MMLC extrusion billet without the V-4Ti-4Cr layer led to intermetallic formation and cracking, thus extrusion was not attempted on this billet. The cause of this failure was pinned down to the hot isostatic pressing (HIPing) procedure, performed on a previous DOE NERI MMLC billet, which resulted in eutectic alloy formation between the Ti barrier layer and the carbon steel used to can and seal the billet for HIPing. The next run of the MMLC billet fabrication will not use HIPing as a result. Corrosion resistance of the outer FeCrSi layer of the MMLC is excellent, both in PWR and high temperature steam oxidation situations, provided 16%Cr is used in the FeCr-2Si layer. Multiscale modeling of MMLC performance using the MOOSE solid mechanics and BISON systems shows that it should survive full fuel cycles in PWR operation. Friction stir welding is believed to be the best way to join the MMLC, both for endcaps and other joints. Finally, a fortuitous neutron irradiation campaign in the MIT reactor to 0.5 DPA showed that irradiation-induced precipitation occurs in both Fe-16Cr-2Si and Fe-20Cr-2Si, though the small, discontinuous precipitates formed in the former demonstrate acceptable performance unlikely to result in radiation embrittlement.

Thus, despite the fact that the industrial-scale billet has not yet been finished, we still expect this new MMLC-ATF concept to meet all the goals of ATF fuel cladding – low neutronic penalty, increased accident coping time, fuel performance within elastic and creep limits of cladding, industrial-scale fabricability, and good corrosion resistance in both normal and accident operation conditions.

Table of Contents

Chapter 1 – Original Project Rationale and Goals 4
- Original Objectives 4
- Background 4
- Original Project Tasks 7
- Summary of Changes to Project Scope as New Results Were Obtained 13

Chapter 2 – Laboratory Scale MMLC Fabrication and Radiation Studies 14
- Diffusion Couple Fabrication and Interlayer Diffusion Results 14
- Neutron Radiation Studies on the Fe-Cr-2Si Alloy Series 28

Chapter 3 – Corrosion Tests of Outer FeCrSi MMLC Layers 31
- Steam Oxidation, SCC, and Flowing Corrosion Tests at Virginia Tech 32
- Additional Steam Oxidation Tests at VTT Technical Research Centre of Finland 69

Chapter 4 – Multiscale Modeling of MMLC Performance 75

Chapter 5 – Joining Methods for MMLCs 90

Chapter 6 – Industrial Scale Fabrication of MMLCs – Iterations and Lessons Learned 111
- Initial Cr-Based MMLC Fabrication Tests 111
- Three-Layer MMLC Billet and Four-Layer MMLC Design 119

Chapter 1 – Original Project Rationale and Goals

Overall Project Objective: In this project, we set out to develop MMLCs to enhance the performance and accident tolerance of current and future LWRs, mainly by removing as much zirconium as possible from the core without significant drops in performance. The tried-and-true design principle of separating component or layer functionality was used to conceive of the MMLC, whereby the strength requirements are satisfied by an inner structural layer, and corrosion/accident tolerance are fulfilled by an outer corrosion-resistant layer. Because the chosen base chemistries (Zr-based structural and Fe-based corrosion resistant) are not microstructurally or chemically compatible, barrier layers were required to bond the layers without introducing additional eutectic or intermetallic formation. No single barrier layer fulfilled all the requirements of the MMLC, thus two barrier layers were used to separate each base alloy from the other and from its incompatible barrier layer, resulting in a four-layer structure. The phase diagrams used in arriving at this decision are shown below as rationale for the overall MMLC design.

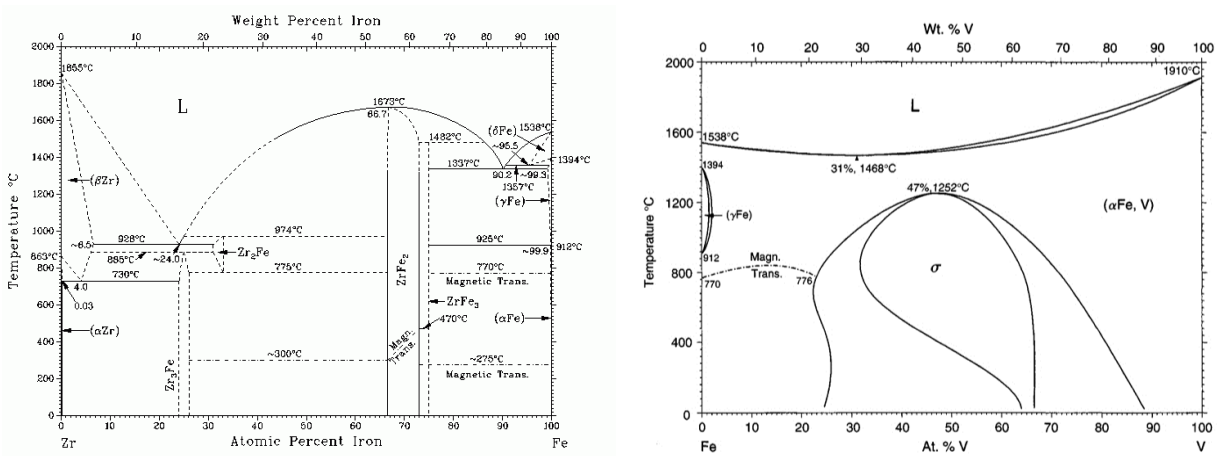

Figure 2: (Left) Fe-Zr phase diagram [1] showing incompatibilities in the form of high temperature intermetallics and low-melting point eutectics. (Right) Fe-V phase diagram[2] showing wide compatibility in only one intermetallic and no low-melting point eutectics.

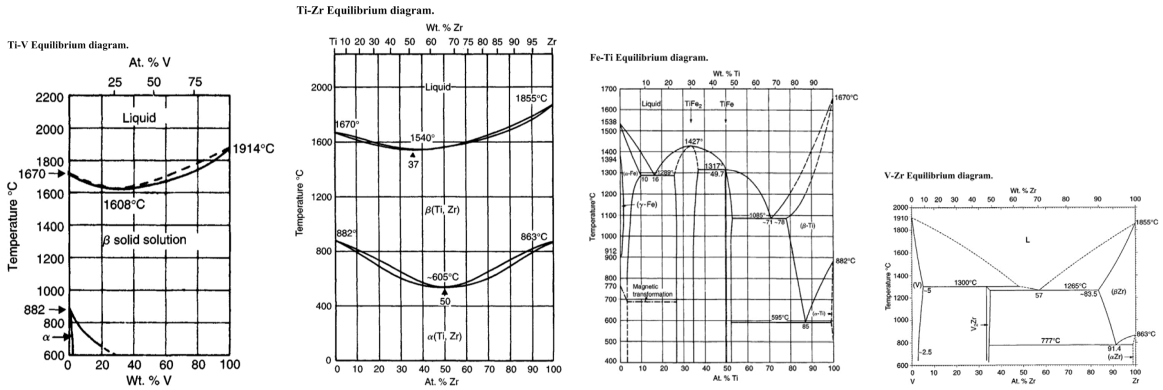

Figure 3: Barrier layer binary phase diagrams[3], showing good compatibility between (left) Ti-V and Ti-Zr, and poor compatibility (right) between Fe-Ti and V-Zr. This four layer system (Fe-V-Ti-Zr) was the final one chosen for the four layer MMLC in this project, for these reasons.

---

[1] Arias, D. & Abriata, J.P. Bulletin of Alloy Phase Diagrams (1988) 9: 597. https://doi.org/10.1007/BF02881963

[2] Smith, J.F. Bulletin of Alloy Phase Diagrams (1984) 5: 184. https://doi.org/10.1007/BF02868958

[3] Smithells Metals Reference Book (8th Edition)

Background: Previous Successes Using Layered Composites in Nuclear Systems: Bi-layered composite materials have recently been successfully designed to resist corrosion and maintain mechanical integrity, and fabricated on an industrial scale. The bi-layers of the new composite are designed to perform specific functions unattainable by single alloys. For example, a recent development effort has made significant progress in this area by combining a newly developed Fe-12Cr-2Si alloy with a high strength steel (T91/F91) in a functionally graded composite (FGC)[4]. The new system is designed to provide both a multi-layer protective film (Fe-Oxide/Cr-Oxide/Si-Oxide) over a wide range of oxygen potentials[5] and, at the same time, provide minimal solubility in liquid Pb or lead-bismuth eutectic (LBE) at very low oxygen potentials, which may occur in crevices or other oxygen-depleted areas. The new FGC has demonstrated excellent resistance to corrosion in Pb/LBE that suggest that corrosion will not be an issue for operation of materials at temperatures up to 700°C. This significant breakthrough on this new composite material encourages us to rethink the current and proposed coating technologies for enhancing Zircaloy accident-tolerance. Therefore this new technology can lead to an MMLC based on existing Zircaloys, while providing both economic and technique benefits over other coatings that are currently being studied.

Background: Previous and Current Work on LWR Accident Tolerant Fuels and Cladding: Several projects have been or are currently funded by the DOE and other agencies on coating development for Zr-alloy for enhanced accident-tolerance. For example, J. C. Brachet et al. of the CEA in France are developing chromium-coated Zircaloys for accident tolerance. B. Cheng et al. of EPRI are working on Mo-based cladding, while R. B. Rebak et al of General Electric and Y. Yamamoto et al. of ORNL are developing advanced steel and FeCrAl fuel cladding, respectively. Westinghouse Electric Company (WEC) was actively pursuing MAX phase (metal-aluminum-carbide) coatings, with Cr-coated cladding now in favor. Multiple teams are exploring SiC as a potential cladding material, though this is beginning to fall out of favor as of this writing. Compared with these on-going studies, we propose to use commercially available and industrial scale welding technologies to fabricate the proposed MMLC. Industrial-scale techniques, such as co-extrusion, weld-overlay, and friction stir welding will be used to fabricate and join commercially-relevant quantities of the MMLC in domestically available facilities. Doing so will demonstrate a higher level of technology readiness as compared to laboratory-scale studies.

The proposed MMLC represents a compromise between the corrosion resistance and neutronic performance of the above accident tolerant fuel concepts, while retaining the highest degree of immediate, domestic fabricability without introducing new brittle failure modes or significant joining and end-cap attachment problems. In particular, SS316 has demonstrated excellent corrosion resistance in LWR applications for decades, while T91 has seen decades of use in fossil power plants at temperatures up to 700°C. In addition, recent studies have shown T91 to have excellent corrosion resistance in supercritical water[6]. While SS316 may be more fabricable, it may suffer from increased radiation swelling. Therefore the choice of the outer corrosion-resistant layer of the MMLC was made carefully, taking into account previous and current work on accident tolerant fuel cladding. In the end a suite of FeCrSi alloys from previous DOE-NE sponsored work were chosen for this effort, and subject to numerous studies in terms of corrosion resistance, weldability, neutron irradiation, and multiscale modeling as detailed in this report.

Research Program as Proposed: The major objective of the proposed project was to develop a new, severe accident-tolerant MMLC for fuel cladding for simultaneously improving LWR fuel performance and resisting rare event accident scenarios. The layers of the as-proposed MMLC (as shown in Figure 1) were designed to perform specific functions unattainable by single alloys. Fuel cladding composed of a stainless steel (SS) or a ferritic/martensitic steel such as T91 overlaid onto a Zircaloy base could reduce the amount of Zr in the reactor, resulting in less hydrogen evolution during a severe accident. In addition, a MMLC will be less susceptible to sudden, brittle failure of fuel cladding due to directional hydride formation in Zircaloys.

---

[4] PI, Co-PI, International-PI. *Nucl. Technol.*, 177(3):366 (2012).

[5] Short, M. P., Ballinger, R. G., Hänninen, H. E. "Corrosion resistance of alloys F91 and Fe-12Cr-2Si in lead-bismuth eutectic up to 715°C." *J. Nucl. Mater.* **434**(1-3):259-281 (2013).

[6] Y. Chen, K. Sridharan, T. Allen, "Corrosion behavior of ferritic–martensitic steel T91 in supercritical water," *Corrosion Science*, 48(9):2843 (2006).

Finally, the water-facing layer of stainless steel will resist corrosion better than Zircaloys, especially during a severe accident. Diffusion barrier layers of Cr and Nb were originally selected to be used in between the Zr and iron-based alloys, to avoid detrimental eutectic phase or intermetallic formation (see binary phase diagrams in Figure 2 and Figure 3). To develop and test this MMLC, we set out to: 1) fabricate the composite, 2) characterize and improve fabrication and joining techniques, including MMLC endcaps on fuel cladding, 3) use multiscale modeling to simulate accident performance and radiation resistance of the MMLC, and 4) Validate these multiscale models with laboratory-scale severe accident testing and corrosion and electrochemical tests.

The full scope of this project as proposed is summarized here, with explanations to follow:

- Design and optimize an MMLC to improve accident tolerance and operating windows of LWRs
- Quantify and validate attainable performance gains by using the MMLC in place of Zircaloys
- Design and characterize processing steps to maximize performance properties of the MMLC
- Develop & implement joining procedures to attach the MMLC to itself and other components
- Quantify the corrosion and mechanical performance of the MMLC compared to Zircaloys
- Determine the technological readiness of the MMLC at the end of the project

Specific Project Goals and Objectives: Developing MMLCs has the potential to simultaneously improve material performance, limit cost, *and* improve the ability to weld or join parts to base structures all at the same time. Following in the footsteps of previous DOE-NE funded work by the PI and one Collaborator on bi-metal composites, systems of alloys with layers tailored to perform specific functions can offer performance gains that individual alloys cannot. For LWRs, fuel cladding composed of a stainless steel (SS) overlaid onto a Zircaloy base could reduce the amount of Zr in the reactor, resulting in less hydrogen evolution during a severe accident. In addition, an MMLC will be less susceptible to sudden, brittle failure of fuel cladding due to directional hydride formation in Zircaloys[7]. Finally, the water-facing layer of stainless steel will resist corrosion better than Zircaloys, especially during a severe accident. In order to avoid detrimental eutectic composition or intermetallic formation[8], diffusion barrier layers of Cr and Nb will be used in between Zr and the iron-based alloy in the proposed MMLC. Additional performance gains may be realized by adding an inner liner of pure Zr, as is done in barrier fuel. The careful design and optimization of ideal layers *and* interfacial properties of each MMLC is therefore one main technical objective of this project.

The proposed MMLC serves mainly to make the fuel cladding more accident tolerant in three main ways. First, increased oxidation resistance would reduce the initial oxide layers that would be present at the start of an accident. Second, reducing the amount of zirconium in the LWR core proportionally reduces the amount of hydrogen generated during a beyond design basis accident (BDBA). Third, Zircaloy-specific modes of localized corrosion, such as iodine-induced stress corrosion cracking, may be stopped by layers of differing compositions through the wall of fuel cladding. Each of these potential accident tolerance enhancements must be quantified using a combination of experiments, modeling, and theoretical calculations. This represents the first technical objective, to quantify and validate performance gains achievable by using the MMLC.

The processing methods used to fabricate the proposed MMLC are intimately linked with its mechanical and corrosion performance. In particular, the effect of each processing step on the *interfaces* between each layer in an MMLC determines most of the robustness of the composite itself. Issues such as diffusional (dilutional) stability, performance under long-term thermal aging, changes in interface microstructure due to irradiation and corrosion, and maintaining the correct balance of hardness and toughness *during each processing step* will affect the quality of the bond between MMLC layers during both processing and service. While only domestic facilities and processes will be used, much work remains to optimize the quality of MMLC

[7] Y. Yan et al. "Observation and Mechanism of Hydride in Zircaloy-4 and Local Hydride Re-Orientation Induced by High Pressure at High Temperatures." In *2013 International High-Level Radioactive Waste Management (2013 IHLRWM)*, Albuquerque, NM, USA.

[8] H. Okamoto. *J. Phase Equilibria and Diffusion*, 27(5):543-544 (2006).

interfaces during and after processing. Therefore, the second technical objective of this project is to design and characterize the processing steps for the MMLC.

The ability to join these multi-metal layered composites to each other and to the base metal components represents a key step in the technological readiness of the proposed MMLC. Examples of required joints include butt-welding of sections of MMLC piping, sealing of MMLC fuel cladding endcaps, joining of internal core structures or coolant inlet/outlet piping to the vessel, and field repairs of observed defects. The sustained robustness of the proposed MMLC hinges upon proper joining and heat treatment methods, which must be carefully characterized and iterated. Therefore, another major technical objective of this project was to demonstrate and optimize joining of the MMLC to relevant reactor structures without significant degradation in structural and corrosion performance, even following thermal aging. In the end this goal has not yet been achieved, due to cracking of the first MMLC billet from HIP can material interactions with the Ti barrier layer. Work on this task will continue in a separately funded effort, to see through the realization of a weldable, four layer MMLC billet.

Only the aforementioned combination of layer design, interface design, processing schedule design, and development of suitable joining methods can result in realistic technology readiness for the MMLC. A technology readiness study, which estimates the maturity of a technology, will help to compare the readiness of the MMLC to existing and prior examples of cladding material developments. This study will also highlight the next major steps required for the MMLC to mature, and ultimately to be field-deployable in terms of manufacture, quality and validation of testing data, irradiation performance, and finally demonstration in a lead test assembly. Thus, a technology readiness study will be the final objective of this study, and will pave the way for future studies to increase the maturity of the MMLC.

Logical Path to Accomplishment:

Task 1: Laboratory and Industrial Scale Fabrication of the LWR MMLC: The forms of the proposed MMLC originally to be fabricated in this project are summarized in Table 1. In the end significant deviations were made from this scope due to findings during the course of the project.

MMLC Layer Order (ID→OD)	Processing Methods	Final Product	Major Technical Advantages
Zircaloy-4 Cr (barrier layer) Nb (barrier layer) 316SS *or* T91 *ZrN Surface Coating*	Tubular form: Concentric extrusion billet production, sleeve co-extrusion, tube drawing Core structures: Weld overlay	Tubular Form: Fuel cladding Core structures: Various	1) Removal of large fraction of Zr from the core, resulting in higher accident tolerance via reduced H_2 production in a severe accident 2) Reduced corrosion resistance during steady-state and accident conditions 3) Reduced susceptibility to through-wall hydride embrittlement 4) Reduced vulnerability to iodine stress corrosion cracking (I-SCC)

*Table 1: MMLC to be fabricated and tested in this study. Structural base layers are in **bold**, optional layers are in italics.*

At first, the proposed MMLC will undergo a review of available thermal, mechanical, and corrosion data, as well as thermodynamic and kinetic literature studies of phase stability, to ensure that the MMLC is optimally designed. Next, laboratory scale samples of both forms of the proposed MMLC will be produced using diffusion bonding and hot isostatic pressing (HIPing), and the quality of each interface will be tested using a combination of mechanical (tensile, bending) tests and optical/electron microscopy. Scanning electron microscopy (SEM) combined with energy dispersive x-ray (EDX) and transmission electron microscopy (TEM) analysis will identify any newly formed phases.

Of particular concern is the possibility for diffusional mixing of the MMLC layers, which function best with a smooth microstructural gradient between *distinct* layers. For example, should the Cr/Nb barrier layers

undergo diffusional mixing, they may not retain their ability to prevent Fe-Zr intermetallic formation. Therefore, diffusion couples of the MMLC will be aged under accelerated testing conditions. The testing temperature can be increased to determine diffusion coefficients (activation energies and prefactors) to quantify the speed of diffusional dilution in the MMLC. This accelerated thermal aging study will be performed to an equivalent end-of-life timeframe at service temperature, to both quantify the speed of diffusional dilution and set guidelines for required thicknesses of each layer to sustain performance throughout components' lifetimes.

Next, industrial scale (~100lb) samples of each form of the MMLC will be manufactured using domestically available facilities and best practices. This task will demonstrate the following: 1) Both forms of the MMLC can be processed without degradation of any layer or bi-layer interface, 2) The MMLC is more technologically ready by demonstrating domestic, industrial fabricability, and 3) The microstructural quality of the MMLC is preserved during processing. The methods of weld-overlay and co-extrusion are selected to process the MMLC as described below in Figure 2.

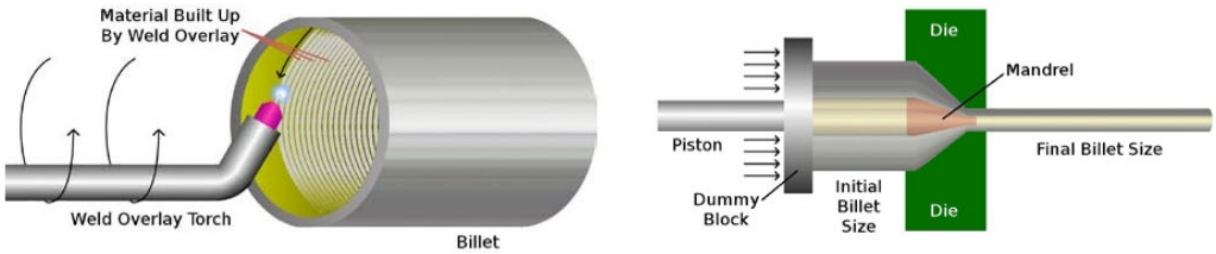

Figure 2: Processing methods of weld-overlay (left) and co-extrusion (right) to produce the MMLC

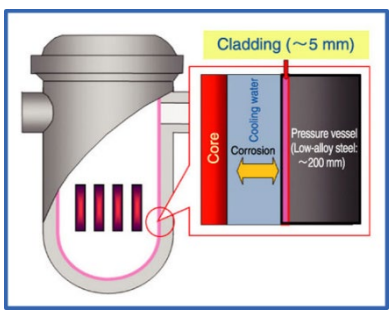

Figure 3: Schematic showing SS weld overlay cladding on LWR pressure vessel[10]

In *weld overlay*, a spiral or oscillating weld bead is deposited along one surface of the base material, leaving behind a mechanically intact overlaid layer. Oftentimes the welding torch is held stationary, while the billet is rotated around it. This process can be repeated multiple times to build up roughly 5mm of thickness of the subsequent layers. Following weld overlay, the multi-layer billet is *co-extruded*, or forced through a die and mandrel at a very high temperature, often 100-200ºC below the melting point of one layer. This results in a dramatic reduction in size and wall thickness in a short amount of time, and is the industrial process of choice for rapid manufacture of large quantities of seamless tubing. LWR Zircaloy fuel rods are currently made en masse using this process. Similar to our proposed research, "barrier fuel," or Zircaloy with a pure Zr inner liner, is currently made by exactly this method of concentric billet manufacture, sleeve co-extrusion, and tube drawing[9]. The weld-overlay technique is also used to apply 308SS onto carbon steel LWR vessels[10], as shown in Figure 3.

Task 2: MMLC Microstructural Evolution Studies: To ensure that deleterious intermetallic phases are not formed, samples of the MMLC will undergo long-term, accelerated diffusional mixing studies. Samples of the MMLC will be ampouled in argon, and heated to various high temperatures to induce thermal mixing and intermetallic formation. The rate of formation will be studied through the analysis in Task 4.

Radiation performance is most often the largest obstacle that must be overcome during the qualification of a new nuclear material. Therefore, it makes sense to start this process immediately following successful MMLC fabrication in Task 2. Sections of each MMLC interface, as well as each joint made between similar and dissimilar materials, will be subjected to both ion and neutron irradiation. Neutron irradiation up to 1dpa of interface, weld, and HAZ sections will be compared directly to self-ion (Ni-ion) irradiations at identical

[9] J. S. Armijo, H. S. Rosenbaum, C. D. Willams. "Method for making fuel cladding having zirconium barrier layers and inner liners." US Patent 5383228 (1995).
[10] Takeuchi, T. et al., *J. Nucl. Mater.*, 415(2):198-204, (2011).

doses, to confirm the suitability of ion irradiation for more accelerated testing. Ion irradiations will then continue to lifetime-relevant doses for each MMLC. Ni^{+2} ions will be used for self-ion irradiation in the case of SS316, and Fe^{+2} ions in the case that T91 is chosen. Proton irradiation to lower doses will also be performed, as recent studies have found that carefully planned proton irradiation experiments are becoming suitable surrogates for neutron irradiations[11].

In the end, because the MMLC billet has not yet been fabricated on an industrial scale, we were unable to complete this sub-task. However, by leveraging a National Scientific User Facility (NSUF) rapid turnaround experiment (RTE), we were able to irradiate the MMLC outer layer candidates to 0.5 DPA of neutrons in the MIT reactor and perform atom probe tomography (APT) analysis to gauge the readiness of this layer to resist neutron irradiation and embrittlement.

A special consideration not often encountered in ion irradiation studies concerns how to ensure that each bi-metal interface is exposed to proper irradiation conditions. In ion irradiation, three key differences limit its applicability to extrapolating performance to neutron environments: 1) Limited range of ions (1-2μm)[13], 2) Injection of self-interstitials suppressing void swelling[12], and 3) Dose rate dependence of the irradiation[13]. These are further aggravated by the need for the incipient ions to cause damage in the interface region, *without* coming to rest within the interface. This leaves a 200-500nm working window, which is nearly impossible to reliably reproduce. Therefore, the authors proposed to make *wedge samples* of each MMLC[14], as shown below for the LWR MMLC in Figure 4, which will expose every depth of the MMLC to the short range of ions.

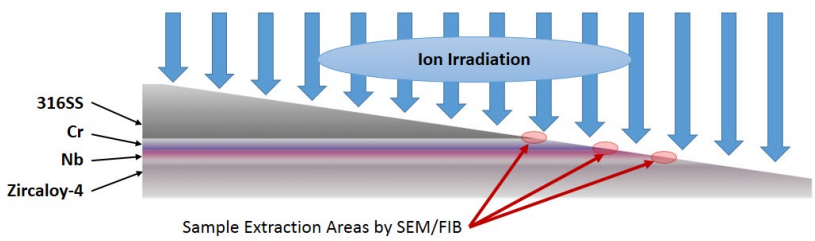

Figure 4: Ion irradiation of a sample "wedge" to expose all MMLC layers to the short range of ions

This way, a defocused ion beam can be broadly applied to the wedge sample, to irradiate every interface in the MMLC at once. Then, SEM/EDX will be used to locate the interface sections by elemental contrast, and the FIB will be used to extract TEM/APT samples from precisely these locations for further analysis. This solves problems (1) and (2) from above. Problem (3) can be addressed by irradiating samples of each MMLC to the same dose, but at different dose rates, to see if the results agree with each other. Finally, helium co-injection may be performed as deemed necessary to investigate the possibility of increased void swelling at bi-metal interfaces. This is due to a propensity for Ni to swell quickly under neutron irradiation, since He is formed under neutron irradiation via thermal neutron (n,α) reactions within Ni metal[15]. Of particular concern is the propensity of the 316SS layer on the LWR MMLC to swell should SS316 be chosen, which will be carefully investigated.

As mentioned above this sub-task is not yet complete, as we are awaiting final fabrication of the four layer MMLC following failure of the three layer MMLC billet.

Task 3: Corrosion, Oxidation and Stress Corrosion Cracking (SCC) Tests: This task has two key goals: 1) Ensure that corrosion performance of each as-manufactured MMLC is comparable to its most chemically robust layer, and 2) Investigate the effects of weld microstructures, microchemistries and defects on corrosion resistance of the steel/Zrly MMLC fuel cladding in PWR primary water, Corrosion tests in

[11] G. S. Was et al. "Emulation of reactor irradiation damage using ion beams", *Scr. Mater.* 88:33 (2014).
[12] E. Kuramoto et al., *JNM* 103:1091 (1981).
[13] N. I. Budylkin, et al. *J. Nucl. Mater.* 375(3):359 (2008)
[14] G. R. Odette et al. "On Using Test Reactor and Charged Particle Irradiations to Help Predict Neutron Irradiation Effects: Opportunities and Challenges." Ion Irrad. Workshop, Ann Arbor, MI, p. 22 (2014)
[15] M. L. Grossbeck et al. "Effects of Radiation on Materials." ASTM STP 1447, p. 530.

pressurized autoclaves and in high temperature (>1200°C) steam will be conducted up to 500 hours, to confirm accident tolerance of the proposed MMLC. In addition, autoclave corrosion testing in prototypical LWR conditions (up to 330°C, 15.5MPa, normal and hydrogen water chemistries) will be conducted to ensure corrosion resistance of the MMLC during steady state. Corrosion testing of welded MMLC endcaps in particular will be studied carefully. In addition, in-autoclave and ex-situ electrochemical tests will be performed to identify the stably passive layer formed the MMLC surfaces.

With this setup, several tests can be run to assess the performance of the passive layer, and the overall stability of the MMLC. The first test is the potentiodynamic scan. Using a potentiostat, the potential between the working electrode (the MMLC) and the counter electrode (W, Mo, or Ta) can be varied so the current between the electrodes can be measured. The resulting data gives the anodic and cathodic Tafel slopes, as well as the corrosion potential (E_{corr}) and corrosion current densities. The second test is the linear polarization resistance (LPR) measurement. This measurement utilizes the potentiostat in a similar manner as the potentiodynamic scan, but only looks at a very small potential range around E_{corr}. The data from an LPR test takes the form of a line, the slope of which, known as the polarization resistance, is related to the corrosion current density and the Tafel slopes. To measure the corrosion rate as a function of time, these two tests will be coupled. To prevent damage to the sample, the potentiodynamic scan will be run in two separate scans: one from approximately 0.5 V above the E_{corr} to E_{corr}, and one from 0.5 V below E_{corr} to E_{corr}. This allows the Tafel slopes to be measured, but prevents excessive damage to the sample. After these scans, an LPR test can be run, and the corrosion rate calculated via the Tafel slopes and the polarization resistance. By plotting these corrosion rates against the time at which the measurements are taken, the stability of the passive layer can be observed. The pitting potential can also be identified by dynamical scans and electrical resistance measurements.

Primary water SCC tests of the MMLC will be performed in a loop that can simulate the PWR primary water environment (325°C, 15MPa, ~1500ppm H_3BO_3, ~3ppm LiOH, ~25 cc/kg H_2). The loop is equipped with a controlled stress loading system, capable of on-line measurement of crack initiation in tensile specimens and crack growth rates. For oxidation studies, the assessment will focus on identifying the influence of external stress/strain on accelerating the oxidation behavior of the MMLC. The oxidation behavior under stressed conditions, due to residual stresses often found in welds and to stresses from loading as a structural material, is also a key to understand the SCC mechanism of the MMLC. The oxidation behavior under stress-free conditions will be first studied by directly exposing test samples to the primary water, followed by exposure to the same environment under varied magnitudes of stress, parallel to the composite interface, applied by both constant and cyclic loading. In addition, corrosion of every interface in the MMLC will be tested at once using a sample extracted by SEM/FIB as shown in Figure 4, to expose all interfaces to the primary water.

The initiation of SCC often requires precursors of corrosion pits or pre-existing flaws that form at the outmost metal surface. In this task, FIB will be employed to produce the precursors, of size from 10nm to microns, by creating designated cavities on the MMLC surface that would be equivalent to a preferred initiation site for SCC. During the SCC tests crack nucleation will be detected, and extension is monitored, in situ by direct current potential drop. Crack initiation events at <100μm are resolved, while crack length resolutions of about ±1μm are routinely measured. Therefore, these tests can (1) measure the response of MMLC joints to extreme environments, and (2) produce post-tested samples with well-controlled conditions for atomic/nano scale materials characterization. PWSCC performance of the MMLC will be compared to those of unclad Zircaloy-4 and SS316 or T91, respectively.

Task 4: Multi-Dimensional Material Joining and Characterization: Following the successful creation and analysis of the as-manufactured MMLCs in Task 2, studies on how best to join MMLC components to others in each reactor system will be undertaken.

The issue of sealing the endcaps of MMLC fuel cladding must be explored, as the endcaps must hold fission gas pressures of a few MPa at the end of life. Weld integrity and heat treatment will be essential, as will the development of a cost-effective, repeatable endcap joining process. A suite of different welding technologies, such as multi-layer V-groove MIG and/or TIG welding, friction stir welding, narrow gap welding, and laser welding of the MMLC to itself and to base metals will be performed in-house, within the collaborator's

facilities. In addition, two ASME code-approved welds will be allotted for each MMLC, to demonstrate the immediate code-approved ability to join MMLCs. Industry established welding and post-weld heat treatment (PWHT) procedures[16] will be used for each MMLC system's structural base material. Of critical importance is the minimization of any heat affected zones (HAZs) formed as a result of rapid cooling of the joint. While approved welding and PWHT procedures account for HAZ formation in single alloys, it must be demonstrated that joining the MMLCs in the same manner does not encourage the formation of a HAZ or degrade material properties. Modified heat treatments may be developed as needed to correct for differences in MMLC and single material joint quality, and avoid weld/HAZ sensitization.

As mentioned above, this task is not yet complete due to the lack of availability of the as-fabricated MMLC. A literature study of best welding methods was conducted by our collaborators at VTT Technical Research Centre in Finland, and they are seeking funding from the Finnish Academy of Sciences to continue this work (it was not secured during this NEUP project, so we are trying again).

Task 5: Multiscale Modeling of Long-Term and Severe Accident Oxidation Performance: A fully coupled, multiscale model of MMLC performance during operation and severe accidents will be developed to predict performance, validated as MMLC experimental data become available. BISON and RELAP-7 will be used to model a significant section of a full core, either ¼ core or a full assembly. Each MMLC fuel rod simulation in BISON will contain tens of mesoscale oxidation simulations using the HOGNOSE code, a CASL-developed, MOOSE-based mesoscale oxidation model. These will be informed by phase field simulations using MARMOT to gauge irradiation performance and microstructural evolution. The MARMOT simulations will be focused on the interaction of point defects generated by irradiation with the interfaces between layers in the MMLC. The goal of these simulations will be to predict irradiation induced microstructure evolution in the layers and how it impacts performance. We will accomplish this with simulations using the phase field method tightly coupled to mechanics and heat conduction. The length scales will be coupled using the MOOSE MultiApp/Transfer system. Predictions of irradiated microstructures from MARMOT models will be compared directly to experiments in Task 2. Finally, the validated models of microstructural evolution of the composite will be used in the BISON fuel performance model, to quantify the potential gains during steady-state and accident performance possible by using this MMLC.

Task 6: MMLC Technology Readiness Study: Following the results of testing in Tasks 1-5, a technology readiness study will determine the level of readiness of the MMLC on an established, industry standard scale of readiness from levels 1-9. Level 1 represents lab-scale experiments only, while level 9 represents proven capability in a full-scale commercial environment. The technology readiness study will identify major technological barriers overcome through this work, and will chart a path for continued development and demonstration of commercial viability.

Relevance and Impact of Outcomes: The proposed work directly addresses recently demonstrated accident tolerance needs of LWRs, as well as simultaneously solving joining problems and industrial-scale technology readiness issues of accident tolerant fuel cladding. In particular it addresses the issue of severe accident tolerance of LWR fuels in a way not currently being investigated by the nuclear materials community. It directly addresses the workscope outlined in FC-2.1, focusing on composite materials to perform functions that single alloys cannot. It also makes full use of NEAMS and CASL developed codes, all written in MOOSE, and coupled together. In addition, the direct stimulation of U.S. commercial interests with nuclear-relevant problems, combined with the training of students in both the science of nuclear materials and the technology of producing industrial-scale solutions to big problems, directly address the scientific, technological, workforce, training, and programmatic goals of the NEUP program.

Facilities Used to Execute the Scope: A combination of in-house and domestic commercial facilities will be used to execute the proposed workscope. Laboratory-scale coupons of the MMLCs will be fabricated by the investigators using commercial sources of raw materials, on in-house rolling mills, welders, and furnaces.

[16] R. E. Curtis, G. Dressler. "Effect of Thermomechanical Processing and Heat Treatment on the Properties of Zr-3Nb-1Sn Strip and Tubing." In *Zirconium in Nuclear Applications, ASTM STP 551*, pp. 104-128 (1974).

Commercial scale fabrication of MMLCs will be performed using established vendors and processing shops, identified through previous DOE-NE work by the PI. Sample preparation, characterization, analysis, and corrosion testing will be performed at the facilities of the PI, Co-PI, and Collaborators, on a suite of established corrosion facilities, mechanical testing machines, shared microscopy and microanalysis machines, and if required, outside analytical facilities identified in previous projects. Advanced welding and joining technique development and execution will take place mainly at the international Collaborator's facilities, with ASME welds to be performed domestically in an approved welding shop. Multiscale modeling of long-term MMLC performance will be performed by the domestic Collaborating institution. Finally, ion irradiation will take place at PI-U.

Unique Challenges and Enabling Innovations: While performing nuclear-grade joints using single metals is hard enough, performing multi-metal welds that perform as well (or better than) their single metal counterparts represents a unique and difficult challenge. The quality of *every* interface involved must be assured, from those intrinsic to each MMLC to those that join the MMLC to other core or vessel components. Fortunately, International University and Industry Partners are world renowned experts in the development and characterization of novel joining techniques, such as ultra-narrow gap welding. Filler metals and optimized welding processes for 316SS and Zircaloys[17] have already been developed. Therefore the chance of welding failure is slim. In addition, simply manufacturing a commercial amount of an MMLC on a university-scale budget could be a daunting task. Luckily, the PI and one Collaborator have established a network of domestic processing facilities for exactly this type of work. Thus the normal problems of making new industry connections and building mutual trust have already been solved.

Roles & Responsibilities of Team Members: MIT was responsible for overseeing the project, administration, and for delivery of all reports to DOE-NE. Laboratory-scale MMLC studies (Task 1) will be performed entirely at MIT, and at shared facilities within. Industrial scale MMLC manufacture (Task 2) were performed at domestic commercial facilities, coordinated by MIT. Welding and joining studies were be performed at Aalto University and VTT in Finland. Microstructural analysis (Tasks 1-3) will be performed at a combination of all partners. Static corrosion studies (Task 4), electrochemical tests, oxidation and SCC studies were performed at Virginia Tech. Multiscale modeling (Task 5) was performed at the University of Florida. The technology readiness study (Task 6) was headquartered at MIT, with input from all partners, both domestic and abroad.

Requirements and Quality Assurance: The research team accepted: (1) Commitment to reporting and budgeting, (2) 10 CFR 851, (3) Export Control, (4) Terms of Standard Research Subcontracts, (5) Commitment to prepare additional contract elements. Specifically, the research team will perform quality assurance related to (1) Procurement document control, (2) Data acquisition and collection, (3) Documentation, 4) Training and personnel qualifications, (5) Purchasing records, (6) Laboratory practices and maintenance of laboratory notebooks, (7) Control of measuring and test equipment. Reports will be provided by the research team at key deliverable dates. Peer review of manuscripts, presentation at national and topical meetings, and graduate student thesis defense will serve as independent review processes. A once-yearly meeting between all PIs, Co-PIs, and collaborators will serve as in-person coordination of the project. International Collaborators may join this meeting via videoconferencing.

[17] P. Rudling et al. "Welding of Zirconium Alloys." IZNA-7 Special Topic Report, ANT Int. (2007).

Summary of Changes to Project Scope as New Results Were Obtained

Significant changes to the MMLC layers, particularly the barrier layer compositions, were implemented as a result of what was learned in this project. The initial idea to use pure Cr or a Cr-Mo layer as a barrier layer were unable to be achieved due to the lack of ductility of pure Cr, and the inability to procure ductile foils of Cr-Mo. In addition, diffusion couple testing showed that the Nb barrier layer originally proposed did not bond well to the Zrly layer, acting as a release agent. **Therefore, the barrier layers were switched to Ti and V-4Cr-4Ti**, based on compatibility with Zircaloy-4 and combined compatibility with FeCrSi and Ti, respectively. In addition, V-4Ti-4Cr has already been demonstrated to resist radiation damage and void swelling when exposed to fast neutrons[18], in fact most V-alloys do so as long as the (Ti+Cr) content remains below 10 at. % (more will be generated due to V transmutation). This occurred mid-way through the project, thus the industrial-scale MMLC fabrication and diffusion couple studies were restarted midway through the project once it was realized that the original concept would not succeed.

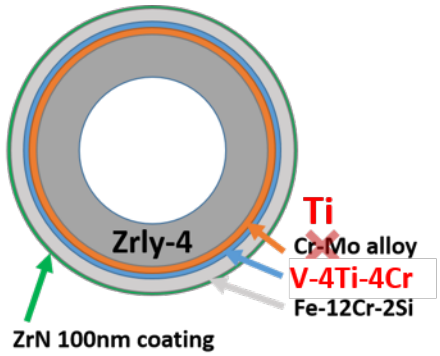

Figure 4: New MMLC layer structure used in the completion of much of the project

The outer corrosion-resistant layer was switched from stainless steel 316 to Fe-16Cr-2Si in the end, following a suite of corrosion and steam oxidation tests on Fe-12Cr-2Si, Fe-16Cr-2Si, and Fe-20Cr-2Si. This was done to avoid an austenitic, Ni-bearing material in the LWR core, which would have incurred significant neutron penalties, helium gas production, and embrittlement. This change was conducted relatively early in the project and resulted in significantly improved MMLC outer layer performance, thus tasks revolving around this outer layer choice were not noticeably affected.

Finally, due to the delays in MMLC fabrication (much of which came from a nine-month battle within MIT to classify the MMLC production as a sub-contract, so as not to incur unbudgeted overhead costs), we have not yet finished a successful four-layer MMLC fabrication. In order to meet the project milestones, **a three layer MMLC billet was fabricated and processed on the industrial scale**, consisting of a Zircaloy-4 layer, a Ti barrier layer, and an Fe-12Cr-2Si overlay. It was hoped that rapid processing and extrusion would avoid the formation of too many intermetallics. However, one major change between previous efforts and this MMLC billet fabrication was the use of hot isostatic pressing (HIPing), performed to improve the bond between layers. This turned out to be a mistake, as **interactions between the carbon steel used to can the MMLC billet and the Ti layer created a layer of what appears to have been liquid eutectic alloy formation**, which penetrated rapidly into the Ti-FeCrSi interface and caused cracking of the outer FeCrSi layer. This was revealed by dye penetrant testing. It was decided not to attempt extrusion of this cracked billet, as though it would have technically satisfied the milestone to extrude, it would have resulted in failure. Instead we are continuing to fabricate a smaller (~50lb.) four layer MMLC billet with the required V-4Ti-4Cr barrier layer, and *without* HIPing. This is expected to be completed at the end of the 2019 calendar year.

[18] Chung, H. M., B. A. Loomis, and D. L. Smith. "Properties of V-4Cr-4Ti for application as fusion reactor structural components." *Fusion engineering and design* 29 (1995): 455-464.

Chapter 2 – Laboratory Scale MMLC Fabrication and Radiation Studies

The purpose of this section is to summarize the findings of the initial diffusion bonding study of this project, when the four MMLC layers were conceived as Zrly/Nb/Cr/FeCrSi and Zrly/Ti/Cr/FeCrSi. The basis for the design of the MMLC is a thick layer of Zircaloy 4 constituting the majority of the volume of the composite, with a thin oxidation–resistant Fe- Cr-Si layer on the outside of the composite cladding tube. The challenge arises in creating a metallurgical bond between these layers that will remain robust across a wide range of temperatures. In order to achieve this, we are pursuing a multilayer bonding approach in which layers of mutually compatible metals are used in order to achieve metallurgical bonding.

The layers were bonded using the hot isostatic pressing (HIP) method of diffusion bonding. Samples were bonded at a temperature of 1000°C and pressure of 14,750 PSI for 4 hours. HIPing was performed by Bodycote at their facility in Princeton, KY. The two layered composites that were produced were Zircaloy4/Nb/Cr/Fe–12Cr–2Si and Zircaloy–4/Ti/Cr/Fe–12Cr–2Si. Figure 5 demonstrates that the Nb-containing composite essentially fell apart during aging. This was due to insufficient bonding between the Nb and Zr layers, most likely due to the dissimilarity in crystal structures with Nb being BCC and Zr being HCP.

After diffusion bonding, the samples were sealed in evacuated quartz ampoules (in order to prevent oxidation during aging) and aged at 700°C for 4, 8, and 16 days. Following aging, the samples were cut, polished, and examined using scanning electron microscopy (SEM) for imaging along with energy dispersive x–ray spectroscopy (EDX) for compositional analysis. This composition data was then analyzed in order to understand the interdiffusion between the layers of the composite. Calculations and diffusion data analysis were performed using the pydiffusion package within python. The diffusivities were calculated using the Sauer-Friese method as implemented in pydiffusion, which is more convenient in the sense that calculation of the Matano plane is not necessary for the calculation of diffusion coefficients, but the results can be somewhat erroneous in the extremes of the composition profile[19].

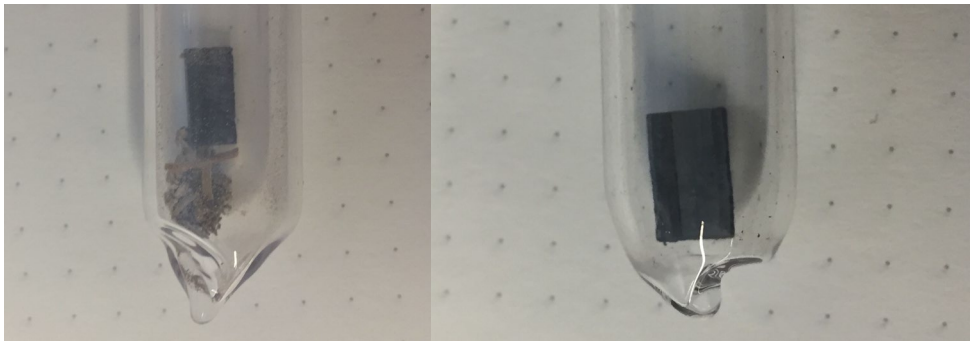

Figure 5: (left) Zircaloy–4/Nb/Cr/Fe–12Cr–2Si after 4 days of aging at 700°C, and (right) Zircaloy–4/Ti/Cr/Fe–12Cr–2Si after 4 days of aging at 700°C

[19] A. M. Delhaise and D. D. Perovic. Study of solid-state diffusion of bi in polycrystalline Sn using electron probe microanalysis. *J. Elect. Mater.*, 47(3):2057–2065 (2018).

As-HIPed Layer Composition and Linescans: The initial composition profiles of the as–bonded composite, as shown in Figure 6 and Figure 7, demonstrate significant interdiffusion and metallurgical bonding between Zr and Ti, which is to be expected considering their similar chemical properties as well as similar crystal structures. The composition profiles at the Ti/Cr interface and at the Cr/Fe–12Cr–2Si interface appear to be much sharper than in the case of Ti and Zr. This is beneficial, as it indicates that diffusion of Cr and Si away from the outer layer will be minimal. Considering that Si and Cr are critical to the oxidation resistance of this outer layer, this is important for the oxidation performance of the composite.

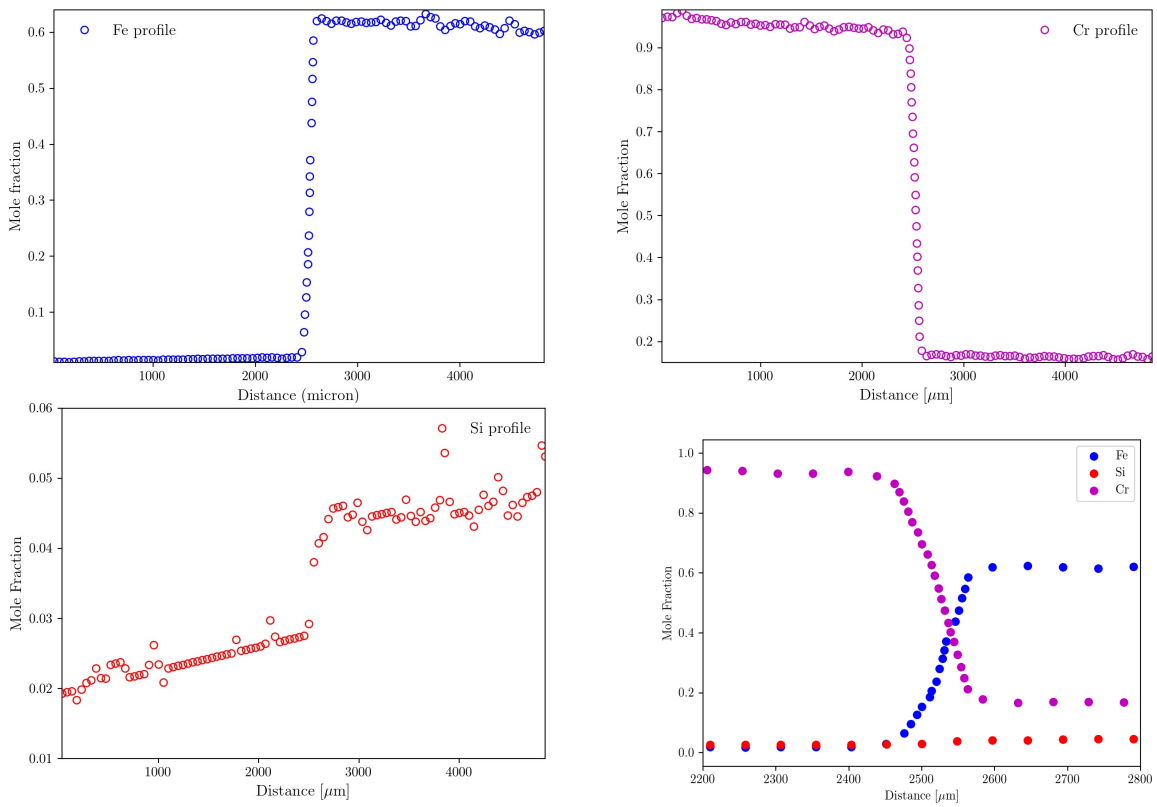

Figure 6: Interfacial composition profiles for (upper-left) Fe, (upper-right) Cr, (lower-left) Si, and (lower-right) a combined profile in the as–bonded sample.

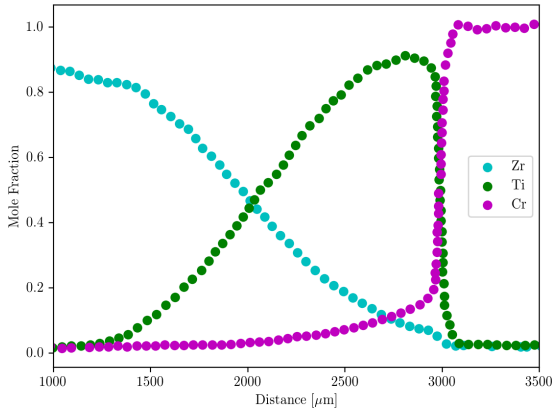

Figure 7: Interfacial composition profiles for Zr, Ti, and Cr in the region containing the Zr/Ti interface and Ti/Cr interface. This plot demonstrates significant interdiffusion of Ti and Zr.

4 Day Aged Sample

Cr/Fe-12Cr-2Si Region: EDX elemental maps in Figure 8 show that the Fe-12Cr-2Si/Cr interface remained fairly sharp without any secondary phase precipitation being observed. The EDX–measured composition profile of Cr and Si at the Fe–12Cr–2Si interface, after 4 days of exposure at 700°C, is shown in Figure 9. There appears to be quite a bit of noise in the Si data, so although we will analyze this data, the data from the 8 day and 16 day exposures will be relied on for quantification of the Si diffusivity. As can be observed in Figure 10, the Cr diffusion data shows an approximately constant diffusivity with respect to concentration, with the diffusivity being

$$D_{\mathrm{Cr}} \approx 10^{-15}\, m^2/s$$

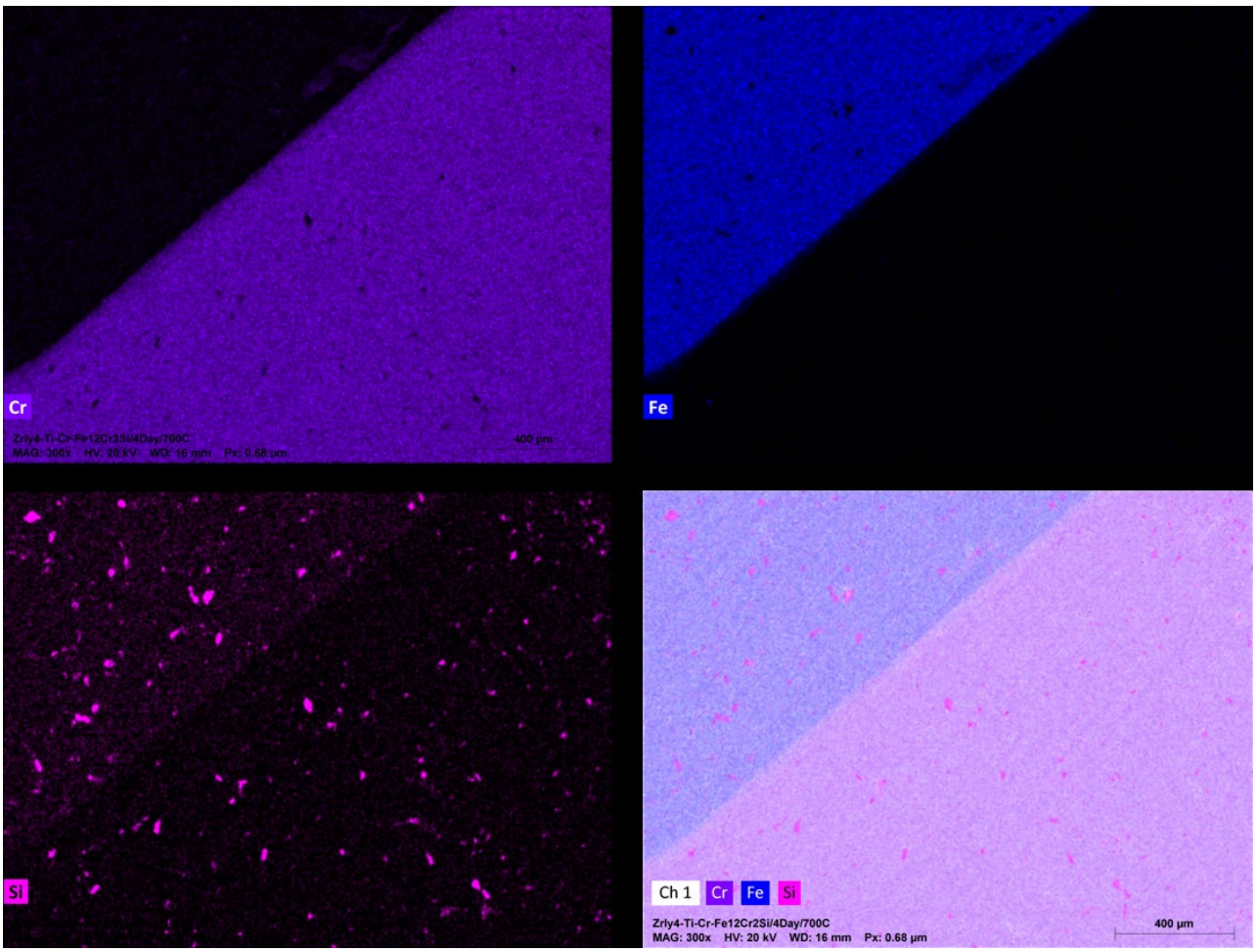

Figure 8: EDX map of the Cr/Fe-12Cr-2Si interface showing very little interaction, indicating an excellent bond. The Si spots present throughout the image are most likely particles of SiC or SiO_2 embedded into the material from polishing, and are not representative of the actual metals' microstructures.

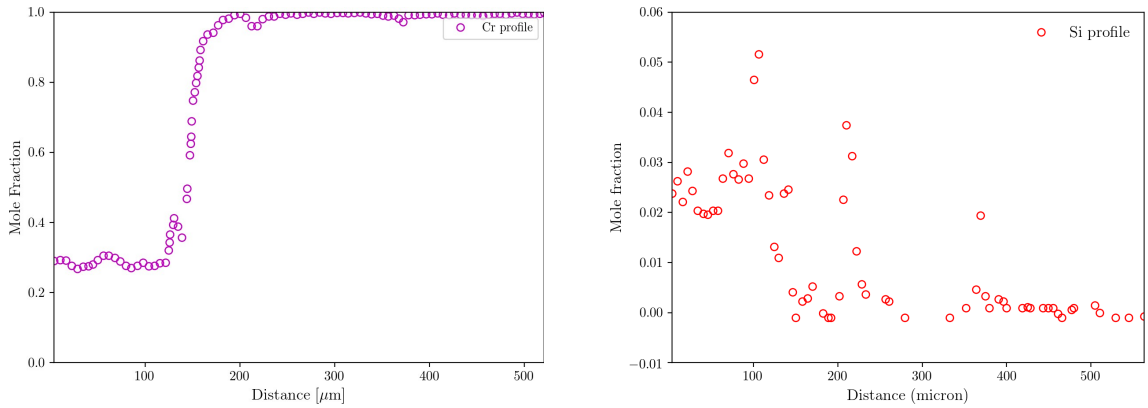

Figure 9: (Left) Measured EDX Cr composition profile in the Fe–12Cr–2Si/Cr interface region. (Right) Measured EDX Si composition profile in the Fe–12Cr–2Si/Cr interface region. Both profiles were measured in the sample aged for 4 days at 700°C after bonding.

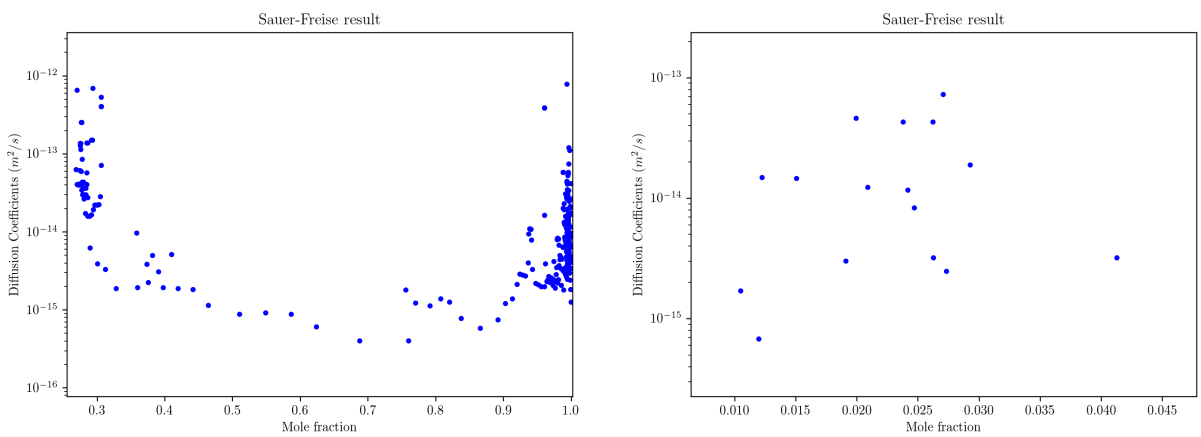

Figure 10: (Left) Cr and (right) Si diffusion coefficients as a function of composition in the Cr/Fe-12Cr-2Si interfacial region. The Si diffusivities appear unreliable in this case.

Ti/Zr/Cr Region: The EDX maps in Figure 11 and Figure 12 demonstrate the presence of a network of both Zr- and Cr-rich zones in the Ti layer. The Cr-rich regions are likely $TiCr_2$ intermetallic precipitates. The Zr-rich regions, on the other hand, are likely grain boundaries which serve as fast diffusion pathways, thus leading to a larger Zr concentration at the grain boundaries. As shown in Figure 13, in the samples which were aged for only 4 days, there appears to be a copious amount of laves intermetallic phase formation. Considering that intermetallic phases tend to be relatively brittle, this could have some deleterious effect on the mechanical properties of the composite. The diffusivites are somewhat obscured by the formation of the laves intermetallic phase of the type (Ti, Zr)Cr_2. Therefore, the data shown in Figure 14 are just for the region where interdiffusion in the solid solution occurred. The Zr calculated diffusion coefficients are shown in Figure 15, with the diffusion coefficients which were obscured by intermetallic formation also being shown. The Zr diffusion coefficient in the Ti layer can be estimated as

$$D_{Zr} \approx 2 \times 10^{-15}\, m^2/s$$

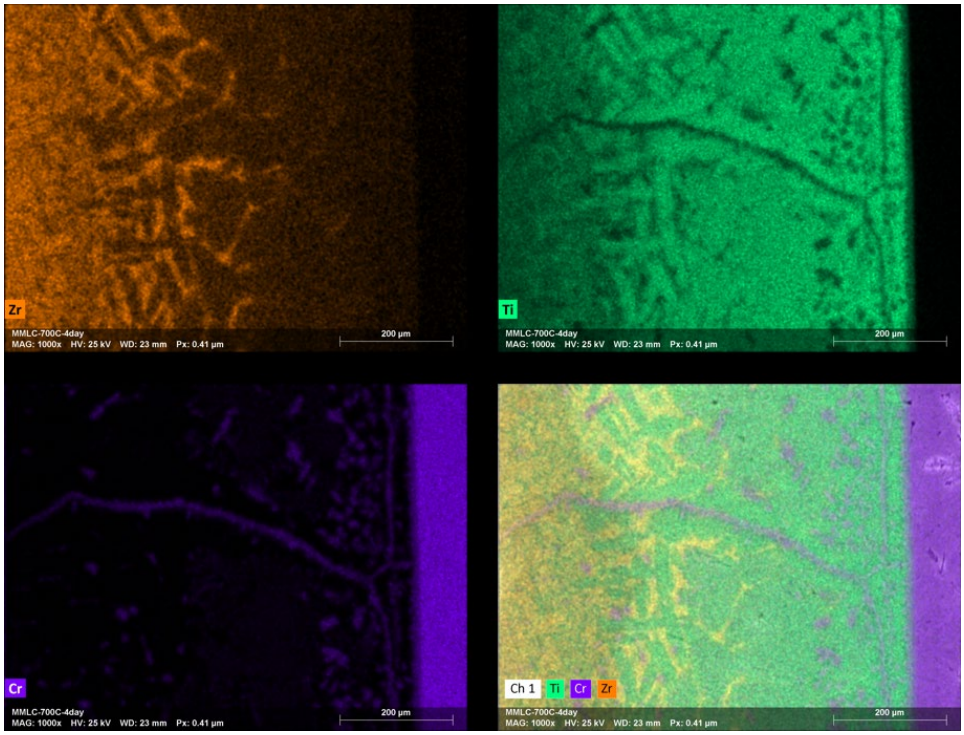

Figure 11: Low magnification EDX map showing both Ti/Cr and Zr/Ti interfaces, with extensive, deleterious secondary phase formation evident

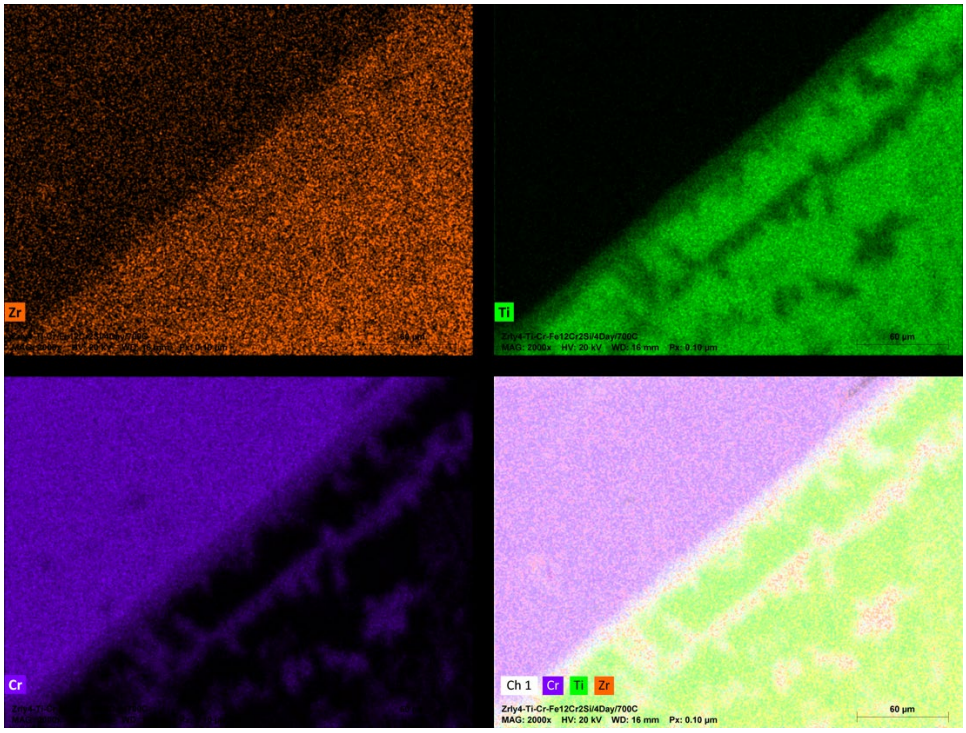

Figure 12: Ti/Cr interface EDX map, with intermetallics likely formed between Zr diffusing through the Ti layer and Cr

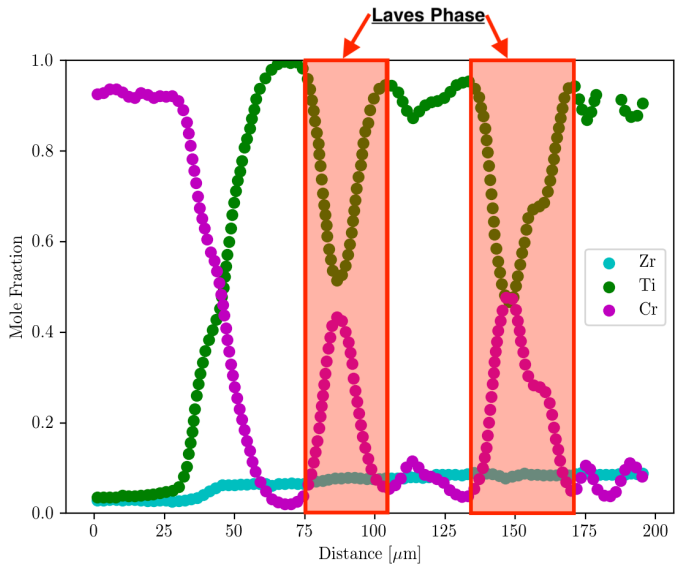

Figure 13: EDX composition profile in the Zr/Ti/Cr region, with the red–shaded regions indicating the presence of (Ti,Zr)Cr_2 laves phase.

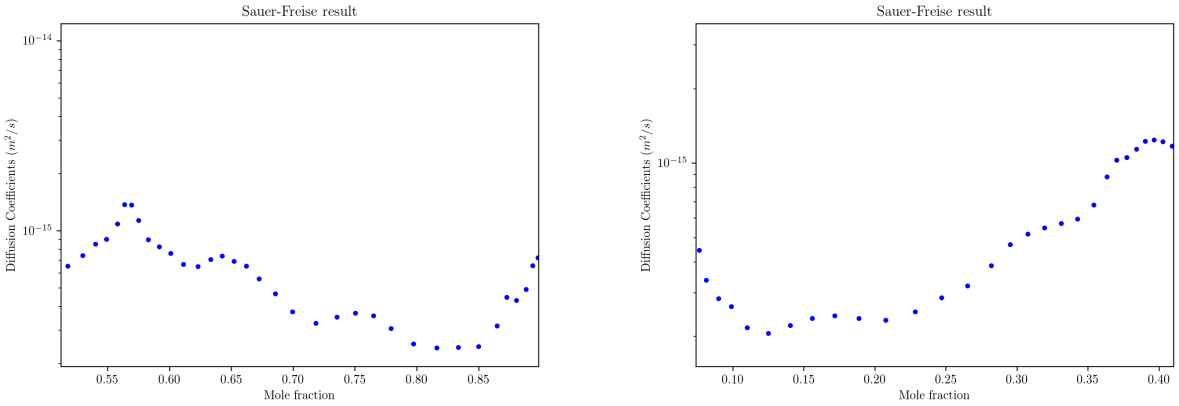

Figure 14: Cr and Ti diffusion coefficients in the Ti/Cr interfacial region as a function of composition. These diffusivities are from the 4 day aged sample.

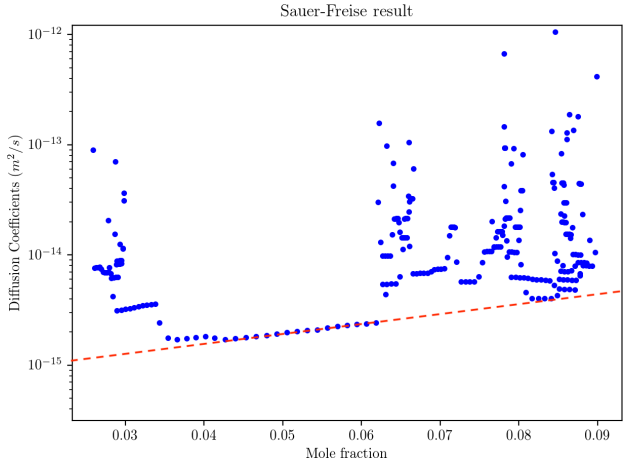

Figure 15: Zr diffusion coefficient at the Ti/Cr/Zr interface, plotted as a function of Zr mole fraction

8 Day Aged Sample

Fe–12Cr–2Si/Cr Region: As is evident in Figure 16, the Fe-12Cr-2Si/Cr interface remains sharp after significant time at high temperature, with no precipitation of secondary phases. Figure 17 shows the composition profile for Fe, Cr, and Si as measured with EDX in the sample aged for 8 days. The interface remains quite sharp, with no intermetallic precipitates apparent. The slight discontinuities are due to residual SiC from the metallurgical polishing process. Figure 18 shows the calculated diffusion coefficients from that composition profile, showing relatively uniform diffusion coefficients for Fe and Cr. That being said, slight depressions in the diffusion coefficient plots are apparent. Figure 19 shows the Si diffusion coefficient calculated from the composition profile in Figure 17. The diffusion coefficient can be roughly estimated at

$$D_{\mathrm{Si}} \approx 10^{-14} m^2/s.$$

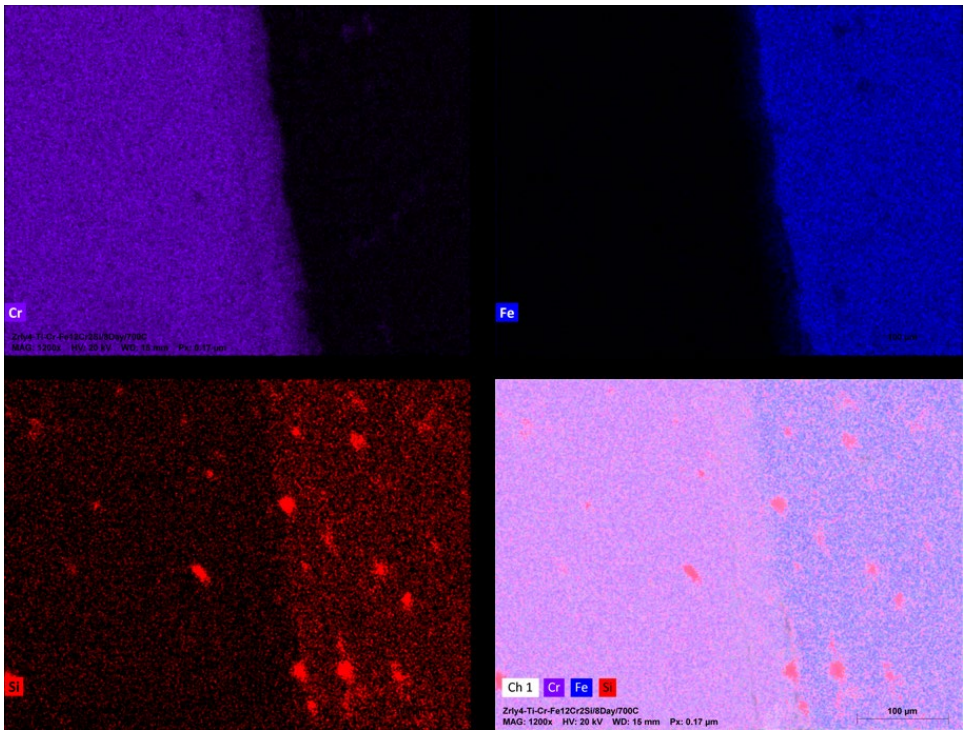

Figure 16: EDX map of the Fe-12Cr-2Si/Cr interface, showing both little/no diffusional dilution and no secondary phase formation. Si pieces are likely embedded SiC and/or SiO_2 particles left over from polishing, further evidenced by their higher presence in the softer Fe-12Cr-2Si layer compared to the harder Cr layer. They are not present in the metals by themselves.

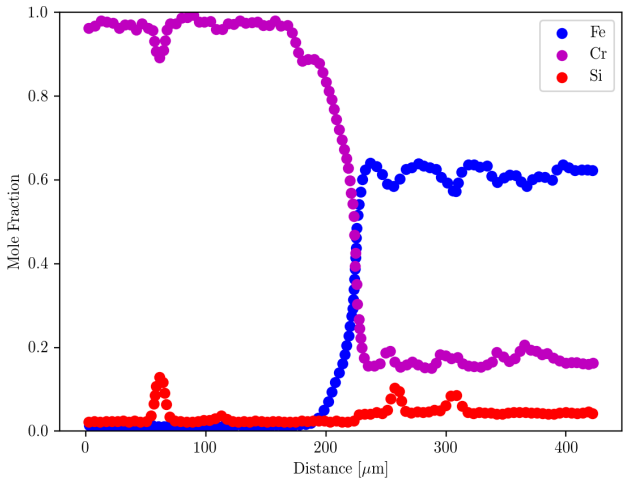

Figure 17: EDX compositional profiles of Fe, Cr, and Si in the Fe–12Cr–2Si/Cr interfacial region of the sample aged for 8 days at 700°C.

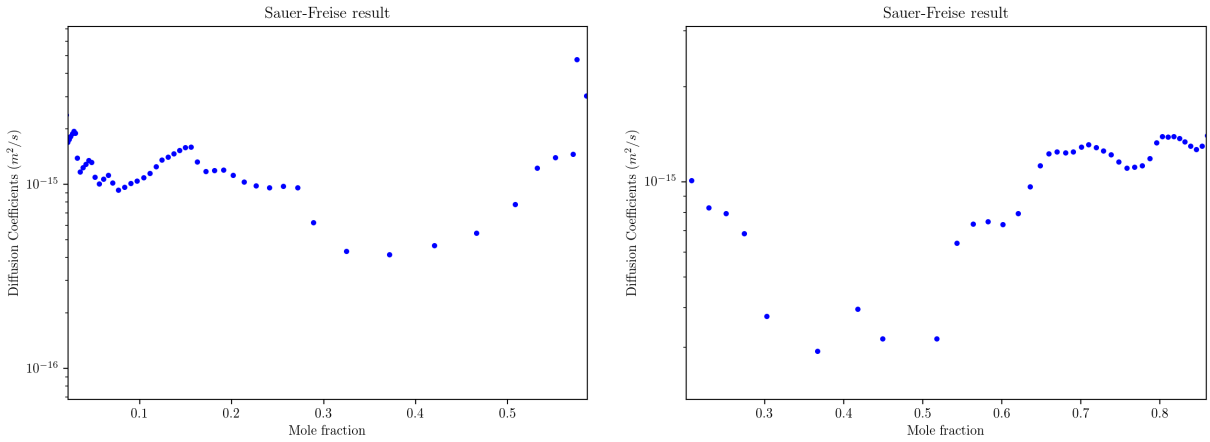

Figure 18: Fe and Cr diffusion coefficients calculated from composition profile in the Fe– 12Cr–2Si/Cr interfacial region of the sample aged for 8 days.

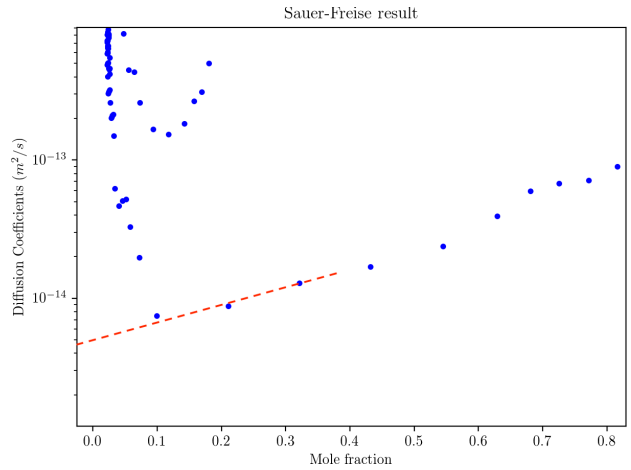

Figure 19: Si diffusion coefficient calculated from composition profile in the Fe–12Cr–2Si/Cr interfacial region of the sample aged for 8 days.

Ti/Zr/Cr Region: In the EDX maps in Figure 20 and Figure 21, we see that Cr-rich precipitates are present even at the Zr/Ti interface, as well as along a grain boundary within the zircaloy. These precipitates are likely $ZrCr_2$ intermetallics. So, an appreciable amount of Cr was able to diffuse across the thin Ti foil (~270µm thick). Figure 22 shows the measured composition profile in the Zr/Ti/Cr interfacial region. Figure 23 shows the diffusion coefficients of Ti and Zr calculated from this profile. Figure 24 shows the Cr diffusivity calculated from the composition profile in Figure 22.

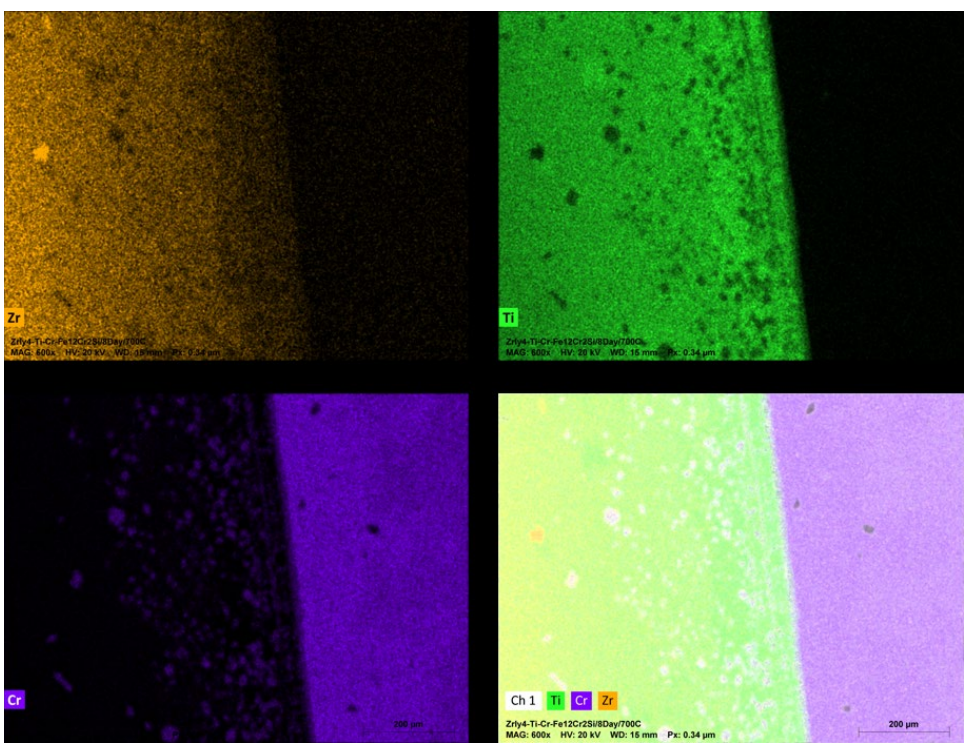

Figure 20: EDX map of the Cr/Ti interface. Cr-rich precipitate morphology is coarser and more spherical compared with the 4-day aged sample.

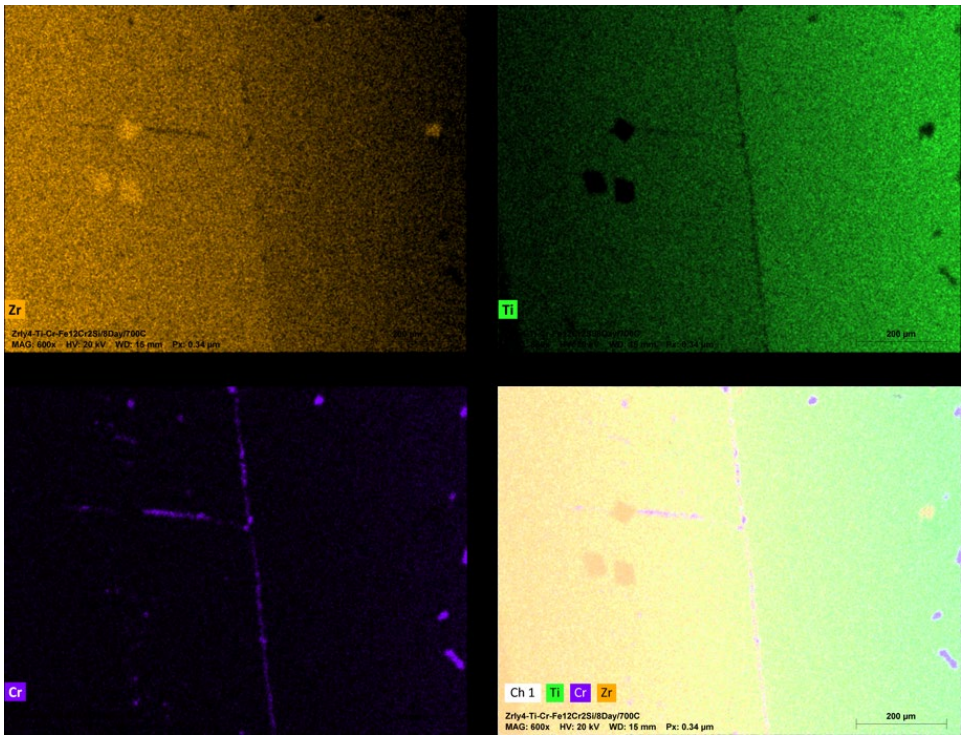

Figure 21: EDX map of the Zr/Ti interface, showing significant diffusional dilution as expected from their high compatibility from the Ti-Zr binary phase diagram

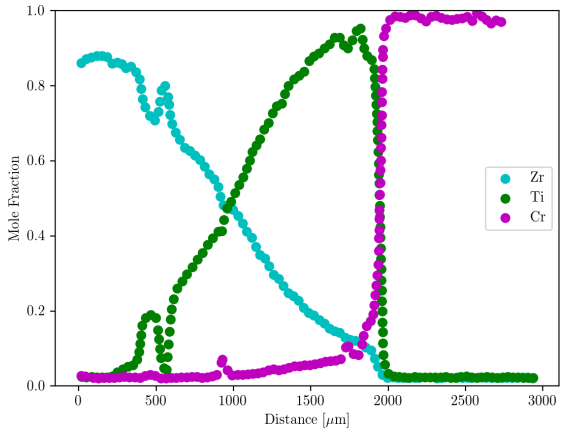

Figure 22: EDX measured Zr, Ti, and Cr composition profiles in the 8 day aged sample, showing significant Zr/Ti interdiffusion and little to no Cr/Ti interdiffusion.

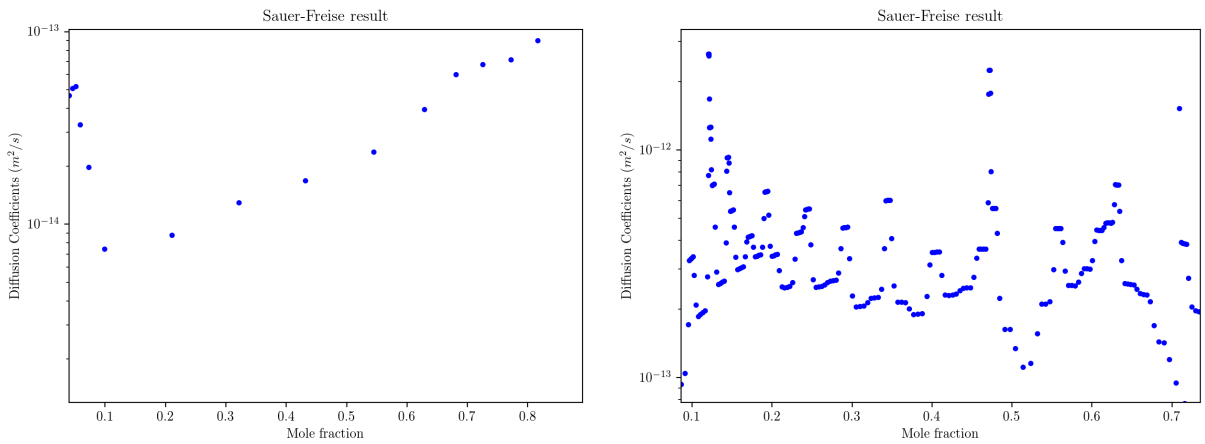

Figure 23: Ti and Zr diffusion coefficients calculated from composition profile in the 8 day aged sample

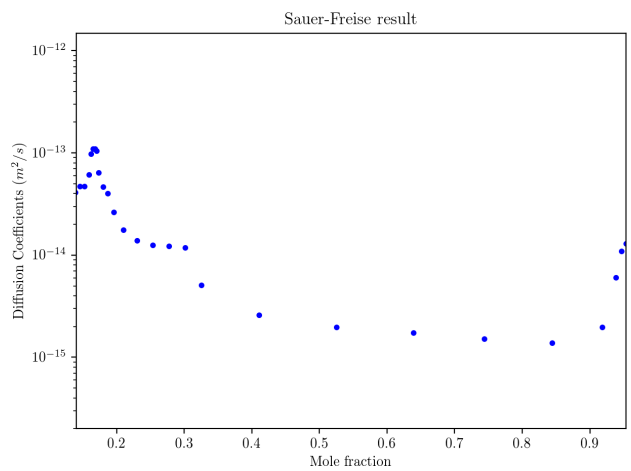

Figure 24: Cr diffusion coefficient calculated in the Zr/Ti/Cr interfacial region in the 8 day aged sample

16 Day Aged Sample

Fe–12Cr–2Si/Cr Region: The EDX map in Figure 25 shows once again that the bond between Fe-12Cr-2Si and Cr is excellent, showing minimal interdiffusion and no deleterious phase formation. Figure 26 shows the measured Fe–12Cr–2Si/Cr interfacial composition profile in the sample exposed to 700°C for 16 days. Note the still sharp composition profile. The Fe and Cr diffusion coefficients calculated from this profile are shown in Figure 27. The calculated Si diffusion coefficient plot is shown in Figure 28.

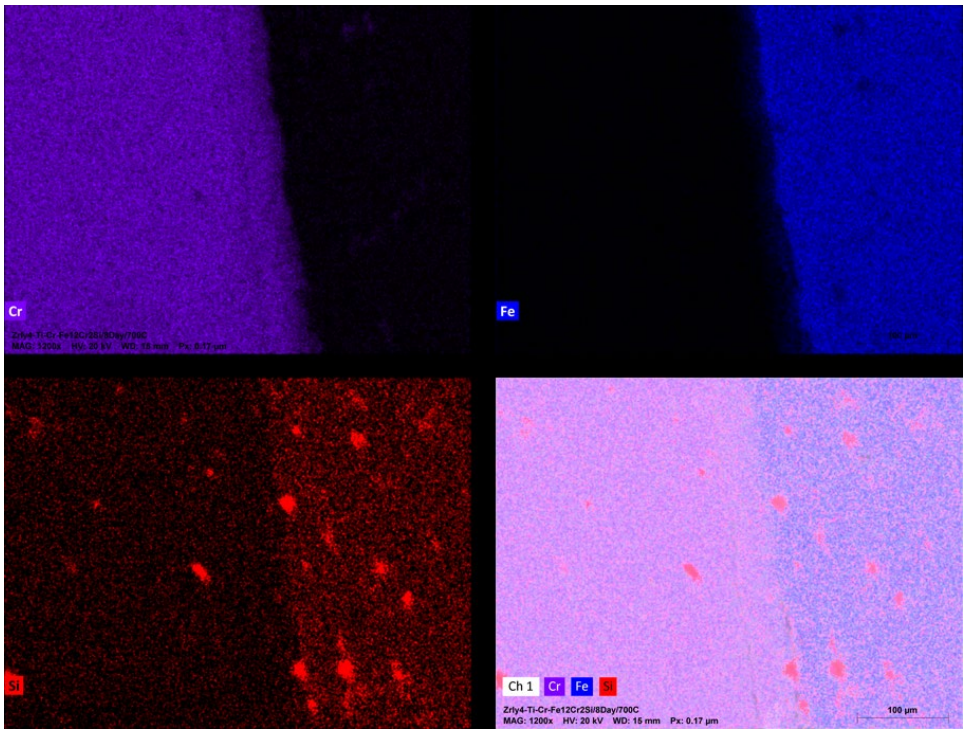

Figure 25: EDX map of the Fe-12Cr-2Si/Cr interface, again showing both little/no diffusional dilution and no secondary phase formation. Si pieces are likely embedded SiC and/or SiO_2 particles left over from polishing, further evidenced by their higher presence in the softer Fe-12Cr-2Si layer compared to the harder Cr layer. They are not present in the metals by themselves.

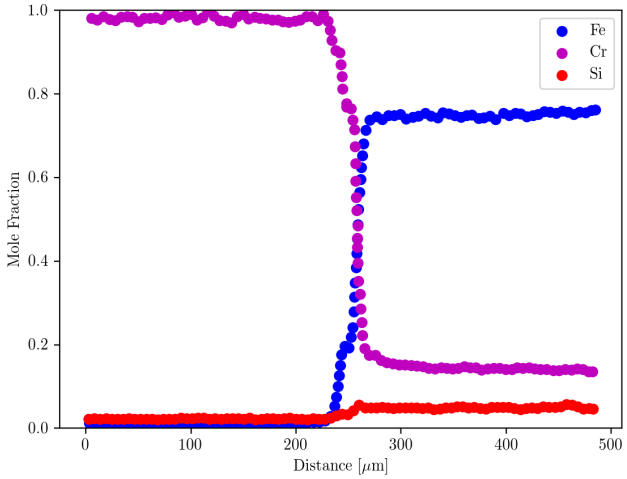

Figure 26: EDX composition profile in the Fe–12Cr–2Si/Cr interfacial area in the 16 day aged sample showing the sharp, yet continuous, interfaces which one would want in a successful MMLC joint.

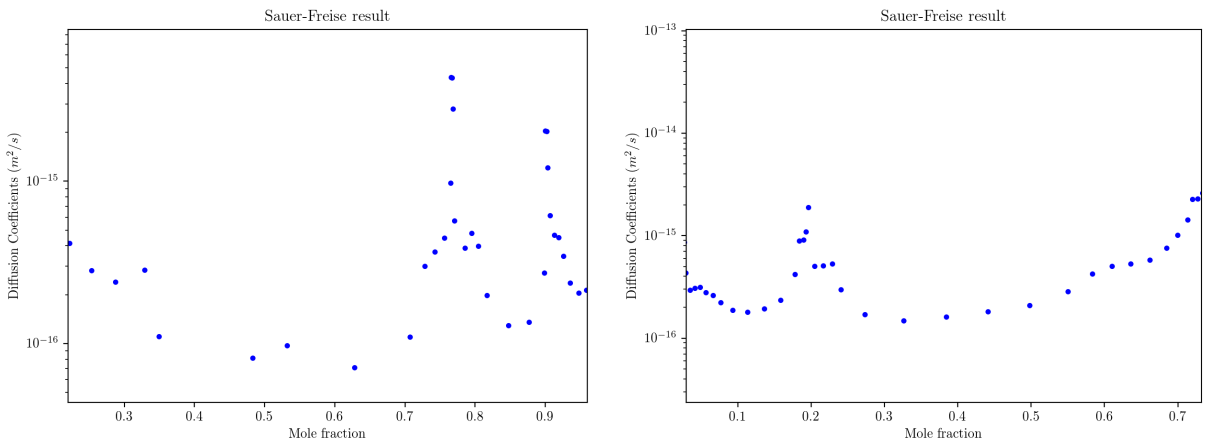

Figure 27: Calculated Cr and Fe diffusion coefficients in the Fe–12Cr–2Si/Cr interfacial region in the 16 day aged sample

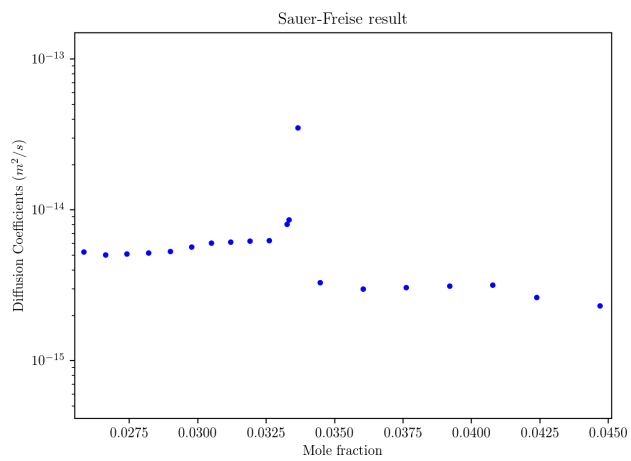

Figure 28: Calculated Si diffusion coefficient in the Fe–12Cr–2Si/Cr region in the 16 day aged sample.

Zrly/Ti/Cr Region: There was an error in the diffusion bonding for this sample as is evident in Figure 29 and Figure 30, which caused the Zircaloy–4 layer to not adhere and bond to the Ti layer. This is likely due to being at the edge of the diffusion couple, and it appears that a piece of the graphite foil (used to prevent oxidation) was caught between the layers, which hindered bonding. We can see here that the Ti diffusion data shows the manner in which Ti diffusion is slow within Cr but rapid within Zr.

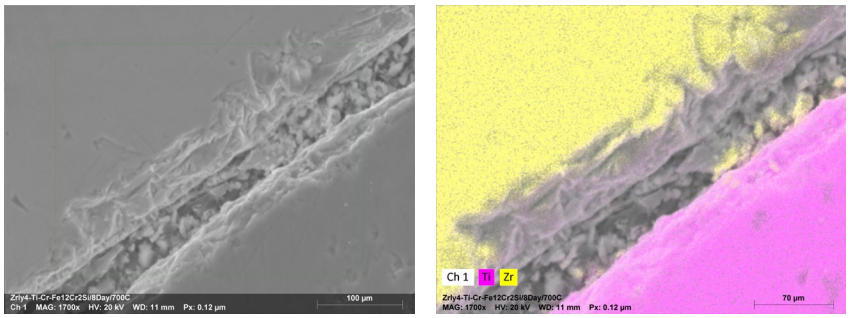

Figure 29: SEM image (left) and EDX map (right) of the gap showing a lack of bonding

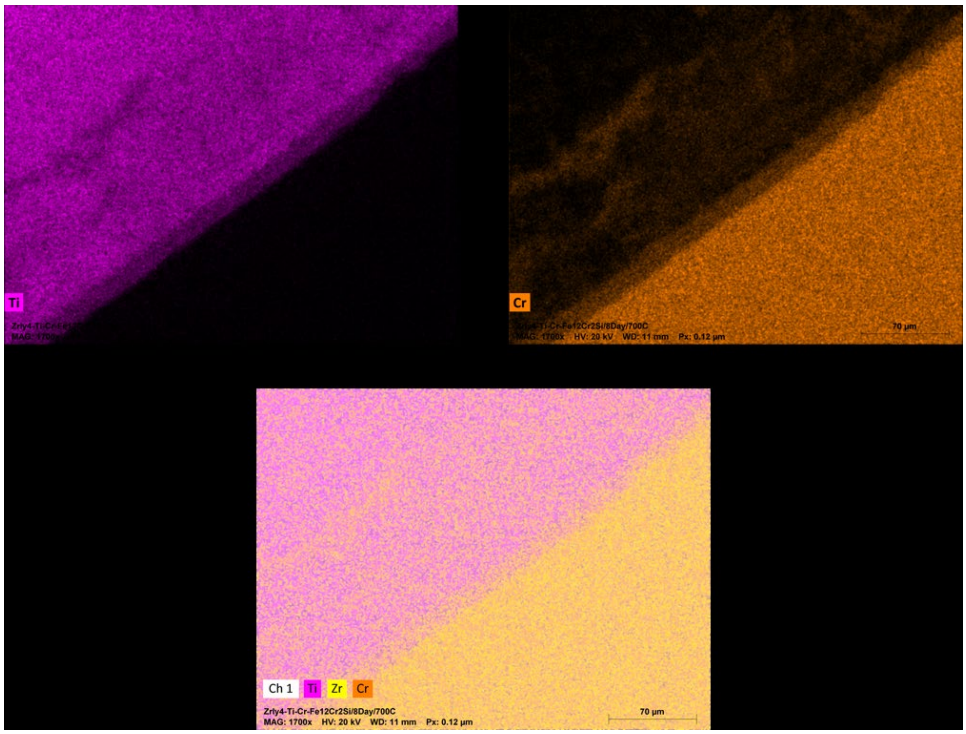

Figure 30: EDX map of the Ti/Cr interface showing a thin (~5µm) layer of interdiffusivity, but no visible deleterious phase formation. This indicates that the barrier layers are compatible as hoped.

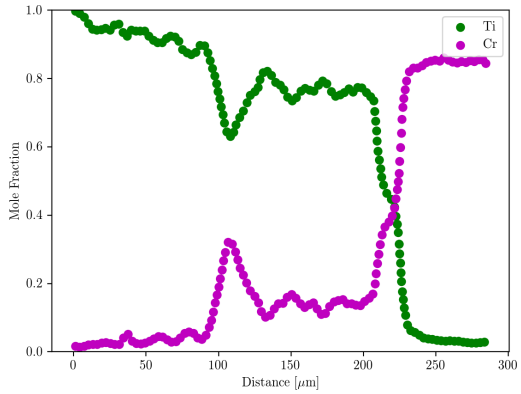

Figure 31: Ti and Cr composition profiles in the Ti/Cr interfacial region from the 16 day aged sample

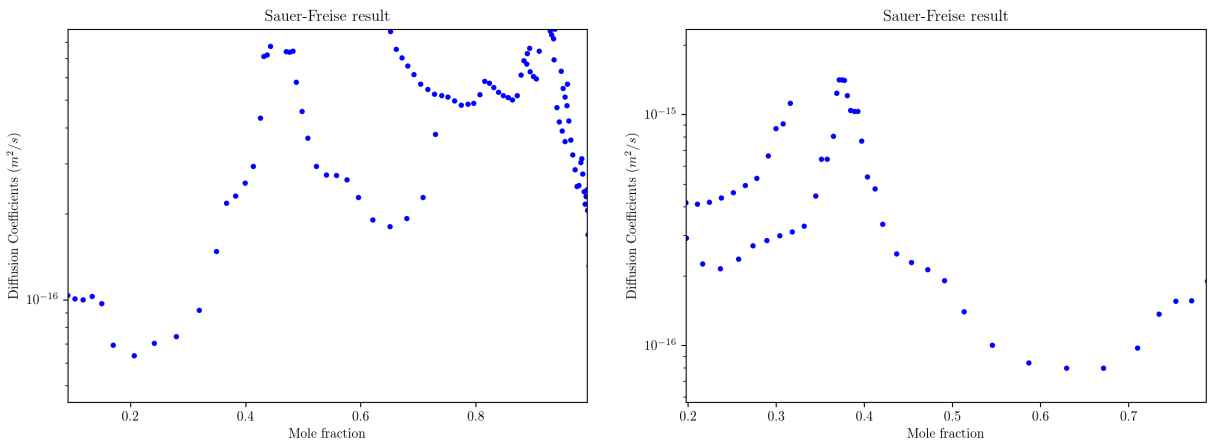

Figure 32: Calculated Ti and Cr diffusion coefficients from the 16 day aged sample

Neutron Irradiation and APT Characterization of Fe-16Cr-2Si and Fe-20Cr-2Si: As corrosion tests continued (see Chapter 3) it became clear that Fe-12Cr-2Si would not contain enough Cr to qualify as accident-tolerant, mainly based on steam oxidation performance. Therefore, once an opportunity arose to sneak some specimens of FeCrSi into an MIT reactor (MITR) irradiation, only Fe-16Cr-2Si and Fe-20Cr-2Si were utilized. Specimens were irradiated in the MITR in the PWR water loop at a coolant temperature of roughly 290°C. The capsule was not instrumented, though due to the small size (~2mm on a side) of the specimens it is not expected that gamma heating would further increase this temperature significantly. An NSUF RTE proposal was accepted to perform atom probe tomography (APT) analyses on the materials, to look for the presence and extent of irradiation-induced precipitate formation.

Shows that Fe-16Cr-2Si exhibited sufficiently few and separated precipitates that irradiation, at least to this low dose level, will not be a concern. By contrast, shows that in Fe-20Cr-2Si the formation of significant, directional precipitates is already found to occur, precluding the use of this alloy in any true nuclear context. This, combined with the steam oxidation results (Chapter 3, to follow), suggest that Fe-16Cr-2Si is the most ideal composition within the Fe-Cr-2Si space to choose as the MMLC outer layer. Further refinement to balance less oxidation in steam (more Cr is better) and less radiation-induced continuous precipitation (less Cr is better) should be conducted to find the best outer MMLC coating material.

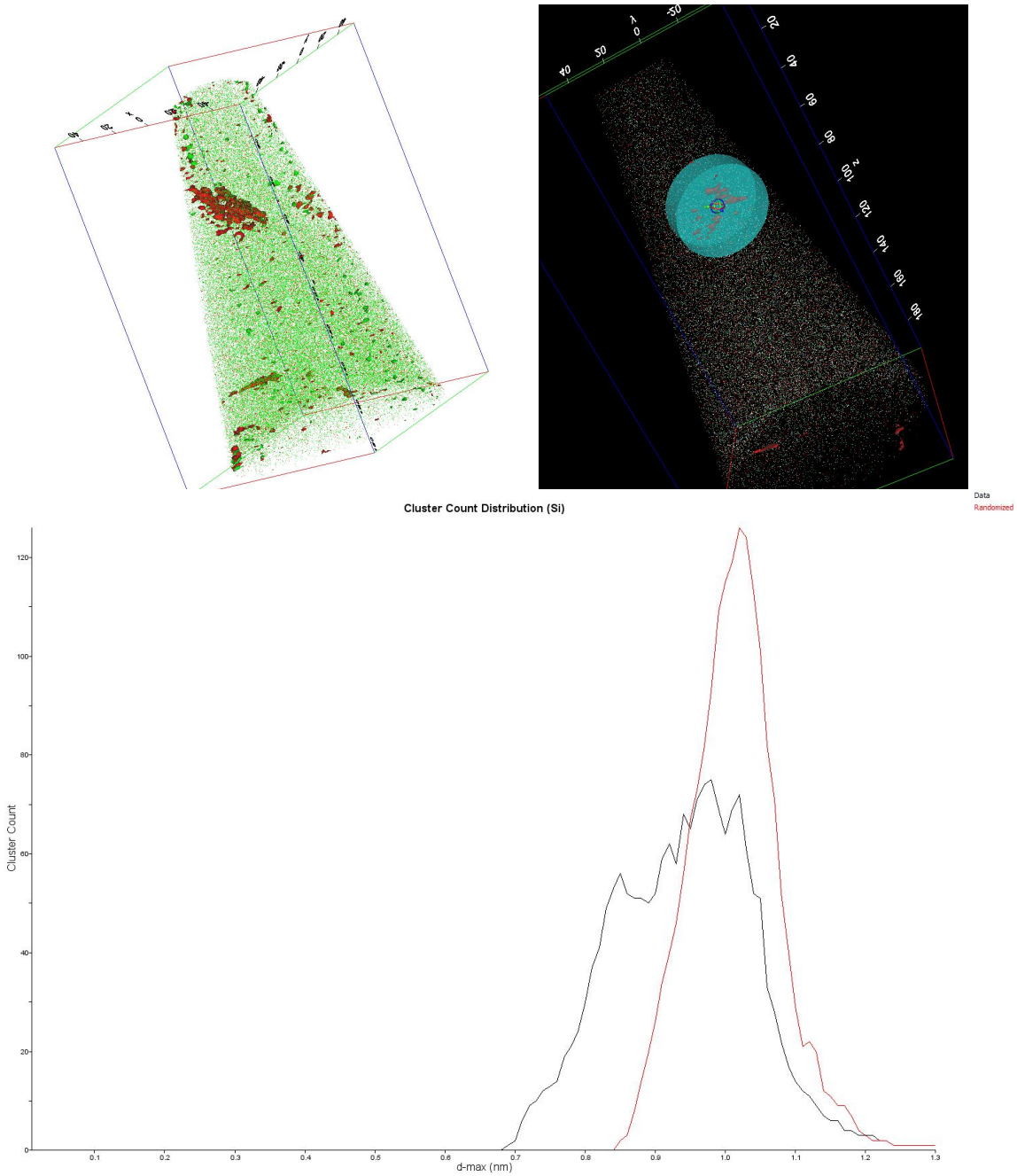

Figure 33: APT analysis of Fe-16Cr-2Si, showing (top-left) isosurfaces of 6% Si (red) and 22% Cr (green). The highly discontinuous nature of precipitation in Fe-16Cr-2Si shows better performance compared to that of Fe-20Cr-2Si, which exhibits "stringers" of high-Cr precipitates. (Top-right) region of interest from which (bottom) Si cluster size data were extracted, showing an average cluster size of about 1 nm. Axis scales are in nanometers.

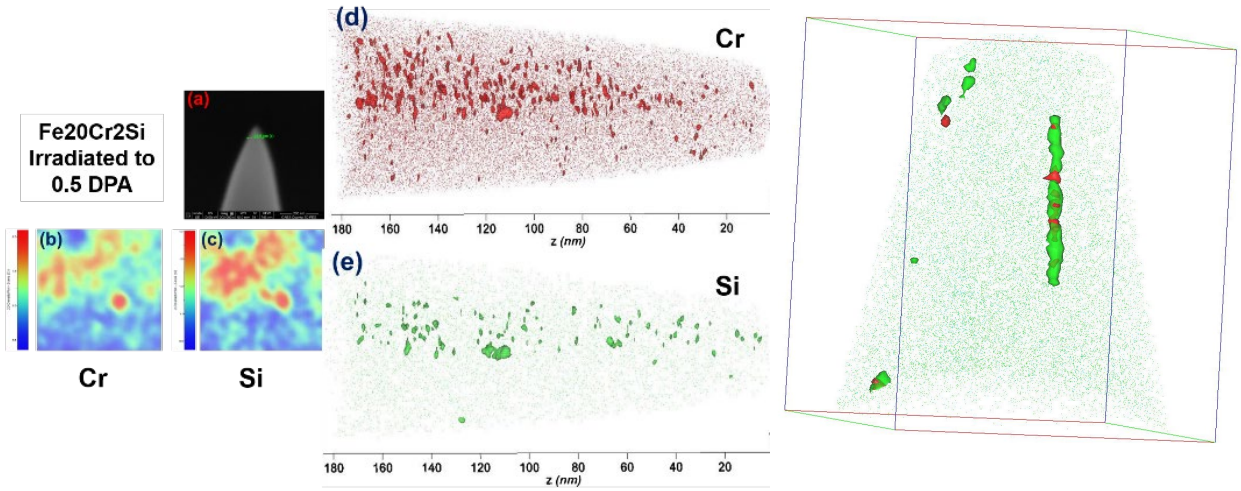

Figure 34: APT analysis of Fe-20Cr-2Si, showing more extensive and continuous precipitation of Si (green) and Cr (red). The more extensive and continuous precipitation network formed here makes Fe-20Cr-2Si a less desirable candidate as an accident tolerant cladding coating.

Concluding Remarks for This Section: The results presented in this report indicate that the general design approach taken here in fabricating this MMLC has promise. There is relatively rapid interdiffusion in the Ti and Zr layers, but the Cr layer serves as an effective diffusion barrier, limiting diffusion of Fe, Cr, and Si into the Ti/Zr region, which should prevent Fe–Zr eutectic formation, while maintaining the oxidation resistance of the outer layer. A potential pitfall of this design is the formation of laves Cr–rich intermetallic phase regions, which could lead to embrittlement of the composite, which might create difficulties in eventual industrial–scale extrusion of MMLC tubing. This is expected to be remedied by switching the outer barrier layer from Cr to V-4Ti-4Cr. Neutron irradiation and APT analysis suggests that Fe-16Cr-2Si will be the best outer corrosion-resistant layer for this study, though the focus in the diffusion couple studies was on Fe-12Cr-2Si. Further interdiffusion tests should be conducted in parallel with the industrial scale fabrication of an MMLC billet with an Fe-16Cr-2Si outer layer and a V-4Ti-4Cr outer barrier layer.

Chapter 3: Multilayer Composite Fuel Cladding and Core Internals for LWR Performance Enhancement and Severe Accident Tolerance

FC-2.1, Advanced Nuclear Fuel, Cladding, and Core Components

Corrosion, Oxidation and Stress Corrosion Cracking (SCC) Tests

by

Nuclear Materials and Fuel Cycle Center
Virginia Polytechnic Institute and State University
1872 Pratt Dr. Ste 1200
Blacksburg VA 24060

Prepared for

Massachusetts Institute of Technology
138 Albany St., NW13-213
Cambridge, MA 02139

September 30th, 2019

1. Steam corrosion tests

1.1. Experimental methods

Samples are inserted into a tube furnace at room temperature, the test system is vacuumed and purged with ultra-high purity argon gas (< 2 ppm O_2) for three times to minimize the amount of oxygen in the system. After the target temperature stabilizes for respective tests, an average steam flow rate of 1 mg/cm^2s with ultra-high purity argon as carrier gas is supplied into the tube furnace from the steam generator. The pressure in the system is maintained at within 1 psi during heating and cooling sessions with ultra-high purity argon gas. The temperature of the environment is measured by an S-type thermocouple placed right above the sample holder. The samples were oxidized in steam conditions for the entire test duration with temperature maintained within ±2% operating temperature.

The samples were fabricated in the dimension of 10 mm × 10 mm × 3 mm. The final surface finish was prepared to 600 grit using SiC sandpaper. The samples were cleaned in acetone using an ultrasonic cleaner, rinsed with deionized water, and dried with flowing air. The samples were placed onto an alumina sample holder with a purity of 99.5% for the test.

1.2. Test matrix

The table below shows the steam oxidation tests matrix at various temperature for Fe-Cr-Si alloys.

Table 1: Steam test matrix

Test ID.	Temperature (°C)	Test Duration (hrs)	Material		
			Fe12Cr2Si	Fe16Cr2Si	Fe20Cr2Si
ST 1001	700	24	1	0	0
ST 1002	900	24	1	0	0
ST 1003	1000	24	1	0	0
ST 1004	1000	24	0	1	0
ST 1005	1000	24	0	0	1
ST 1006	1000	36	1	1	1
ST 1007	1000	168	1	1	1
ST 1008	1200	24	1	0	0
ST 1009	1200	24	0	1	1
ST 1010	1200	168	1	1	1

1.3. Weight Loss Measurements

All pre-test steam specimens with similar surface finished are measured as base-metal pre-test weights. The final weight loss of specimens was obtained through repetitive cleaning cycles, done both chemically and mechanically by the same removal procedure also known as descaling. After steam tests, the post-test weight of the specimen is measured while a quarter of the specimen is removed

from bulk for descaling. The weight of the removed descaling sample was normalized with the post-test weight. The specimens are immersed into 10% diluted nitric acid in an ultrasonic cleaner at 60°C for 20 minutes per cycle. The specimen is then rinsed with DI water and dried; this cycle repeats until a small change in weight loss is observed. A typical weight loss against number of cleaning cycle curve is shown in the following figure, where the actual weight loss is approximately at point B where the two curves intersect. Finally, the weight losses were normalized to the area of surfaces of the individual descaled specimens.

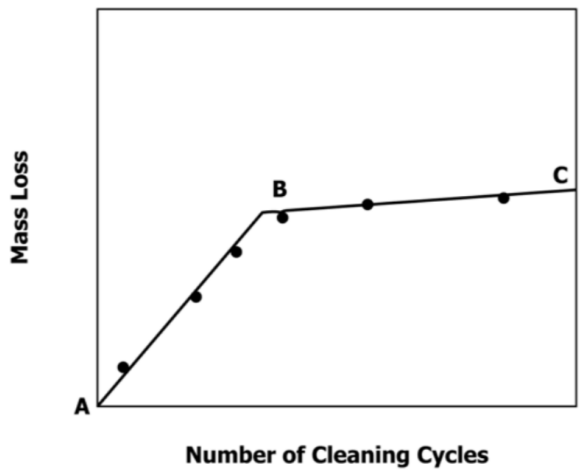

Figure 35: Typical curve of mass loss of corroded specimens as a result from repetitive cleaning cycle (ASTM G1, Standard Practice for Preparing, Cleaning, and Evaluating Corrosion Test Specimens, 2017)

The color of the mass loss data points for Fe12Cr2Si, Fe16Cr2Si, and Fe20Cr2Si are shown as blue, yellow, and green respectively. Figure 36 shows the post-descaling weight loss measurements of Fe-Cr-Si alloys in 1000°C at three different test durations. Fe16Cr2Si and Fe20Cr2Si alloys exhibit linear mass loss behavior as a function of test duration, however Fe12Cr2Si alloy suffers significant mass loss at 36 hours. The weight loss difference between Fe16Cr2Si and Fe20Cr2Si alloys are very similar while the weight loss of Fe20Cr2Si is slightly higher. On the contrary, Fe20Cr2Si alloys loss more weight in comparison to Fe16Cr2Si at 1200°C as shown in Figure 37.

Figure 38 shows the summarized weight loss data where the different steam oxidation temperatures are indicated with different shapes and the different Fe-Cr-Si alloys are indicated by color. Based on this figure, the effect of steam temperature on Fe-Cr-Si alloys are clearly seen, where the increase of steam temperature increases the weight loss/corrosion of the specimens. These results suggest that optimum Cr wt.% for Fe-Cr-Si alloys lies between 16-20 wt.% and lower Cr wt.% could potentially achieve good corrosion resistivity.

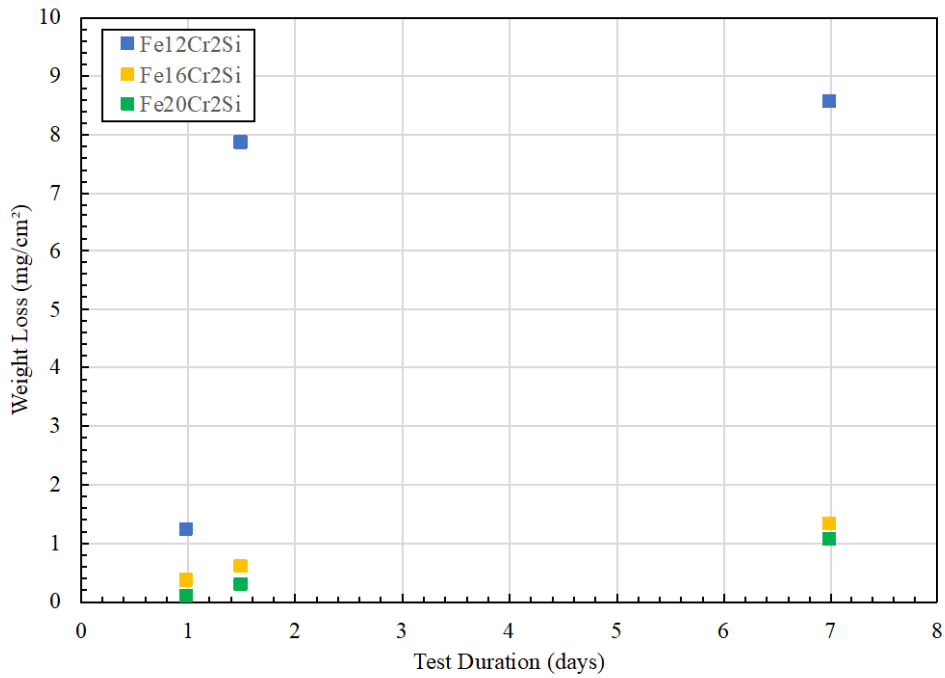

Figure 36: Weight loss measurements of Fe-Cr-Si alloys oxidized in steam at 1000°C

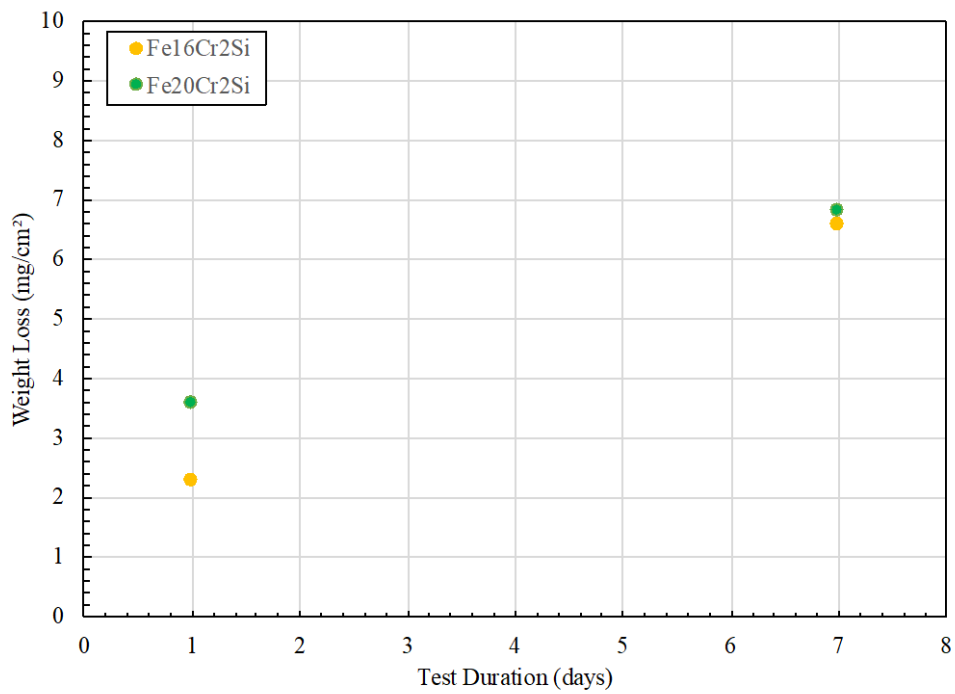

Figure 37: Weight loss measurements of Fe-Cr-Si alloys oxidized in steam at 1200°C

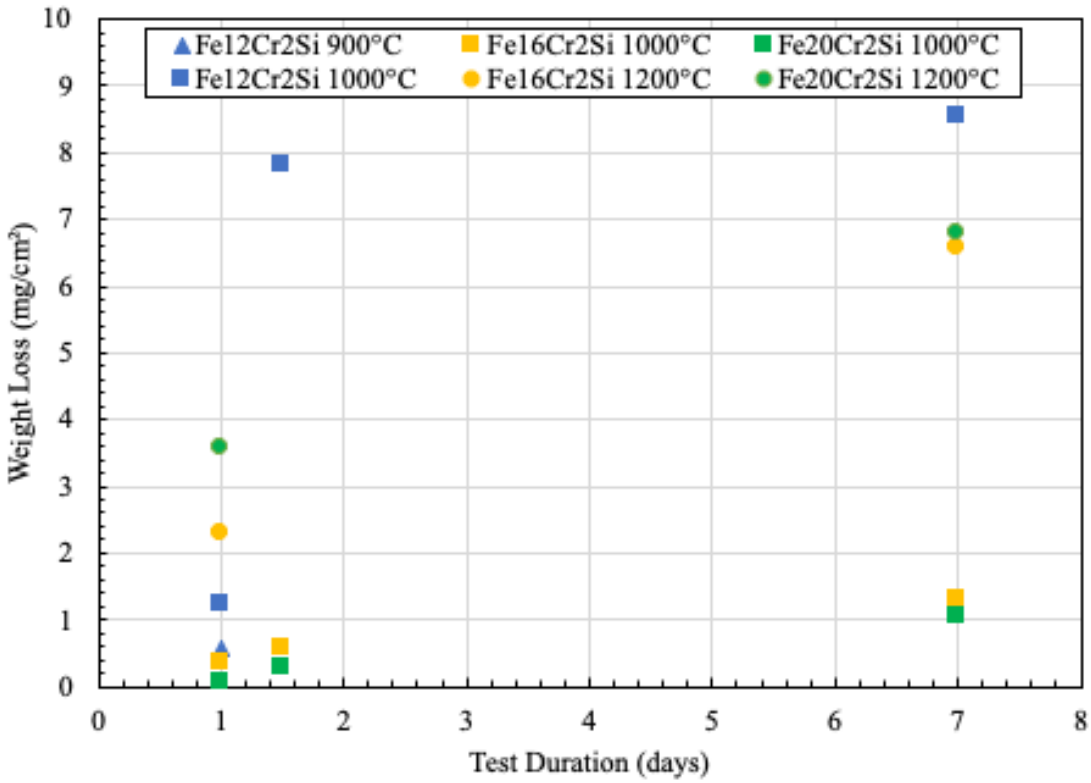

Figure 38: Summary of weight lost measurements of Fe-Cr-Si alloys against test duration at different various temperatures.

1.4. Surface oxide characterization

The outer surface of the samples was analyzed using X-ray diffraction (PANalytical X'Pert PRO) with monochromatized Cu K_α source generated at 45kV and 40mA with a scan rate of 0.06°/s and a step size of 0.2° and the peaks compared to Inorganic Crystal Structure Database (ICSD). The following figures in this section shows the effect of steam temperature on Fe-Cr-Si alloys.

XRD patterns shown in Figure 39 are patterns of Fe12Cr2Si alloys exposed to steam at 700°C and 900°C for 24 hours. The peaks were identified to be Cr_2O_3 (ICSD 075577), Cr (ICSD 064712), and Fe (ICSD 064998). Due to the extremely thin oxide layer from Fe12Cr2Si at exposed in steam 700°C, the oxide phase could not be detected by XRD. The high background intensities in XRD spectrums are caused by the fluorescence of Fe by Cu radiation, resulting in a lower signal to noise ratio. Apart from this slight discordance, the relative peak intensity of Cr and Fe peaks from bulk metal diminished as temperature increase due to the increased oxide layer thickness.

Similarly, Cr_2O_3 were found on Fe-Cr-Si alloys exposed to steam at 1000°C for 24 hours as shown in Figure 40. The peaks identified were similar to the ones from Figure 39. In comparison to Fe16Cr2Si and Fe20Cr2Si, the relative peak intensity of Cr_2O_3 of Fe12Cr2Si was much higher than Fe and Cr peaks, with Cr_2O_3 of Fe20Cr2Si having the weakest peak intensities, indicating that the oxide layer is very thin.

Cr_2O_3 was also found on Fe-Cr-Si alloys exposed to steam at 1000°C for 36 and 168 hours as shown in Figure 41 and Figure 42. Fe and Cr peaks are still found in the XRD patterns, therefore, this suggests that the Cr_2O_3 are not uniform on the surface caused by oxide spallation. An entire pattern peak shift of 0.7° was observed on Fe12Cr2Si alloy exposed to steam at 1000°C for 168 hours.

XRD patterns shown in Figure 43 are patterns of Fe-Cr-Si alloys exposed to steam 1200°C for 24 hours. A major change on surface oxide layer composition was observed on Fe12Cr2Si alloy with steam temperature at 1200°C. The peaks of Fe_3O_4 (ICSD 028664), Fe_2SiO_4 (ICSD 069460), Al_2O_3 (ICSD 031545), Cr_2O_3 (ICSD 075577), Cr (ICSD 064712), and Fe (ICSD 064998) were found. Al_2O_3 was present in the XRD pattern because the alumina sample spacer adhered with the specimen. There is no difference in surface oxide layers for Fe16Cr2Si and Fe20Cr2Si since Cr_2O_3 is the only oxide present. The oxide layers from 1200°C after 24 hours are much thicker because the Fe and Cr peaks diminished.

After exposing Fe-Cr-Si alloys in 1200°C after 168hours, the XRD patterns found on the surfaces were Fe_2SiO_4 (ICSD 041006), Fe_2O_3 (ICSD 201099), Fe_3O_4 (ICSD 028664), SiO_2 (ICSD 047219), SiO_2 (ICSD 100753), Cr_2O_3 (ICSD 075577), Cr (ICSD 064712), and Fe (ICSD 064998). In addition to Cr_2O_3, some SiO_2 were found on Fe16Cr2Si, while only Cr_2O_3 was found on Fe20Cr2Si. The XRD findings appear to be well substantiated by the good agreement with SEM/EDS data discussed in later sections, while slight discrepancies are caused by non-uniformity of oxide layers.

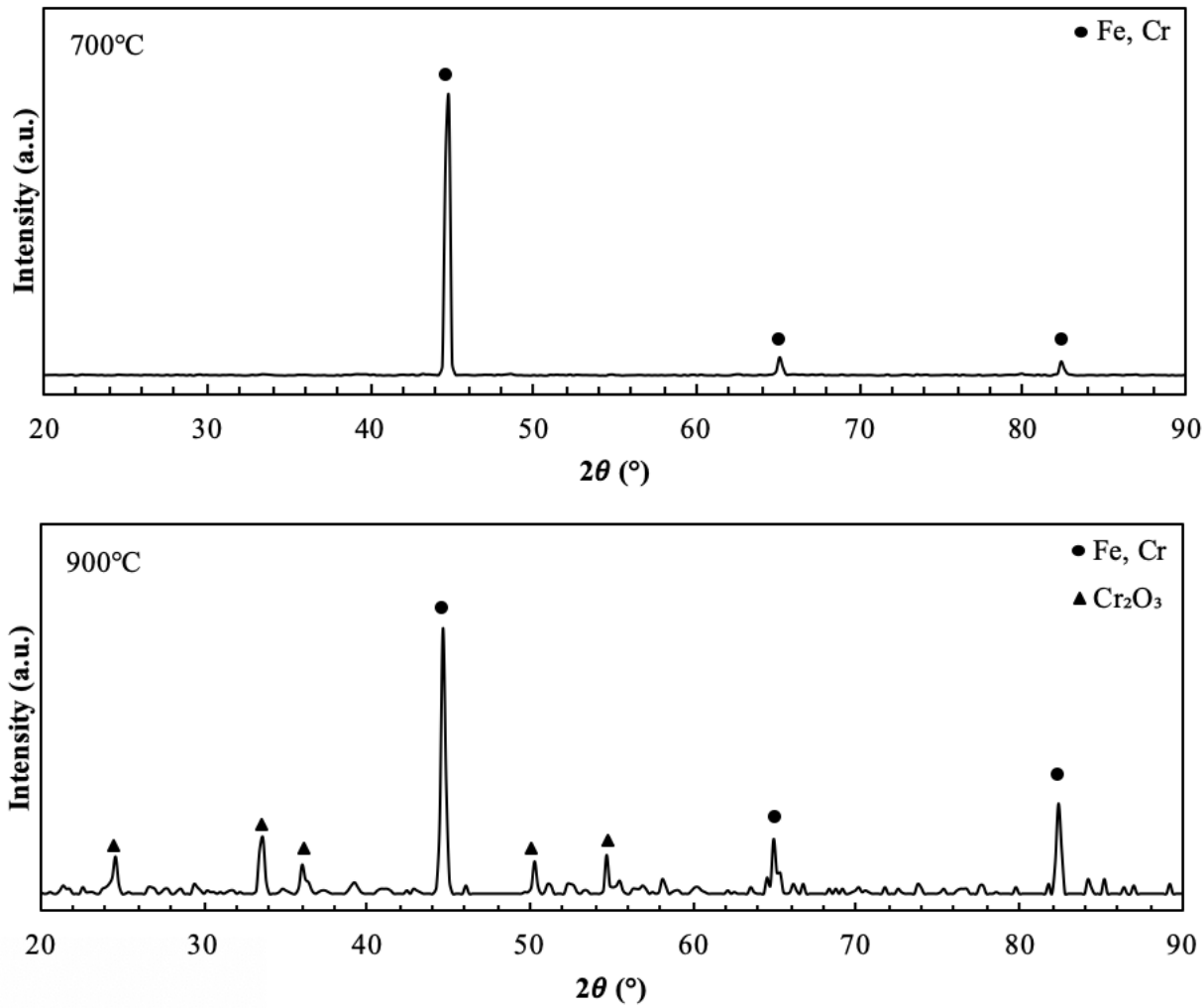

Figure 39: XRD patterns of Fe12Cr2Si alloys exposed to steam at 700°C and 900°C for 24 hours.

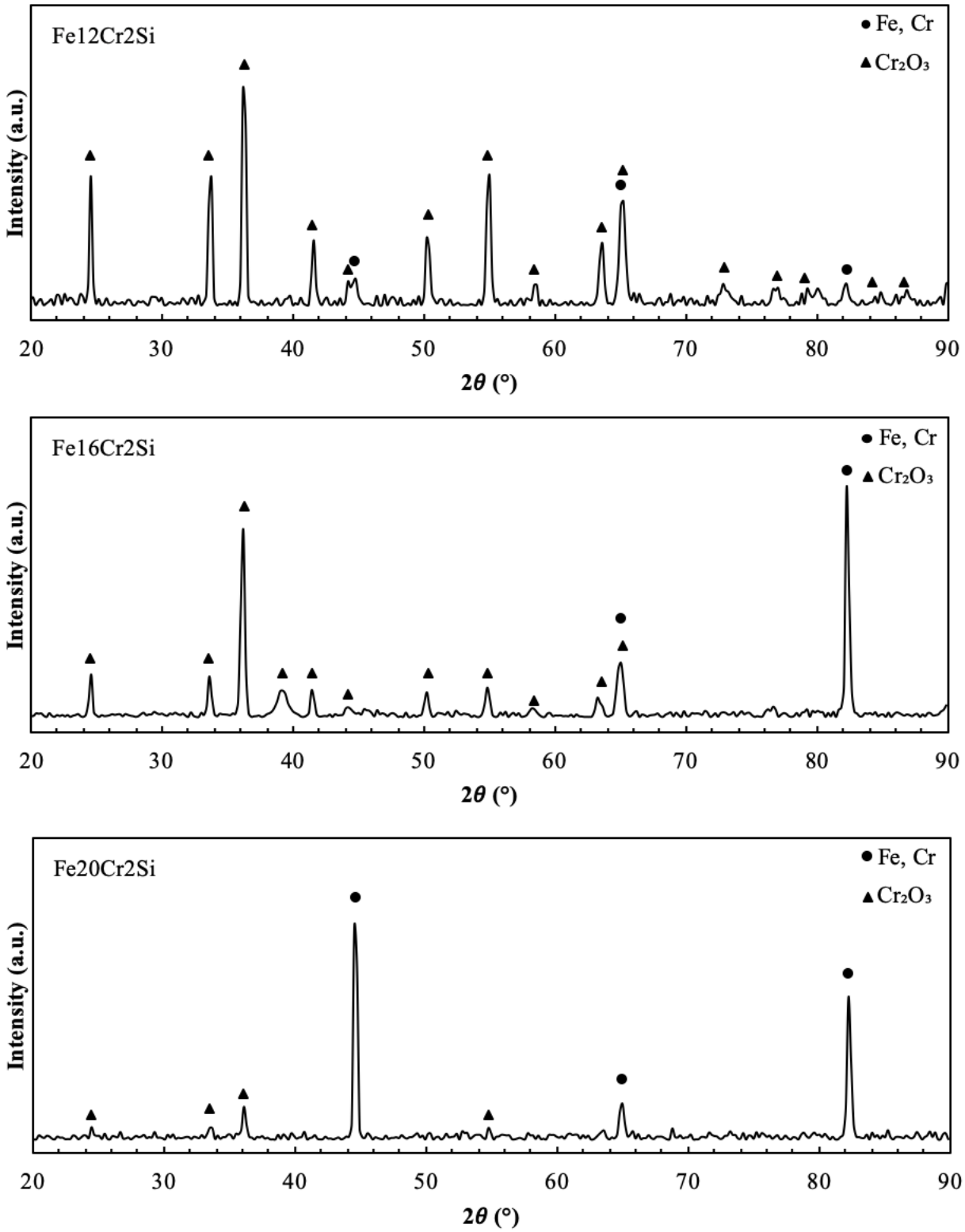

Figure 40: XRD patterns of Fe-Cr-Si alloys exposed to steam at 1000°C for 24 hours.

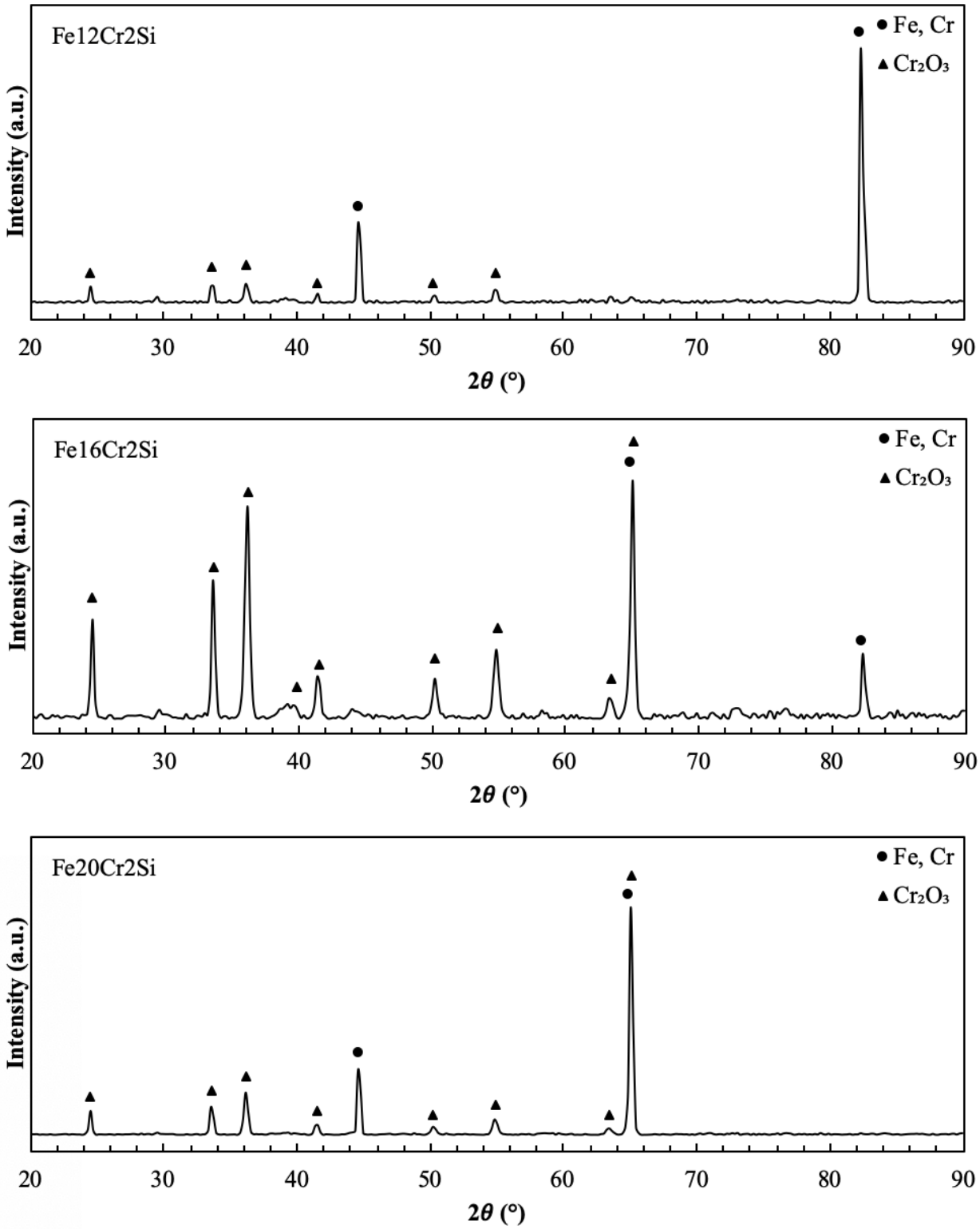

Figure 41: XRD patterns of Fe-Cr-Si alloys exposed to steam at 1000°C for 36 hours.

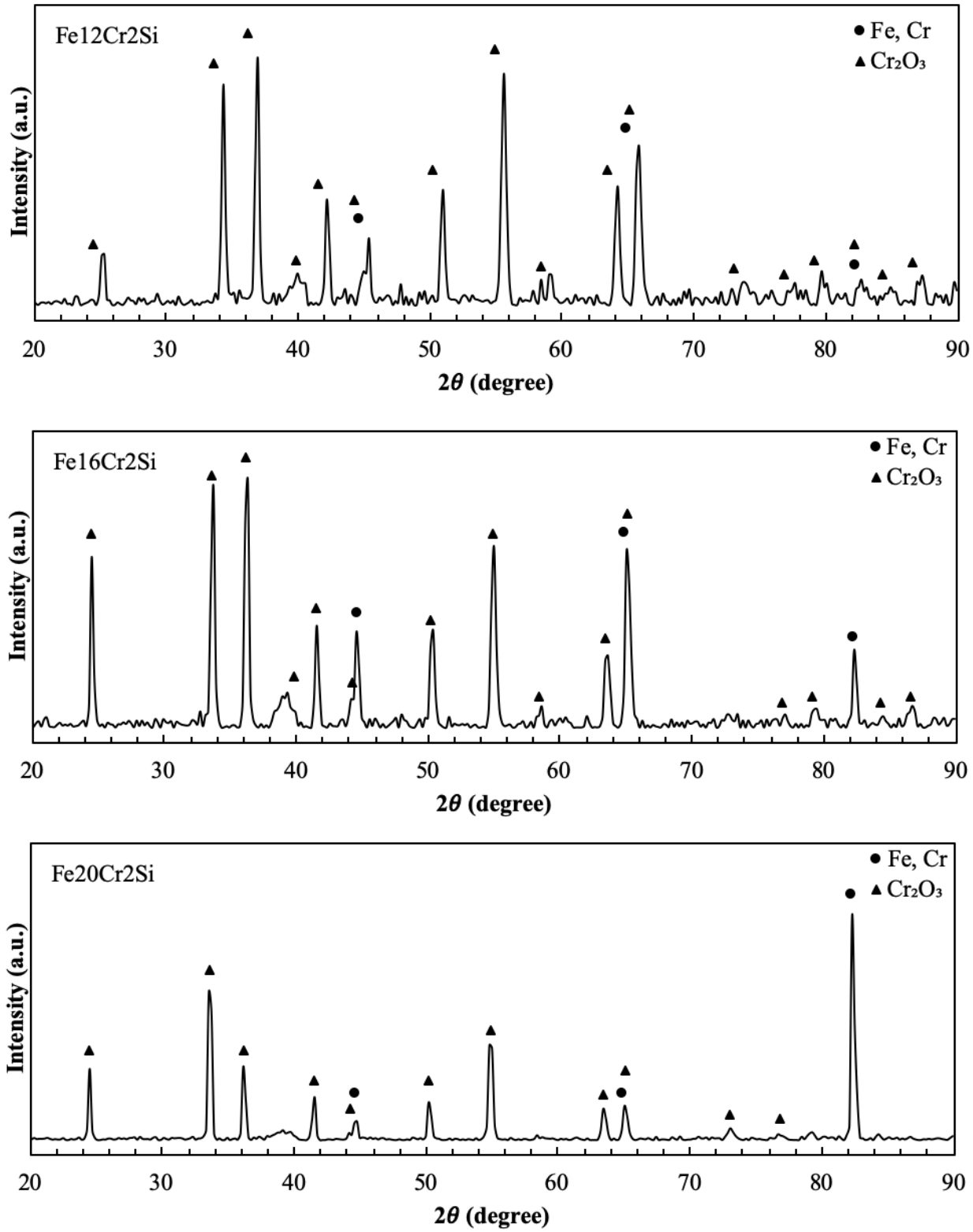

Figure 42: XRD patterns of Fe-Cr-Si alloys exposed to steam at 1000°C for 168 hours.

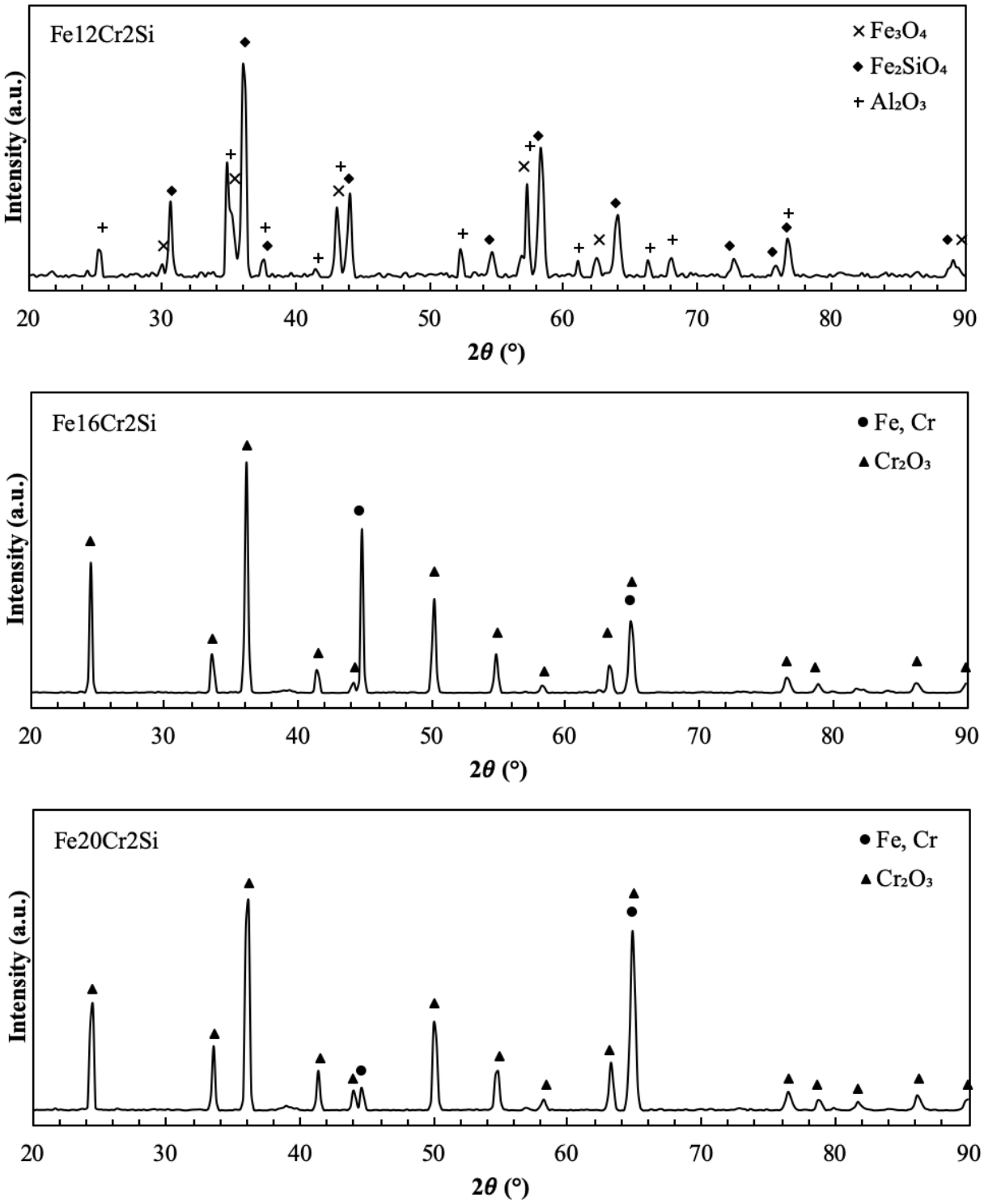

Figure 43: XRD patterns of Fe-Cr-Si alloys exposed to steam at 1200°C for 24 hours.

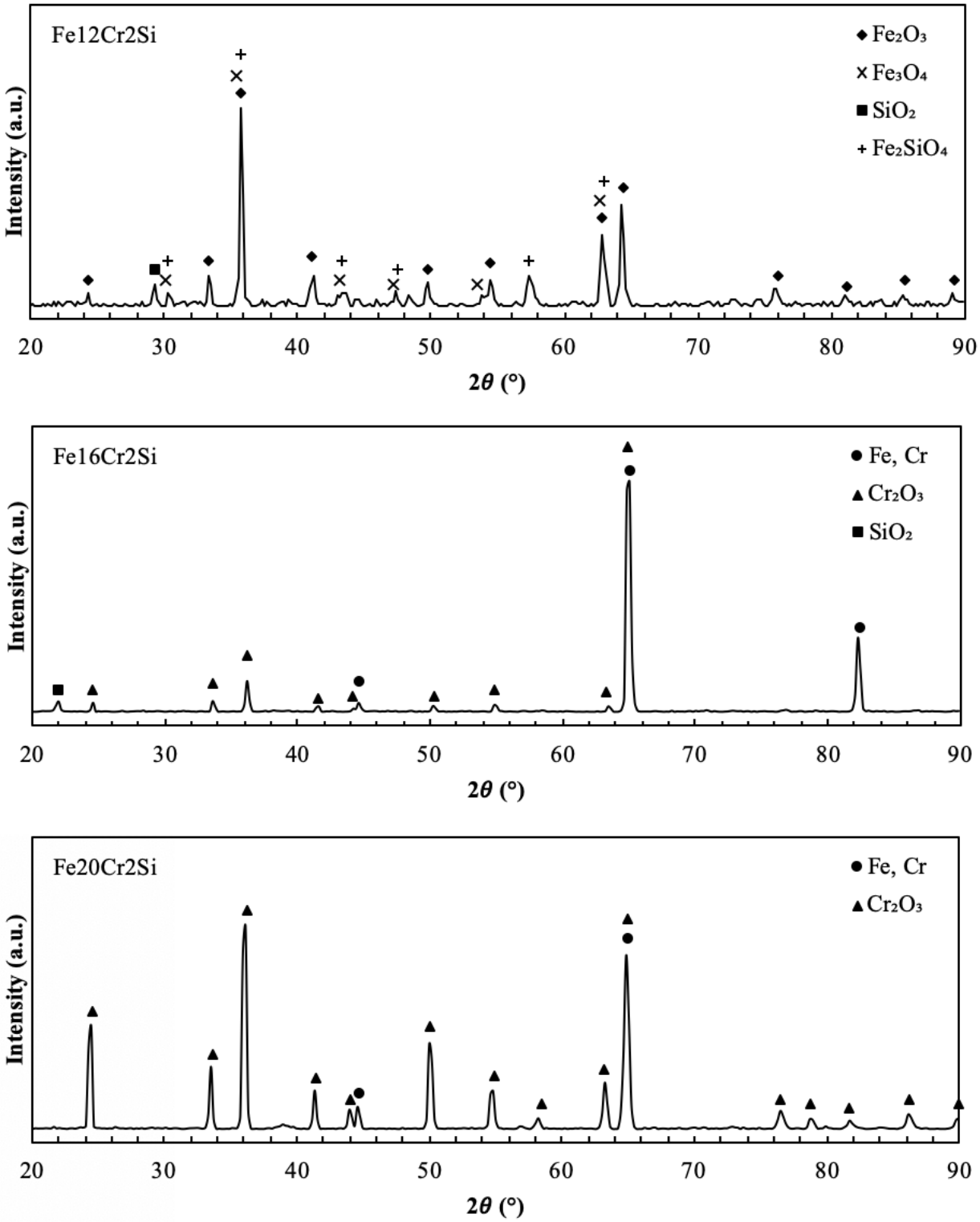

Figure 44: XRD patterns of Fe-Cr-Si alloys exposed to steam at 1200°C for 168 hours

1.5. Oxide Thickness

The SEM and energy dispersive X-ray spectrometry (EDS) analysis was conducted on the specimens using FEI Quanta 600 FEG with Bruker Quantax 200 silicon drift detector. Surface and cross-section SEM analysis were conducted using an incident electron beam at a voltage of 15 keV. To determine the thickness of thin oxide layers below 1 μm, the incident electron beam voltage was varied at 0.1 keV resolution. The incident beam was set at a voltage above the X-ray ionization energy level of elements of interest. This method of thickness measurement will be discussed later. The average oxide layer thickness of Fe-Cr-Si alloys after steam oxidation at various temperatures are listed in Table 2. Some specimens showed large oxide layer thickness variation.

Table 2: Summary of oxide thickness of Fe-Cr-Si alloys exposed to steam at various temperatures and test durations.

Material	Test Duration (hours)	Temperature (°C)	Oxide Thickness (μm)
Fe12Cr2Si	24	700	≈ 0.014
Fe12Cr2Si	24	900	0.6 - 1.8
Fe12Cr2Si	24	1000	1.7 - 3.5
Fe16Cr2Si	24	1000	5.0 - 7.0
Fe20Cr2Si	24	1000	1.86 - 3.71
Fe12Cr2Si	36	1000	2.42 - 4
Fe16Cr2Si	36	1000	1.20 - 3.08
Fe20Cr2Si	36	1000	2.11 - 3.09
Fe12Cr2Si	168	1000	4.76 - 5.95
Fe16Cr2Si	168	1000	3.75 - 5.42
Fe20Cr2Si	168	1000	3.29 - 10.43
Fe12Cr2Si	24	1200	2910 - 3030
Fe16Cr2Si	24	1200	240.4 - 285.1
Fe20Cr2Si	24	1200	13.6 - 17
Fe12Cr2Si	168	1200	843.1 - 1993
Fe16Cr2Si	168	1200	84.6 - 113.9
Fe20Cr2Si	168	1200	27.0 - 99.0

Cr_2O_3 was found surface EDS mapping on specimen surface oxidized at 700°C as shown in Figure 45, however the oxide layer was too thin and was not observed in from cross-section, therefore another approach was used to approximate the thickness of the oxide layer. The depth of the analyzed region is influenced by electron incident beam energy and energy required to ionize X-ray emission based on the following equation.

$$z_m\ (\mu m) = 0.033(V^{1.7} - V_K^{1.7})\frac{A}{\rho Z}$$ Equation 1

where V Primary beam energy (keV), V_K threshold ionization energy of underlying x-ray emission (keV), A is the mean atomic mass of the bombarded point, Z is its mean atomic number and ρ the local density (g/cm^3) (Castaing, 1960).

Preliminary results from SEM show that Cr_2O_3 monolayer is on top of the bulk material and the oxide layer is rather thin, therefore the setting of the primary incident beam energy begins at the energy enough to excited Fe characteristic x-rays. Gibbs free energy of Fe-rich oxide is higher than Cr_2O_3, therefore Fe should only exist below Cr_2O_3 in from the 700°C steam test. Longer EDS acquisition time were used with varying primary beam energy every 0.1keV until difference in Fe concentration was observed. An approximated minimum oxide thickness was found to be 14nm at 0.8keV. The results were verified on Fe12CrSi alloy from the 1000°C exposed in steam for 24 hours. A small fraction of Fe characteristic x-rays were detected in EDS at 15keV, therefore the penetration depth of the beam has pass through the Cr_2O_3 and have reached the bulk surface. The oxide layer thickness is estimated to be 3.604μm, very close to the oxide layer thickness observed as under SEM as shown in Figure 46 (b). The dissimilarity could be caused by the different chosen of site locations on the surface and cross-section.

Cr_2O_3 monolayer was found on sample surfaces at temperatures below 1000°C at 24 hours as shown in Figure 46. At low temperatures and short oxidation times, a much thicker oxide layer was formed on Fe16Cr2Si in comparison to Fe12Cr2Si and Fe20Cr2Si. These results are inconsistent with the weight loss measurements, due to spallation of oxide and adhesivity of Cr_2O_3 to metal bulk. Based on Figure 47, the observed oxide thickness of the Fe-Cr-Si alloys are slightly thicker after 36 hours exposure in steam except for Fe-16Cr2Si. The Cr_2O_3 monolayer is observed in low temperature steam oxidation up to 1000°C, however at 168 hours some SiO_2 was found below Cr_2O_3 as shown in Figure 48. This suggests that at temperatures below 1000 °C, the formation of SiO_2 takes longer period of time.

On the contrary, multi-layer of Fe, Cr, and Si-rich oxide were observed on both 24 and 168 hours specimens exposed at 1200°C steam as shown in Figure 49 and Figure 51. Higher temperature accelerates the oxidation rate, while the oxide is the thickest for Fe12Cr2Si followed by Fe16Cr2Si and Fe20Cr2Si. Fe-rich oxide was found on the surface of Fe016Cr2Si, however only Cr_2O_3 was observed on XRD pattern from 1200°C exposed in steam for 24 hours, therefore the formation of Fe-rich oxide is not uniform on the surface. At 1200°C steam temperatures, the formed intermediate oxide layers are Fe-rich and Cr-rich oxides such as $FeCr_2O_4$ and Fe_2SiO_4, while the innermost oxide layer is SiO_2 concentrates between the substrate and the bulk.

The inconsistency of the oxide layer thickness results with the weight loss results are caused by spallation of oxide and unevenness of thickness of oxide left on specimen.

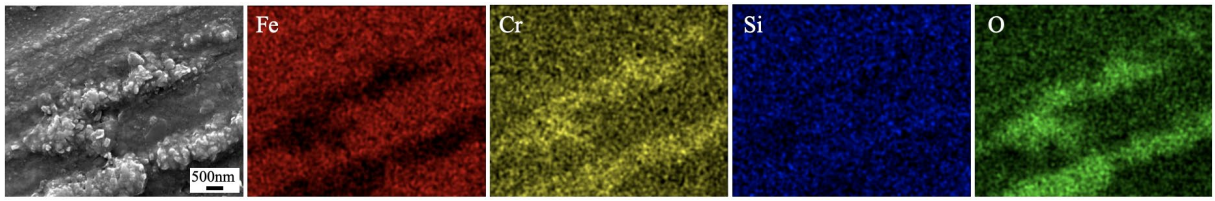

Figure 45: Secondary electron (SE) SEM images with EDS mapping showing the elemental distribution of Fe, Cr, Si, and O on the post-test Fe-12Cr-2Si surface at the test temperature of 700°C (Leong, Zhang, & Xie, 2019).

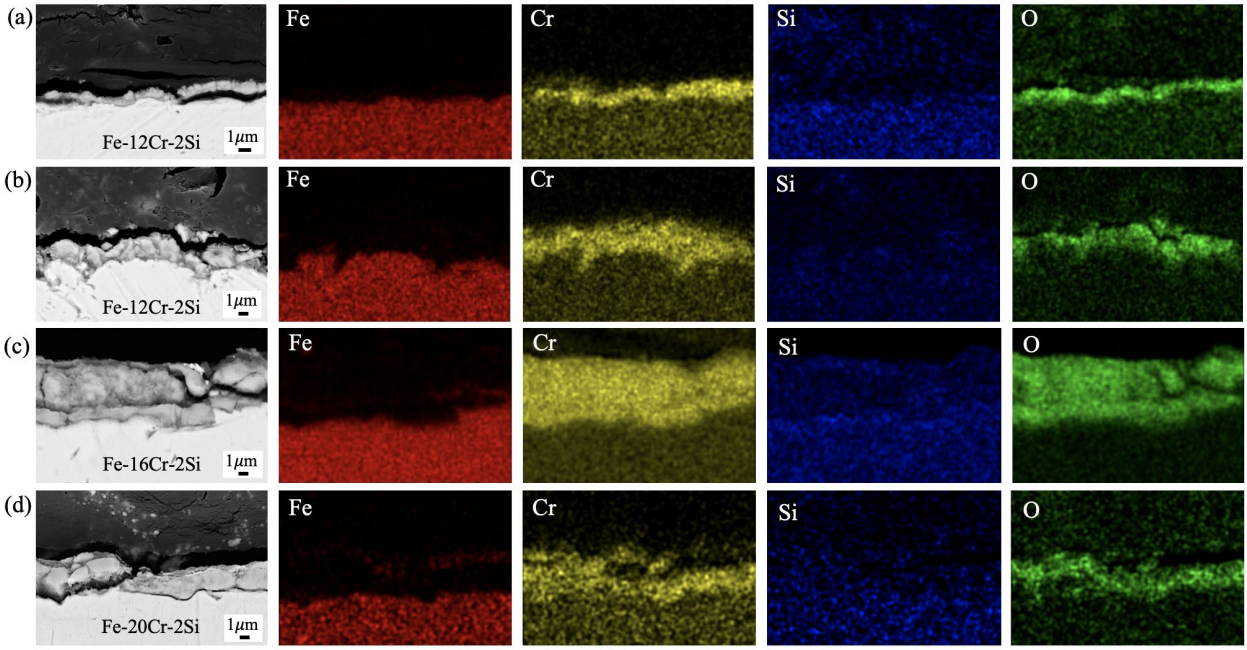

Figure 46: Backscattering (BSE) EDS mapping of Fe, Cr, Si, and O for (a) Fe12Cr2Si expo (Leong, Zhang, & Xie, 2019)sed to steam at 900°C, (b) Fe12Cr2Si, (c) Fe16Cr2Si, and (d) Fe20Cr2Si exposed to steam at 1000°C for 24 hours.

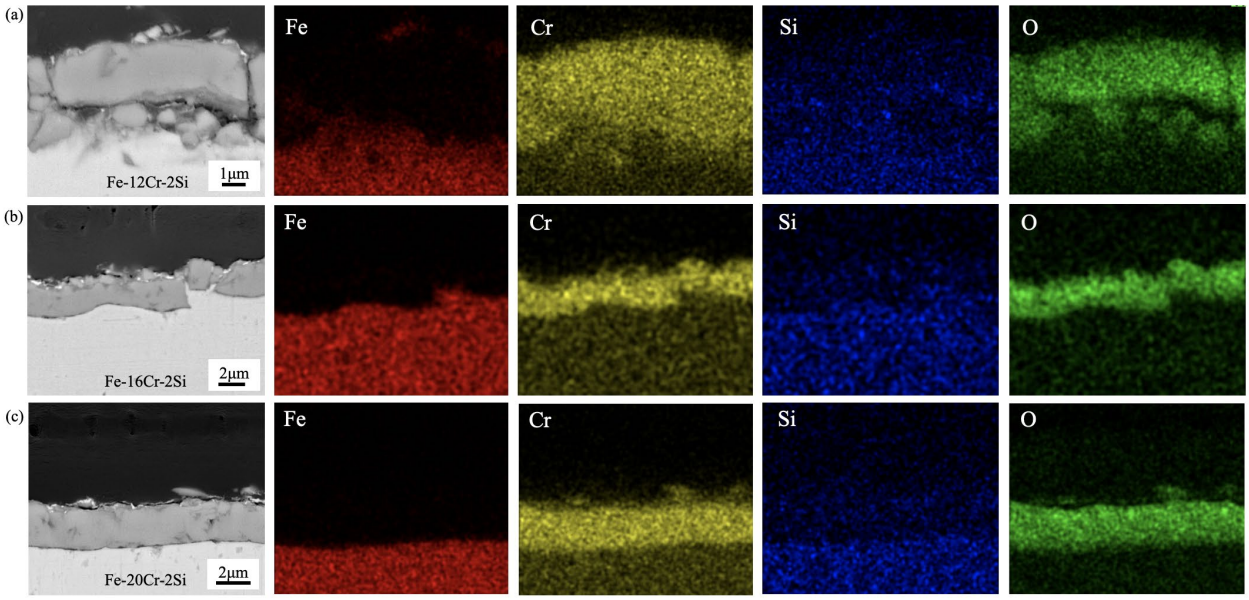

Figure 47: EDS mapping of Fe, Cr, Si, and O for (a) Fe12Cr2Si, (b) Fe16Cr2Si, and (c) Fe20Cr2Si exposed to steam at 1000°C for 36 hours (BSE).

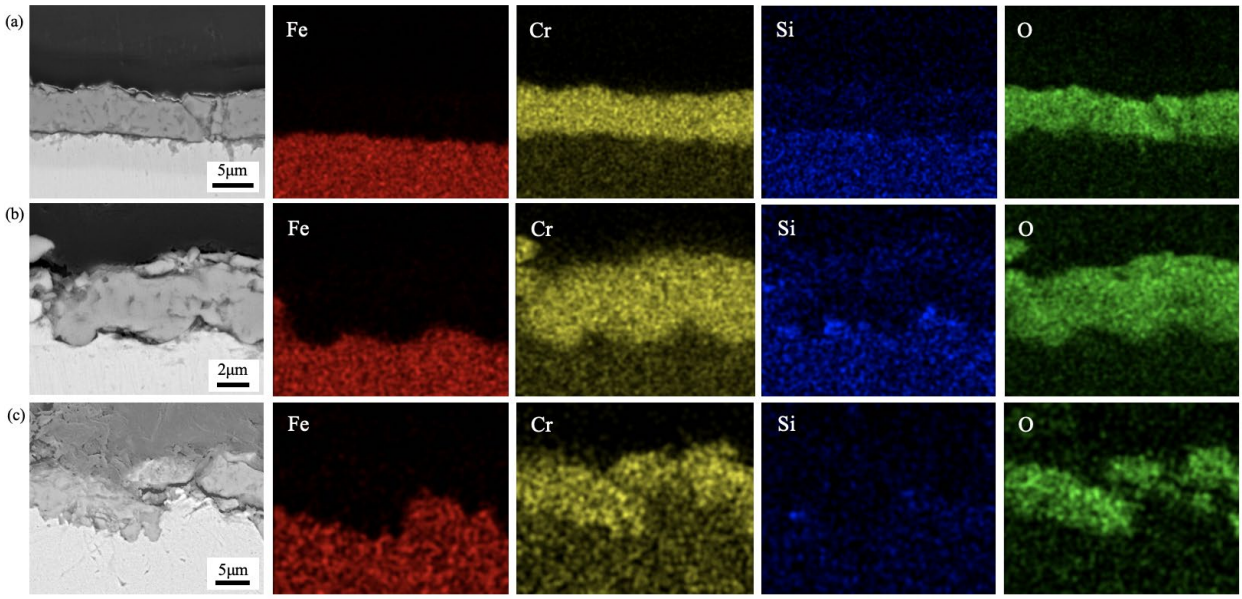

Figure 48: EDS mapping of Fe, Cr, Si, and O for (a) Fe12Cr2Si, (b) Fe16Cr2Si, and (c) Fe20Cr2Si exposed to steam at 1000°C for 168 hours.

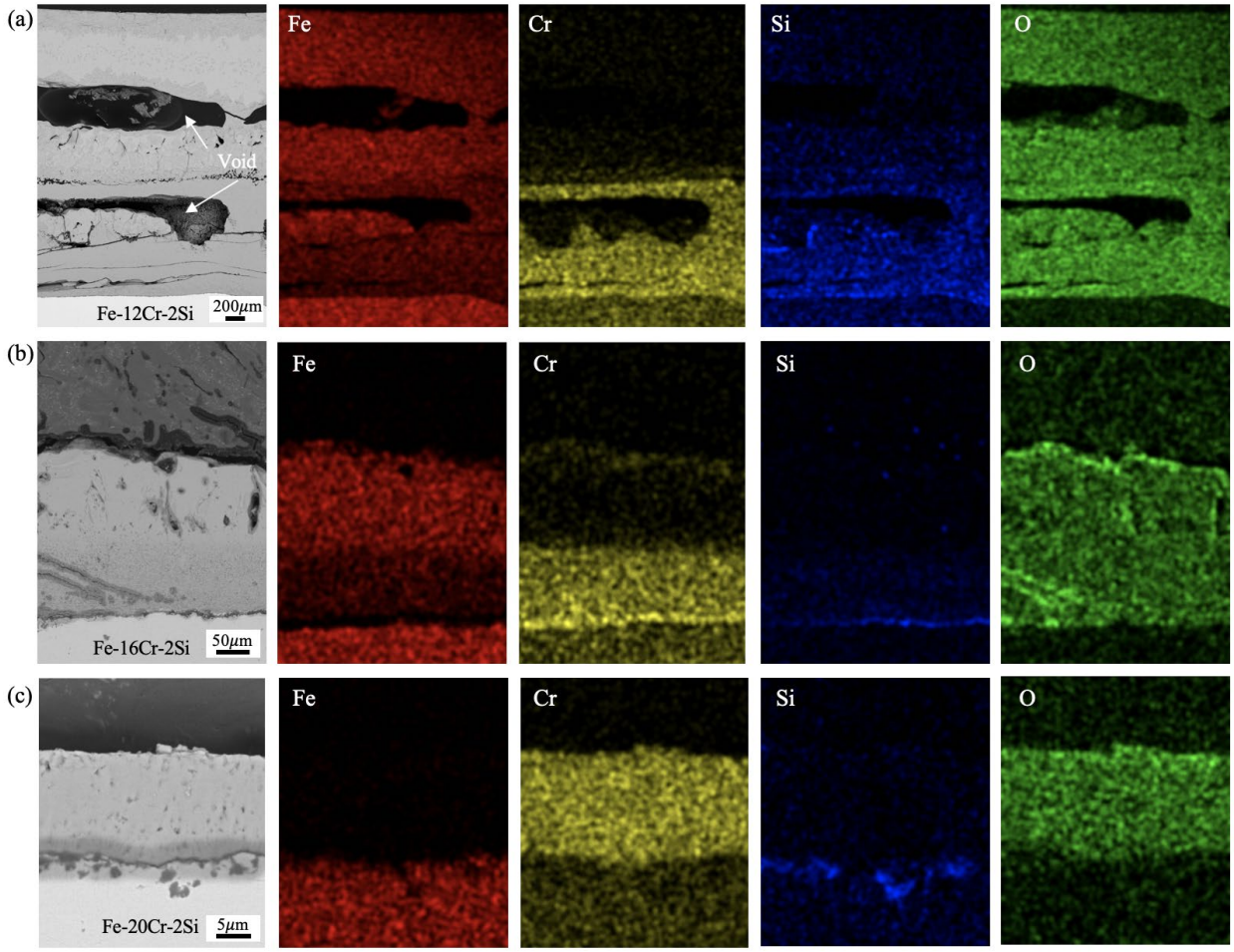

Figure 49: EDS mapping of Fe, Cr, Si, and O for (a) Fe12Cr2Si, (b) Fe16Cr2Si, and (c) Fe20Cr2Si exposed to steam at 1200°C for 24 hours (BSE).

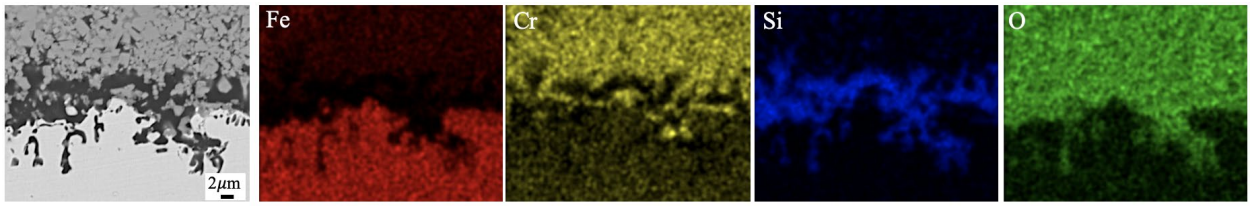

Figure 50: EDS mapping of Fe, Cr, Si, and O for the Fe12Cr2Si tested at 1200 °C showing the elemental distribution at the oxide/substrate interface (BSE).

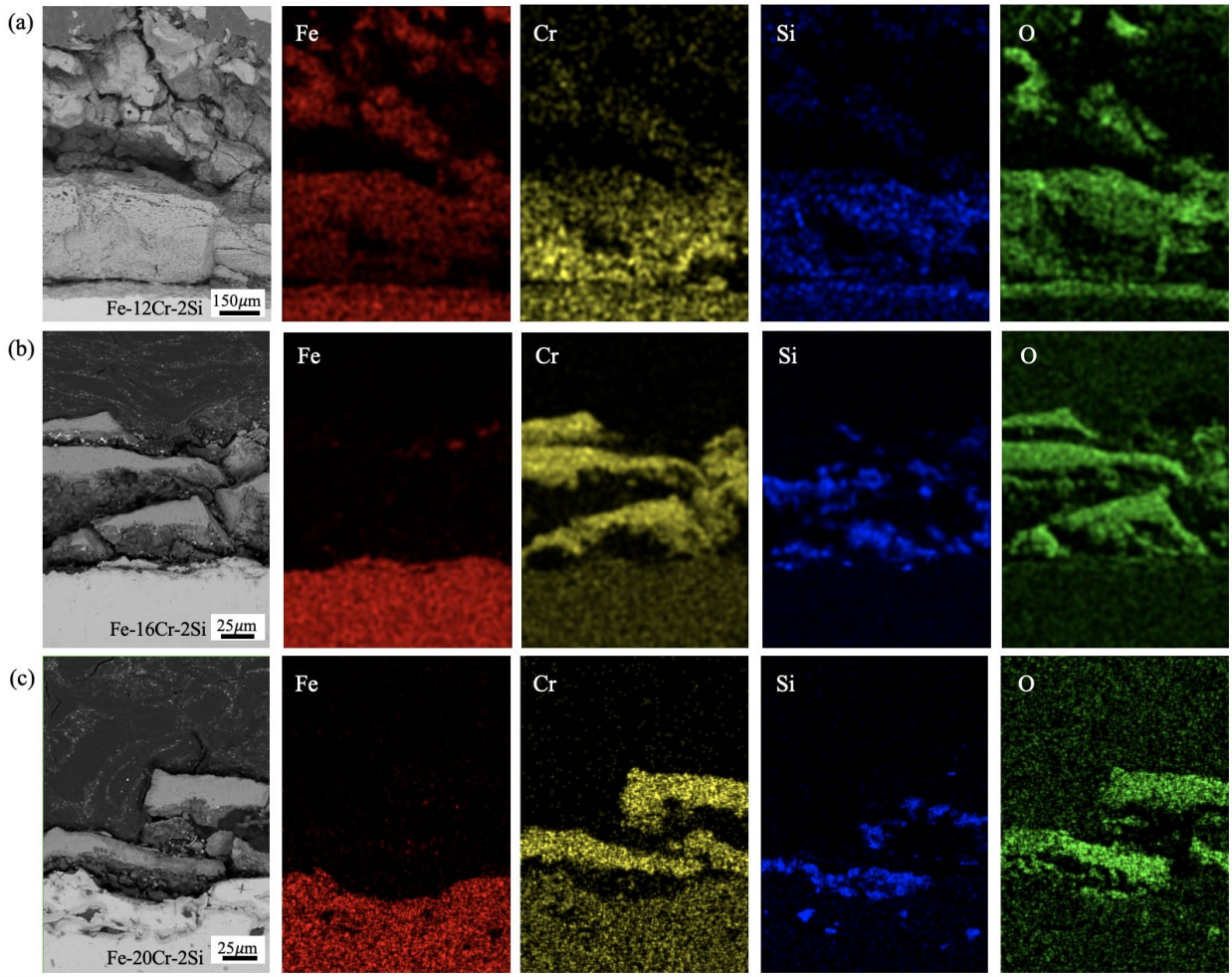

Figure 51: EDS mapping of Fe, Cr, Si, and O for (a) Fe12Cr2Si, (b) Fe16Cr2Si, and (c) Fe20Cr2Si exposed to steam at 1200°C for 168 hours (BSE).

2. Pressurized Water Reactor (PWR) normal operating conditions

2.1. Experimental methods

Immersion tests and electrochemical measurements are conducted in PWR normal operating environments. The PWR primary water corrosion test facility consists an autoclave made from stainless steel 316, a high purity argon gas supply with an oxygen concentration less than 4ppm, and a heating mantle with a PID temperature controller. To ensure that impurities from the autoclave did not leach into the test environment, the autoclave surface was oxidized prior to the experiment.

The immersion tests specimens are made into dimensions of 10 mm x 10 mm x 3 mm with a 2.25 mm outer diameter hole were polished up to 600 grit using SiC paper, followed by ultrasonic cleaning with ethanol and deionized (DI) water. Specimens were hung in this autoclave using a wire sheathed with PTFE to avoid galvanic corrosion. The test coupons were immersed into the different PWR environments as listed in Table 3.

The electrochemical tests specimens are made into cylinders of 5 mm diameter and 11.4 mm tall, while the flat surfaces of the cylinders was to polished up to 600 grit using SiC paper, followed by ultrasonic cleaning with ethanol and deionized (DI) water. These test specimens are used as the working electrode for electrochemical measurements, where the center flat surface of the cylinder was spot welded to a platinum wire sheathed with PTFE. The electrochemical measurements are conducted in a three-electrode cell, using Fe-Cr-Si alloys as working electrode, high temperature Ag/AgCl reference electrode, coiled platinum wire as counter electrode, and Gamry Reference 600+ Potentiostat. The test matrix is shown in Table 4, the test solution was prepared with 1500ppm B and 3ppm Li in DI water. In the same test setup, two samples each from Fe-Cr-Si alloys are immersed into the autoclave for weight change measurements. A sequence for 336 hours was setup in placed for periodical electrochemical impendence spectroscopy (EIS) measurements to study the behavior of the oxide. Open circuit potential (OCP) measurements are conducted at every 7.5 hours intervals between EIS measurements to obtain stable voltage reading between working and reference electrodes.

2.2. Test matrix

Table 3: Immersion tests test matrix in PWR conditions

Test ID.	Temperature (°C)	Pressure (psi)	Test Duration (hrs)	Concentration (ppm)	
				Li	B
HTHP 2011	280	2000	500	5	1400
HTHP 2012	280	2000	120	100	1400
HTHP 2013	280	2000	120	5	1400

Table 4: Electrochemical tests test matrix in PWR conditions

Test ID.	Temperature (°C)	Pressure (psi)	Test Duration (hrs)	Material
E-HTHP 3001	280	2000	336	Fe12Cr2Si
E-HTHP 3002	280	2000	336	Fe16Cr2Si
E-HTHP 3003	280	2000	336	Fe20Cr2Si

2.3. Weight change measurements

The color of the mass change data points for Fe12Cr2Si, Fe16Cr2Si, and Fe20Cr2Si are shown as blue, yellow, and green respectively, while the different PWR solution concentration values are indicated with different shapes in Figure 52. No weight change was observed on all Fe-Cr-Si alloys with Li 5 ppm, and B 1400 ppm at 120 hours. At low Li concentrations, the Fe-Cr-Si alloys experience weight gains as length of test duration increases where the highest weight change order is from Fe12Cr2Si, Fe16Cr2Si, and Fe20Cr2Si. However, the order switches in higher Li concentration environments. Therefore, a significant change in Li concentration will encourage material dissolution.

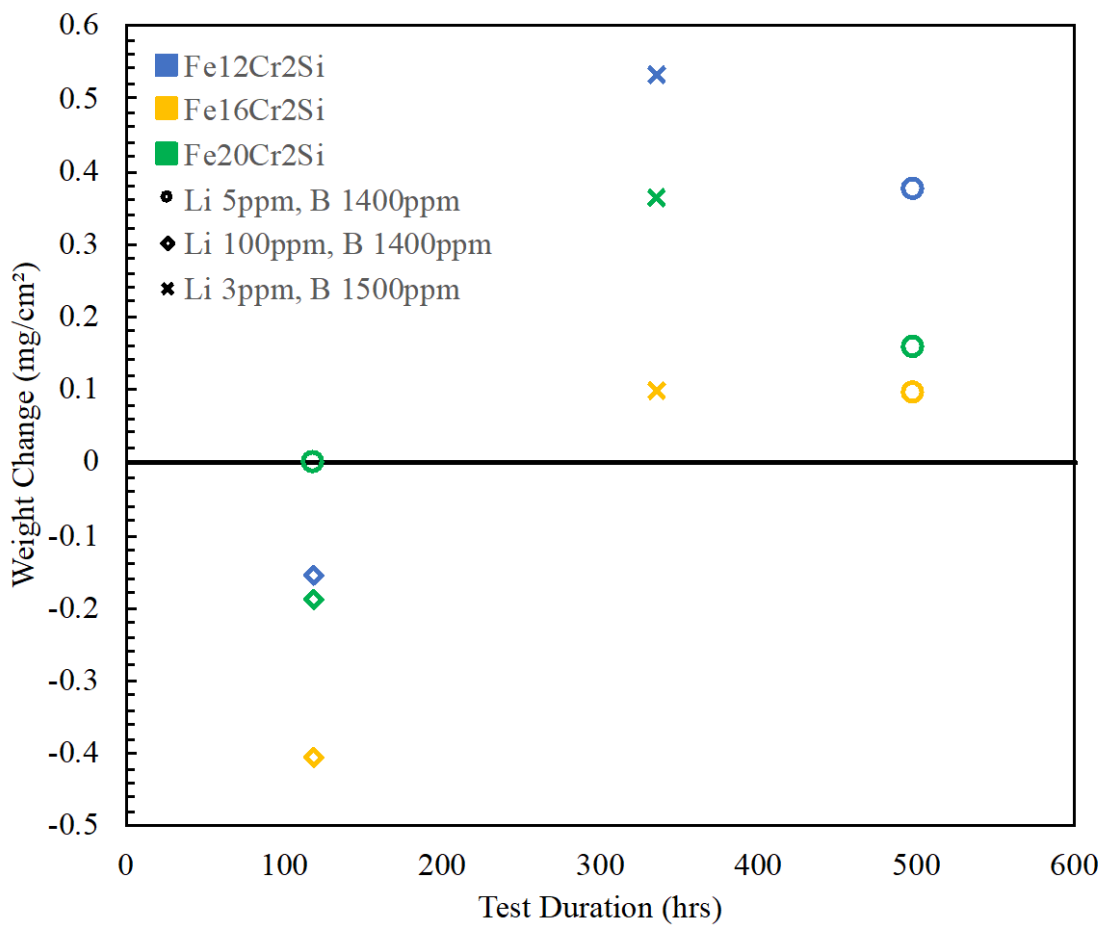

Figure 52: Weight change of Fe-Cr-Si alloys exposed in PWR environments for different test durations from immersed coupons.

2.4. Surface morphology

Fe-rich oxides are observed on the surface of the samples from the immersion test from 5ppm Li and 1400ppm B environment as shown in Figure 53. Fe-rich oxides formed on Fe12Cr2Si shows large non-uniformity on the particle sizes followed by Fe16Cr2Si and Fe20Cr2Si.

Similar to the steam tests, the outer surface of the samples was analyzed using X-ray diffraction (PANalytical X'Pert PRO) with monochromatized Cu Kα source generated at 45kV and 40mA with a scan rate of 0.06°/s and a step size of 0.2° and the peaks compared to ICSD. The oxide layer from Fe16Cr2Si and Fe20Cr2Si was not observed in the XRD pattern due to the stronger peak intensities from the bulk material as shown in Figure 54. However, SEM results shows that Fe-rich oxide were found on the surfaces, therefore the oxide layers are very thin and does not fully cover the bulk material. The case was different for Fe12Cr2Si for Fe-oxides were observed, however Fe3O4 (ICSD 028664) and FeCr2O4 (ICSD 044526) peaks were very close and indistinguishable.

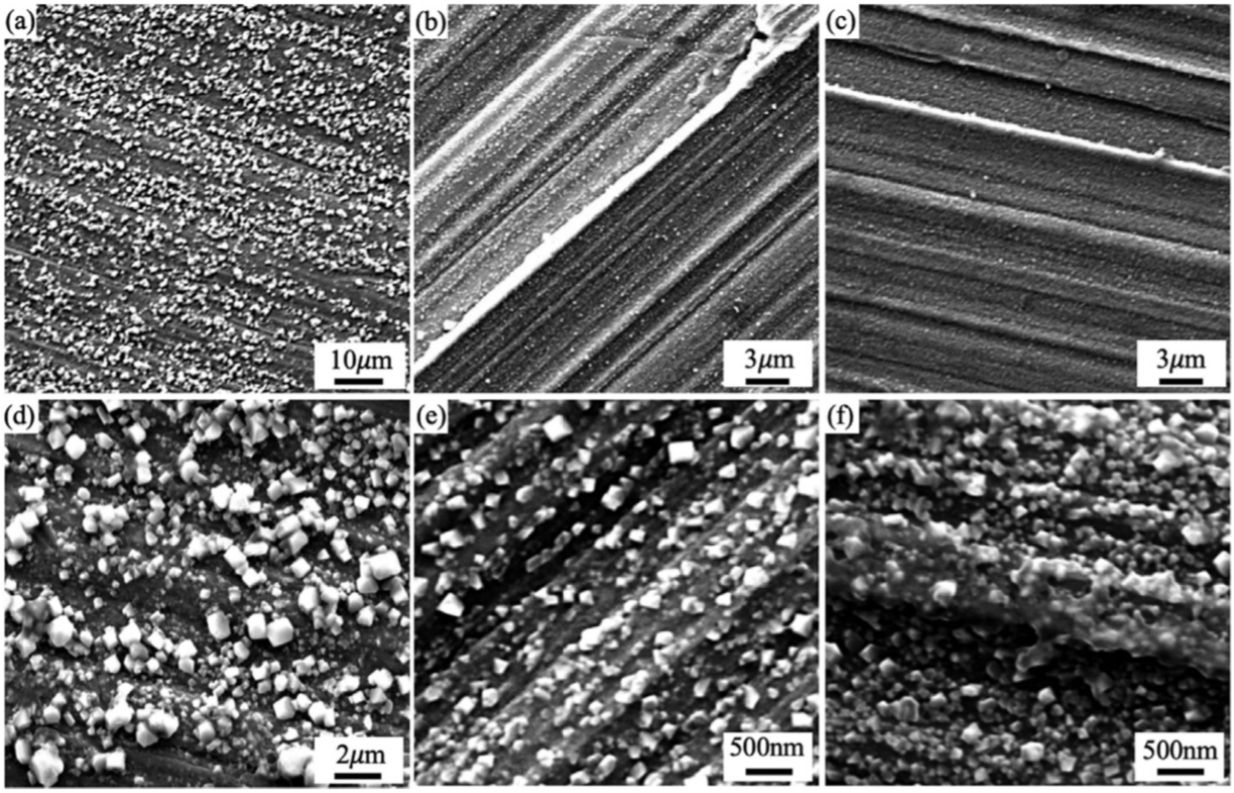

Figure 53: SEM images of surface oxides of Fe-Cr-Si alloys after 500 h of exposure in simulated PWR with 5ppm Li and 1400ppm B: (a) Fe12Cr2Si, (b) Fe16Cr2Si, and (c) Fe20Cr2Si. Polyhedral oxides observed on (d) Fe12Cr2Si, (e) Fe16Cr2Si, and (f) Fe20Cr2Si.

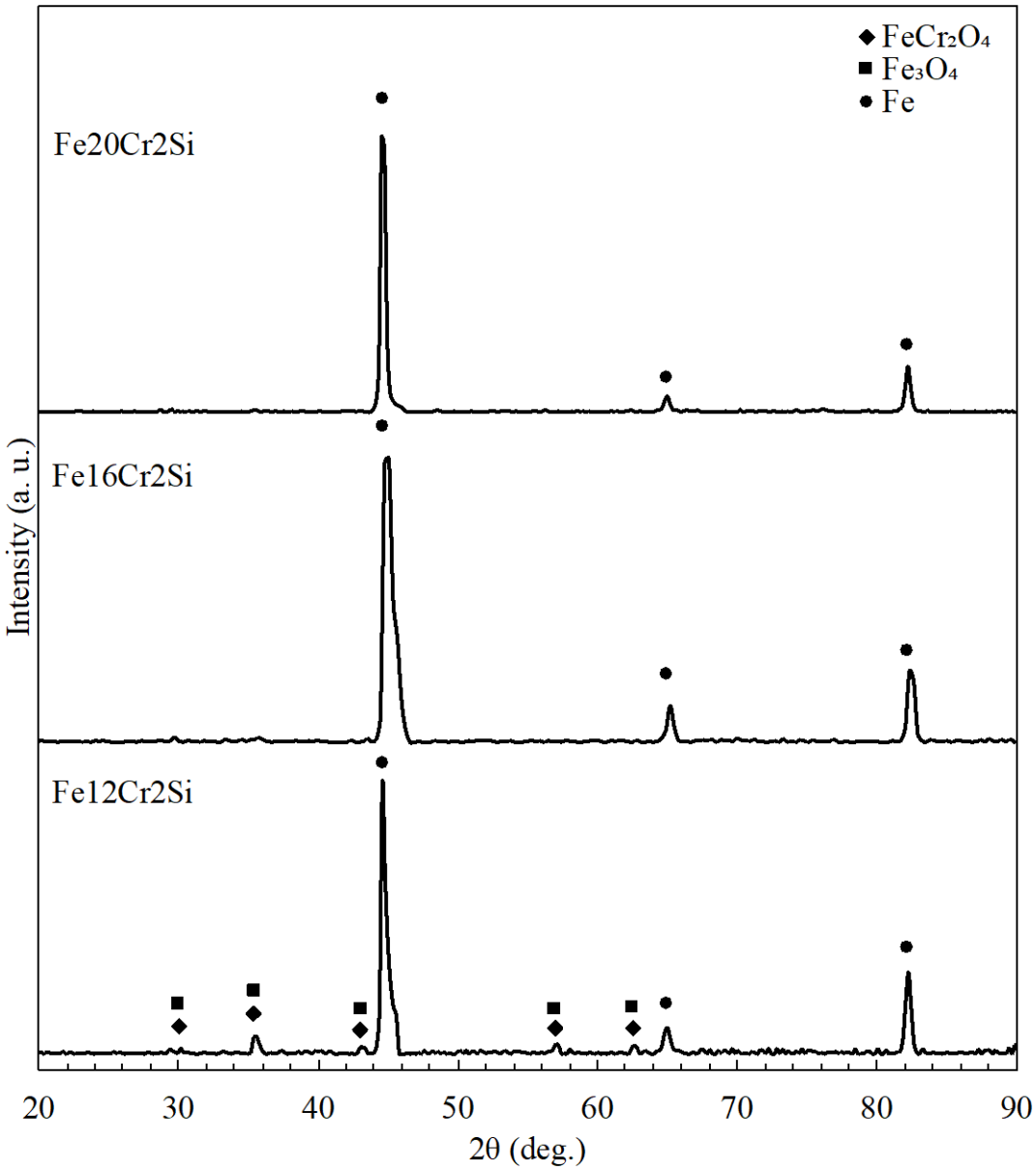

Figure 54: XRD patterns of (a) Fe12Cr2Si, (b) Fe16Cr2Si, and (c) Fe20Cr2Si exposed to simulated PWR primary water for 500 h alloys after 500 hrs in simulated PWR with 5ppm Li and 1400ppm B (Qiang, Leong, Zhang, & Short, 2019).

2.5. Oxide thickness

XPS characterization was performed on a PHI VersaProbe III scanning XPS microscope using a monochromatic Al Kα X-ray source (1486.6 eV) to identify the chemical structure of the surface oxide layers. XPS survey spectra were acquired with 100 mm/100 W/20 kV X-ray settings over a 1400 mm × 100 mm area from 0-1100 eV with a resolution of 1 eV to first identify the existence of different elements as shown in Figure 55. Detailed spectra with a resolution of 0.1 eV were taken at these peaks to identify the binding states in those elements shown in Figure 56. The chemical states of elements were identified based on the PHI and NIST XPS Database v4.1.

The deconvoluted Fe $2p_{3/2}$ peaks are 706.9eV, 709.4eV, and 711.5eV which corresponds to Fe metal from Fe^0, FeO from Fe^{2+}, and Fe_2O_3 from Fe^{3+} respectively. The surface of the Fe-Cr-Si alloys are not fully covered because Fe^0 was observed on the surface. Fe_3O_4 was found on the surface of Fe-Cr-Si alloys based on the SEM results above, however the ratio of Fe^{2+} and Fe^{3+} from XPS detailed spectra was not 1:2, caused by the non-uniformity of Fe_3O_4 particle sizes. Cr_2O_3 are observed on all three Fe-Cr-Si alloys based on the XPS binding energy of Cr $2p_{3/2}$.

Silicon peaks found on the surface of the alloys originate from silicate. The peak energies of Fe12Cr2Si is 102.5eV while Fe16Cr2Si and Fe20Cr2Si are both at 102.1eV. There is a slight binding energy peak difference of Si^{4+} caused by the low counts and deviation in carbon peak, however Si^{4+} should exist on all Fe-Cr-Si alloys from 5ppm Li and 1400ppm B environment. The Si 2p binding energy of 102.8eV suggests that Fe_2SiO_4 is formed on the surface as the data is comparable to $ZrSiO_4$ silicate of same binding energy from NIST XPS Database.

The oxide thickness on Fe12Cr2Si, Fe16Cr2Si, and Fe20Cr2Si were around 984 nm, 105 nm, and 115 nm respectively with respect to 3 keV Ar^+ ion bombardment to give a sputtering rate of 9.3 nm/min for SiO_2. A schematic of the Fe-Cr-Si alloys surface condition are constructed by combining SEM, XRD, and XPS data as shown in Figure 58.

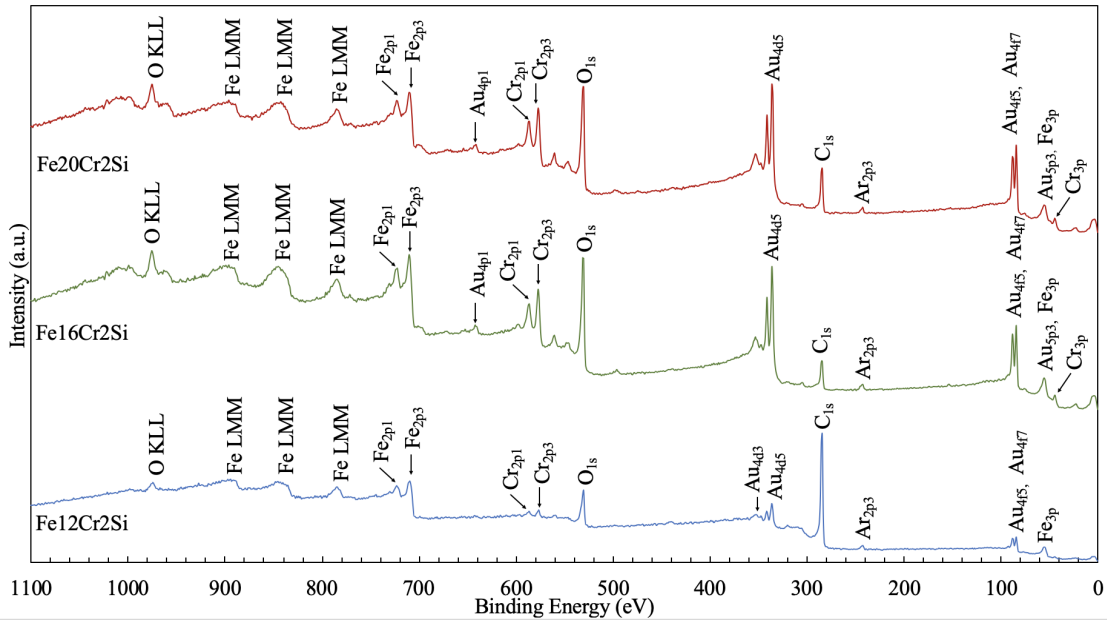

Figure 55: XPS survey spectra of the oxide layers for three Fe-Cr-Si alloys exposed to simulated PWR primary water for 500 h shows surface compositions of three alloys are similar (Qiang, Leong, Zhang, & Short, 2019).

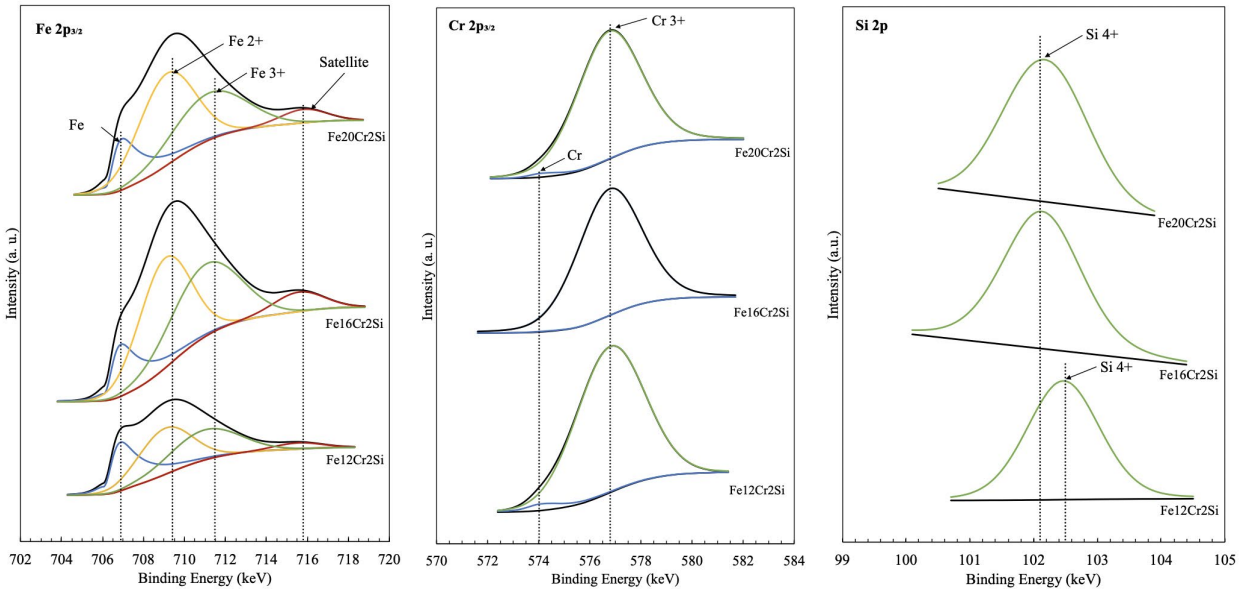

Figure 56: Detailed XPS spectra of Fe, Cr, and Si found in oxide layers on three Fe-Cr-Si alloys exposed to simulated PWR primary water for 500 h (Qiang, Leong, Zhang, & Short, 2019).

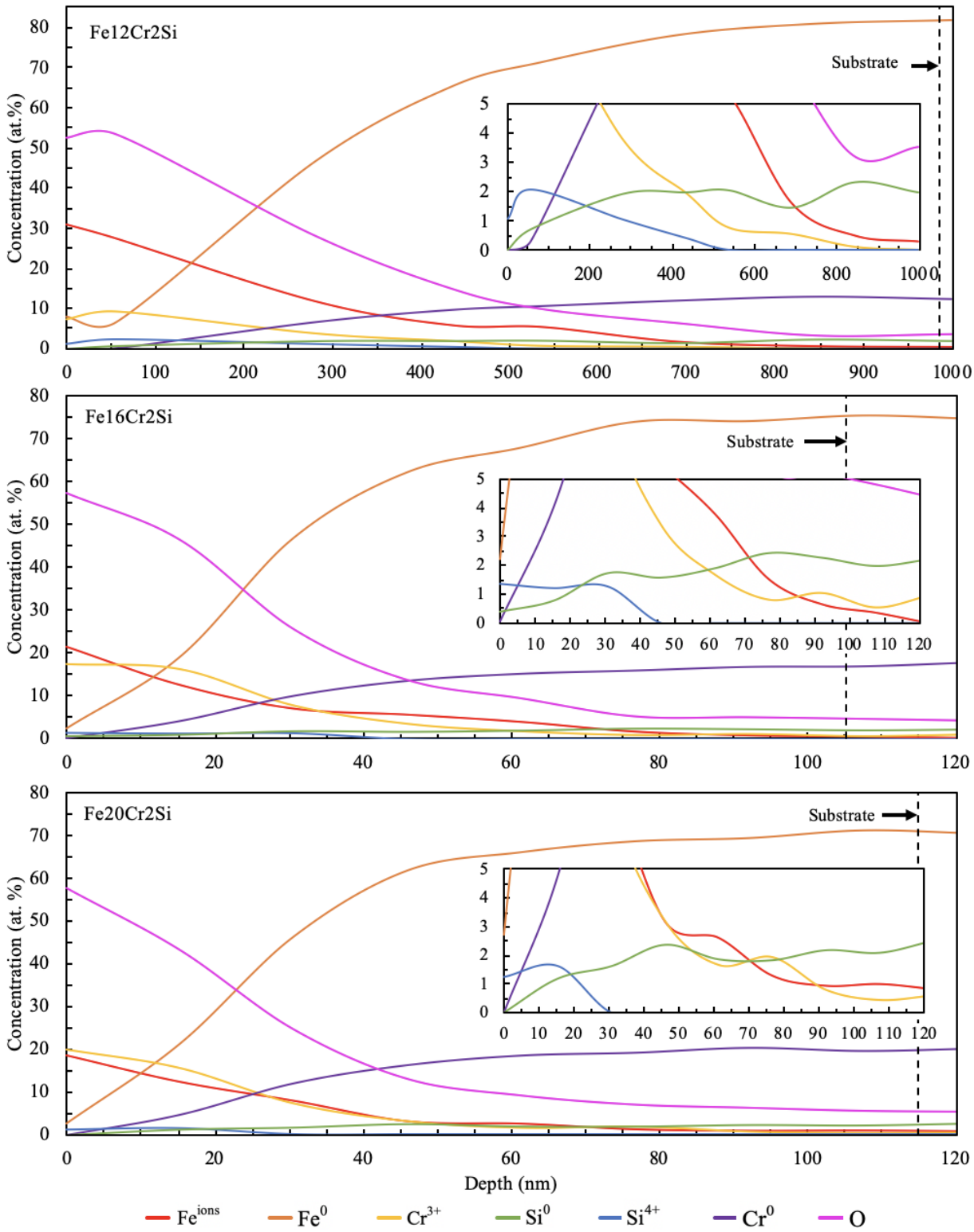

Figure 57: Depth profile of Fe-Cr-Si alloys exposed to simulated PWR primary water for 500 h with magnified lower concentration region (Qiang, Leong, Zhang, & Short, 2019).

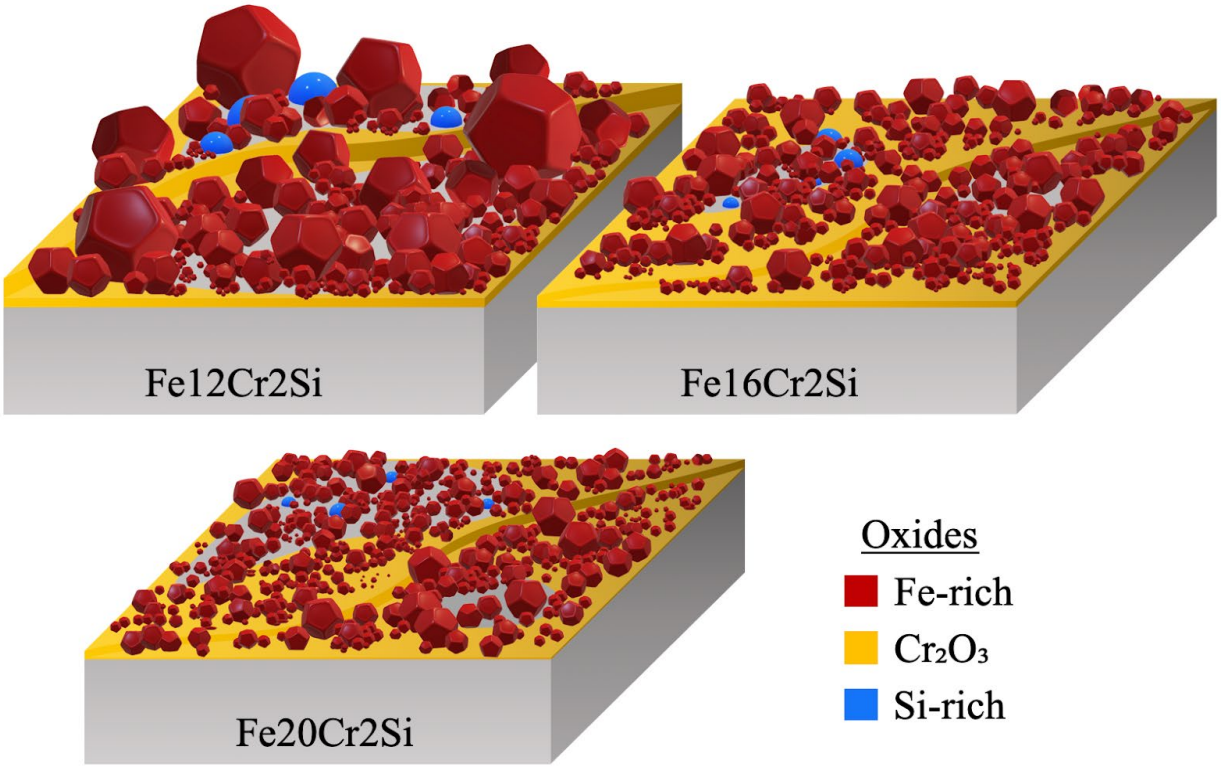

Figure 58: *Schematics of oxide layers on Fe-Cr-Si alloys exposed to simulated PWR primary water for 500 hours in 5ppm Li and 1400ppm B* (Qiang, Leong, Zhang, & Short, 2019).

2.6. Electrochemical impedance spectroscopy (EIS)

EIS curves at earlier stages from the tests had significant fluctuation because the formation of passive oxide layer of Fe-Cr-Si alloys in PWR environments were slow. Therefore, only the final EIS curves are shown in Figure 59-Figure 61, while the data outliers above 10% deviation are removed from the model fitting curve. The black curves are fitted based on the equivalent circuit developed in Figure 62. R_{sol} is the solution resistance, $Q_c = 1/ (Y_c j\omega)^n$ is the capacitance of the oxide film represented as a constant phase element (CPE), R_{po} is the pore resistance, $Q_{cor} = 1/ (Y_{cor} j\omega)^m$ is the double layer capacitance between metal surface and surrounding solution represented as a CPE, and R_{cor} is the corrosion resistance of metal surface.

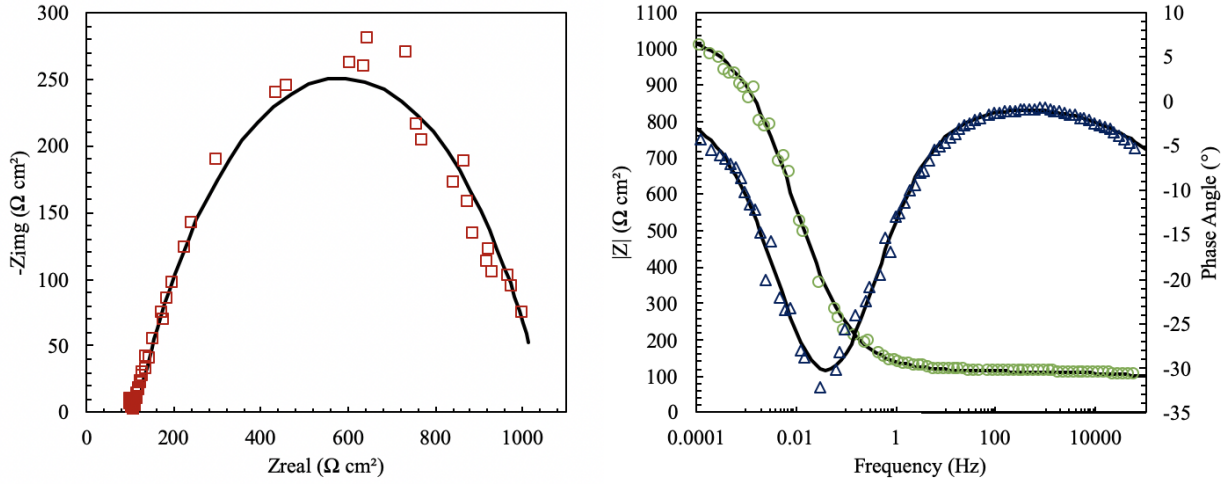

Figure 59: EIS nyquist (left) and bode plot (right) of Fe12Cr2Si exposed in PWR environment after 270 hrs.

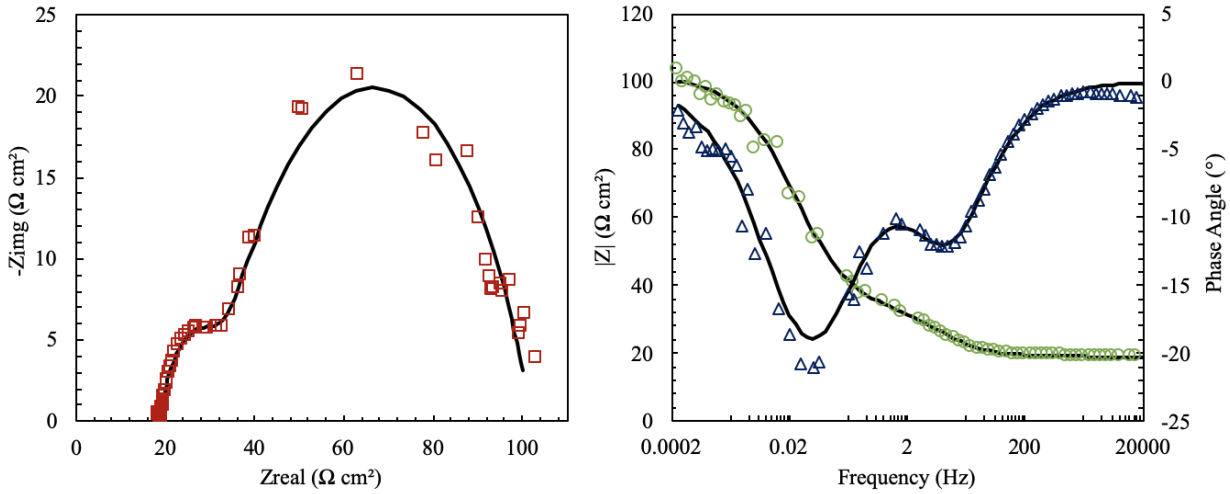

Figure 60: EIS nyquist (left) and bode plot (right) of Fe16Cr2Si exposed in PWR environment after 300 hrs.

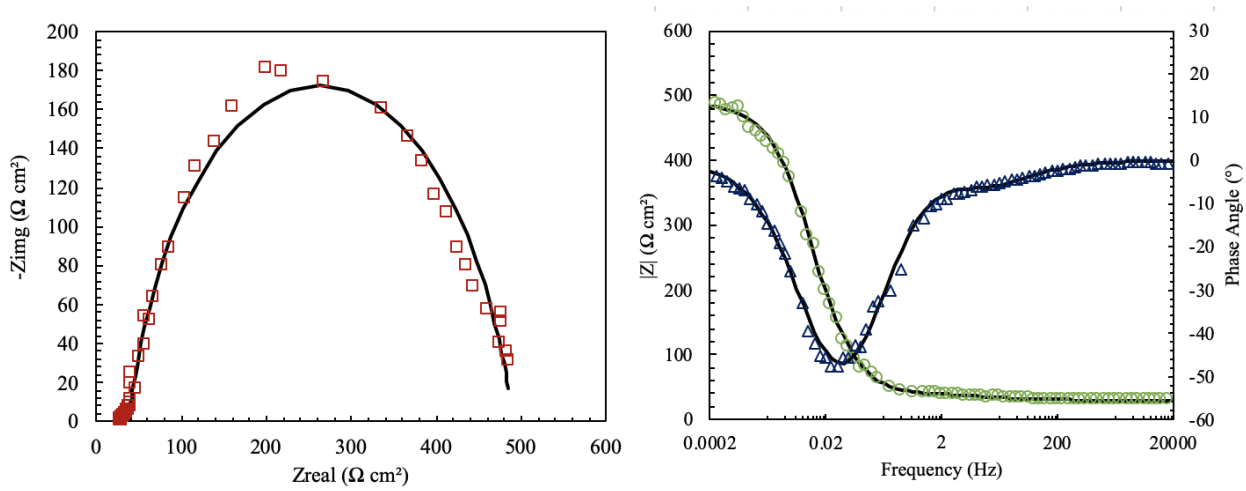

Figure 61: EIS nyquist (left) and bode plot (right) of Fe20Cr2Si exposed in PWR environment after 300 hrs.

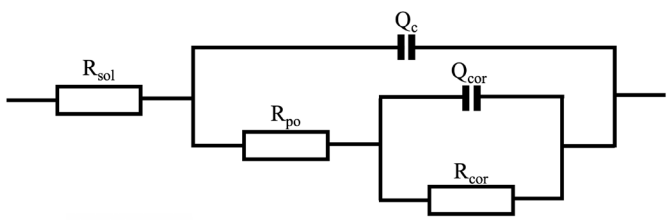

Figure 62: Equivalent circuit based on fitted experimental data

Table 5: Value for elements used in equivalent circuit

Element	Fe12Cr2Si	Fe16Cr2Si	Fe20Cr2Si
Rsol (Ω cm²)	36.95	18.95	29.82
Qcor (μF $cm^{-2}s^{n-1}$)	7.65×10^3	5.83×10^2	2.27×10^2
n	0.624	0.669	0.863
Rpo (Ω cm²)	75.93	15.22	11.74
Qc (μF $cm^{-2}s^{m-1}$)	8.32×10^6	3.80×10^3	4.55×10^3
m	0.455	0.762	0.715
Rcor (Ω cm²)	941.5	67.8	449.6

Based on the fitted element values from Table 5, the oxide layer of Fe12Cr2Si behaves very differently from Fe16Cr2Si and Fe20Cr2Si. This is because the double layer capacitance and the oxide film capacitance of Fe12Cr2Si is much higher compared to Fe16Cr2Si and Fe20Cr2Si. Moreover, the high pore resistance of Fe12Cr2Si indicates that the developed oxide layer is less porous and have less ion conducting paths in comparison to Fe16Cr2Si and Fe20Cr2Si.

The concentrations of dissolution of material are shown in Table 6. The indicated concentrations are obtained based on the difference between pre and post test samples collected from the test solution. The dissolution of Fe12Cr2Si is dominated by Fe, thus along with the EIS data, a Fe-oxide passive layer are most likely formed on the surface. Moreover, the formation of Fe-oxide passive layer may also inhibit the dissolution of Cr and Si, therefore the dissolution concentration of Cr and Si in Fe16Cr2Si and Fe20Cr2Si are much higher than Fe12Cr2Si.

In addition, based on the XPS data from Figure 57, the oxide layer at 5ppm Li after 500 hours does not fully cover the base metal, however the weight gain of Fe12Cr2Si and Fe16Cr2Si is more in 3 ppm Li after 336 hours than 5 ppm Li after 500 hours. This suggests that protective passive oxide layer could be formed on Fe12Cr2Si and Fe16Cr2Si. The high oxidation resistance of Fe20Cr2Si results in less protective oxide layer, which suggests the higher dissolution of elements.

Table 6: Dissolution of elements from Fe-Cr-Si alloys post electrochemical tests in PWR environment after 14 days.

Test ID.	Material	Concentration (ppb)		
		Fe	Cr	Si
E-HTHP 3001	Fe12Cr2Si	129.4	0.22	2178
E-HTHP 3002	Fe16Cr2Si	34.1	2.53	5434
E-HTHP 3003	Fe20Cr2Si	24.3	3.27	5547

3. Stress corrosion cracking (SCC) tests

3.1. Mechanical properties

The material properties of the Fe-Cr-Si alloys were needed to estimate and validate the stress intensity factor from SCC tests. Therefore, tension tests were conducted to obtain the tensile yield strength and ultimate tensile strength. All specimens were tested on an Instron loading machine in room temperature. Unfortunately, the loading machine wasn't built for high temperature testing, therefore the material properties of Fe-Cr-Si alloys were measured in room temperature. The standard test procedure for the tensile tests were conducted in accordance to ASTM E8/E8M standard.

Table 7: Measured Material Properties of Fe-Cr-Si alloys at 25°C.

Material	Yield Strength (MPa)	Ultimate Tensile Strength (MPa)	Modulus of Elasticity (GPa)	Vickers Hardness (HV)	Density (g/cm³)
Fe-12Cr-2Si	340.1 ± 0.3	447.6 ±1.5	216.4 ± 8.5	184.9 ± 17.4	7.37 ± 0.30
Fe-16Cr-2Si	450.6 ± 7.0	503.4 ± 11.0	200.5 ± 19.5	195.8 ± 10.2	7.52 ± 0.34
Fe-20Cr-2Si	412.3 ± 17.4	497.6 ± 13.4	209.4 ± 14.6	212.7 ± 10.2	7.26 ± 0.02

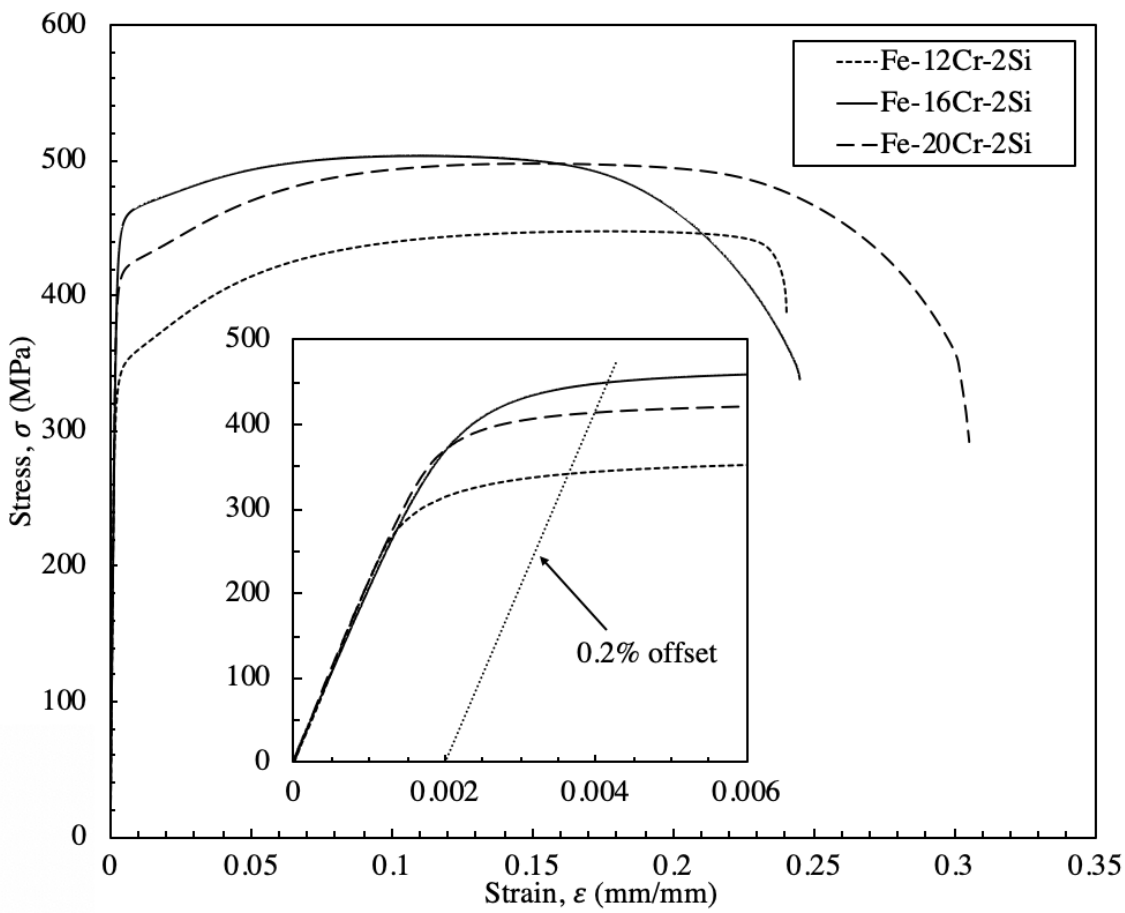

Figure 63: Stress-strain curve of Fe-Cr-Si alloys at room temperature with magnified view on elastic region.

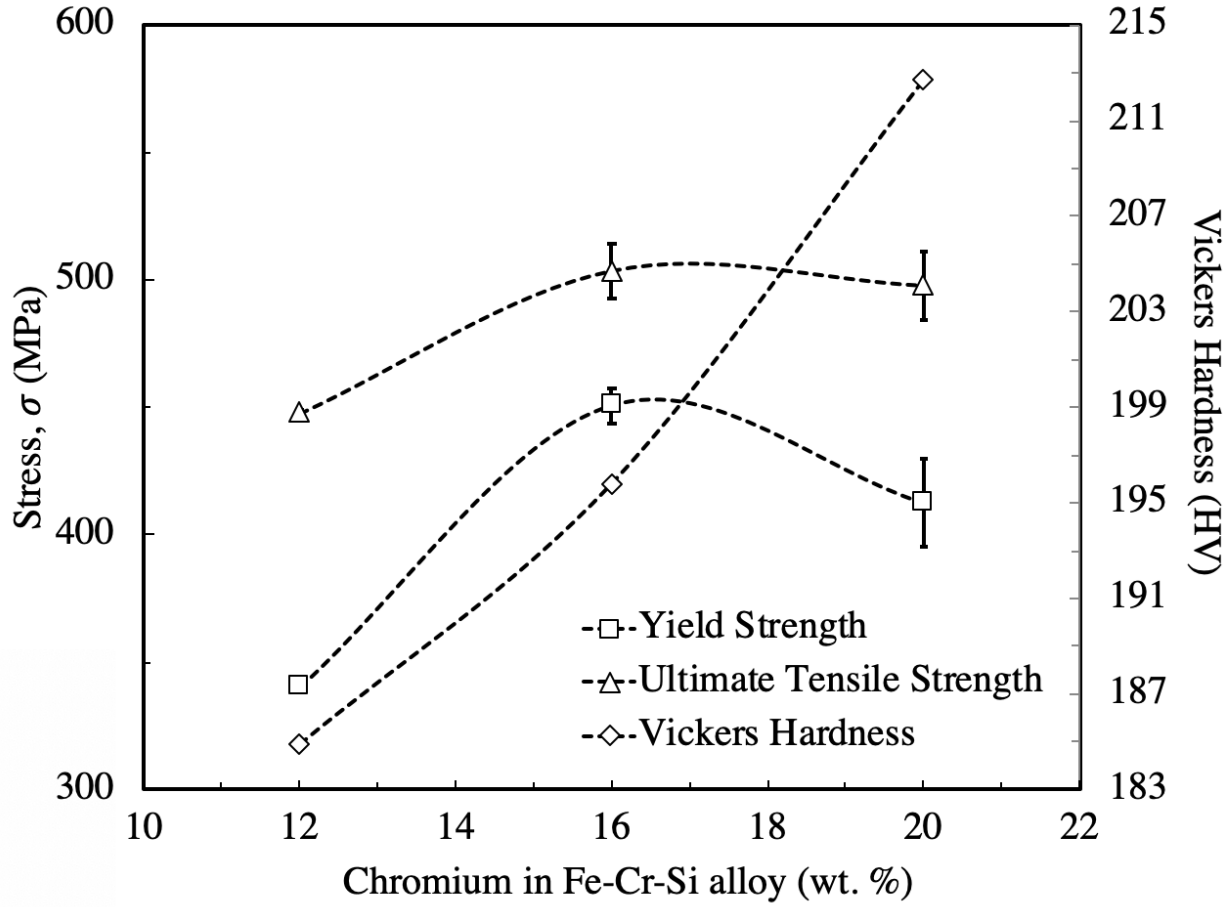

Figure 64: Mechanical properties of Fe-Cr-Si alloys tested as a function of chromium wt.% at room temperature.

3.2. Experimental Methods

Fe12Cr2Si alloy was tested in boiling water reactor (BWR) environment at 288°C. The material was fabricated into a 0.5CT specimen as shown in Figure 65, while a direct current potential drop (DCPD) technique was used to measure the crack growth of the specimen. The platinum wire leads are spot welded on to the positions as indicated in red. The placement of the wire leads is presented in Table 8 as these positions are important to obtain accurate and reproducible DCPD measurements. The CT specimen is loaded using clevis pins and electrically insulated by zirconia and PTFE washers. A constant current of 3A is supplied to the specimen with a pole reversal every 0.5s to eliminate thermoelectric effect. Ultra-high purity DI water of 18.2MΩ cm was circulated inside the system and it is regulated to 1500psi at 288°C. The loading of the specimen is controlled by Interactive Instruments 5K servo motor controller. The dissolve oxygen (DO) in the solution is monitored by periodical sampling of water using CHEmets test kits. The control of the DO level is controlled by controlling the flow rate of N_2 gas.

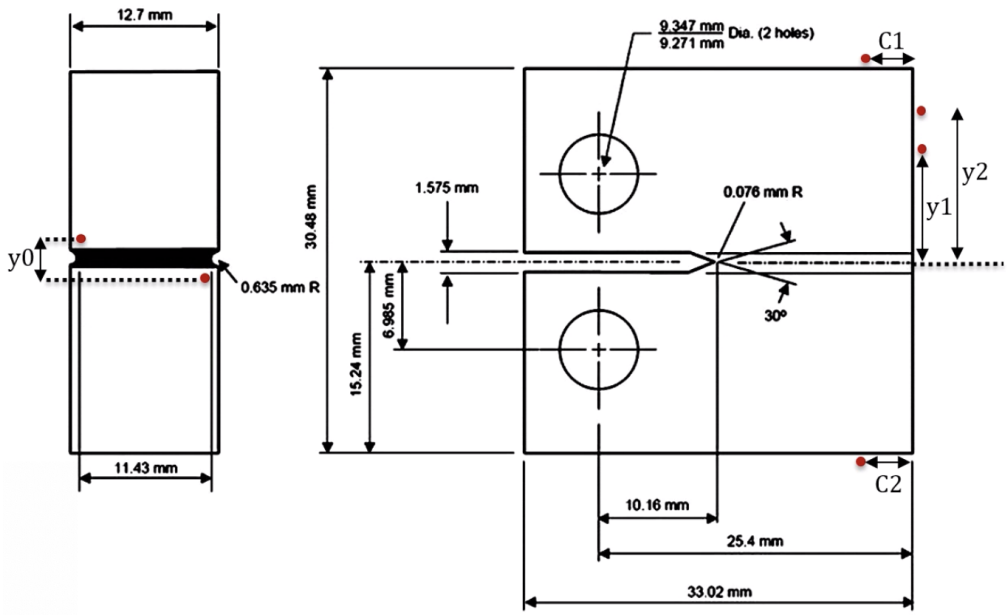

Figure 65: Schematic drawing of CT specimen and placement of wire lead locations marked in red.

Table 8: Typical weld locations of wire leads on CT specimen

Weld Location	Label	Distance (mm)
Current Top	C1	4.75
Current Bottom	C2	4.75
Active Voltage	y0	3.175
Reference Voltage 1	y1	7.62
Reference Voltage 2	y2	13.97

The pre-crack initiation sequence is presented in Table 9, this procedure was used to grow the crack beyond the pre-cracking plastic zone and allow the transition of transgranular (TG) crack into SCC crack growth mechanism with constant K. The material properties from the previous section was used to estimate the max stress intensity K factor. In this test the K_{max} was set at 25MPa√m. The SCC crack growth rate (CGR) of Fe12Cr2Si under differing DO environments was investigated.

Table 9: Pre-Cracking and Crack-Transitioning Procedure Used for Subsequent SCC Crack-Growth Testing at 25 MPa√m

Step #	Kmax (MPa √m)	Frequency (Hz)	Load Ratio (R)	Wave Type	Hold Time (s)	Crack Length Increment (mm)
1	22	1.5	0.3	haversine	N/A	1.7
2	23.5	1.5	0.5	haversine	N/A	0.2
3	23.5	1.5	0.6	haversine	N/A	0.2
4	25	1.5	0.7	haversine	N/A	0.13
5	25	0.1	0.7	haversine	N/A	0.16
6	25	0.01	0.7	haversine	N/A	0.27
7	25	0.001	0.7	haversine	N/A	0.15
8	25	0.001	0.7	trapezoid	235200	0.17
9	25	N/A	N/A	constant K	N/A	N/A

3.3. Crack growth rate

The Fe12Cr2Si specimen transitioned into SCC mechanism after a constant K is achieved. Throughout the test duration, the DO in the exposed environment was manipulated to study the CGR of the sample. The CGRs measurements of the specimen at different test durations are shown in Figure 66. The CGRs are between 1.59×10^{-5} to 9.15×10^{-6} mm/s at 0.8 to 1 ppm DO, 7.22×10^{-6} to 7.8×10^{-6} mm/s at 1.5 ppm DO, and 1.16×10^{-7} to 4.34×10^{-7} mm/s at 2 ppm DO. Increasing DO in the water reduces the CGR of Fe12Cr2Si in BWR environment while decreasing the DO results in higher CGR.

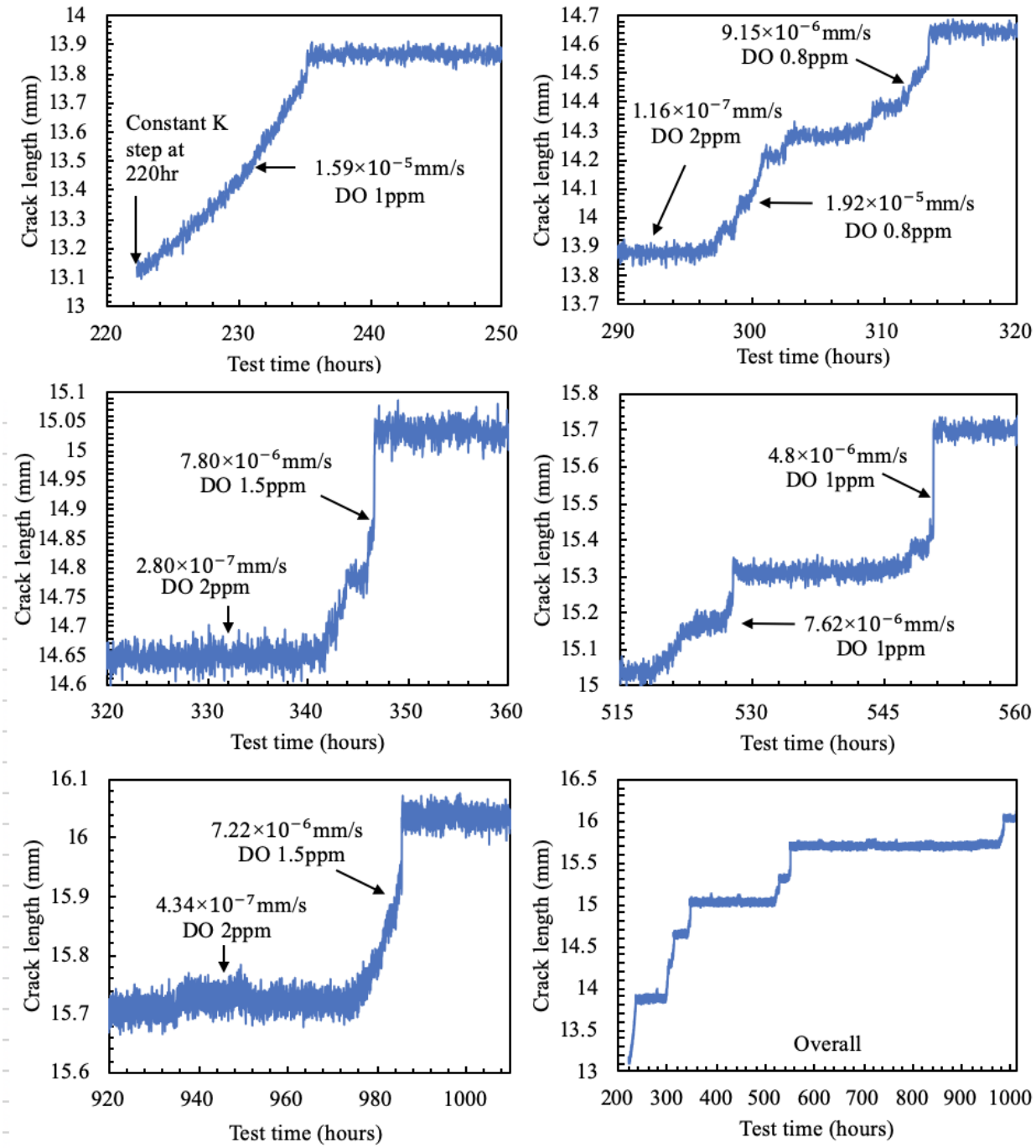

Figure 66: Crack length vs. time of Fe12Cr2Si 0.5CT specimen in 288°C BWR environment at constant K=25MPa√m, showing the effect of DO on CGR.

3.4. Crack growth mechanism

Figure 67 shows the crack line of the Fe12Cr2Si in SCC environment, mixed IG and TG cracks are observed along the path. The final crack tip ends with TG crack while small IG cracks growth are found

along the crack line as shown in Figure 69. Oxide were formed over the surfaces of both IG and TG cracks.

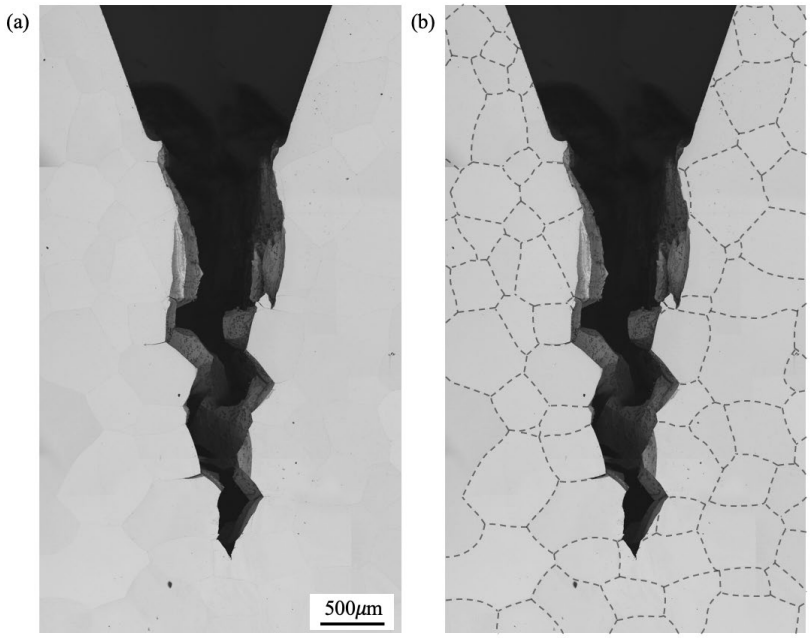

Figure 67: (a) BSE image of Fe12Cr2Si alloy crack path in BWR conditions showing IG and TG cracks and (b) with labeled grain boundaries (BSE).

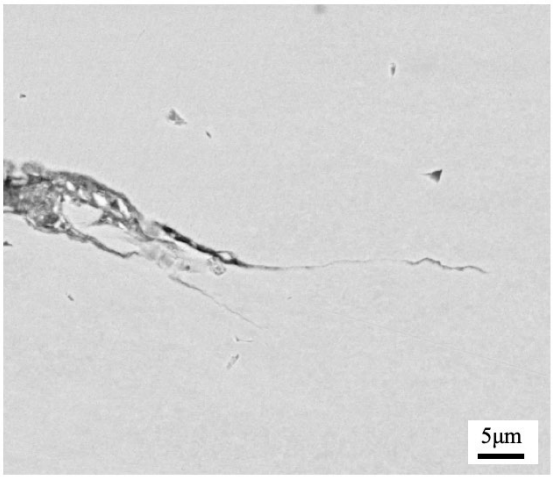

Figure 68: SEM image on the crack tip of Fe12Cr2Si tested in BWR conditions (BSE).

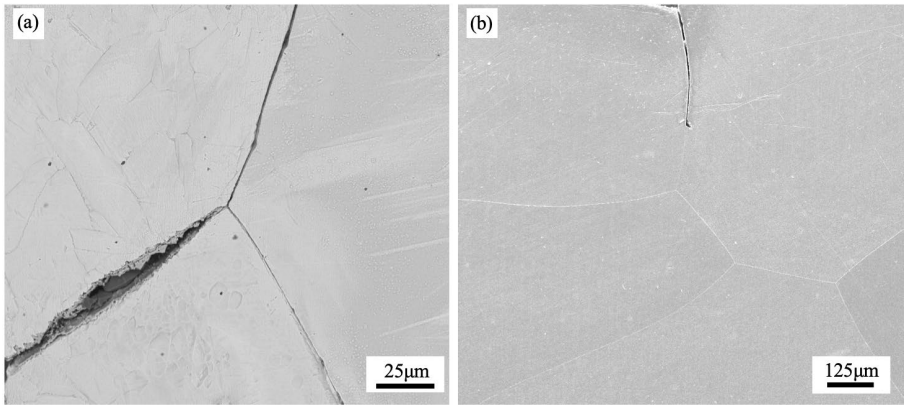

Figure 69: IG crack along the crack line at the (a) top and (b) bottom (BSE).

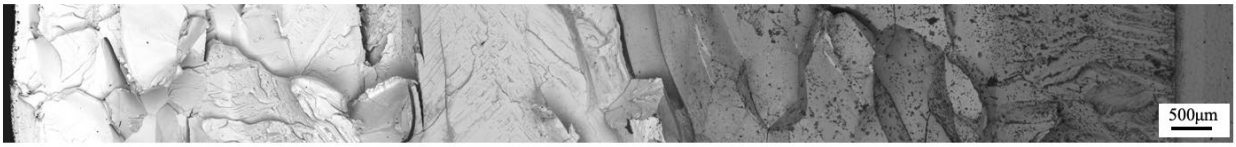

Figure 70: Fracture surface of Fe12Cr2Si merged from multiple images (BSE).

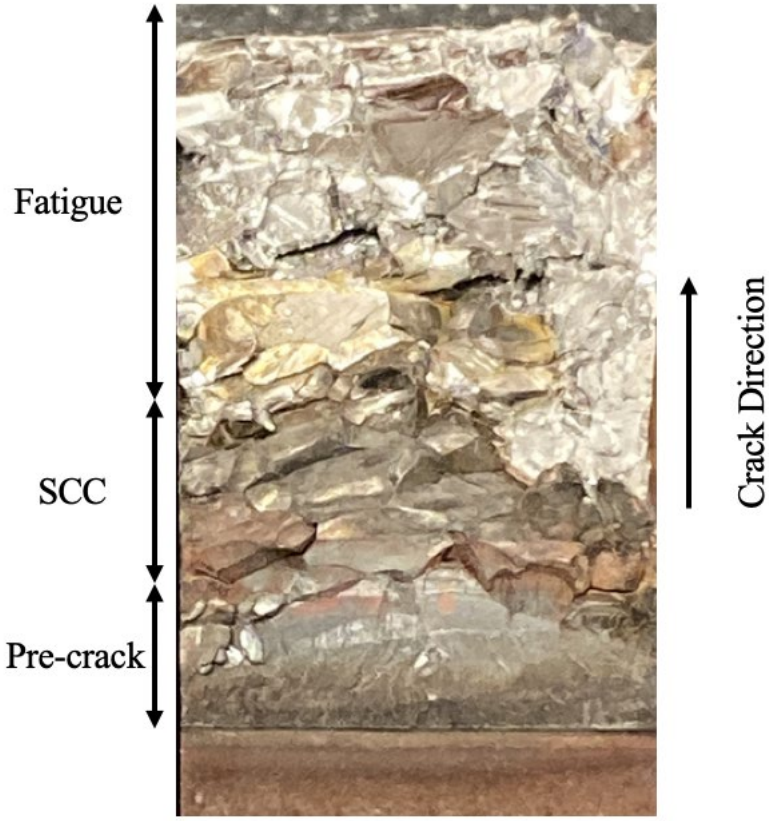

Figure 71: Fracture surface of Fe12Cr2Si with showing different regions of crack mechanism along crack direction.

References

(2017). *ASTM G1, Standard Practice for Preparing, Cleaning, and Evaluating Corrosion Test Specimens.*

Castaing, R. (1960). Electron Probe Microanalysis. *Advances in Electronics and Electron Physics, 13*, 317-386.

Leong, A., Zhang, J., & Xie, Y. (2019). Corrosion of Fe-12Cr-2Si alloy in High Temperature Steam Environments. *19th International Conference on Environmental Degradation of Materials in Nuclear Power Systems - Water Reactors.* Boston.

Qiang, R., Leong, A., Zhang, J., & Short, M. P. (2019). Corrosion behavior of Fe–Cr–Si alloys in simulated PWR primary water environment. *526*.

Additional Steam Oxidation Tests at VTT: In addition to the tests above at Virginia Tech, steam oxidation tests were conducted at a second facility at VTT Technical Research Centre of Finland. The results agreed strongly with each other, showing that Fe-12Cr-2Si suffered heavy corrosion in steam from 1100-1300C, while both Fe-16Cr-2Si and Fe-20Cr-2Si showed excellent performance up to 1200C. All alloys experienced significant steam oxidation at 1300C, which is to be expected given that every 10-15C increases general (Arrhenius-controlled) corrosion rates by a factor of two.

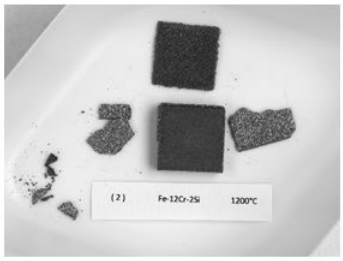

NEUP steam tests at VTT – preliminary results

Ulla Ehrnstén, Sami Penttilä and Seppo Peltonen

The steam oven at VTT - schematic

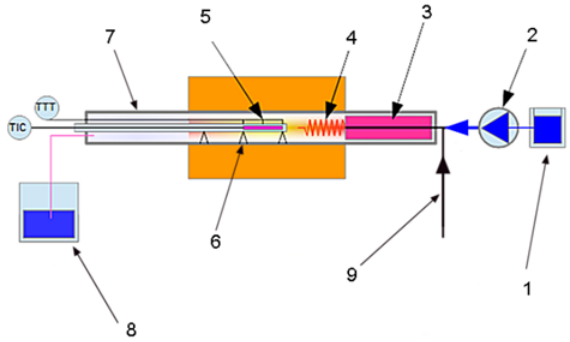

¶

1. Water reservoir (re-circulation loop)	6. Alumina support
2. HPLC pump	7. Alumina tube
3. Preheater	8. Cooling pool
4. Helical super-heater	9. Argon feed line
5. ATF cladding tube with internal heating and temperature control	

Test matrix

Material \ Environment	1100C/1h	1200C/30min	1300C/5min
Fe-12Cr-2Si	Done	Done	Done
Fe-16Cr-2Si	Done	Done	Done
Fe-20Cr-2Si	Done	Done	Done

- We adjusted the original test plan based on the first results showing heavy oxidation and spalling of the oxide
- The specimens (10x10mm) are identified by cut corners, which are individual for all specimens (conventional marking is not visible after tests)

Steam tests at 1200C/30min and 1100C/1h

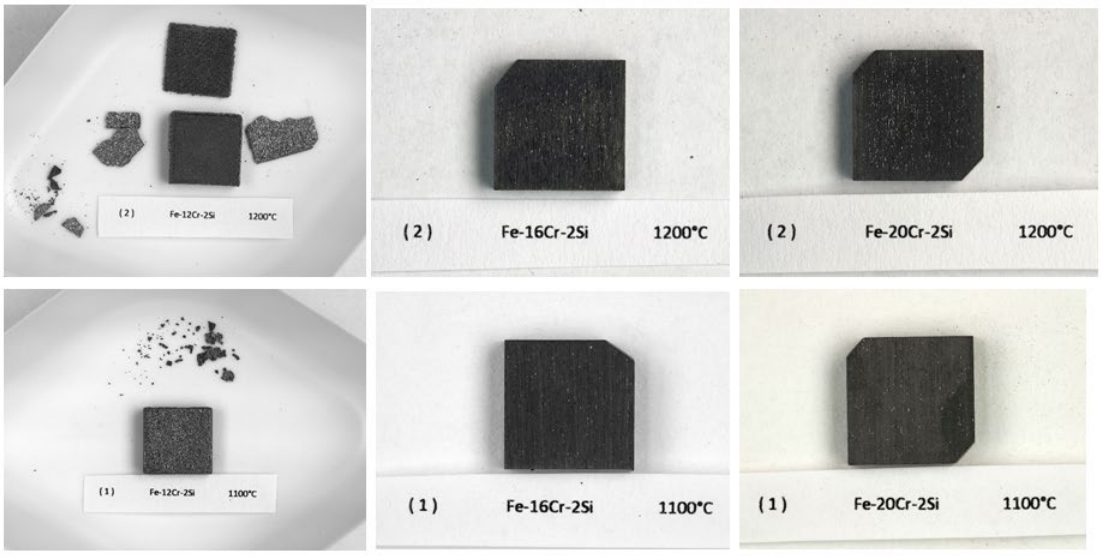

- Extensive oxidation and spalling in Fe-12Cr-2Si material

Steam tests at 1300C/5min

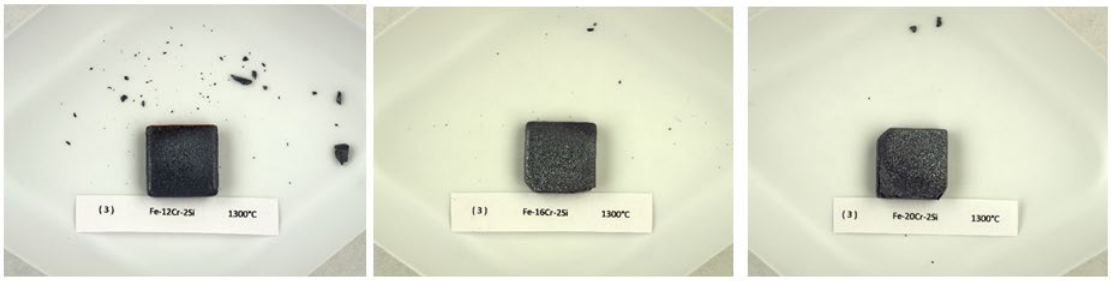

- Most extensive oxidation and spalling in Fe-12Cr-2Si material

Weight gain results

T/t	Fe-12Cr-2Si / MIT	Fe-16Cr-2Si / MIT	Fe-20Cr-2Si / MIT
1100C / 1h	5,41 %	0,09 %	-0,08%
1200C / 30 min	11,22 %	0,15 %	-0,12 %
1300/5min	13,45 %	11,10 %	9,88 %

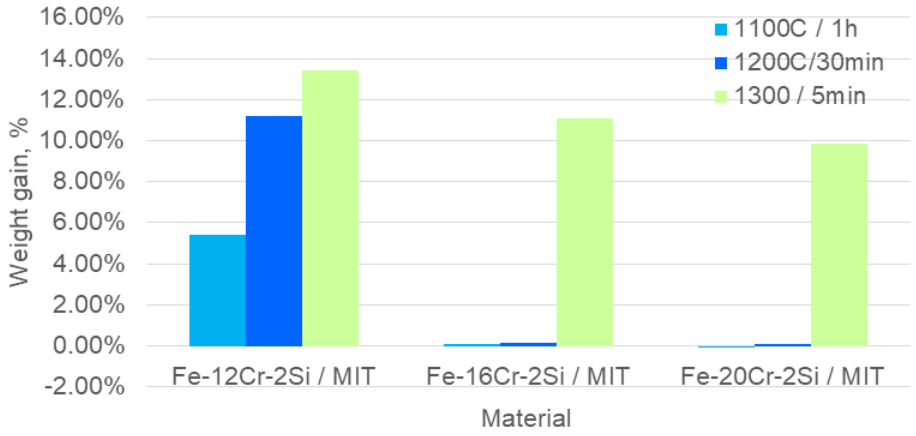

Chapter 4 – Multiscale Modeling of the Four Layer MMLC

Note: All the results from this task have been accumulated into a journal manuscript draft, which will be shortly submitted for publication. The results are presented in this form rather than recompiling and reformatting.

Highlights

Evaluations of the Performance of Multi-metallic Layered Composite Cladding for the Light Water Reactor Accident Tolerant Fuel

Aashique A Rezwan,Michael R Tonks,Michael P Short

- Fuel performance of multi-metallic layered composite (MMLC) cladding shows promise
- MMLC stresses are predicted to be lower than zircaloy cladding throughout operation
- MMLC cladding exhibits lower creep strain and smaller pellet-clad gap than zircaloy
- FeCrSi layer may creep beyond elastic limit, remediated with 40-60 μm pellet-clad gap
- MMLC fission gas release higher than that of zircaloy cladding of similar thickness

Evaluations of the Performance of Multi-metallic Layered Composite Cladding for the Light Water Reactor Accident Tolerant Fuel

Aashique A Rezwan[a], Michael R Tonks[b] and Michael P Short[c]

[a]Department of Mechanical Engineering, The Pennsylvania State University, University Park, PA 16801
[b]Department of Material Science and Engineering, University of Florida, Gainesville, FL 32611
[c]Department of Nuclear Science and Engineering, Massachusetts Institute of Technology, Cambridge, MA, 02139, USA

ARTICLE INFO

Keywords:
Light Water Reactor (LWR)
Nuclear Fuel Performance
Multi-metallic Layer Composite (MMLC)
BISON

ABSTRACT

In this study, an assessment is carried out to evaluate the performance of a multi-metallic layered composite (MMLC) cladding, designed to sustain a longer period of time during accident scenarios for light water reactor (LWR) fuel. The proposed MMLC cladding concept will increase the corrosion resistance but result in a neutron absorption penalty. This cladding could also result in negative impacts due to mismatches between the mechanical behavior of the various layers. In this study, the mechanical performance of the MMLC has been evaluated using two types of simulations: small scale thermo-mechanical simulations and a full-length fuel rod simulations. Both types of simulations were carried out using the BISON fuel performance code. The small scale simulations predicted a reduction in residual stress and elastic deformation compared with the standard zircaloy cladding. The fuel rod simulations showed a decrease in creep strain, larger pellet-clad gap and possible plastic deformation under long time use when compared to zircaloy and stainless-steel cladding. The performance of various gap widths and layer thicknesses were compared to assist in the design of MMLC cladding.

1. Introduction

The Fukushima Daiichi nuclear power plant disaster in 2011 motivated the nuclear community to incorporate more accident tolerance in Light Water Reactor (LWR) fuel and cladding materials. A major goal in this effort is to determine alternative materials for cladding that provide improved resistance to oxidation in accident conditions. There have been many efforts to develop new cladding materials, including coatings on zircaloy tubes such as MAX phase, chromium, or iron-chrome-aluminum (FeCrAl) [1, 2, 3], advanced stainless steels such as oxide dispersion strengthened (ODS) steels or FeCrAl [4, 5], and silicon carbide composites [6]. Mo alloys [7] and multi-metallic layered composites (MMLCs) of ferritic steels on Zircaloys are also being considered [8, 9, 10, 11].

A conceptual MMLC fuel cladding is currently being developed at the Massachusetts Institute of Technology to enhance performance and accident tolerance by removing all coolant contact with zirconium while introducing only limited amounts of new materials with higher neutron cross-sections. The MMLC concept is composed of four metallic layers, each of which is designed to perform specific functions unattainable by single alloys. However, the introduction of multiple materials could result in problematic behaviors due to different mechanical properties in the different layers, such as thermal expansion or creep. In this study, we evaluate the performance of the proposed MMLC using a thermomechanical simulation of fresh cladding, fuel performance simulations of steady operation for five years and fuel performance simulations of a transient experiment. No significant stresses were identified in the fresh cladding, but the MMLC was shown to cause elevated fuel centerline temperature and accelerated fission gas release. These effects could be reduced by changing the layer thicknesses or by decreasing the gap width. The details of the MMLC concept and the material properties of the various layers are provided in Section 2. The modeling approach is summarized in Section 3 and the results are discussed in Section 4.

*Corresponding author
michael.tonks@ufl.edu (M.R. Tonks)
ORCID(s):

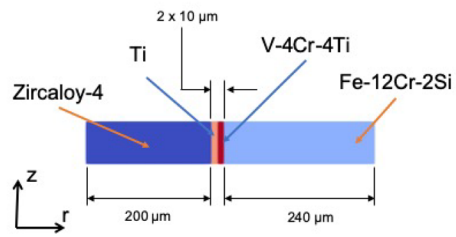

Figure 1: Proposed MMLC cladding layers with their respective thickness.

2. Composite Cladding Concept and its Different Layer's Properties

Composite materials are widely used in the nuclear industry in the manufacture of fuel cladding, where an overlay or sleeve of pure Zirconium is applied to a billet of Zircaloy and co-extruded [12]. This approach is also used in the fossil boiler industry, where a high-strength, creep-resistant material is clad with an overlay of high chromium alloys [13].

The MMLC cladding concept, shown in Fig. 1, is composed of a Fe-12Cr-Si alloy layer (Fe layer) overlaid onto a Zircaloy-4 layer (Zr layer). The Zr layer is there to minimize

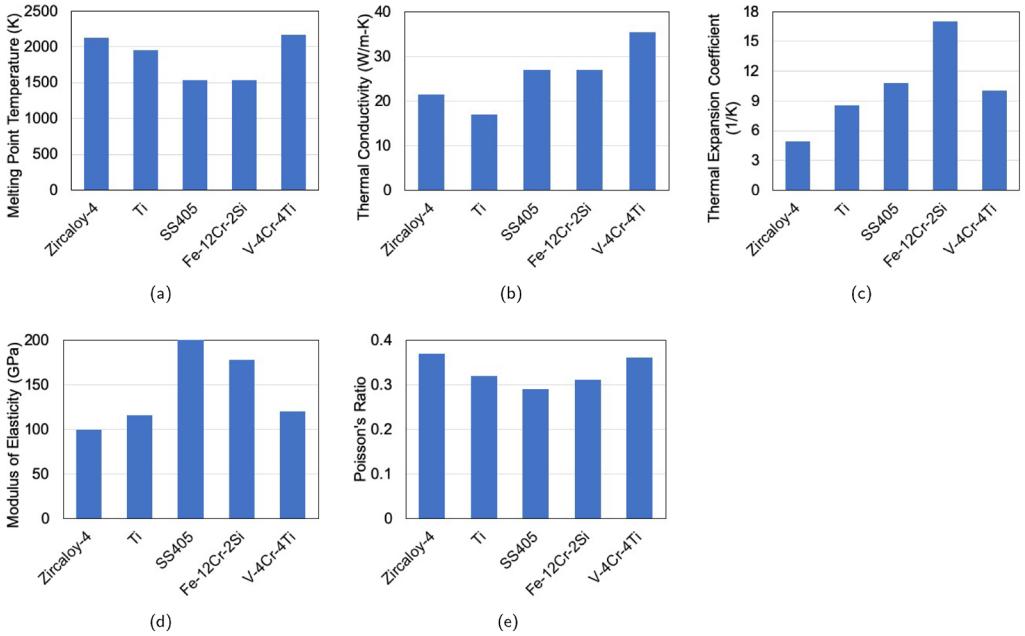

Figure 2: Properties for different layer materials (a) Melting Point, (b) Thermal Conductivity, (c) Thermal Expansion Coefficient (d) Modulus of Elasticity and (e) Poissons Ratio [14, 15, 16, 17, 18, 19, 20, 21].

the neutron cross-section, while the water-facing Fe layer resists corrosion better than Zr [10], especially during a severe accident. Between these two layers, there is a commercially pure Titanium layer (Ti layer) and a vanadium alloy (V-4Cr-4Ti) layer (V layer) to avoid the formation of a detrimental eutectic phase between the Zr and Fe layers. These two diffusion barrier materials have high melting temperatures and high thermal conductivity, as shown in Fig. 2a and 2b, so they will not negatively impact the cladding performance. It is expected that the MMLC will incur a neutronic penalty of four to five times since all the other layers have much higher cross-sections than Zircaloy-4 [22, 23, 24, 25] (see Table 1). The MMLC is fabricated by making each layer separately as a cylindrical billet, followed by a thermal fit process where they are machined to an exact tolerance. After machining, the layers are heated, slid into each other, and then allowed to cool and bond tightly.

Heat is generated within the fuel pellets, transported through the gap and cladding and then carried away by the coolant. Thus, the temperature profile in the cladding is impacted by the fuel rod geometry, neutron flux, thermal conductivity of the fuel and cladding, and coolant flow conditions. The temperature gradient across the cladding results in a thermal expansion gradient, and thus a stress gradient. The different thermal expansion coefficients of the layers in the MMLC could significantly increase this stress gradient. In addition, the different elastic moduli, yield stresses, and creep behavior of the layers could also hurt the performance. The goal of this project was to investigate the impact of the four layers on the performance of the MMLC cladding concept under normal LWR operating conditions. We will not consider residual stress in the MMLC cladding due to fabrication, oxidation, or hydride formation.

Table 1
Thermal neutron absorption cross-section for different materials and their alloys [22, 23, 24, 25].

Elements	Thermal Neutron Cross-Section (Barns)	Cross-Section ratio
Zirconium (Zr)	0.185	1
Iron (Fe)	2.55	15
Vanadium (V)	5.04	30
Titanium (Ti)	7.84	45
Zircaloy-4	0.2	1
FeCrAl	2.43	15

3. Modeling and Simulation Consideration

The evaluation of the MMLC was performed with two types of simulations using the BISON fuel performance code [26]. First, a small scale cladding unit was used to simulate the thermal stresses in fresh cladding due to a temperature gradient representative of steady reactor operation. Sec-

ond, the performance of the MMLC cladding in a full length fuel rod was evaluated during normal reactor operation. In sections 3.1 and 3.2, we discuss the modeling approach and boundary conditions for the small scale simulations. Next, in sections 3.3 and 3.4 we present the fuel performance modeling approach and the material models that were used for the full length fuel rod.

3.1. Model Formulation for the Simulation of Thermal Stresses in Fresh Cladding

The small scale simulations were performed to evaluate the thermal stresses that form in fresh cladding due to a temperature gradient representative of steady-state reactor operation. In this case, the temperature profile was evaluated using the steady-state heat conduction equation,

$$\nabla \cdot k \nabla T = 0, \tag{1}$$

where k is the local thermal conductivity of the layer material and T is the temperature of the domain. The thermal conductivities of the different layers used in the simulations are presented in Fig. 2b.

The thermal strain was calculated by

$$\epsilon_T = \alpha(T - T_0)\mathbf{I}, \tag{2}$$

where, ϵ_T is the thermal strain tensor, α is the thermal expansion coefficient (Fig. 2c), and $\mathbf{I}$ is the second-order identify tensor. In the present study, the thermal expansion coefficient is considered constant and isotropic. T_0 is the reference stress-free temperature and it is assumed to be equal to the inlet coolant temperature, 580 K.

The stress tensor $\boldsymbol{\sigma}$ in the cladding blocks depends on both the elastic strain ϵ and the thermal strains ϵ_T by

$$\boldsymbol{\sigma} = \boldsymbol{C}(\epsilon - \epsilon_T), \tag{3}$$

where, $\boldsymbol{C}$ is the elasticity tensor. The elasticity tensor for the different layers is assumed to be isotropic and thus described by two elastic constants presented in Fig. 2d and 2e.

All of the layer materials for the small scale simulation were assumed to be linear elastic. While linear elasticity was assumed, we explicitly compared the resultant stresses to the corresponding yield stresses, to investigate the validity of the assumption. Mechanical equilibrium was assumed and the displacements were calculated by the stress divergence equation in steady state,

$$\nabla \sigma = 0. \tag{4}$$

3.2. Geometry and Boundary Conditions for the Simulation of Thermal Stresses in Fresh Cladding

A two-dimensional axisymmetric section from the full cylindrical cladding was meshed using the open source GMSH code [27]. A mesh with 46,258 quad elements separated into four blocks representing the four metallic layers was used to model the cladding, as shown in Fig. 3. First-order Lagrange elements were used in the simulations. The left edge (interior) of the cladding was a distance R_f from the center of the cylinder.

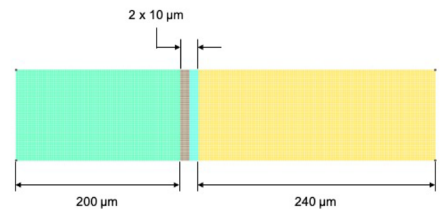

Figure 3: Mesh for the axisymmetric section of the MMLC fuel cladding. First-order Lagrange elements were used.

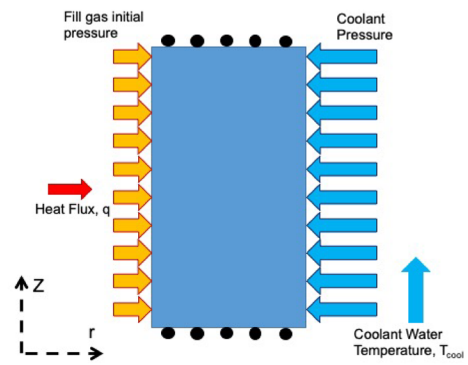

Figure 4: Boundary conditions considered for the MMLC cladding thermal stress simulation. All parameters remain fixed in temperature to simulate the normal operating condition of LWR.

Table 2
Parameter for thermal BC for steady state simulation

Parameter	Value
Linear Heat Rate (LHR)	25 kW/m
Gap Thickness (t_{gap})	70 μm
Radius of Fuel Rod (R_f)	4.03 mm
Convective Coefficient of Coolant (h_{cool})	25 $kW/(m^2 - K)$
Fill Gas Thermal Conductivity (k_{gap})	$16\times10^{-4}T^{0.79}$ $W/(m - K)$
Coolant Pressure	15.5 MPa
Fill Gap Pressure	2 MPa
Coolant Temperature	580 K

The boundary conditions of the cladding section, shown in Fig. 4, were similar to those from Wu et al [28] to simulate LWR normal operating condition. The parameters used for the boundary conditions are shown in Table 2. A heat flux was applied on the interior of the cladding (Fig. 4) calculated using the fuel linear heat rate (LHR) and pellet radius (R_f):

$$q = \frac{LHR}{2\pi R_f}. \tag{5}$$

On the exterior of the cladding, a fixed temperature was applied that was related to the coolant flow temperature using the equation

$$T_{out} = T_{cool} + \frac{LHR}{2\pi R_f h_{cool}}, \tag{6}$$

where the coolant temperature T_{cool} and the convective coefficient of the coolant h_{cool} were held constant.

The displacement in the z-direction was fixed on the top and bottom, effectively modeling an interior section of a long tube. Initial fill gas pressure and coolant water pressure were applied normal to the inner and outer cladding surfaces. Helium was considered as the initial fill gas in the gap to simulate the start of a nuclear reactor.

3.3. Model Formulation for the Full Length Fuel Rod Simulations

Full-length fuel rod simulations were carried out to evaluate the reactor performance of the MMLC. The fuel rod was represented with a series of 1D axisymmetric layers (often called 1.5D). In the present study, the model consisted of 10 cylindrical layers, each layer having 54 elements.

For each axial slices, the transient version of Eq. (1),

$$\rho C_p \frac{dT}{dt} - \nabla \cdot k\nabla T - q = 0, \tag{7}$$

and the stress divergence equation (Eq. (3)) were solved simultaneously, assuming 1D axisymmetric behavior. Here, ρ is the density and C_p is the specific heat. q is the volumetric heat generation rate and is calculated using the local power density. The power density was calculated using the DIONISIO model as described in [29, 30].

The mechanical contact between the fuel pellet and cladding was applied through node constraints and accomplished using the algorithm proposed by Heinstein and Laursen [31]. The gap heat transfer was calculated in the conventional manner by computing the gas conductance within the gap [32]. The model also included the effect of solid-solid heat transport, once the mechanical contact between the fuel pellet and the cladding was established.

The geometry and operating conditions used in the simulations are shown in Table 3.

3.4. Material Models for the Full Length Fuel Rod Simulations

3.4.1. Uranium dioxide fuel

In our study, uranium dioxide (UO_2) was considered as the fuel. The fuel thermal conductivity was calculated using the Nuclear Fuel Industry Research (NFIR) model [33, 34]. Change in fuel pellet volume depends on the solid fission products, gaseous fission products, and the densification. The densification of the fuel was calculated using the ESCORE empirical model [35] with simplification for temperatures over 750 °C. Solid swelling, which is linearly proportional to the burnup, was approximated with the empirical model outlined in MATPRO [36]. The fission gas release and gaseous swelling were calculated by the model presented in Refs. [37, 38]. The modified-ESCORE model, as suggested by Kramman et al. [39], was used to account for the fuel pellet cracking and relocation before the gap closed. The model was calibrated with the data presented in Ref. [40] to better match the experimental IFA data.

Table 3
Fuel rod specification and input condition for normal operating condition

	UO_2/Cladding
Number of pellets	10
Fuel enrichment (%)	5
Pellet Length (mm)	11.86
Pellet Outer Diameter (mm)	8.2
Radial gap width (μm)	80
Cladding thickness (overall) (mm)	0.460
Rodlet diameter (mm)	8.74
Initial fill pressure (MPa)	2
Plenum height (mm)	27
Initial fuel grain radius (μm)	10
Coolant inlet mass flux ($kg/m^2 - s$)	3800
Coolant pressure (MPa)	15.5

3.4.2. Zr Layer (Zircaloy-4)

As shown in Fig. 1, the inner layer of the MMLC is Zircaloy-4. The elastic modulus and Poisson's ratio of the Zr layer were held constant at the values typically used in BISON [41]. The temperature-dependent specific heat and thermal conductivity were adopted from Ref. [28]. Strain due to anisotropic thermal expansion in the Zr layer was calculated as described by the function in MATPRO [42]. The increment of the cladding axial strain due to the irradiation growth was calculated using the equation presented in Ref. [43], where the material properties are taken from Ref. [35]. The irradiation-induced creep in the Zr layer was computed using the empirical model presented in Ref. [44], which relates the creep rate to the current fast neutron flux and stress. The primary and secondary thermal creep rate was calculated using the Limback-Andersson model given in Ref. [45].

3.4.3. Fe Layer (Fe-12Cr-Si)

Fe-12Cr-2Si is used for the coolant facing layer in the MMLC. The sum of thermal and irradiation creep at steady state were calculated using the equation proposed in Refs. [46, 47]. The mechanical constitutive model for the Fe layer was J2 plasticity, using the elastic modulus and Poisson's ratio from Fig. 2 and the plastic hardening parameter was calibrated using the model presented in Ref. [21]. In the absence of data, we assumed no significant swelling or irradiation hardening in the layer.

For comparison, we have also presented results using a single layer Fe cladding described using the same materials models as the Fe layer, with the exception that deformation was assumed to be linear elastic.

3.4.4. V Layer (V-4Cr-4Ti) and Ti Layer

Material properties for the V and Ti layers in the MMLC were held constant throughout the simulation and are the same as used for the small scale model (Fig. 2). Thus, we assumed no significant irradiation effects in the thin diffusion barrier layers.

4. Results and Discussions

The goal of this research is to evaluate the performance of the proposed MMLC and to make recommendations for its optimal design. The results are presented as follows: Section 4.1 presents the results form the simulation of thermal stresses in fresh cladding; Section 4.2 presents the results of the full-length fuel rod simulations; Sections 4.3 and 4.4 investigate the impact of the layer thicknesses and the gap size on the MMLC behavior, respectively; Section 4.5 compares the MMLC performance with experimental results from the TRIBULATION database.

4.1. Simulation of Thermal Stresses in Fresh Cladding

The temperature and the resultant radial stress in the MMLC cladding section due to the boundary conditions shown in Fig. 4 are presented in Fig. 5a. Both change slope in the different layers, but there are no sudden changes between layers. This is because we assumed no interface thermal resistance and that the layers are strongly bonded together.

Figure 5 shows the axial and hoop stress within the layers. For comparison, the stresses within homogeneous Zircaloy-4 and Fe-12Cr-2Si claddings (referred to as Zr cladding and Fe cladding, respectively) are also shown. The compressive hoop stress in the Zr layer in the MMLC was smaller than that in the Zr cladding, while it was larger in the Fe layer than in the Fe cladding (Fig. 5b). The compressive hoop stress in the V and Ti layers was somewhat larger than in the Zr layer. Similar to the hoop stress, the compressive axial stress in the Zr layer was smaller than in the homogeneous Zr cladding, while it was larger in the the Fe layer than in the homogeneous Fe cladding (Fig. 5c). The compressive axial stress in the Ti layer was slightly smaller than that in the Zr layer, while it was larger in the V layer than in the Zr layer.

To determine if the stresses in the layers were large enough to cause yielding, we calculated the ratio of the von Mises stress to the yield stress, as shown in Fig. 5d. For comparison, the ratio in the Zr and Fe claddings is also shown. The von Mises stress is below the yield stress in all layers, suggesting that the layers will only deform elastically at the beginning of reactor operation.

The neutron penalty incurred by the MMLC compared to homogeneous Zr cladding could be reduced if the Fe layer thickness were decreased and the Zr layer thickness increased, keeping the overall cladding thickness the same. However, the impact on the stress of this change in geometry (defined by the change in the ratio of the Zr layer thickness to the Fe layer thickness) needs to be analyzed. For this reason, we simulated MMLC claddings with thickness ratios ranging from 0.5 to 10 (the geometry from Fig. 1 has a thickness ratio of 0.83). The resultant ratios of the maximum von Mises stress to the yield stress in the Zr and Fe layers for the various thickness ratios are shown in Fig. 6. With increasing thickness ratio, the maximum stress ratio increases in both layers but with decreasing slope. Thus the stresses will remain elastic for all thickness ratios.

The simulations of the thermal stresses in fresh cladding indicate that the residual stresses induced by the different thermal expansion coefficients will not be large enough to induce plastic deformation, irrespective of the relative thicknesses of the Zr and Fe layers.

4.2. LWR Fuel Rod Performance using the MMLC

While the beginning of life simulations showed that the residual stresses induced in the MMLC are below the yield stress, the fuel and cladding behavior change significantly during reactor operation. Thus, we simulated the MMLC (with layer thicknesses as depicted in Fig. 1) under normal LWR operating conditions. The linear heat rate was ramped to 25 kW/m over 3 hrs and then held constant for the next 4 years, as was done in Refs. [48, 28, 49]. As before, homogeneous zircaloy-4 and SS405 cladding (referred to as Zr cladding and Fe cladding, respectively) were also simulated for comparison.

In Fig. 7a, the fuel centerline temperature in the MMLC, Zr and Fe cladding is shown throughout the simulation. The centerline temperature is initially higher for both the MMLC and Fe cladding than the Zr cladding until the pellet-cladding mechanical interaction occurs. Pellet-cladding gap closes around 20,000 hr for MMLC and the Fe cladding (Fig. 7b), while for Zr cladding it closes around 5000 hr. After the pellet-cladding mechanical interaction the fuel centerline temperature for all the cladding follows the same slope in temperature. The higher thermal expansion coefficient of the Fe layer corresponds to the larger pellet-clad gap.

Figure 7c represent the hoop stress for the different cladding. The MMLC was modeled using the isotropic plasticity with hardening for the Fe layer and creep strain modeled for both the Zr and Fe layers. For comparison, the radial and hoop stress of the homogeneous Zr and Fe cladding is also plotted alongside. The radial and hoop stress is lower at the early life of irradiation for the MMLC than the Zr cladding. But after the pellet cladding gap closes, the stress increases and surpluses the stress of Zr cladding at around 25,000 hr. Due to the onset of plastic deformation for the Fe layer at the end of the lifetime of reactor operation, the stress again decreases for the MMLC cladding. The Fe cladding was modeled with linear elasticity and the stress is seen to be increasing towards the end.

The higher initial temperature of the MMLC cladding also contributes to the higher fission gas release in the early life of the fuel rod. Figure 7d shows the increased fission gas release for the MMLC and the Fe cladding. After the pellet-cladding gap closes, the total fission gas release fol-

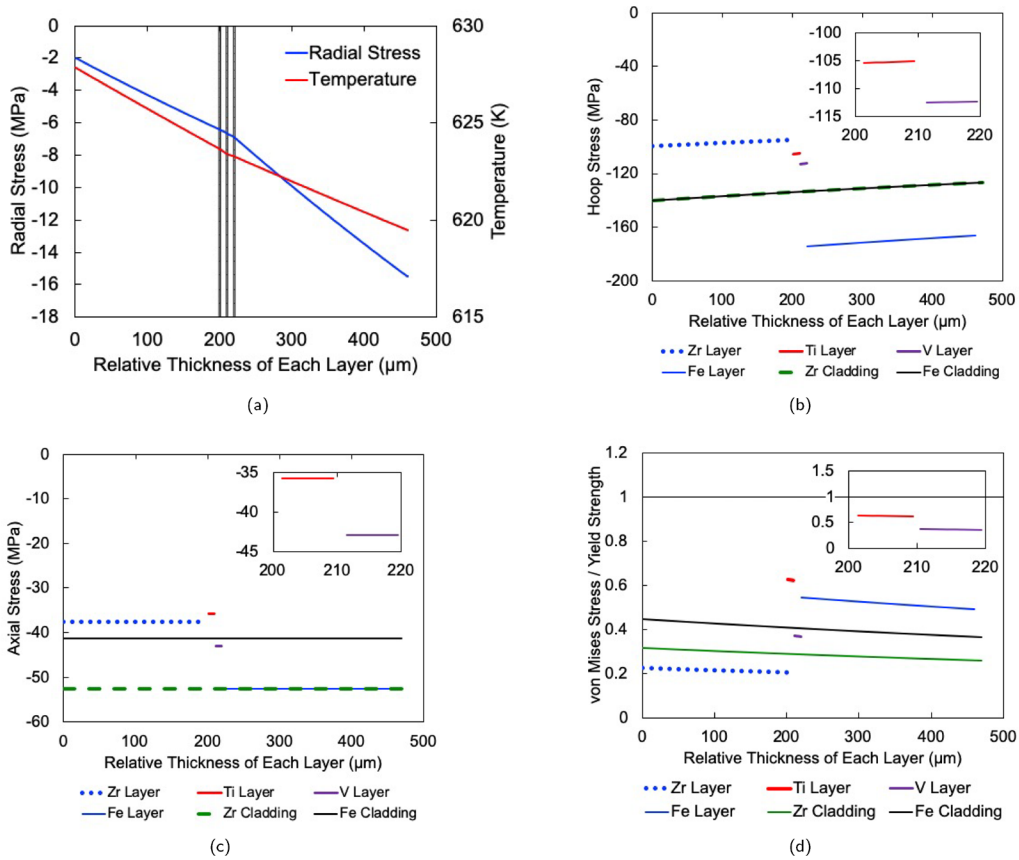

Figure 5: (a) Continuity of the radial stress and the temperature within the MMLC cladding using linear elasticity. The continuity of radial stress exhibits the rigid bonding assumption between the MMLC layers. (b) Hoop and (c) axial stress distribution throughout the cladding system using the linear elastic model. All the layers in the MMLC cladding experiences compression. The stress in the Zr layer in MMLC cladding is lower than the single layer Zr cladding, but for the Fe layer in MMLC the stress is higher than the single layer Fe cladding. (d) The ratio of von Mises stress to the yield stress. All the layer exhibit elastic deformation at steady state.

lows the slope of the Zr cladding and is lower at the end of the irradiation lifespan.

4.3. Effect of Thickness Ratio

The MMLC shows elevated fuel centerline temperature and fission gas release in the early lifetime of the nuclear reactor operation. Another goal of this study is to recomend optimum design for the MMLC cladding. In this respect, a set of simulation was run to determine the optimum thickness ratio and the size of the initial gap size of the pellet and cladding. In this section we presents the performance analysis of the MMLC by varying Zr and Fe layer thickness keeping the total cladding thickness constant.

Figure 8a shows the fuel centerline temperature for the different thickness ratio. Increasing the Zr layer thickness decrease the fuel centerline temperature. This affects the pellet-clad gap closer time (Fig. 8b). The gap closes earlier for the thicker Zr layer and afterwords the temperature profile follow the same slope as of homogeneous Zr cladding.

The pellet-clad gap also affects the hoop stress exertion in the cladding. The average hoop stress for the lifespan of the fuel rod is shown in figure 8c. Before the gap closer, the average hoop stress in the cladding is same for all cases. But as soon as the gap closed, the stresses increased. Thus, for the higher thickness of Zr layer, the stresses become larger at the end of the fuel rod lifespan.

Figure 8d illustrates the total fission gas released throughout the simulation. The fission gas released is higher

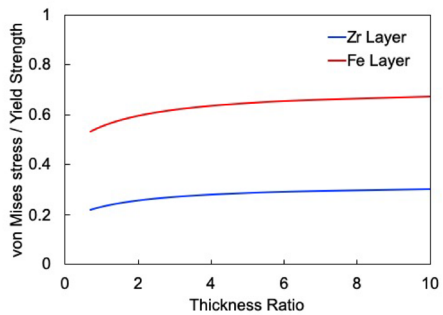

Figure 6: Ratio of the maximum von Misses stress to the yield strength in the Zr and Fe layers with increasing Zr thickness. In both layers, the stress increases with increasing Zr thickness but tends to a maximum value. This suggests that the layers will remain elastic for all thickness ratios at steady state.

for the lower thickness ratio and decreased with increasing thickness of Zr layers.

4.4. Effect of Initial Pellet Cladding Gap Size

In this section, we present the results from varying initial gap size. All the parameters of the simulation are the same as the previous section, except the gap size was varying in each of the simulations. This will give an idea for the optimum gap size may be carried out to design the MMLC for the future reactor design.

With smaller gap size the time required for the pellet-cladding gap to be closed decreases. Thus the fuel centerline temperature follows the Zr cladding temperatyre profile from the very early (Fig. 9a). With increasing gap size the fuel centerline temperature increases and due to the delayed pellet cladding interaction (Fig. 9b fuel centerline temperature for the MMLC follows the fuel centerline temperature of the Zr cladding later.

Figure 9c shows the average hoop stress in the cladding. The hoop stress in the cladding is same for all the cladding in consideration until the cladding-pellet mechanical interaction. After the gap closes, the stresses in the MMLC and Fe cladding increased significantly. With the onset of plastic deformation, the stresses in MMLC layer slows down in the end of the simulation.

The fission gas release also affected by the delayed interaction of the pellet cladding gap for the larger initial gap size. Figure 9d shows the total fission gas release for the MMLC with different initial pellet cladding gap size. For comparison, the total fission gas release for the Zr and Fe cladding is also plotted in the same figure. The fission gas release is much higher in the beginning of the reactor operation for all the cases for MMLC. With decreasing the gap size the total fission gas release decreases and closely matches with single layer Zr cladding for the gap size of 20 μm. This is indicating that for a better fuel rod performance in the LWR a smaller initial gap size would be preferable.

Table 4
Fuel rod specification and input condition for the selected test rod refereed as BN 1 × 3 from the TRIBULATION experimental data

	BN 1 × 3
Number of pellets	1
Fuel enrichment (%)	8.25
Pellet Length (m)	1.0019
Pellet Outer Diameter (mm)	8.2
Radial gap width (μm)	100
Cladding thickness (overall) (mm)	0.460
Rodlet diameter (mm)	8.76
Initial fill pressure (MPa)	2
Plenum height (mm)	88.3
Initial fuel grain radius (μm)	11
Coolant inlet mass flux ($kg/m^2 - s$)	3800
Coolant pressure (MPa)	15.5

The smaller initial gap size reduces the total fission gas release while increasing the stress in the Fe layer. Thus for optimum design of the MMLC, the initial gap size between 40 and 60 μm is recommended.

Figure 9e illustrates the hoop stress through the different layers at 20,000 hr of the irradiation period for different initial gap sizes. The stress is higher in the Fe layer for all the initial gap sizes, where for 80 μm gap thickness this stress become compressive. The interaction of the pellet-cladding also affects stress development in the Fe layer. Earlier contact of the pellet-cladding influences the stress to be higher in the Fe layer. With increasing the initial gap size, the interaction delayed and the stress-induced in the Fe layer also found to be smaller and subsequently changes stress nature from tensile to compressive.

4.5. Performance Comparison of the MMLC with Experimental Data

To better understand the performance of the MMLC, a simulation study was performed with the input parameter from an experimental study. TRIBULATION is an international program organized jointly by BelgoNucleaire and the Nuclear Energy Centre at Mol (CEN/SCK) with the co-sponsorship of 14 participating organizations [50]. One of the objectives of this program is to assess the fuel rod behavior at high burn up with an earlier transient. This experimental research has been chosen to compare the MMLC performance with the experimental results. The input power for this study uses a cyclic loading (Fig. 10a) where the power shut down to zero after a year and again started from zero which varies with time.

TRIBULATION also aims to investigate the performance of different rod design. For this comparison study, we chose a single rod design from the TRIBULATION program data and match the simulation model fuel rod with that design. The specification of the selected test rod referred to as BN 1 × 3 is presented in the table 4. Both creep strain and plasticity with hardening was modeled for the Fe layer while only the creep strain was modeled for the Zr layer. For com-

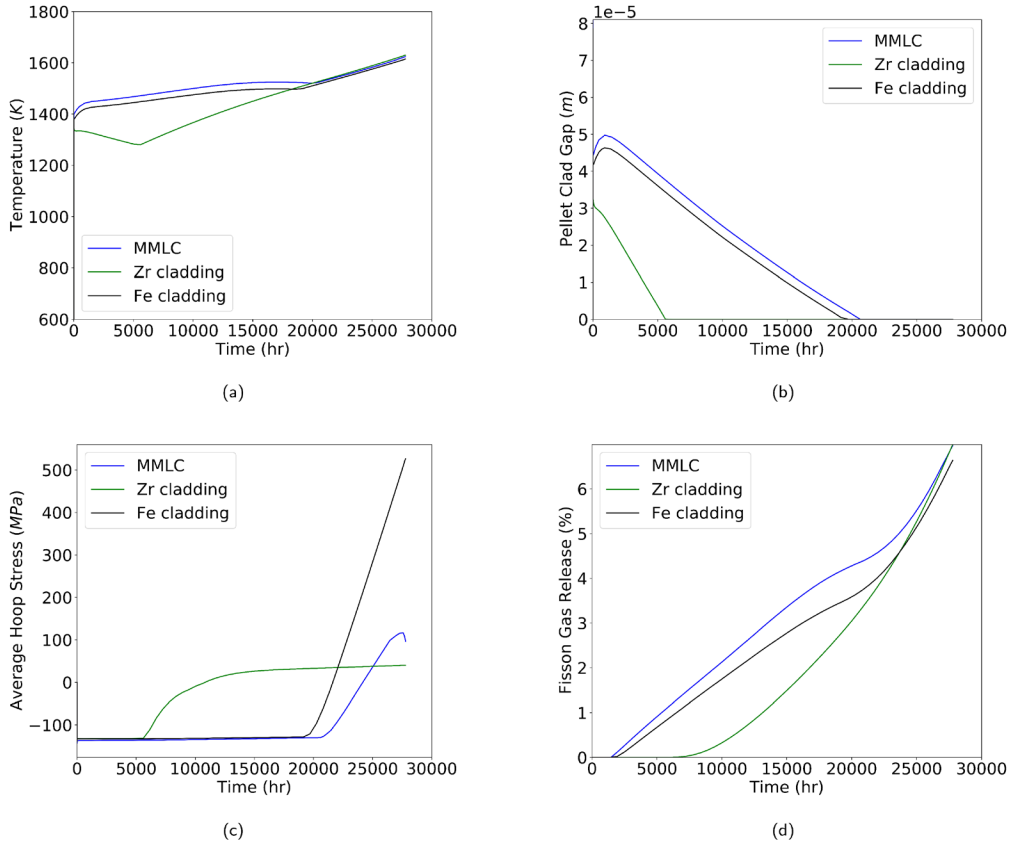

Figure 7: Comparison of the MMLC cladding with single layer Zr and Fe cladding under the LWR normal operating condition for the fuel rod performance evaluation: (a) Fuel centerline temperature, (b) Pellet-cladding mechanical interaction, (c) Average hoop stress (d) Total fission gas release,.

parison, homogeneous Zr and Fe cladding were also simulated with the same input specification.

The results for the total fission gas released available for the TRIBULATION experiment is from the destructive puncture test at the end-of-life. The results from the simulation are compared with this data and are illustrated in the figure 10b. The BISON simulation over predicted the total fission gas released for the single Zr cladding, but the same results using BISON is also confirmed by the researcher [51]. Comparing with the Zr cladding from the simulation with the MMLC results, it is seen that for the MMLC the total fission gas release is much higher.

On the other hand, the creep strain results (Fig. 10c) shows that the creep strain is present in the MMLC cladding, but comparing with the Zr cladding, it is seen to be much lower. These results showed that the MMLC can be used as a potential cladding material for the LWR which effectively lower down the creep strain comparing with the current single-layer Zr cladding when using a cycling loading condition typically operated in a LWR conditions.

5. Conclusion

The objective of this study is to evaluate the performance of the proposed MMLC and recommending optimum design parameters so that it can achive the goal of accident tolerant fuel campaign. The proposed MMLC has Fe-12Cr-2Si as an outer layer which will resist the corrosion better, while the Zr layer minimizes the neutronic cross-section. The accident tolerance could not be judge until the proposed MMLC performed similar or better under the normal operating condition of the LWR. This performance analysis was performed in two approaches, one with an axisymmetric small scale model of the fresh cladding using the steady-state condition

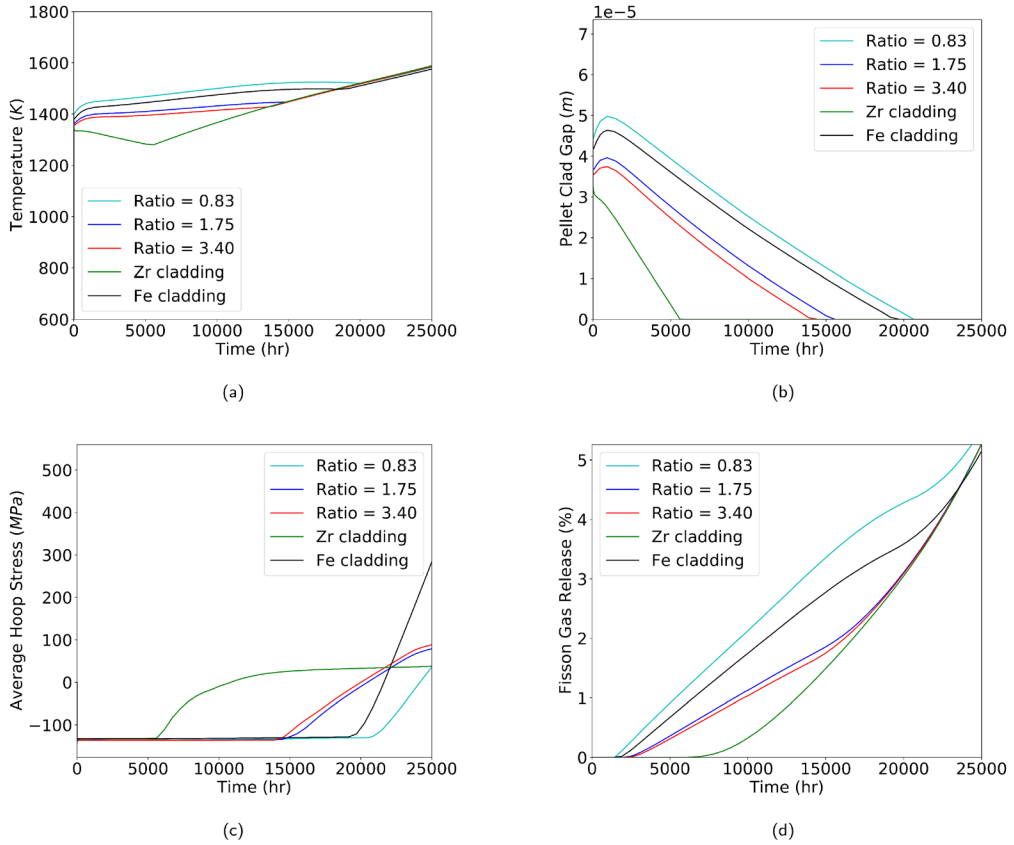

Figure 8: The effect of different thickness ratio of Zr and Fe layer depicting with (a) fuel centerline temperature, (b) pellet cladding gap over the lifespan, (c) average hoop stress and (d) total fisson gas released. For comparison, the results from single layer Zr and Fe cladding also plotted alongside with the MMLC.

and the other one is the full-length fuel rod simulation with transient input power. Both results show acceptable performance in every case with the added benefit of lower creep strain than the current Zr cladding. The fresh cladding simulation results predicted lower residual stresses. The fuel rod simulation compares the performance under the normal operating condition of an LWR and predicts the reactor behavior of the MMLC as a cladding material. The pellet-cladding gap interaction occurs much later in the lifespan of the fuel rod which affects the total fission gas release at the beginning of the fuel rod life. This effect can be minimized by reducing the initial gap size and closing the gap earlier. A gap size between 40 μm and 60 μm is recommended for the optimum design of the MMLC. The ratio of the thickness of the Zr and Fe layer can also be modified but with increasing Zr thickness the Fe layer in the MMLC is susceptible to the plastic deformation at a certain lifetime in the fuel rod. This should be considered for designing the MMLC. At the last, this study showed the performance of the MMLC by modeling and comparing the results using experimental data. The cycling loading of the experimental input power does not change the performance of the MMLC a lot, while it still shows a lower creep strain for the MMLC.

This analysis indicates a potential for using the multi-metallic layered composite cladding for LWR nuclear fuel cladding. Further analysis under the extreme environment of the nuclear reactor and the loss of coolant accident scenarios can measure the extent of this model in such a condition. In short, the MMLC cladding concept shows promising results in LWR performance under normal reactor conditions, which have the inherent opportunity for accident tolerant fuel uses.

References

[1] Jung-Hwan Park, Hyun-Gil Kim, Jeong-yong Park, Yang-Il Jung, Dong-Joon Park, and Yang-Hyun Koo. High temperature steam-oxidation behavior of arc ion plated cr coatings for accident tolerant fuel claddings. *Surface and Coatings Technology*, 280:256–259, 2015.

[2] Hyun-Gil Kim, Il-Hyun Kim, Yang-Il Jung, Dong-Jun Park, Jeong-Yong Park, and Yang-Hyun Koo. Adhesion property and high-temperature oxidation behavior of cr-coated zircaloy-4 cladding tube prepared by 3d laser coating. *Journal of Nuclear Materials*, 465:531–539, 2015.

[3] Youho Lee and Mujid S Kazimi. A structural model for multi-layered ceramic cylinders and its application to silicon carbide cladding of light water reactor fuel. *Journal of Nuclear Materials*, 458:87–105, 2015.

[4] Yukinori Yamamoto, Bruce A Pint, Kurt A Terrani, Kevin G Field, Ying Yang, and Lance Lewis Snead. Development and property evaluation of nuclear grade wrought fecral fuel cladding for light water reactors. *Journal of Nuclear Materials*, 467:703–716, 2015.

[5] Jun Lim, Il Soon Hwang, and Ji Hyun Kim. Design of alumina forming fecral steels for lead or lead–bismuth cooled fast reactors. *Journal of Nuclear Materials*, 441(1-3):650–660, 2013.

[6] CP Deck, GM Jacobsen, J Sheeder, O Gutierrez, J Zhang, J Stone, HE Khalifa, and CA Back. Characterization of sic–sic composites for accident tolerant fuel cladding. *Journal of Nuclear Materials*, 466:667–681, 2015.

[7] Bo Cheng, Young-Jin Kim, and Peter Chou. Improving accident tolerance of nuclear fuel with coated mo-alloy cladding. *Nuclear Engineering and Technology*, 48(1):16–25, 2016.

[8] MP Short, S Morton, SE Ferry, and RG Ballinger. Diffusional stability of ferritic–martensitic steel composite for service in advanced lead–bismuth cooled nuclear reactors. *International Heat Treatment and Surface Engineering*, 4(2):74–80, 2010.

[9] Michael Philip Short and Ronald George Ballinger. A functionally graded composite for service in high-temperature lead-and lead-bismuth–cooled nuclear reactors-i: Design. *Nuclear Technology*, 177(3):366–381, 2012.

[10] MP Short, RG Ballinger, and HE Hänninen. Corrosion resistance of alloys f91 and fe–12cr–2si in lead–bismuth eutectic up to 715 c. *Journal of Nuclear Materials*, 434(1-3):259–281, 2013.

[11] Xunxiang Hu, Kurt A Terrani, Brian D Wirth, and Lance L Snead. Hydrogen permeation in fecral alloys for lwr cladding application. *Journal of Nuclear Materials*, 461:282–291, 2015.

[12] Philippe Moinard and Yvon Millet. Process for the production of a tubular zircaloy 2 blank internally clad with zirconium and suitable for ultrasound monitoring of the zirconium thickness, March 11 1997. US Patent 5,609,697.

[13] George Y Lai. *High-temperature corrosion and materials applications*. ASM international, 2007.

[14] LR Bunnell, JL Bates, and GB Mellinger. Some high-temperature properties of zircaloy-oxygen alloys. *Journal of Nuclear Materials*, 116(2-3):219–232, 1983.

[15] AZO Material. Zircaloy-4(alloy zr4) (uns r60804). https://www.azom.com/article.aspx?ArticleID=7644, 2013.

[16] AZO Material. Titanium (ti) - the different properties and applications. https://www.azom.com/article.aspx?ArticleID=9118, 2013.

[17] AZO Material. Stainless steel - grade 405 (uns s40500). https://www.azom.com/article.aspx?ArticleID=6810, 2012.

[18] HM Chung, BA Loomis, and DL Smith. Properties of vîŮÿ 4crîŮÿ 4ti for application as fusion reactor structural components. *Fusion engineering and design*, 29:455–464, 1995.

[19] JM Chen, T Nagasaka, T Muroga, SY Qiu, C Li, and N Nita. Mechanical properties of v–4cr–4ti strengthened by precipitation and cold rolling. *Journal of Nuclear Materials*, 374(1-2):298–303, 2008.

[20] Kwadwo Kese. Hydride re-orientation in zircaloy and its effect on the tensile properties. Technical report, Swedish Nuclear Power Inspectorate, 1998.

[21] Jeonghyeon Lee, Taeyong Kim, Il Soon Hwang, Ronald G Ballinger, and Ji Hyun Kim. Development of pilgering process of hybrid-layer cladding for advanced small modular fast reactor application.

[22] Ian Younker and Massimiliano Fratoni. Neutronic evaluation of coating and cladding materials for accident tolerant fuels. *Progress in Nuclear Energy*, 88:10–18, 2016.

[23] Cesar Roberto de Farias Azevedo. Selection of fuel cladding material for nuclear fission reactors. *Engineering Failure Analysis*, 18(8):1943–1962, 2011.

[24] Zhengang Duan, Huilong Yang, Yuhki Satoh, Kenta Murakami, Sho Kano, Zishou Zhao, Jingjie Shen, and Hiroaki Abe. Current status of materials development of nuclear fuel cladding tubes for light water reactors. *Nuclear Engineering and Design*, 316:131–150, 2017.

[25] Varley F Sears. Neutron scattering lengths and cross sections. *Neutron news*, 3(3):26–37, 1992.

[26] Richard L Williamson, JD Hales, SR Novascone, MR Tonks, DR Gaston, CJ Permann, D Andrs, and RC Martineau. Multidimensional multiphysics simulation of nuclear fuel behavior. *Journal of Nuclear Materials*, 423(1-3):149–163, 2012.

[27] Christophe Geuzaine and Jean-François Remacle. Gmsh: A 3-d finite element mesh generator with built-in pre-and post-processing facilities. *International journal for numerical methods in engineering*, 79(11):1309–1331, 2009.

[28] Xu Wu, Tomasz Kozlowski, and Jason D Hales. Neutronics and fuel performance evaluation of accident tolerant fecral cladding under normal operation conditions. *Annals of Nuclear Energy*, 85:763–775, 2015.

[29] A. Soba, A. Denis, L. Romero, E. Villarino, and F. Sardella. A high burnup model developed for the DIONISIO code. *Journal of Nuclear Materials*, 433:160–166, 2013.

[30] A. Soba, M. Lemes, M.E. González, A. Denis, and L. Romero. Simulation of the behaviour of nuclear fuel under high burnup conditions. *Annals of Nuclear Energy*, 70:147–156, 2014.

[31] Martin W Heinstein and Tod A Laursen. An algorithm for the matrix-free solution of quasistatic frictional contact problems. *International journal for numerical methods in engineering*, 44(9):1205–1226, 1999.

[32] AM Ross and RL Stoute. *Heat Transfer Coefficient Between UO2 and Zircaloy-2: CRFD-1075*. AECL, 1962.

[33] A. Marion (NEI) letter dated June 13, 2006 to H. N. Berkow (USNRC/NRR). Safety Evaluation by the Office of Nuclear Reactor Regulation of Electric Power Research Institute (EPRI) Topical Report TR-1002865, "Topical Report on Reactivity Initiated Accidents: Bases for RIA Fuel rod Failures and Core Coolability Criteria". http://pbadupws.nrc.gov/docs/ML0616/ML061650107.pdf, 2006.

[34] W. F. Lyon. Summary report: Gd thermal conductivity model updates. Technical Report ANA-P1400138-TN03 Rev. 2, Anatech Corp., 2015.

[35] Y Rashid, R Dunham, and R Montgomery. Fuel Analysis and Licensing Code: FALCON MOD01. Technical report, Electric Power Research Institute, December 2004.

[36] C. M. Allison, G. A. Berna, R. Chambers, E. W. Coryell, K. L. Davis, D. L. Hagrman, D. T. Hagrman, N. L. Hampton, J. K. Hohorst, R. E. Mason, M. L. McComas, K. A. McNeil, R. L. Miller, C. S. Olsen, G. A. Reymann, and L. J. Siefken. SCDAP/RELAP5/MOD3.1 code manual, volume IV: MATPRO–A library of materials properties for light-water-reactor accident analysis. Technical Report NUREG/CR-6150, EGG-2720, Idaho National Engineering Laboratory, 1993.

[37] G. Pastore, L. Luzzi, V. Di Marcello, and P. Van Uffelen. Physics-based modelling of fission gas swelling and release in UO_2 applied to integral fuel rod analysis. *Nuclear Engineering and Design*, 256:75–86, 2013.

[38] G. Pastore, D. Pizzocri, S. R. Novascone, D. M. Perez, B. W. Spencer, R.L. Williamson, P. Van Uffelen, and L. Luzzi. Modelling of transient fission gas behaviour in oxide fuel and application to the BISON code. In *Enlarged Halden Programme Group Meeting, Røros, Norway, September 7–12*, 2014.

[39] Eds. M. A. Kramman, H. R. Freeburn. Escore–the epri steady-state core reload evaluator code: General description. Technical Report

EPRI NP-5100, Electric Power Research Institute, February 1987.

[40] L. P. Swiler, R. L. Williamson, and D. M. Perez. Calibration of a fuel relocation model in BISON. In *Proceedings of the International Conference on Mathematics and Computational Methods Applied to Nuclear Science and Engineering*, Sun Valley, Idaho, May 5-9, 2013.

[41] JD Hales, RL Williamson, SR Novascone, G Pastore, BW Spencer, DS Stafford, KA Gamble, DM Perez, and W Liu. Bison theory manual the equations behind nuclear fuel analysis. Technical report, Idaho National Lab.(INL), Idaho Falls, ID (United States), 2016.

[42] LJ Siefken, EW Coryell, EA Harvego, and JK Hohorst. SCDAP/RELAP5/MOD3.3 Code Manual: MATPRO–A Library of Materials Properties for Light-Water-Reactor Accident Analysis. Technical Report NUREG/CR-6150, Vol.4, Rev.2, U.S. Nuclear Regulatory Commission, 2001.

[43] DG Franklin. Zircaloy-4 cladding deformation during power reactor irradiation. In *Zirconium in the Nuclear Industry*. ASTM International, 1982.

[44] N. E. Hoppe. Engineering model for zircaloy creep and growth. In *Proceedings of the ANS-ENS International Topical Meeting on LWR Fuel Performance*, pages 157–172, Avignon, France, April 21-24, 1991.

[45] Y. Matsuo. Thermal creep of zircaloy-4 cladding under internal pressure. *Journal of Nuclear Science and Technology*, 24(2):111–119, February 1987.

[46] FA Garner and DL Porter. Irradiation creep and swelling of aisi 316 to exposures of 130 dpa at 385–400 c. *Journal of Nuclear Materials*, 155:1006–1013, 1988.

[47] Holm Altenbach and Yevgen Gorash. High-temperature inelastic behavior of the austenitic steel aisi type 316. In *Advanced Materials Modelling for Structures*, pages 17–30. Springer, 2013.

[48] Kyle A Gamble, Tommaso Barani, David Pizzocri, Jason D Hales, Kurt A Terrani, and Giovanni Pastore. An investigation of fecral cladding behavior under normal operating and loss of coolant conditions. *Journal of Nuclear Materials*, 491:55–66, 2017.

[49] Ryan Sweet, Nathan George, Kurt Terrani, and Brian Wirth. Bison fuel performance analysis of fecral cladding with updated properties. *Oak Ridge National Lab.(ORNL), Oak Ridge, TN (United States), p. Medium: ED*, 2016.

[50] OECD Nuclear Energy Data Bank. Technical report, IFPE/Tribulation Database, May 2002.

[51] Danielle M Perez, RL Williamson, SR Novascone, G Pastore, J Hales, and BW Spencer. Assessment of bison: A nuclear fuel performance analysis code. *Idaho National Laboratory, Idaho Falls*, 2013.

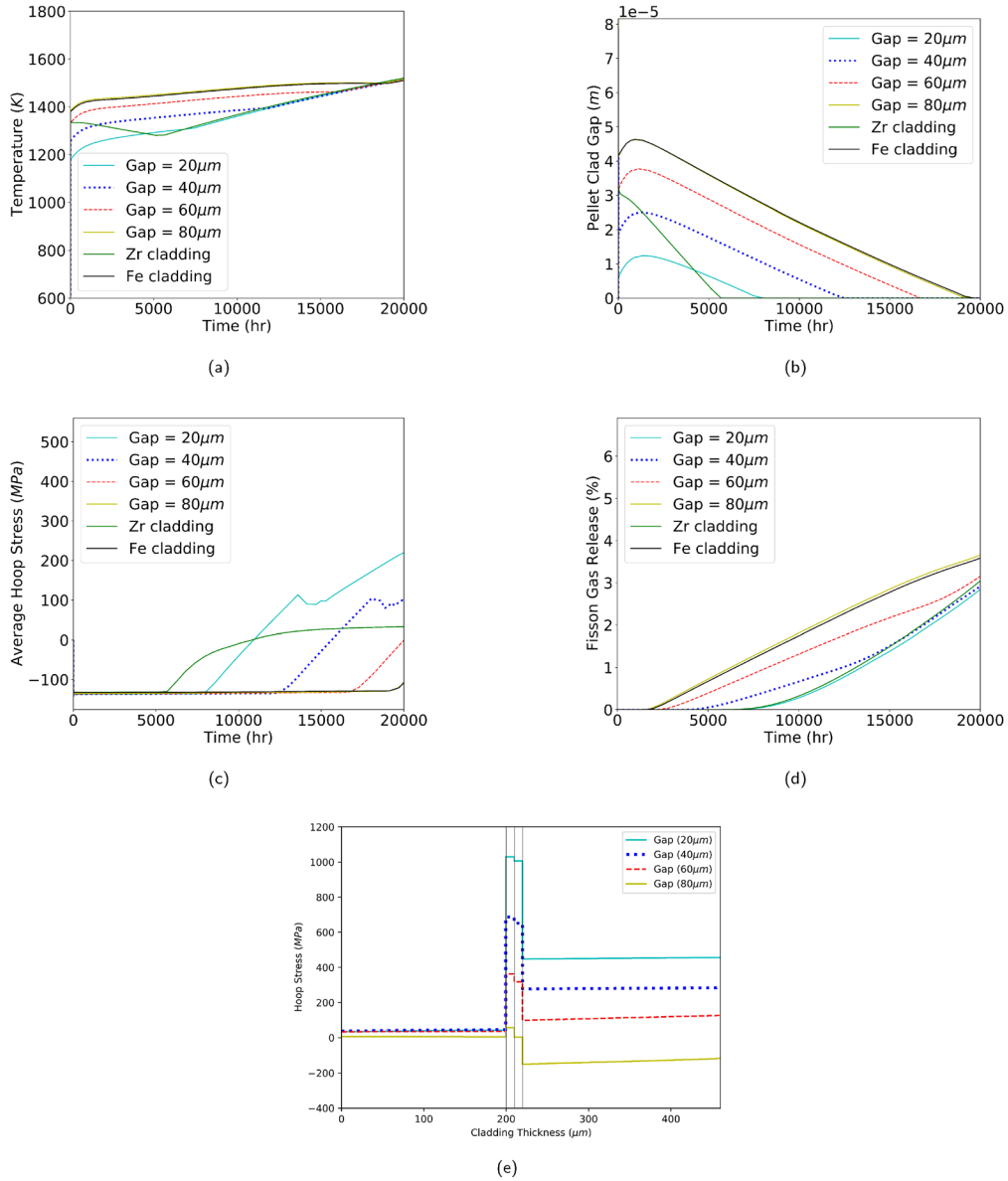

Figure 9: The effect of different initial pellet cladding gap size depicting with (a) fuel centerline temperature, (b) Pellet cladding gap over the lifespan, (c) average hoop stress, and (d) total fission gas released. For comparison, the results from single layer Zr and Fe cladding also plotted alongside with the MMLC. (e) Hoop stresses through different layers of MMLC at 20000 hr.

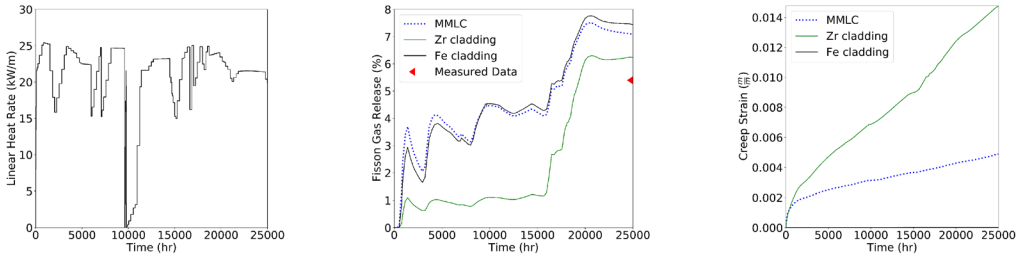

Figure 10: Comparison of the performance of MMLC using experimental data: (a) The maximum linear heat generation rate from the TRIBULATION experimental data, (B) The total fission gas release where the measured data is available at the end of the life of the fuel rod. (b) Comparison of the creep strain for the MMLC and the single layer Zr and Fe cladding.

Chapter 5 – Joining Methods for the MMLC

While the industrial-scale billet creation is not yet finished, a thorough review of available multilayer metallic joining methods was undertaken by the VTT Technical Research Centre in Finland. The following technical report summarizes the findings of this study, which settled upon friction stir welding and rotary friction stir welding as the most promising methods of joining of MMLCs. Because funding on the Finnish side was not secured and tubular MMLC samples were not available, work from this task is still ongoing. Once the four-layer MMLC billet is extruded, specimens will be sent to VTT for rotary friction stir weld tests and characterization.

RESEARCH REPORT

VTT-R-04064-16

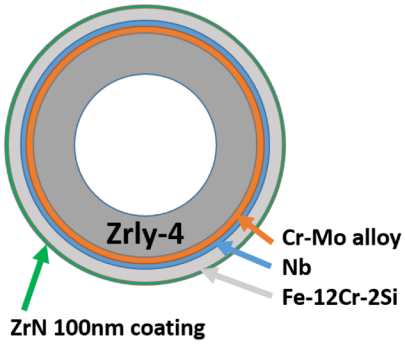

Literature study on welding of zirconium based fuel cladding materials

Authors: Ulla Ehrnstén[1], Hannu Hänninen[2], Pekka Nevasmaa[1], Rami Pohja[1] and Teemu Sarikka[2]

[1]VTT, [2]Aalto University

Confidentiality: Restricted to the Academy of Finland MENUCHAR and MIT-NEUP project consortiums

Report's title	
Literature study on welding of zirconium based fuel cladding materials	
Customer, contact person, address	**Order reference**
Professor Michael Short Massachussents Institute of Technology Department of Nuclear Science and Engineering	No. 277364, Letter of commitment, February 2015
Project name	**Project number/Short name**
MIT-NEUP / Academy of Finland MENUCHAR	101315
Author(s)	**Pages**
Ulla Ehrnstén[1], Hannu Hänninen[2], Pekka Nevasmaa[1], Rami Pohja[1] and Teemu Sarikka[2] [1]VTT, [2]Aalto University	19/-
Keywords	**Report identification code**
Welding, MMLC, zirconium, fuel cladding	VTT-R-04064-16

Summary

This report explores welding of new materials for nuclear fuel cladding, which can reduce the consequences of possible accidents in current light water reactors (LWRs). This study is part of the large international MIT-NEUP program which involves contributors from MIT, Ohio State, Penn State as well as VTT and Aalto University from Finland. MIT-NEUP project aims to develop a multi-metallic layered composite (MMLC) as a new accident-tolerant fuel cladding concept. This differs from other current investigations as it utilizes multiple layers for specific purposes, prevents interlayer interactions and compromises between the neutronic performance of Zircaloy and the accident tolerance of steel.

Gas tungsten arc welding, laser beam welding, electron beam welding, diffusion bonding and friction stir welding methods were reviewed. All methods are used for welding zirconium alloys. However, very little open literature data is available on welding zirconium based multi-layer materials, which shows that the topic is novel and require development of optimal joining parameters.

Confidentiality	Restricted

Espoo 17.10.2016

Written by	Reviewed by	Accepted by
Ehrnstén Ulla Principal Scientist	Penttilä Sami Research Scientist	Helynen Satu Vice President, Nuclear Safety

VTT's contact address

Kivimiehentie 3, PO Box 1000, FI-02044VTT

Distribution (customer and VTT)

Academy of Finland, Professor Michael Short MIT, VTT archive and electronic database for reports in nuclear

The use of the name of VTT Technical Research Centre of Finland Ltd in advertising or publishing of a part of this report is only permissible with written authorisation from VTT Technical Research Centre of Finland Ltd.

Preface

This report explores welding of new materials for nuclear fuel cladding, which can reduce the consequences of possible accidents in current light water reactors (LWRs). This study is part of the Academy of Finland MENUCHAR project in Finland and the large international MIT-NEUP program which involves contributors from MIT, Ohio State, Penn State as well as VTT and Aalto University from Finland. MIT-NEUP project aims to develop a multi-metallic layered composite (MMLC) as a new accident-tolerant fuel cladding concept. This differs from other current investigations as it utilizes multiple layers for specific purposes, prevents interlayer interactions and compromises between the neutronic performance of Zircaloy and the accident tolerance of steel.

The MENUCHAR funding is highly appreciated.

Espoo 17.10.2016

Authors

Contents

Preface....2
Contents....3
1. Introduction....4
2. Welding of zirconium based fuel cladding....6
3. Welding methods for composites....9
3.1 Gas Tungsten Arc Welding....9
3.2 Laser Beam Welding....10
3.3 Electron beam welding....13
3.4 Diffusion bonding....15
3.5 Friction stir welding....16
References....17

1. Introduction

Fukushima accident has increased the interest in advanced materials for accident-tolerant fuel claddings that could withstand accident scenario environments, such as very high temperature exposure in steam, for several hours, and studies for alternative cladding materials have been proposed and are ongoing.

This report explores welding of new materials for nuclear fuel cladding, which can reduce the consequences of possible accidents in current light water reactors (LWRs). This study is part of the large international MIT-NEUP program which involves contributors from MIT, Ohio State, Penn State as well as VTT and Aalto University from Finland. MIT-NEUP project aims to develop a multi-metallic layered composite (MMLC) as a new accident-tolerant fuel cladding concept, Figure 1. This differs from other current investigations as it utilizes multiple layers for specific purposes, prevents interlayer interactions and compromises between the neutronic performance of Zircaloy and the accident tolerance of steel. Academy of Finland project MENUCHAR is supporting activities to resolve fundamental questions related to ATF (Accident Tolerant Fuel) materials testing in accident conditions. The preliminary objective of the project was achieved in 2016 by setting up a steam furnace system capable of working up to 1600°C to study the breakaway oxidation of potential accident-tolerant material solutions. The planned work in MENUCHAR project will be performed in an active collaboration with high level research groups in the US and Finland.

The objectives of this joint program are:

- Optimize and fabricate the MMLC on an industrial scale;
- Characterize and improve fabrication and joining techniques, including end plugs and MMLC fuel cladding;
- Simulate accident performance and radiation resistance of the MMLC using multiscale materials modelling techniques;
- Validate the multiscale models with laboratory-scale severe accident testing and corrosion and electrochemical tests.

This project will result in a new accident-tolerant cladding concept, which is ready for test reactor irradiation studies.

A schematic of the prosed MMLC, based on the latest layer selection, is seen in Figure 1. Fe-12Cr-2Si is selected as the outer layer instead of AISI 316 SS or T91 as its accident tolerance believed to be similar to FeCrAl, but its weldability is better. The layers are Zircaloy-4 (Zrly-4, about 350-450 microns), then Nb (10 microns), then Cr-Mo (10 microns), then Fe-12Cr-2Si (100-200 microns), and finally eventually a ZrN layer. The thickness of the Fe-12Cr-2Si layer is wanted to be minimized, and that will depend on the 1200°C steam oxidation tests. If it can be made even thinner than 100 microns, it is preferable. All layers will be first weld-overlaid and co-extruded. They will be about 0.3-0.6 cm thick in the weld overlay, and after extrusion they are expected to be about 10 microns thick.

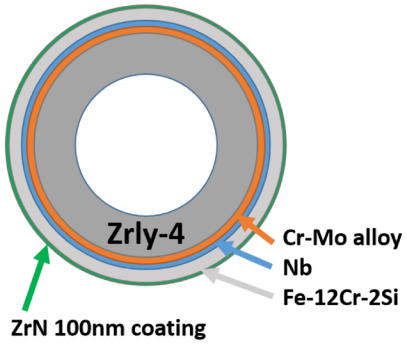

Figure 1. Schematic of the prosed MMLC fuel cladding, based on the latest layer selection. Fe-12Cr-2Si is selected as the outer layer instead of AISI 316 SS or T91 as its accident tolerance believed to be similar to FeCrAl, but its weldability is better.

The end plugs will be about 1-2 cm tall, plus any section that must fit inside the cladding for a good bond. Figure 2 gives an idea about its shape. Welding techniques with a minimal heat-affected zone will be important in welding end plugs for the MMLC concept, in general. It is also important that the Zircaloy-4 layers on the MMLC and end plug will be welded together, to avoid fission gas pressure and any narrow crevices acting as internal stress concentrators. The welding methods which may be suitable are laser beam welding (LBW), electron beam welding (EBW), friction stir welding (FSW), gas tungsten arc welding (GTAW) and resistance welding. The last one may be problematic, as partially joined regions will drop in resistance significantly during welding. It is important to note also, that the end plugs will be the coolest parts of the rod before/during any accident.

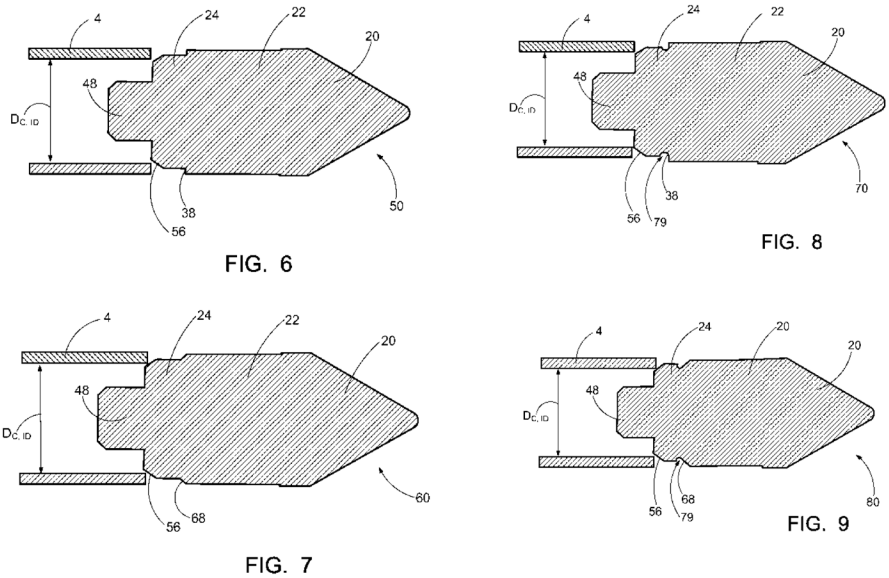

Figure 2. Examples of the cross-section of end plug with fuel rod cladding suitable for resistance welding [1].

Welding of zirconium alloys is briefly reviewed in Chapter 2. The relevant welding techniques for the composites in question in this project, partly similar to those used for Zr-alloy welding, are explained in more detail in the chapters dealing with welding of composites. The possible joining methods for end plugs and tube are reviewed in Chapter 3.

2. Welding of zirconium based fuel cladding

Zirconium alloys are used in a wide variety of industrial and chemical processing applications in addition to the considerable use in the nuclear power industry. They are particularly resistant to corrosive attack in a range of environments and have good mechanical properties at elevated temperatures.

In light water reactors, the nuclear fuel, consisting of ceramic pellets of uranium oxide, is inserted into thin-walled zirconium alloy tubes, which are called the fuel cladding. Typical PWR fuel rod with a hollow top end plug is presented in Figure 3 [2]. Usually the tube and end plugs are made from zirconium-based alloys, such as Zircaloy-4. The dimensions of a fuel cladding tube are about 0.6-0.7 mm wall thickness and 10 mm diameter. First, the bottom plug is welded to the tube, and then the pellets are inserted into the tube, which is then pressurized with helium. Both BWR and PWR fuel rods are pressurized with helium, to counterbalance the system pressure and limiting creep. The pressure in BWR fuel rods are typically 5 - 10 bars and 30 - 70 bars for PWR fuel rods [3]. After insertion of a hold-down spring, the upper end plug is welded, sealing the tube. Numerous of these tubes are then inserted into grid support pieces that firmly hold the tubes in their precise lattice. The complete set of these numerous tubes forms a fuel assembly (also called a fuel bundle). The shape of the assembly and the configuration of the assemblies in the core are different in different reactor types to optimize the reactor physics.

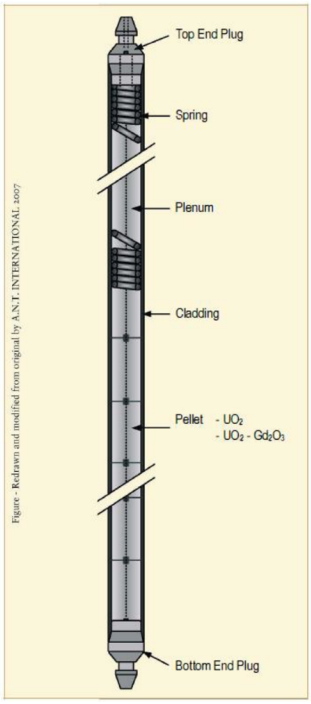

Figure 3. Typical PWR fuel rod with a hollow top end plug [2].

The first fuel claddings were made from stainless steel, but suffered from stress corrosion cracking and were abandoned [3,4]. Since the early 60´s fuel claddings have been manufactured from zirconium alloys, due to their low neutron absorption cross-section, being 0.185 barns compared to that of iron, for which it is 14 times higher, i.e. 2.55 barns [5]. Other selection criteria are tolerance for neutron flux and fluence effects, mechanical properties, corrosion properties, melting temperature, thermal conductivity, manufacturability, gas retention and availability [6].

Zirconium alloys are alloyed with small amounts on other elements for improved properties. The different zirconium-based alloys used in BWR, PWRs and VVERs are presented in Table 1 [1,3,2,6,8]. Constant development of zirconium-based fuel claddings is ongoing, with development of, e.g., the metal manufacturing process from ore to metal, optimization of alloying and manufacturing methods, introduction on a liner, improved understanding of degradation issues etc., all to enable both good performance and a high burnup.

Table 1 Zirconium alloys used for fuel claddings and their use in BWR, PWR and VVER reactors [1,3,2,6,7,8]

Name	**Alloy**	**Plant type**
Zircaloy-2	Zr 1.5 Sn 0.15 Fe 0.10 Cr 0.05 Ni	BWR
Zircaloy-4	Zr 1.5 Sn 0.20 Fe 0.10 Cr	PWR
M5	Zr 1.0 Nb	PWR
Zirlo	Zr 1 Sn 1 Nb 0.1 Fe	PWR, VVER
Optimized Zirlo	Zr 0.7 Sn 1 Nb 0.1 Fe	PWR
E110, E110K	Zr 1 Sn 1 Nb	VVER

The fuel rod end plugs can be welded using GTAW, resistance welding (upset shape welding, pressure resistance welding or butt resistance welding), EBW or LBW. As zirconium is very reactive with oxygen, welding must be performed in high vacuum or at least shielding gas. Welding is therefore usually performed in a welding chamber [2]. Zirconium has also a very high solubility, not only with oxygen, but also with hydrogen, nitrogen and carbon at high temperatures, which may result in embrittlement of the whole weld. The inert environment must cover not only the weld, but also the heat-affected zone (HAZ) to avoid detrimental effects from impurities. If welding is done using shielding gas only, passive gases shall be used, i.e., argon or helium. Of these, helium is favored in the nuclear industry. The benefits of helium gas are higher heat content and good weld penetration properties [9].

The crystal structure of the zirconium alloys in question is hexagonal close packed, which means that the mechanical properties are different in different orientations, i.e., they are anisotropic. The yield strength is higher in the direction opposite to the rolling direction, while the tensile strength is slightly higher in the rolling direction [10]. Zirconium has several characteristics which makes welding easier compered to many other alloys. It has a low thermal expansion coefficient and a low elastic modulus, which results in small welding distortion and residual stresses. Zirconium does not suffer from remarkable hot- or cold cracking problems, as long as the cleanliness is secured. Further, precipitations are not easily formed during welding, as the zirconium oxides are soluble in the metal [11]. Also the weld pool and solidification behaviors are similar to most other metals, and good welding results can be achieved with normal welding techniques. However, welding the end plugs is far from trivial, and fuel manufacturers have developed their own procedures, where the skill is in the details of the welding. All details are therefore not found in the open literature.

One of the criteria for a successful welding result is extreme cleanliness, i.e., absolute purity of the shielding gas or the inert environment, the cleanliness of the surfaces to be welded and or the welding wire, if such is used. The purity of the argon shielding gas, e.g., shall be 99.996% [9]. Zirconium alloys containing niobium are prone to nitrogen absorption with consequent reduced corrosion resistance of the weld. The recommended vacuum is 10^{-4} torr or filling the welding chamber with a passive gas. As a cleaning process before welding, the

following steps are recommended (i) pre-cleaning with a suitable solvent, e.g., acetone, methanol or butanone (methyl ethyl ketone, MEK), followed by rinsing in alcohol, (ii) pickling in nitric acid-fluoric acid solution (35% HNO_3 – 5% HF) and finally (iii) rinsing in water and drying with hot air. If the surfaces are only slightly oxidized, as indicated by a blue color, the surfaces can be brushed using a clean brush made from austenitic stainless steel followed by acid treatment. If the surfaces are heavily oxidized, as indicated by a grey color, the surfaces can be ground. Cleaned surfaces shall not be handled by bare hands. Welding shall be performed as soon as possible after cleaning, or be shielded by paper or plastic [9,12]. Preheating is not usually utilized for welding zirconium alloys. The welds must be shielded from air contact until they have cooled below 480 °C [9]. The shielding should cover all surfaces where the temperature can raise to 200 – 300 °C [12].

The strength of the weld is usually slightly higher and the ductility slightly lower compared to the fine-grained base material. This is due to the change in crystal structure from α to β during welding. Welding causes also coarsening of the microstructure in the HAZ, which has a slightly detrimental effect on the mechanical properties. Further, segregation of impurities to the grain boundaries occurs in the HAZ close to the α - β-phase transition temperature, resulting in slightly decreased corrosion properties and ductility [10]. During cooling, the β - α-phase transition results in a Widmannstätten-type microstructure of α-phase. The faster the cooling is, the finer the structure becomes. Thus, a low heat input and fast cooling rate are beneficial parameters [10]. This is especially important when welding thin-walled structures such as cladding tubes. Therefore, e.g. plasma arc welding and metal arc welding are not suitable methods. The welds are usually post-weld heat treated in inert environment. If stress relief heat treatment is necessary, this should be performed at 540 – 595 °C for 0.5 – 1 h [9,12,13]. According to available public information GTAW-welding is today used mainly by older MOX-fuel production plants.

EBW is used for welding of fuel cladding end plugs, e.g., by Westinghouse Electric Sweden (WSE). A large advantage of EB-welding is a small total heat input, a high welding speed and the purity of the welding zone. A disadvantage is the high plugital investment cost of the equipment. WSE use EBW and high vacuum, 10^{-5} mbar to protect against oxidation [14]. Characteristic for EBW is high effect- and energy-density of the arc, a high temperature and a small size of the weld pool. Beam welds solidify and cool rapidly, and consequently the heat input per length unit remains small. The EB weld is a result of a high-energy beam which is focused with high precision to an area of 0.2 mm. Tin will partly evaporate during EBW resulting in degradation of the corrosion properties compared to the base metal.

LBW can also be used for end plug welding. Mainly CO, Nd YAG lasers are used and the welding is performed in normal pressure using an Ar, He or a mixture of these as a shielding gas. Due to the small heat pulse, the microstructural changes in the HAZ are small [2,3]. Welding of tin-containing alloys cause, similar to EBW, vaporization of tin with consequent reduction of the corrosion properties [11]. Although no detailed information on the use of laser welding for fuel end plug welding was found in the open literature, Westinghouse Sweden has released a patent application for pulse laser welding on the end plugs, indicating that this method is at least an interesting alternative for the end plug welding [1].

Resistance welding refers to a group of welding processes (pressure resistance welding, resistance butt welding, upset welding etc.) using electrical resistance to produce the coalescence of the two surfaces. The materials to be joined do not macroscopically melt in resistance welding, but the joining is a result of the increased temperature and the mechanical pressing of the two surfaces together, which results in local melting. The benefit of resistance welding is that a fine-grained structure is formed at the site of the joining, a small width of the HAZ and no need for weld wires. The drawbacks are that the excessive material formed must be removed by machining and that the quality of the resistance welds is hard to assess using NDT techniques [2]. The quality of resistance welds are therefore rather checked by a measurement of the dimensional profile and control and on-line check of

the welding parameters [15].Upset shape welding is an optimized resistance butt welding method developed in which the fuel rod and the plug are forged together at elevated temperature. The welding zone exhibits higher strength than the base materials [2].

Resistance welding is used in Russia, Ukraine, South Korea, India and for CANDU fuel rods. Also Areva Siemens uses resistance welding, and the technique was also adopted in France as a mitigation measure to avoid failures of M5 fuel due to seal weld contamination in GTAWand laser welds. The improved procedure has been used in the US (Areva US uses resistance butt welding) since 2004 and in French plants since 2007 to produce about 6500 fuel assemblies [6,16,17,18].

3. Welding methods for composites

3.1 Gas Tungsten Arc Welding

In applications requiring high quality welds in thin sheet metals, tungsten inert gas (TIG) welding is the most suitable arc welding method available. GTAW welding, also known as gas tungsten arc welding (GTAW) is a fusion welding process in which an arc is created between a non-consumable tungsten electrode and a workpiece. The welding process is isolated from the environment using an inert gas shield, usually argon, helium or a mixture of the two. The purpose of the gas shield is to protect the weld from chemical reactions with the atmosphere and to prevent the tungsten electrode from degradation. GTAW welding can be performed either by using filler metal or, as is often the case with thin sheets, without a separate filler metal and with different current modes, including direct current (DC), with the electrode negative (EN) or positive (EP), alternating current (AC), or pulse current.

GTAW welding provides good control of heat input, weld penetration, and weld pool as well as the ability to produce metallurgically high quality welds. GTAW welding can be applied to thin workpieces and the lower the thickness of the workpiece the more suitable the pulse current option becomes. Pulse current provides lower heat input resulting in reduction in distortion, thus, allowing the welding of even thinner workpieces.

GTAW welding is one of the welding techniques that have been used in welding of zirconium alloy components, such as nuclear fuel rods and end plugs. GTAW welding of zirconium alloys is usually carried out in a welding chamber that can be evacuated and then backfilled with inert gas. However, nowadays GTAW welding for fuel rod closure is used to a large extent only in the older MOX-fuel production plants [2,19]. The main defect in GTAW welded zirconium alloy welds is fine porosity [2].

Chauve et al. [19] have studied GTAW welded zirconium alloy joints and characterized a single pass zirconium GTAW weld to contain two main zones shown in Figure 4. The fusion zone (melted zone) consisted of rather coarse prior β-phase grains. The HAZ could be divided into two areas; an area having reached the β-phase region during the welding with the prior average β grain and an area having reached the α+β-phase region during the welding which has an intermediate structure. The interfaces of these zones were not always well defined. For multi-pass welds, the basic phenomena remained the same, but the configuration became more complex. Each layer reached the β-phase region during the deposition of the following layer. The overlapping of several passes increased the dimensions of the prior β phase grains, which could grow up to a size of several millimeters, which leads to a loss of ductility.

GTAW welded zirconium alloy joints have also been studied by Ahmad et al. [20] who studied a GTAW joint between Zircaloy-4 and 304L stainless steel. They observed rod-shaped intermetallic $Zr(Cr, Fe)_2$ and eutectic Zr_2Fe–Zr_2Ni phases in the fusion zone of the welded joints.

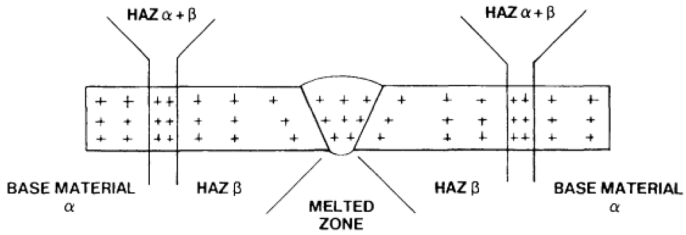

Figure 4. Structural zones around a single pass weld [19].

In the case of the outer layers of a composite structure, Cr-Mo alloys are in general weldable by GTA welding. However, if the Cr-Mo alloys are quenched and tempered alloys with ferritic/martensitic microstructure, the welding may cause significant microstructural changes in the different weld zones resulting in significant degradation of mechanical properties of the welded component.

Concerning the welding of Si-containing stainless steel (Fe-12Cr-2Si), the addition of high amount of Si can make the alloy difficult to weld due to Si forming a number of iron silicides (FeSi, Fe_2Si, Fe_3Si, Fe_5Si_3) and intermetallics (Cr_3Si), which all have a tendency to embrittle the weld. As a steel alloying element, Si expands the sigma phase formation composition range and improves the fluidity of molten steel. Si is known to segregate to the weld center line during solidification resulting in the formation of low melting eutectic constituents, especially in combination with Ni [21].

3.2 Laser Beam Welding

The Light Amplification by Stimulated Emission of Radiation (LASER) produces a monochromatic (one wavelength) and coherent (in phase) beam of light with the aid of particular laser active media (gases, liquids, solids). The medium is excited to a higher energy state such that an incident quantum of light will cause emission. Mirrors are then used both to arrange and amplify the stimulated emission into a collimated beam. The LB welding is a method utilizing highly amplified and focused laser light beam having the power density up to 10^{10} W/m^2. The laser beam is capable of vaporizing metals and of maintaining a deep, small diameter keyhole type weld pool. LBW can be carried out by using continuous beam or by exposing a pulsed laser beam to the joint [2,22].

To achieve fully penetrated high quality LB weld it is necessary to set optimal combination of processing parameters. They involve three different groups: (i) LB properties (wavelength, power, diameter, divergence), (ii) material properties (density, thermal conductivity, specific heat, latent heat of melting and vaporization, thickness, joint configuration) and (iii) important interaction parameters (welding speed, focusing element length, focus plane position towards the material surface, shielding gas direction and flow, absorptivity of material surface). At room temperature almost all metals have absorptivity of about 10 - 20 %, which increases during material heating to 80 - 90%, when metal melting point is reached [2,22].

The possible fuel rod end structure is schematically illustrated in Figure 5. Using the LBW method the end plug and the cladding tube can be joined together by full penetration weld between the tube and the end collar of the end plug and with butt-weld between the end of the tube and the second collar of the end plug. Fuel rod end plug welding is usually performed in a welding chamber. The welding chamber and the fuel rod are evacuated to expel all air and then backfilled with helium. The helium may be pressurized to backfill the fuel rod to the required elevated pressure or may be filled to atmospheric pressure. In the latter case the fuel rod needs to be pressurized in a second operation. The welding chamber

in most instances has an oxygen detection device to ensure that the welding atmosphere is free of air and most importantly nitrogen.

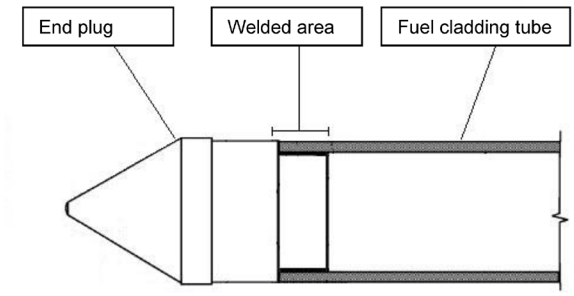

Figure 5. Schematic illustration of the joint between the cladding tube and the end plug [1].

Welding causes microstructural changes in the HAZ of material, resulting in a change in its mechanical (and often corrosion) properties. The fusion zone constitutes material that has been heated in excess of the melting temperature while the HAZ corresponds to the area where the combination of time and temperature has been such that a change in microstructure of the material has taken place. The extent of the HAZ varies. The amount of heat injected by the welding process plays an important role. Processes like LBW and EBW give a highly concentrated, limited amount of heat, resulting in a small HAZ. GTAW welding has a higher heat input and consequently results in a larger HAZ [2].

The LBW of Zircaloy-4 has been investigated in several studies [2,23,24,25,26]. Kim et al. [23] compared the GTAW welding and LBW of Zircaloy-4 using Nd:YAG laser of 500W average power with optical fiber transmission. The LBW method resulted in deeper weld penetration and more narrow fusion and heat-affected zone compared to GTA welding. The microstructure of the weld zone in both GTAW and laser welded specimens appeared to be of a mixed structure, where the martensitic α' structure and the Widmannstätten α-phase in the prior β grains were intermixed.

In a study carried out by Tao et al. [26], the weldability of Zircaloy-4 was studied using pulsed Nd:YAG laser (TRUMPF TruPulse 556) with a maximum peak power of 10 kW for pulsed laser spot welding. In the study, columnar grains and equiaxed grains were observed in fusion zone and heat affected zone of welded specimens, respectively. The fusion zone consisted of a mixture of α- and β-phases among which lamellar Widmannstätten structure α + Zr_3Fe was distributed. After the annealing treatment, the $Zr(Fe, Cr)_2$ second phase particles were precipitated inter- and intragranular of α grains adequately. TEM image of the fusion zone is presented in Figure 6.

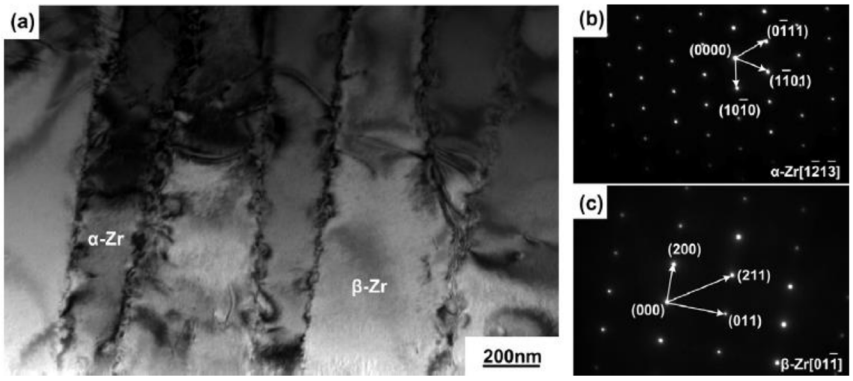

Figure 6. TEM investigation of fusion zone of the weld bead (a) TEM micrograph, (b) and (c) SADP of α-Zr and β-Zr [26].

When producing dissimilar metal joints with zirconium alloys and Fe-based alloys, brittle intermetallic phases may form. Shankar et al. [27] studied the dissimilar joining of Zircaloy-4 to Type 304L stainless steel by friction welding. From the three-point bend test, the Zircaloy-4 to Type 304L stainless steel joint exhibited only 5° bend angle at fracture and fracture occurred mainly at the interface. The main cause for the low bend ductility of Zircaloy-4 to Type 304L weld joints was due to the formation of intermetallic compounds like $Zr(Cr,Fe)_2$, $FeZr_4$, and $FeZr_2$ as observed from the XRD results. The hardness profile of the Zircaloy-4 to 304L joint is presented in Figure 7. Ahmad et al. [28] reported the formation of rod-shaped $Zr(Cr,Fe)_2$ intermetallic compound near the HAZ on the stainless steel side of EB welded Zircaloy-4 to stainless steel joint. The hardness of $Zr(Cr,Fe)_2$-phase was found to be three times higher than the average value of the molten zone [28]. EBW of Zircaloy-4 to stainless steel has also produced dendritic structure with ZrC_2-liquid (Zr,Fe) and eutectic phase with Zr_2Fe-Zr2Ni [25]. The presence of these brittle intermetallic compounds can impair mechanical properties of the joint. Higher bend ductility can be achieved by eliminating the formation of these brittle intermetallic phases or at least by avoiding formation of continuous layers of intermetallic compounds.

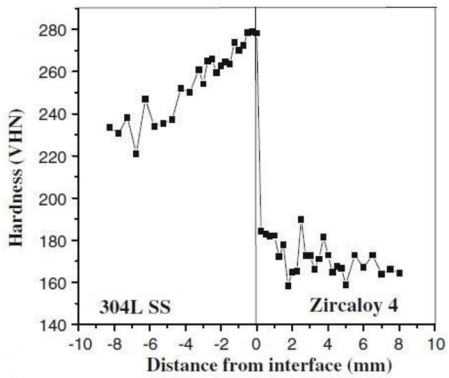

Figure 7. The hardness profile of the Zircaloy-4 to 304L joint [27].

Although successful LBW of zirconium alloys have been reported [23,25], no directly applicable literature data regarding LBW of multimetal systems, such as Zr-Nb-CrMo-FeCrSi, was available for this report. Mainly same principles apply for LBW as for EBW, especially when LBW is carried out in welding chamber in gas shielded environment. LBW results in

low heat input and a small molten weld pool, but the weldability of zirconium and niobium is expected to determine the weldability of the Zr-Nb-CrMo-FeCrSi multimetal system.

3.3 Electron beam welding

Electron beam welding (EBW), such as laser beam welding (LBW), belongs to the group of high energy density welding processes (HEDW) which are characterized by constricted high-temperature arc hence high arc energy and power density even up to 10 kW/mm^2. These characteristic features of EBW enable welding in a key-hole mode, which in turn results in advantages such as small molten pool, narrow weld cross-section and heat-affected zone (HAZ) area, as well as low heat input (per unit length). Constricted, columnar arc and low heat input also tend to minimize deformations, distortions and residual stresses during welding. The vaporization reactions of metal, elements and impurities, however, are more intense in EBW than conventional arc welding processes, which may cause problems. Typically, the depth-to-width ratio of EB welds is very large; on the other hand, also the weldable material thickness range (using the same equipment) is extremely large, which permits welding of very thick, as well as extremely thin sections (of less than 1 mm in thickness) [9,11,12,29-34].

The essential requirements for welding of zirconium are (i) careful protection of the molten weld pool, solidified weld metal and elevated temperature HAZ from any air atmosphere during the entire welding, as well as (ii) demands for utmost cleanliness of the welded parts to be joined by removing any contaminations of grease, oil, dirt, rust, humidity, etc. In this sense, the requirements for welding zirconium are very similar to welding of titanium alloys [9,12].

Thus far, EBW has in general been applied to weld zirconium alloys to a much lesser extent than arc welding processes, such as GTAW (TIG), or using resistance welding [9]. The use of EBW, however, provides some obvious benefits for the welding of zirconium. Since EBW is generally performed in a vacuum chamber, it is ideal for welding zirconium that has a strong oxidation tendency and therefore requires careful protection from air atmosphere during the entire welding operation, not only in a molten stage, but also during weld/HAZ cooling until temperatures as low as 480-200 °C [9,12].

General requirements for the chamber conditions to protect zirconium during welding are: (i) the use of vacuum (under-)pressures as low as 10^{-4} torr, (ii) the use of ultra-pure inert shielding gas (i.e. 99.995… 99.996 % argon) to completely fill the chamber, and (iii) the facilities to monitor the contents of oxygen, nitrogen and humidity (in case of gas-filled chamber), or alternatively, (iv) to monitor the level of (under-)pressure / vacuum level in EBW vacuum chamber. Especially for EBW of zirconium that has a strong affinity for oxygen and nitrogen, welding should be performed in a high-vacuum chamber under a pressure of 10^{-3}…10^{-5} torr in order to avoid any gas contaminations. These welding conditions facilitate deep penetration, narrow weld width and small weld contraction [9,12,35].

During welding, most zirconium alloys (e.g. Zircalloy-2, M5™, Zr-Nb-alloys) undergo the α-β phase transformation. In the heating stage, a relatively coarse lamellar β-phase structure is formed in the weld metal and the coarse-grained HAZ in the immediate vicinity of the fusion boundary, with the associated increase in strength and reduction in ductility and toughness. Additionally, some segregation of impurity elements occurs in the HAZ at peak temperatures close to the α-β-phase transformation temperature (and within the α-β two-phase region), which to some extent impairs ductility and corrosion resistance [10,34]. Further from the fusion boundary in the outer HAZ, re-crystallization of the grain structure takes place [12]. During the weld cooling stage, the occurrence of the β-α-phase transformation generally results in Widmanstätten type coarse lath-like single α-phase microstructure without any β-phase. In fact, β-phase does not exist in the final weld microstructure even if the weld cooling rate was high, like in the EBW. The faster the weld cooling rate, the finer is the lath size in

the resulting microstructure [10,34]. Low heat input and high weld cooling rate characteristic of EBW therefore diminish the coarseness of the lath size in the resulting weld/HAZ microstructure.

As an alloy, zirconium has many advantages regarding welding. Due to its low thermal expansion coefficient and elastic modulus, the welding deformations and weld residual stresses remain low. Using EBW these weld deformations can be minimized even further. Moreover, zirconium does not suffer from weld hot cracking or cold cracking problems provided cleanliness of the parts to joined is taken care, nor inclusion formation due to good solubility of zirconium oxides at high welding arc temperatures [11,12]. Welding of zirconium neither requires any preheating, which is an obvious benefit regarding the performance of EBW in a vacuum chamber that might limit the use of preheating equipment. In cases where post-weld heat treatment (PWHT) such a stress-relief treatment of a welded detail is required, which is often the case in NPP applications, the PWHT should be carried out in an inert gas atmosphere at 540 - 595 °C for 0.5 - 1 h [9,12,37,38]. It has been reported that due to the presence of tensile residual stresses and susceptibly of the Zr2.5Nb welds to delayed hydrogen cracking (DHC) in NPP environment, post-weld head treatment (PWHT) of Zr2.5Nb EB welds is required [39].

Typical weld defects in EBWs of zirconium alloys are gas pores (gas pockets/holes/traps) forming during weld solidification, as well as lack-of fusion like defects (spills). Also weld porosity can appear - if so, their formation can be minimized by (i) careful cleaning of the base materials (and filler materials) to be joined, (ii) lowering the travel speed, (iii) using slight to moderate preheating, and by (iv) improving the vacuum / gas shielding during welding [9,12,36,38].

Certain metallurgical limitations need to be accounted of when welding zirconium alloys. The Zr-alloys containing tin (such as Zircalloy-2 and Grade 704: Sn ≥ 1.5%) exhibit evaporation of Sn due to high vapor pressure of Sn and high energy density of the EBW process. This leads to a deterioration of corrosion resistance of EB welds in relation to non-welded zirconium base material [11,12].

Another limiting factor in fusion welding zirconium is a low solubility of certain elements such as C, Si, P, as well as Nb, Sn, Cr, Fe and Ni with amounts exceeding their solubility into zirconium. Excess amounts of these elements can therefore lead to the formation of complex intermetallic phases impairing the ductility and corrosion resistance of the weld [9,12,11]. EBW welds between Zircaloy-4 and stainless steel (304L) used in the nuclear industry have revealed diffusion of Fe, Cr and Ni in Zircaloy-4 near the molten zone and of Zr and Sn in the stainless steel. A rod-shaped intermetallic compound $Zr(Cr,Fe)_2$ and eutectic phases $ZrCr_2$–liquid (Zr,Fe) and Zr_2Fe–Zr_2Ni were recognized in the molten zone. The hardness of the molten zone, containing $Zr(Cr,Fe)_2$, was thereby much higher than the rest of the molten zone and the HAZs [40].

The possibility of such embrittlement may exist when welding Nb-layer - Zr-pipe bi-metal joints, as well as Nb-layer -ferritic steel layer bi-metal joints encountered in the present case. It is not, however, clear which of the two reactions: (i) evaporation of elements (e.g. Zr, Nb) accentuated by the high energy and power density in EBW, or (ii) the formation of complex, intermetallic (Nb, Zr, Fe) phases due to high amounts of these elements exceeding their solubility limits, occurs first during the EBW of zirconium-niobium bi-metallic joints. Nevertheless, a low overall heat input and a small molten weld pool characteristics of EBW should be a benefit also for welding of Nb-alloys and ferritic stainless steels. Consequently, the possibility of occurrence of these detrimental phenomena in the EB welding of Zr-Nb-Cr-Mo multi-material system requires actual welding experiments.

As far as multi-metal Zr-Nb-CrMo-FeCrSi system is concerned, no directly applicable literature data on EBW were found. Such as for zirconium alloys, EBW employing a vacuum chamber is reported to be also suitable for welding of Nb-alloys, often in a full-penetration,

smooth underbead mode [41]. The possibility of embrittlement due to intermetallics may, however, exist when welding Nb- layer - Zr-tube bi-metal joints, as well as Nb-layer - ferritic steel layer bi-metal joints, encountered in the present case. It is not, however, clear whether the two reactions: (i) evaporation of elements (e.g. Zr, Nb) accentuated by the high energy and power density in EBW, and (ii) the formation of complex, intermetallic (Nb, Zr, Fe) phases due to high amounts of these elements exceeding their solubility limits, really have a dominant role in EBW of zirconium-niobium bi-metallic joints. Nevertheless, availability of vacuum chamber, low overall heat input and a small molten weld pool characteristic of EBW should be a benefit also for welding of Nb alloys (and ferritic stainless steels). Consequently, to study the possibility of occurrence of detrimental metallurgical phenomena in the EB welding of Zr-Nb-CrMo-FeCrSi multi-material system is concluded to deserve further attention via actual welding experiments. Nevertheless, from the viewpoint of EBW as a process, weldability of zirconium and niobium will obviously dictate the weldability of the Zr-Nb-CrMo-FeCrSi multimetal construction.

3.4 Diffusion bonding

Diffusion Bonding (DB) or Diffusion Welding is essentially a solid state joining process in which carefully prepared material surfaces are brought tightly together at an elevated temperature. Application of pressure at the joining temperature causes smoothening of the roughness of the two contacting surfaces thereby bringing them into intimate contact, which enables the bond between the interfaces by creating an array of interfacial voids [42]. The main parameters describing the DB process are (i) temperature, (ii) pressure, (iii) duration of the joining process, and (iv) surface roughness of the materials to be joined [43].

In the DB process, possible physical mechanisms of subsequent bonding and preceding void closure at the interfaces include time-dependent plastic flow, including creep and superplasticity, and diffusion processes. These phenomena transport atoms to the void surfaces from adjacent regions, so reducing their volume. Given sufficient time, the voids will disappear completely, leading to an atom-to-atom contact across the original interface. There is no macroscopic deformation of the parts being bonded and, unlike welding, the bond zone itself is not melted. Hence, its microstructure is identical to that of areas remote from the bond and it has the same mechanical properties [42]. Surface roughness of the materials, in particular, has a significant effect on the DB process. Thus, providing of high surface finish makes possible obtaining more homogeneous joints without detectable defects and uniform microstructure already within shorter duration times at the selected bonding temperature [43].

Zirconium has much in common with titanium in that both metals appear in the same group of the periodic table and are isostructural, having a hcp (α) lattice at low temperatures and a bcc (β) lattice at elevated temperatures [42.] As the outer electron shells have a similar electronic configuration, zirconium is expected to have a similar chemical response and reactivity to Ti. This is important regarding solid-state joining because it is well known that Ti alloys may be joined by DB. In the case of α/β Ti alloys which exhibit superplasticity, DB may be combined with superplastic forming (SPF) to produce cellular structures of high rigidity and high strength-to-weight ratios [42]. Ti alloys have the ability to take the surface oxide into solution at elevated temperatures and in this respect zirconium appears to be similar, since experiments and predictions have shown that the oxide layer on zirconium tends to dissolve rapidly at temperatures of 760 °C and above, hence enabling sound joints to be obtained [42].

It has been reported that DB of zirconium can be successfully carried out under isostatic conditions and pre-determined conditions of argon pressure (10–30 MPa) within the 750–810 (…820) °C temperature range (i.e., in the α-phase field) using bonding times of 0–6 (…10) h [42]. It is anticipated that bonding in the α-phase region would enable the original base material microstructure to be retained [42]. As-received zirconium sheet material is often processed to produce an equiaxed α-grain structure containing a dispersion of $Zr(FeCr)_2$

precipitates. If this material is heated into the two-phase region (> 820 °C) this structure is lost and replaced by α-phase with grain boundary β-phase [42]. Bonding studies of zirconium (i.e. Zircalloy 4) have shown that at 800 °C temperature and with bonding pressure of 20 MPa, interface void closure occurs by constrained plastic collapse and diffusion. The progressive increase of plastic constraint during void closure leads to a dominance of diffusion. According to the experiments, it takes about 10 h until bonding will be complete [42].

In the case of DB of dissimilar materials and multi-metal joints, an interlayer inserted between substrates is often necessary to prevent the formation of intermetallic compounds and to reduce the residual stress in the joints [44,45]. DB can thereby overcome the metallurgical problem of zirconium - steel joints associated with the formation of brittle intermetallic compounds such as $FeZr_2$ and $FeZr_3$ in the weld pool encountered in conventional fusion welding, which impairs the strength of the welded joint [46]. Joining zirconium alloys to stainless steel, it has been found that the titanium based interlayer with higher content of titanium has favorable wetting behavior on the surface of the zirconium alloy at 850 °C. As titanium and zirconium decrease the activity of carbon in the steel, it leads to a significant shift in wetting transition towards higher temperatures. In the 800 - 900 °C temperature range, the intermetallics density was higher in the specimens bonded at the higher bonding temperature [47]. The isothermal solidification behavior of the bonds indicated that Ti is main controlling melting point depressant element and dissolution of Fe with the small liquid at the vicinity of the stainless steel causes microstructural development during the bonding process, altering the microhardness values. The optimum shear strength of 99 MPa with minimum deformation was found to be for specimens bonded at 850 °C for 15 min. The micrographs of fractography showed that at the lower bonding temperature intergranular fracture occurred while at the higher bonding temperature a mixed fracture with appearance of dimples alongside of the cleavage patterns was observed [46]. The titanium-based interlayer also operates as a barrier for diffusion of Fe and Cr and prevents the formation of brittle intermetallic compounds like Zr_3Fe_2, Zr_2Ni and Zr_3Fe [46].

Besides titanium, also niobium, copper and nickel have been reported usable as intermediated layers in zirconium to stainless steel DB joints [46]. A strength of 80% UTS of Zircaloy-2 has been achieved for specimen bonded at 870 °C, 2 h, using niobium, copper and nickel as the intermediate layers. These DB techniques can produce joints sound and dense enough to pass, e.g., the helium leak test [46,48].

As far as multi-metal Zr-Nb-CrMo-FeCrSi system is concerned, no directly applicable literature data on DB were found. Equally to zirconium, niobium and Nb-alloys exhibit high activity towards gases on heating, for which reason the best shielding medium is vacuum. Nb-alloys should therefore be joined by DB at temperatures below the recrystallization point so as to avoid saturation of the metal with gases (O_2, H_2 and N_2) and grain growth on heating. This requires the use of interlayers (e.g. nickel) applied to the mating surfaces and use of vacuum, enabling higher rate of diffusion [46].

3.5 Friction stir welding

Friction stir welding (FSW) is a solid state (no metal melting) low heat input joining technology which typically results in a fine, equi-axed grain structure weld nugget composed of recrystallized microstructure. FSW produces a smooth weld surface and lower residual stresses and distortion. In case of Zircaloy FSW welds are expected to be less susceptible to hydrogen-induced cracking and have reduced heat-affected zone (HAZ).

Friction stir welding of zirconium alloys is not studied much, yet [49]. However, it has been shown that defect-free welds with a fine equi-axed grain structure are possible to obtain for zirconium alloys [49]. Joining Zircaloy parts together, such as in case of joining end plugs with cladding tubes in assembling the fuel rods, FSW may be also connected to so-called

transient liquid phase bonding (TLPB) which combines advantages of both DB and brazing. In TLPB a thin layer of liquid forms at the joint interphase, wets the contacting surfaces, and then solidifies isothermally. TLPB for joining Zircaloy using Ni foil as an interlayer has been successfully tried [50]. Ni is a versatile corrosion resistant material and has high strength at elevated temperatures.

The integrity of the nuclear fuel end plug welds is essential to the nuclear fuel performance and safety as well as usability of the power plant. Dissimilar metal joining between MMLC fuel cladding and Zircaloy end plug through friction stir welding technology is critical technology gap of joining these materials. Specific objectives are (i) developing the process parameters to consistently produce defect-free welds of the same and dissimilar metals, (ii) optimizing the microstructure features in weld to match the properties of the base metals and, (iii) produce representative weld joints and welded components to support future testing evaluation at high temperature and irradiation environments.

New joint design for the MMLC fuel cladding – end plug welding has to be developed with eventual interlayer metal foils using orbital welding method with welding chamber preventing contamination with hydrogen. Optimal welding conditions according to the properties of the materials have to be developed in the future.

References

1. Lee, J. et al. United States Patent Application, Pub. No.: US 2013/0272484 A1, Pub. Date: Oct. 17, 2013.
2. Rudling, P et al. Welding of Zirconium Alloys. ANT International annual report 2007.
3. Borell, S., Rostvall, T. Westinghouse Electric Sweden Ab; Patent Application Titled "Method of Laser Welding a Nuclear Fuel Rod", September 18, 2014.
4. Weidinger, H. Zr-alloys, the nuclear material for water reactor fuel. A survey and update with focus on fuel for pressurized water reactor systems. 7th international conference on WWER fuel performance, modelling and experimental support. Albena, Bulgaria, 17-21 September 2007.
5. Busby, J. Materials of construction for light water reactor applications. Halden summer school 2011.
6. Barrett, K. Bragg-Sitton S., Galicki, D. Nuclear fuel cladding system development. Trade-off study. INL/EXT-12-27090, 2012.
7. Adamson R. et al. Performance Evaluation of New Advanced Zr Alloys for PWRs/VVERs. ANT International annual report 2011.
8. NRC request for additional information, May 18, 2005, http://pbadupws.nrc.gov/docs/ML0514/ML051440548.pdf accessed 16.8.2016.
9. ASM Handbook Vol. 6: Welding, brazing and soldering. ASM International.
10. Metals Handbook Vol. 2: Properties and selection: Nonferrous alloys and special-purpose materials. ASM International.
11. Welding handbook, Vol 4, 7th edition. Metals and their weldability. AWS, 1983.
12. Ruusila, J. Manufacturing of zirconium structure – welding (in Finnish). Presentation given at VTT 19.9.1984. VTT Symposium (in Finnish)
13. Roberge, P. Handbook of corrosion engineering. McGraw-Hill, 1999.
14. Thulin,E., Arborelius, J. Fuel Manufacturing and its Environmental Effects, ATS YGN meeting in Espoo, November 3, 2006. http://www.ats-fns.fi/images/files/presentations/2006/YG_syysseminaari_2006_thulin.pdf
15. Quality and reliability aspects in nuclear power reactor fuel engineering. IAEA nuclear energy series No NF-G-2.1, Vienna, 2015.
16. Gaillac, et. al. Numerical Modeling of Fuel Rod Resistance Butt Welding. Zirconium in the Nuclear Industry: 17th International Symposium. STP 1543, 2015. pp 331 – 345. http://hal-bioemco.ccsd.cnrs.fr/ENSMP_CEMEF/hal-01163654

17. Le point de vue lÍRSN sur la suretet et la radioprotection du parc electronucleaire Fracais en 2008. IRSN report no 316.
18. Setty, D. et al. resistance butt welding of zirconium alloy material. Materials and manufacturing processes, 23: 844-851, 2008.
19. Chauve, H.et al. Zirconium use for large process components, IAEA-TECDOC-421 (1987) 165–192.
20. Ahmad, M. et al. Microstructure and characterization of phases in TIG welded joints of Zircaloy-4 and stainless steel 304L. J. Mater. Sci., 2007, Vol. 42, pp. 328-331.
21. Lippold, J.C. and Kotecki, D.J. Welding Metallurgy and Weldability of Stainless Steels. John Wiley & Sons, New Jersey, USA. 2005. 357 p. ISBN: 0-471-47379-0.
22. Chmelíčková, H. and Šebestová, H. (2012). Pulsed Laser Welding, Nd YAG Laser, Dr. Dan C. Dumitras (Ed.), ISBN: 978-953-51-0105-5.
23. Kim, S-S. et al. Investigation on Nd:YAG Laser Weldability of Zircaloy-4 End Plug Closure for Nuclear Fuel Elements. Journal of the Korean Nuclear Society, Vol. 33, No. 2, pp. 175-183, 2001.
24. Han, Q. et al. Laser pulsed welding in thin sheets of Zircaloy-4. Journal of Materials Processing Technology 212 (2012) 1116–1122.
25. Boutarek, N. et al. Microstructure change in the interface of co_2 laser welded zirconium alloys. Physics Procedia 2 (2009) 1159-1165.
26. Tao, W. et al. Pulsed laser spot welding of intersection points for Zircaloy-4 spacer grid assembly. Materials and Design 52 (2013) 487–494.
27. Shankar, R. et al. Dissimilar Joining of Zircaloy-4 to Type 304L Stainless Steel by Friction Welding Process. Journal of Materials Engineering and Performance, Volume 18(9) (2009).
28. Ahmad, M. et al. Hardness and Microstructural Studies of Electron Beam Welded Joints of Zircaloy-4 and Stainless Steel, J. Nucl. Mater., 2002, 301, p 118–121.
29. Strasser, A. & Rudling, P. Fuel Fabrication Process Handbook. 2004.
30. Adamson, R., Cox, B., Garzarolli, F., Rudling, P. & Strasser, A. IZNA-3 Annual Report. Surahammar. Advanced Nuclear Technology International, 2004.
31. Tenckhoff, E. Review of Deformation Mechanisms, Texture and Mechanical Anisotropy in Zirconium and Zirconium Base Alloys. Teoksessa: Zirconium in the nuclear industry. Fourteenth International Symposium. ASTM, 2005. S. 25 - 50. STP 1467. ISBN 0-8031-3493-2.
32. Adamson, R.B. & Rudling, P. Dimensional Stability of Zirconium Alloys. IZNA-2 Special Topics Report. Uppsala. Advanced Nuclear Technology International, 2003.
33. Sarlin Lämpökäsittelytekniikkakirja. Helsinki, 1992. 99 s. ISBN 952-90-3282-X.
34. Metals Handbook Vol. 3 (9th Edition): Properties and Selection: Stainless Steels, Tool Materials and Special-Purpose Materials. ASM International. ISBN 0-87170-009-3.
35. Smith, E. H. Mechanical Engineer's Reference Book 12th edition. Elsevier, 1998.
36. Aleksandrov, A. B., Zhukov, Y. A., Vasyukov, V. N., Gruzman, I. S., Karlov, Y. K., Marchenko, V. G. & Spektor, A. A. Automatic Detection of Spills and Gas Pockets upon Ultrasonic Checking of Welds in Zirconium Fuel Claddings. Russian Journal of Nondestructive Testing, (2004). Vol. 40, No. 4, 233 - 238.
37. Kutz, M. Handbook of Materials Selection. John Wiley & Sons, 2002. ISBN 0-471-35924-6.
38. Roberge, P.R. Handbook of Corrosion Engineering. McGraw-Hill, 1999. ISBN 0-07-076516-2.
39. Muránsky, O. et al. Evaluation of residual stresses in electron-beam welded Zr2.5Nb0.9Hf Zircadyne flange mock-up of a reflector vessel beam tube flange. Journal of Nuclear Materials 438 (2013) 154–162.
40. Ahmad, M. et al. Hardness and microstructural studies of electron beam welded joints of Zircaloy-4 and stainless steel. Journal of Nuclear Materials, Issues 2–3, (March 2002), 118-121.
41. J.L. Kirchgessner. Forming and Welding of Niobium for Superconducting Cavities. Proceedings of the Third Workshop on RF Superconductivity, Argonne National Laboratory, Illinois, USA. SRF87E05, (1988) 533-543.

42. Hill, P.S., Todd, R.I., Ridley, N. Mechanism of the HIP bonding of Zircaloy-4 in the α-phase field. Journal of Materials Processing Technology 135 (2003) 131–136.
43. Yakushina, E., Reshetov, A., Rosochowski, A. Optimisation of diffusion bonding parameters of Ti alloys through the structure and surface conditions. Materials Science Forum Vols. 783-786 (2014) 2845-2850. © (2014) Trans Tech Publications. Switzerland.
44. Chatterjee, S., Kundu, S., Sam, S., Mishra, B. Diffusion Bonding of Duplex Stainless Steel and Ti Alloy with and without Interlayer. Materials Science Forum Vols. 783-786 (2014) 9-14. © (2014) Trans Tech Publications. Switzerland.
45. Ramos, A.S. et al. Production of intermetallic compounds from Ti/Al and Ni/Al multilayer thin films - A comparative study. J. Alloys Comp. 484 (2009). pp. 335-340.
46. Bhanumurthy, K. et al. Tubular transition joint between Zircaloy-2 and stainless steel. Journal of Materials Processing Technology 54 (1995) 322-325.
47. Mazar Atabaki, M., Bajgholi, M.E., Dehkordi, E.H. Partial transient liquid phase diffusion bonding of zirconium alloy (Zr–2.5Nb) to stainless steel 321. Materials and Design 42 (2012) 172-183.
48. Kazakov N.F. (ed.): Diffusion Bonding of Materials. Elsevier, Pergamon Press Ltd (2013) 175–176.
49. Sato, Y.S. et al. Microstructural studies of friction stir welded Zircaloy-4. Scripta Materialia, 67 (2012) 241-244.
50. Chen, H. et al. Interfacial microstructure and properties of the self-joined Zircaloy-4 joints with Ni foil. J. Nuclear Materials, 453 (2014) 275-279.

Initial Tests of Cr-Based MMLC Layer Joining: While corrosion and diffusion couple tests were underway, MIT contracted Arc Applications Inc. to perform an initial weld overlay of Fe-12Cr-2Si onto a Cr substrate for the purpose of analyzing the quality of the interface. It was quickly found that Cr was too brittle to be sourced, thus it was decided instead to create an overlay of Fe-12Cr-2Si onto a substrate, machine it off, and then electroplate Cr onto this free overlay to form the interface. HIPing was planned to be used to join the Ti and Zrly-4 layers to this billet. However, it was discovered upon Cr plating that numerous small holes existed throughout the electroplated layer. This, combined with the difficulty of sourcing Cr or CrMo wire and its brittleness, resulted in deciding not to move forward with the Cr-barrier based MMLC concept. The following report from Arc Applications summarizes this initial MMLC fabrication effort, with the evidence that led to this change in decision.

Arc Applications, Inc.
AAI 21720-Fe12Cr2Si/Titanium Coupons 07/20/2017

Welding and Chrome Plating of a Fe12Cr2Si Deposit for HIP Bonding

Introduction

MIT Plasma Science & Fusion Center contracted AAI to provide a Fe12Cr2Si all weld metal deposit with a layer of chrome as defined in the scope of work Q1684 Rev 5/17/17. MIT planned to use this coupon in a follow up diffusion bonding trial using hot isostatic pressing (HIP) to analyze the interface bonding of the stack-up of materials as depicted in Figure 1.

Figure 1

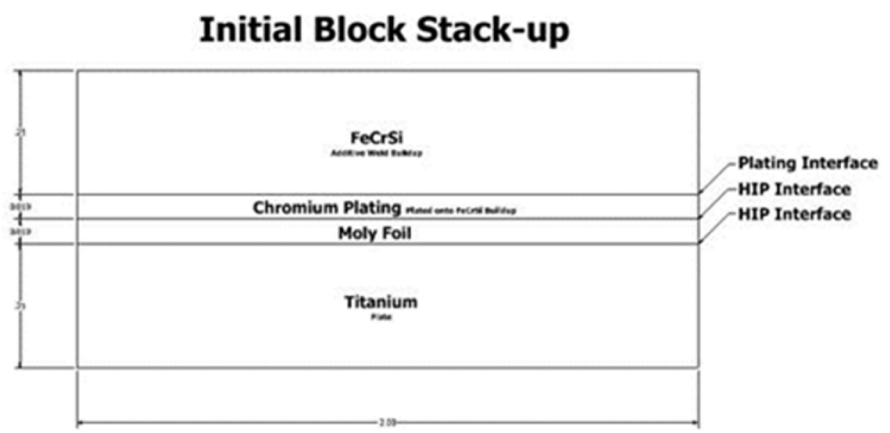

Material bonding for a transition from Titanium to Fe12Cr2Si

Fe12Cr2Si Buildup

A Cold Wire GTA deposit of Fe12Cr2Si was made for the purpose of creating an all weld metal coupon. The filler wire used was 0.035 inch diameter Haynes Alloy 405 (Heat:E031009-02) deposited on a CrMoV steel plate. The welding procedure (Ref: Appendix I) was used to make the 5.25 x 7.75 x 0.45 inch Fe12Cr2Si buildup, Figure 2. Upon completion of welding, the buildup was saw cut to produce the all weld metal 3.25 x 3.25 inch coupon, Figure 3. All surfaces of the coupon were then machined in preparation for Cr plating.

Figure 2

First layer of Fe12Cr2Si weld deposit

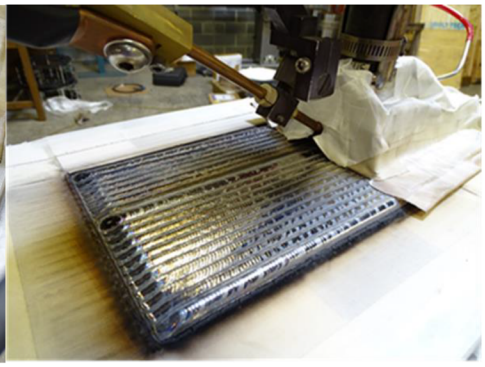

Second layer of Fe12Cr2Si deposit

Figure 3

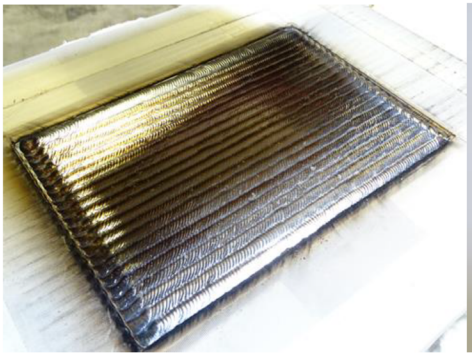

Final layer of Fe12Cr2Si weld deposit

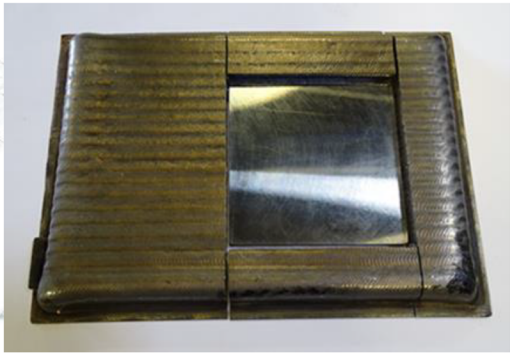

Machined coupon of the Fe12Cr2Si buildup

Cr Plating

The coupon was then sent to US Chrome (New York facility) to be chrome plated to a gross thickness of 0.060 inches to achieve a net thickness of 0.050 inches after surface grinding. During the plating process the coupon was removed from the tank after 0.005 inches of deposit for an in-process evaluation. Visually, three small pits were observed, Figure 4.

It was speculated that these pits were caused from small features induced in the surface during the machining of the surface. Chrome plating was discontinued and the coupon was surface ground back into the Fe12Cr2Si deposit to provide a more uniform surface for plating to initiate from than what the machined surface provided. After surface grinding was complete, the Cr plating resumed with no further visually detectable pitting occurred through the full 0.060 inch thickness.

Figure 4

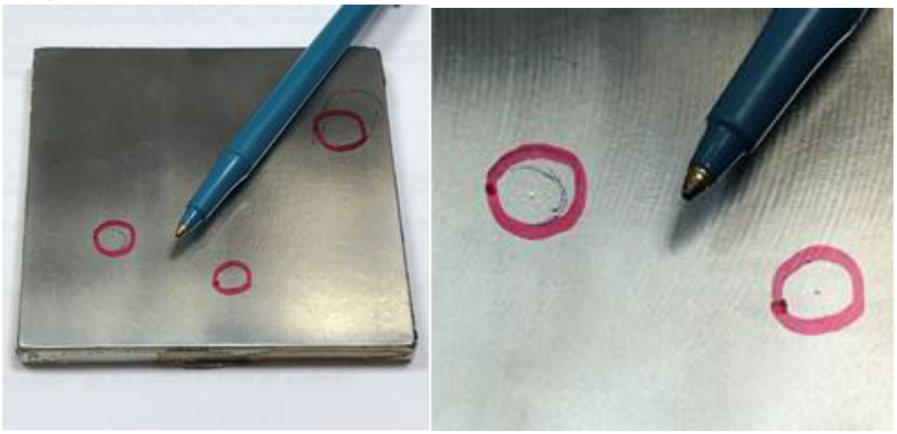

Pitts after 0.005 inches of plating. Note surface texture from machining prior to plating.

Surface Grinding

Upon completion of the chrome plating, the coupon was surface ground to unsure the top surface was a uniform plane to promote bonding in the HIP trial. The gross Cr plating thickness was 0.060 inches but the net thickness after surface grinding was 0.050 inches. Figure 5 shows the Cr plated Fe12Cr2Si coupon before and after final surface grinding.

Figure 5

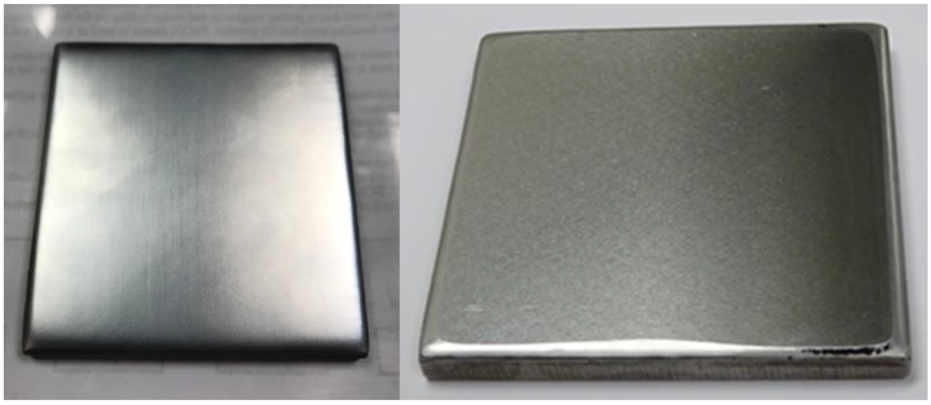

Fe12Cr2Si after Cr plating **Fe12Cr2Si Cr plating after final surface grinding**

EDM Cutting

Taper effect of Cr plating at the edges and corners of the Fe12Cr2Si coupon is shown in Figure 6. It was for this reason that a 2 x 2 inch coupon was removed by EDM cutting from the larger 3.25 inch x 3.25 inch Cr plated Fe12Cr2Si coupon, Figure 7. A small 0.6 x 1.0 inch rectangle was also removed for the purpose of metallurgical analysis.

Figure 6

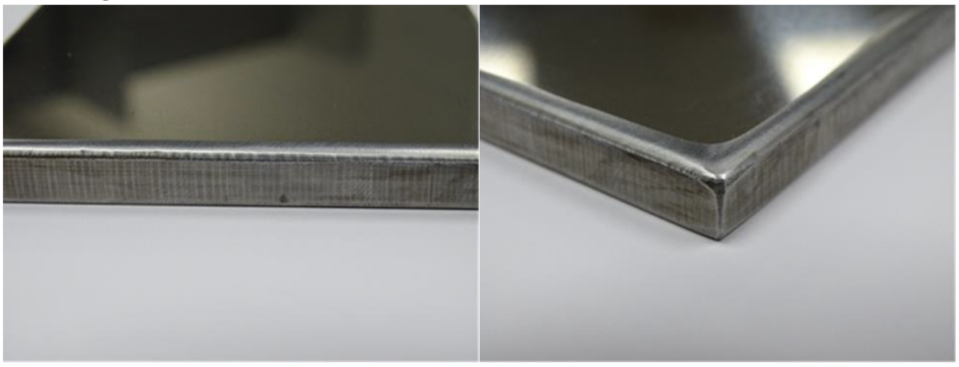

Cr plating taper effects at the edges of the Fe12Cr2Si coupon

Figure 7

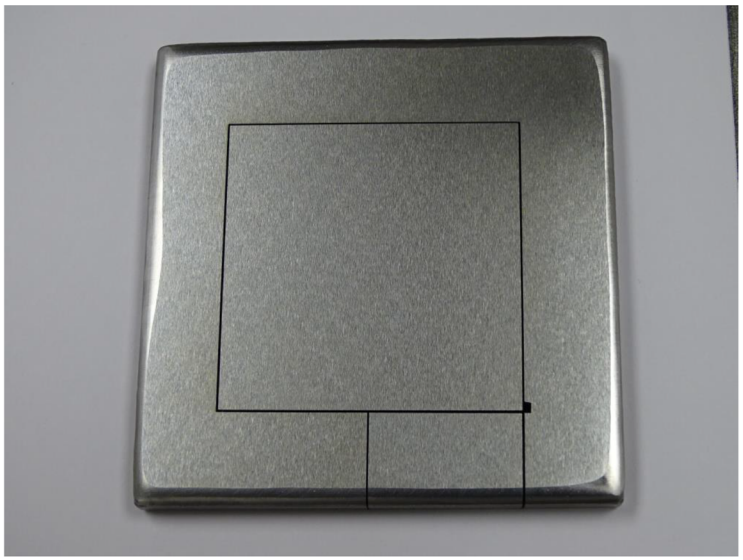

Cr plated Fe12Cr2Si coupon after EDM cutting

Arc Applications, Inc.

AAI 21720-Fe12Cr2Si/Titanium Coupons 07/20/2017

CP Titanium Coupon

AAI provided MIT with two CP titanium pieces. One was planned to be used in the HIP stack up with no surface preparation/conditioning. This coupon was in the as-received sheet condition, Figure 8 (left). The second coupon had the surface oxide removed with reverse polarity cathodic cleaning, Figure 8 (right). The intent was to provide both surfaces for analysis to determine if cathodic cleaning of titanium would potentially promote better diffusion bonding during the HIP trial. After completing the welding, plating and cleaning processing, the plated deposit and titanium coupons were shipped to MIT for HIP and metallographic evaluations.

Figure 8

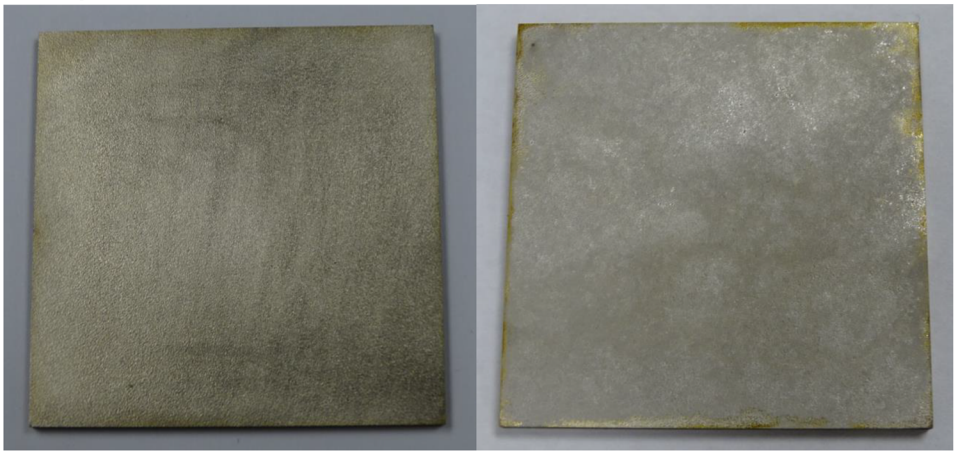

As-received titanium coupon surface **Cathodically cleaned titanium coupon surface**

Appendix I

Welding Parameter Documentation

ARC APPLICATIONS, INC.

WELDING RECORD COLD WIRE

Test#	21720 Fe12Cr2Si Buildup
Groove	Deposit Buildup
Weld type	
Position	Flat
Base Material	
Type	CrMoV
Filler Material	Haynes Alloy 405
Ht#	E031009-02
Dia. (in)	0.035
Tungsten	
Type	1.5% La
Dia. (in)	0.125@10°
Ext. (in)	0.375
Taper (deg)	20° - 30°
Flat (in)	0.02 – 0.04
Cup Dia. (in)	0.75
Shielding Gas	
Type	50/50ArHe
Flow (cfh)	45-60
Trailing Gas	
Type	Argon
Flow (cfh)	50-60
Interpass Temp.(C°)	450-700

SETUP

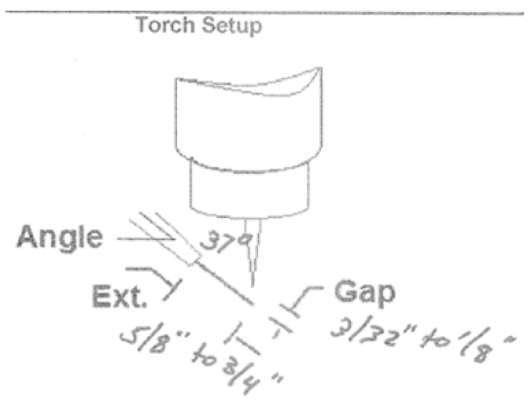

PARAMETERS

Prepurge	15	Post Purge	15
Upslope	5	Downslope	5
AVC Start Delay	2	AVC Stop Delay	0.1
Wire Feed Start Delay	5	Wire Feed Stop Delay	4.3
Travel Start delay	5	Travel Stop Delay	0

PASSES	All
PRI AMPS (amps)	225
BCK AMPS (amps)	150
PRI AVC (volts)	11.0
PRI WIRE (ipm)	65
BCK WIRE (ipm)	55
PRI PLS (sec)	0.3
BCK PLS (sec)	0.3
STEP OFFSET (in)	0.25
TVL SPD (IPM)	6.5
INTERPASS TEMP (°F)	450-700°F

Arc Applications, Inc.

AAI 21720-Fe12Cr2Si/Titanium Coupons 07/20/2017

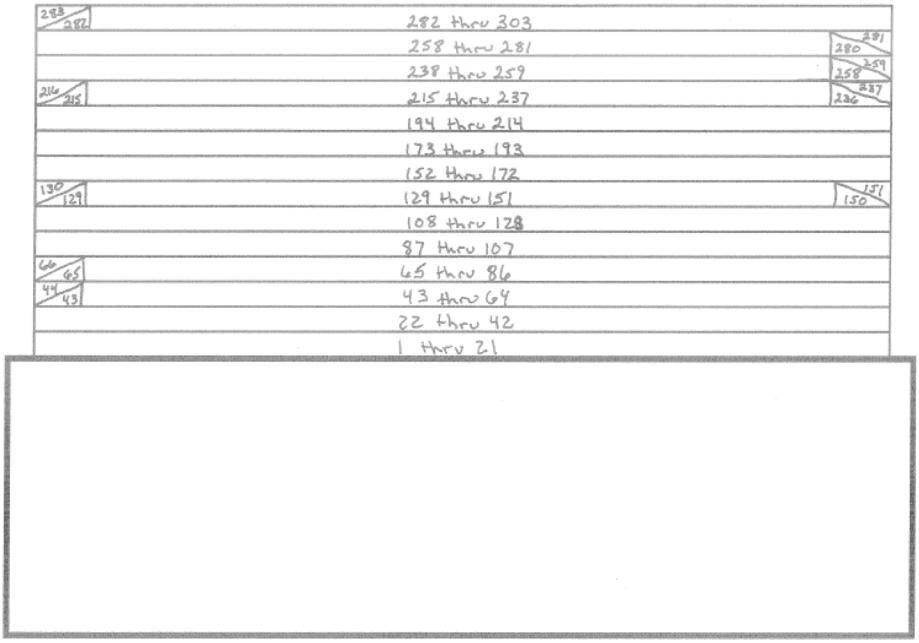

(coldwire)

Industrial-Scale Fabrication of Three-Layer MMLC Billet: Following the new design of the billet (detailed in the report in the following few pages), it was decided that to make an attempt at the major milestone for the industrial scale fabrication task that a full scale billet would be manufactured on a best effort basis. Initial attempts to fabricate the four layer billet halted once the vanadium expert from Specialty Alloys, our vanadium layer contractor, retired early with no replacement. Specialty Alloys then declined further work and refunded the invoice for that billet, leaving us back at square one. Another source of scrap V-alloys was found at ATI Specialty Alloys, though the only pieces remaining were smaller billets left over as sprues and remanents from earlier castings of V-3Fe-1Si, V-4Ti-4Cr, and V-15Ti-15Cr. Thus it was decided to use the V-4Ti-4Cr mini-billet to begin fabrication of a smaller (~50lb.) four layer MMLC billet in parallel with full scale (~500lb.) billet fabrication of a three layer billet, consisting of Zircaloy-4, a Ti barrier layer, and the Fe-12Cr-2Si overlay. While it was known that Fe and Ti react deleteriously to form intermetallic compounds, the fabrication procedure was modified to absolutely minimize time-at-temperature of the Fe-based and Ti layers. The theory was that minimizing time-at-temperature would also minimize Fe/Ti layer interaction, though the HIP cycle turned out to be too much time-at-temperature. Instead of weld overlaying Fe-12Cr-2Si onto the Ti layer, a "thermal fit" process was designed whereby a pipe of CP-2 (commercial purity, Grade 2) Ti was machined into a tube slightly smaller than the Zircaloy-4 billet, heated up, slid onto the Zircaloy-4, and allowed to thermally contract. Then, an Fe-12Cr-2Si weld overlay build-up was performed on a carbon steel substrate, which was fully machined out to be just narrower in diameter than the Ti layer. This too was thermally fit by heating, sliding onto the Zrly-4/Ti billet, and contracting around it.

Because of the thermal fit interfaces, it was believed that hot isostatic pressing (HIPing) would help remove any interfacial porosity. The same HIP parameters from a previous DOE-NE funded effort using Fe-12Cr-2Si were used – 4 hours at 1050C – to shore up the interface. It worked too well – the carbon steel used as the HIP can rapidly interacted with the Ti layer, forming a low melting point eutectic and penetrating through the Fe-12Cr-2Si buildup. These and other intermetallic phases formed subsequently cracked upon cooling, as revealed by dye penetrant inspection. Thus the HIPing process was the undoing of this billet, and it was decided not to attempt extrusion of this larger, three-layer MMLC billet. Instead, the last remaining funds for the project were dedicated to completing and extruding the four-layer MMLC billet with the V-4Ti-4Cr barrier layer in place without HIPing. This is expected to complete at the end of the 2019 calendar year.

The following report from Arc Applications details all the steps, rationale, fabrication, and post-fabrication examination of the three-layer MMLC billet. As of this report writing, the four layer billet is nearing completion at Arc Applications, at which point it will be extruded on ATI's smaller scale extrusion press.

Development of Technologies for Manufacturing Multi-Metallic Layers Composite LWR Fuel Cladding to Enhance Accident Tolerance and CRUD Deposition Resistance

Performed Under:

MIT PO 154869

AAI Order 21813

Prepared For:
Dr. Michael Short

Massachusetts Institute of Technology
130 Albany Street NW13-213
Cambridge, MA 02139

Prepared by:

Jason Rausch
Welding Engineer

Approved By:

Jonathan T. Salkin
President

September 18, 2019

ARC APPLICATIONS, INC.

AAI 21813 Multi-Metallic Composite Fuel Cladding 09-18-19

Welding Development Program Overview

This report documents the work completed by Arc Applications, Inc. (AAI) on behalf of Massachusetts Institute of Technology (MIT) for the development of technologies for manufacturing multi-metallic layers composite LWR fuel cladding to enhance accident tolerance and CRUD deposition resistance under PO 154869. The scope of work was to prepare an extrusion blank that was constructed of multiple layers of differing materials that were all concentrically oriented and sheathed upon each other, Figure 1. The innermost material and the one that constituted the majority of the mass, was to be Zircaloy-4 with an approximate wall thickness of 2.25 inches. The subsequent layers moving outward from the Zircaloy-4 were to be commercially pure Grade 2 titanium with a 0.05 inch wall thickness, followed by a vanadium alloy (V-15Cr-5Ti-0.05Si) of a 0.050 inch wall thickness, and then an Fe12Cr2Si alloy of a 0.3 inch wall thickness. All of the interfaces between these material layers were machined to provide minimal oversized slip fit tolerance. Once assembled the extrusion blank was to undergo a HIP cycle and final machining in preparation for an extrusion operation.

Figure 1

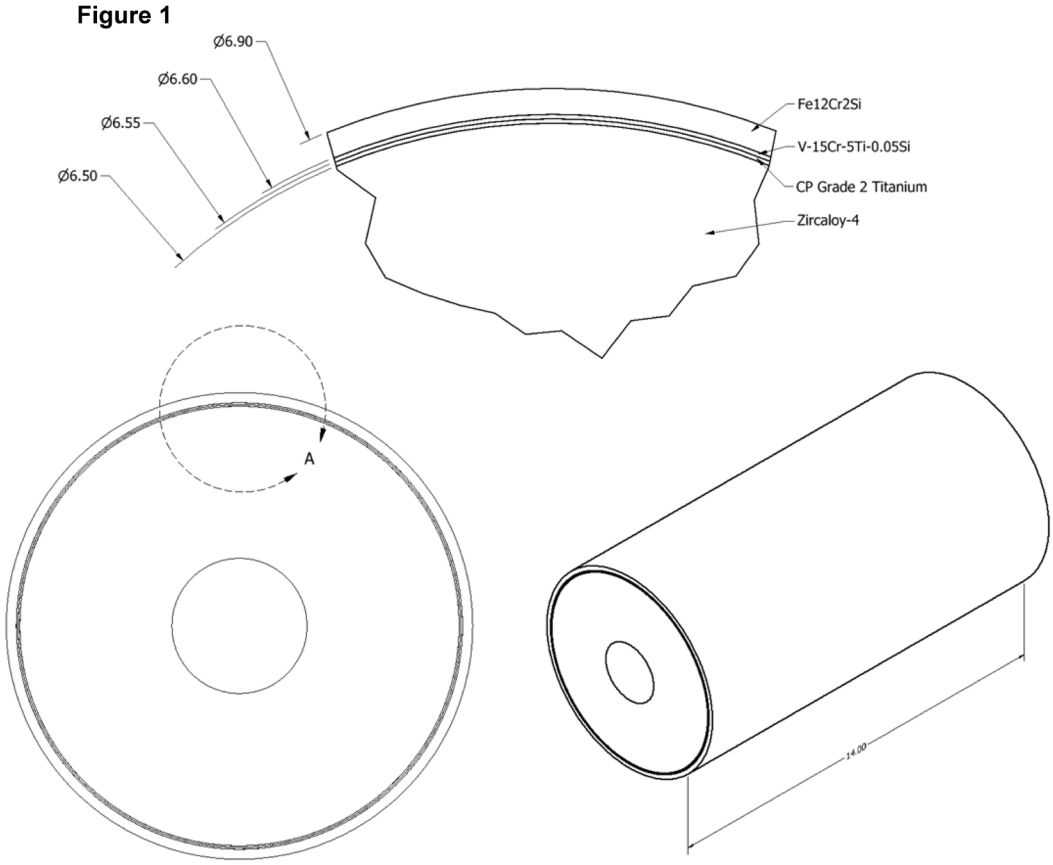

Original design concept for extrusion blank

ARC APPLICATIONS, INC.

AAI 21813 Multi-Metallic Composite Fuel Cladding 09-18-19

Vanadium Sourcing Challenge

Per the original scope of work, there was a layer of a Vanadium alloy, V-15Cr-5Ti-0.05Si that was to be a boundary layer between the titanium and Fe12Cr2Si layers. Prior to the start of the project, AAI confirmed that a custom alloy casting house could cast this alloy to the dimensions needed. Once the project started, the purchase order was released to this casting house, however, they were unable to meet the commitment. AAI attempted at great lengths to find a vendor that would cast a small volume of this custom vanadium alloy at an acceptable cost per the budget of the project. AAI could find no such vendor. In order to keep the project moving forward, MIT agreed to remove the vanadium layer and continue with the construction of the extrusion blank with just the Zircaloy-4, titanium, and Fe12Cr2Si material layers. To compensate for this change, the planned thickness of the titanium layer was increased from 0.0.50 inches to 0.0125 inches.

Zircaloy 4 Base Preparation

AAI received the Zircaloy-4 (Zr-4) billet material from MIT in the as-extruded condition from the ATI plant in Albany, Oregon, Figure 2. The as-received dimensions of the billets were 6.460 inch OD x 1.900 inch ID x 14.375 inches long.

Figure 2

As-received Zirc-4 billets

In order to achieve good and consistent material thicknesses during assembly machining steps, titanium extensions were inserted into the ID on each end of the Zr-4 billet, Figure 3. Fillet welds were made between the Zr-4 billet and the titanium extensions. The first machining step was to machine the titanium extensions concentric to the OD of the Zr-4 billet. The machined extensions served as the machining datum for the preparation of the Zr-4 base billet and the titanium layers final OD machining step.

ARC APPLICATIONS, INC.
AAI 21813 Multi-Metallic Composite Fuel Cladding 09-18-19

Figure 3

Titanium extensions added to the Zirc-4 billet

The Zr-4 billet was machined to an OD of 6.347 inches in preparation to have the titanium layer sheathed down around and along the length, Figures 4 and 5.

Figure 4

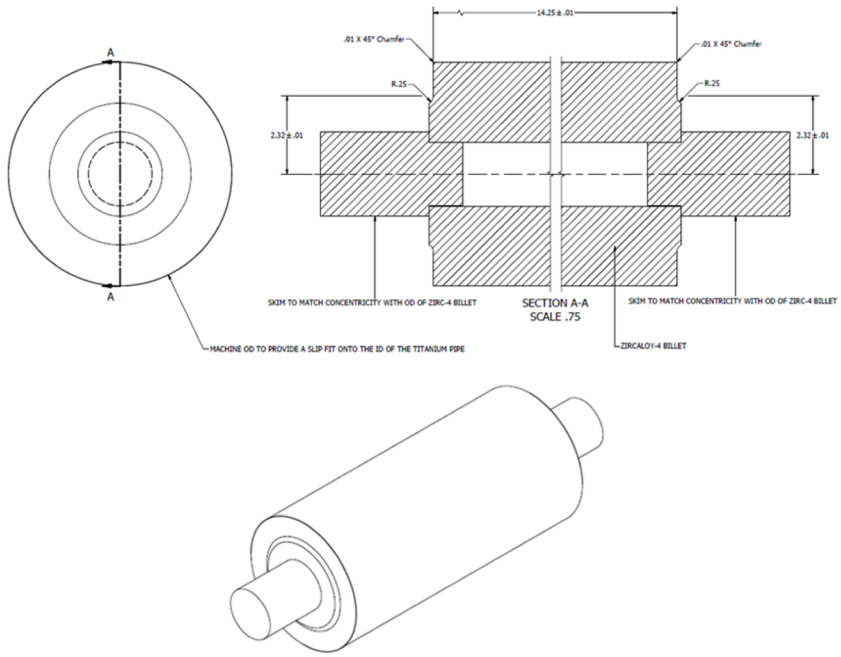

Zirc-4 base billet machining stage

Figure 5

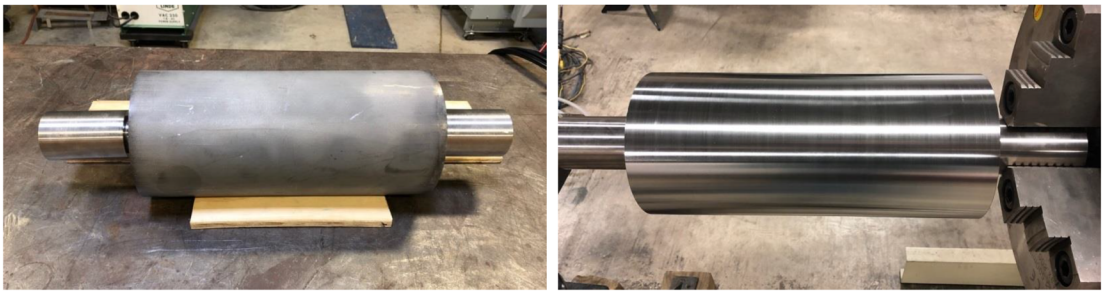

Zirc-4 base billet prior to machining OD (left) and after machining OD (right)

Titanium Layer Preparation

The titanium layer material was commercially pure Grade 2 titanium in the form of nominal 6 inch schedule 10 pipe. The actual as-received cross sectional pipe dimensions were 6.625 inch OD x 0.134 inch WT. This material was fabricated by rolling sheet material and welding the longitudinal seam. Knowing that the thin wall titanium pipe would not be sufficiently rigid to undergo an ID machining operation, a steel pipe was procured for the purposed of being temporarily sheathed around the OD of the titanium tube by means of a heat shrink fit. This temporary arrangement would provide structural stability to the thin wall titanium pipe for the necessary machining step that would prepare its ID for the slip fit around the OD of the Zr-4 base billet.

Figure 6

CP Grade 2 titanium pipe (right) and encapsulating 'heat shrink' pipe

ARC APPLICATIONS, INC.

AAI 21813 Multi-Metallic Composite Fuel Cladding 09-18-19

The as-received OD dimensions were measured around the circumference of the thin wall titanium pipe to map the actual OD. An appropriate ID dimension was then calculated and machined on the ID of the steel pipe to provide a heat shrink fit around the thin wall titanium pipe. Resistance heater pads were wrapped around the OD of the steel pipe followed by wrapping the heating pad with ceramic insulation. The steel pipe was heated to 800°F and the titanium tube was cooled to 20°F, a temperature differential of 780°F. Once the steel pipe had thoroughly soaked at 800°F, the titanium tube was inserted down inside the steel pipe and the assembly allowed to cool. An argon purge was applied to the ID of the titanium pipe during the cooling stage to limit any amount of oxygen that may diffuse into the titanium surface.

The steel pipe/titanium pipe heat shrink assembly was then machined to have an ID of 6.357 inches providing a slip fit tolerance onto the Zr-4 base billet of 0.010 inches across the OD. The Zr-4 base billet and the steel pipe/titanium pipe heat shrink assembly were thoroughly cleaned and then sheathed onto each other.

Figure 7

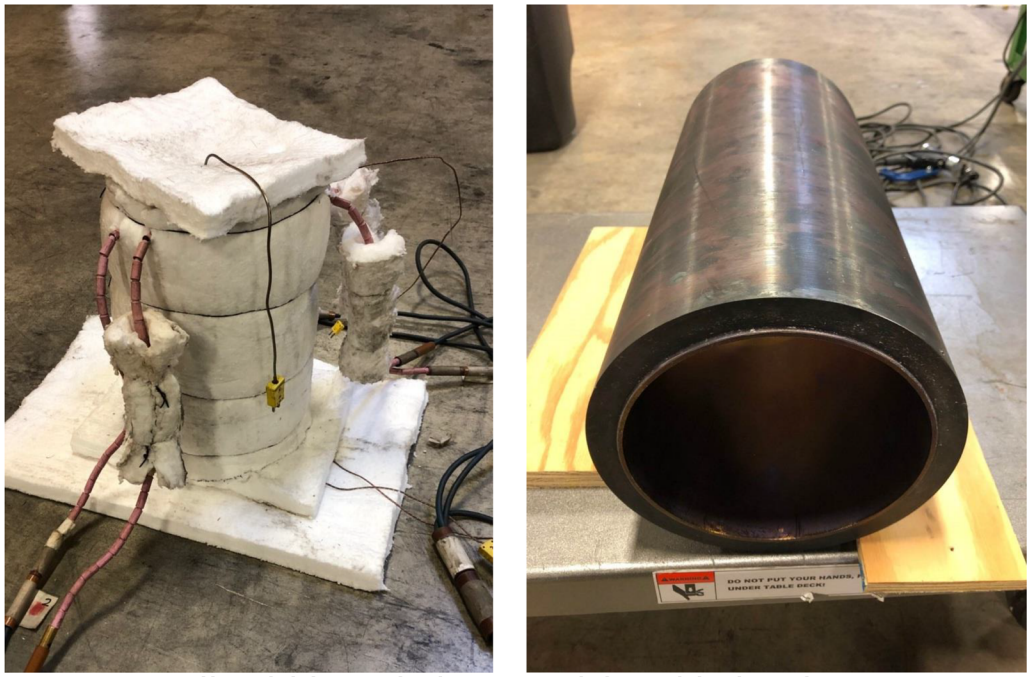

Heat shrink operation between steel pipe and titanium tube

Figure 8

ID of titanium tube machined for slip fit over Zirc-4 base (left) and slip fit operation preparations (right)

In order to keep the titanium layer from spinning on the Zr-4 base during machining, tack welds were made at both end of the assembly at the Zr-4 and the titanium layer interface. The filler was matching CP Grade 2 titanium.

Figure 9

Tack welds to keep titanium layer from slipping on Zirc-4 base

ARC APPLICATIONS, INC.

AAI 21813 Multi-Metallic Composite Fuel Cladding 09-18-19

By a machining operation, the steel heat shrink pipe was separated from the OD of the titanium tube. The assembly was then machined so that the titanium layer OD was at 6.604 inches rendering the titanium layer to a thickness of ~0.1235 inches. After machining the OD of the titanium layer, the titanium extensions were removed from the Zr-4 billet.

Figure 10

As-received OD of the titanium tube after removal of the steel heat shrink tube

Figure 11

Extrusion blank after machining of titanium tube OD and removal of titanium extensions

ARC APPLICATIONS, INC.

AAI 21813 Multi-Metallic Composite Fuel Cladding 09-18-19

Fe12Cr2Si Layer Preparation (Appendix A)

Figure 12

Carbon steel base pipe for Fe12Cr2Si additive buildup

From previous projects MIT had the Fe12Cr2Si material in 0.045 inch diameter weld filler wire form. This wire material was used to create a cylinder form by means of additive buildup using the gas tungsten arc welding (GTAW) process. A base carbon steel pipe was placed in rotational positioner and oriented in the horizontal position. A GTAW torch was mounted on the end of the column and boom manipulator. As the positioner rotated the pipe the boom moved the welding torch along the axis of the pipe creating a spiral cladding welding process on the OD surface of the pipe. Layers were deposited in this fashion rendering the deposit thickness of 0.75 inches. Figure 13 shows the in-process welding of the first layer and the first layer after welding was complete. Figure 14 shows the additive buildup upon completion and a cross section of the build after the ends were cut off.

ARC APPLICATIONS, INC.
AAI 21813 Multi-Metallic Composite Fuel Cladding 09-18-19

Figure 13

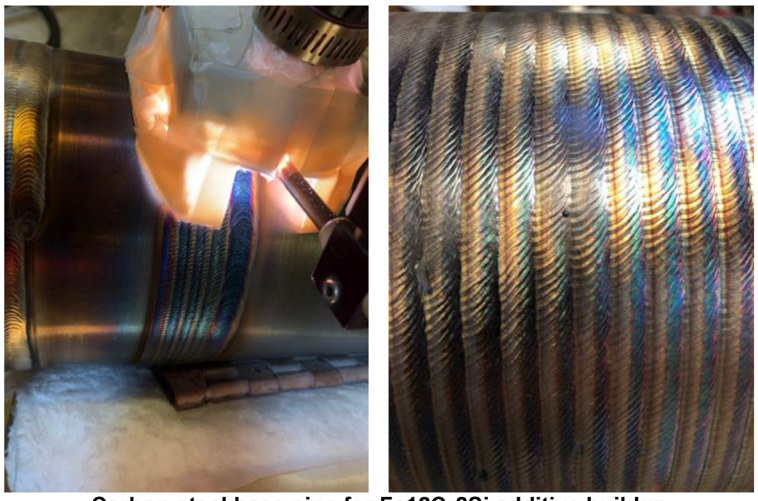

Carbon steel base pipe for Fe12Cr2Si additive buildup

Figure 14

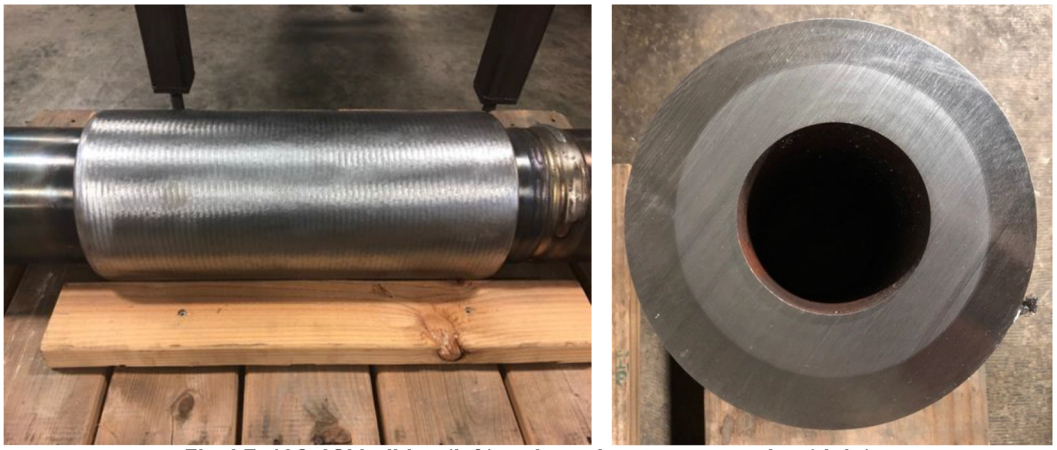

Final Fe12Cr2Si buildup (left) and rough cut cross section (right)

The base carbon steel pipe was machined off the ID of the Fe12Cr2Si buildup and the OD of the buildup was skimmed clean, Figure 15. The ID of the Fe12Cr2Si buildup was machined to 6.614 to inches remove any dilution and render a 0.010 inch slip fit to the OD of the titanium layer. Figures 16 and 17 show the Fe12Cr2Si machined cylinder after it has been sheathed onto the zr-4/titanium assembly.

ARC APPLICATIONS, INC.
AAI 21813 Multi-Metallic Composite Fuel Cladding 09-18-19

Figure 15

Machined Fe12Cr2Si cylinder layer

Figure 16

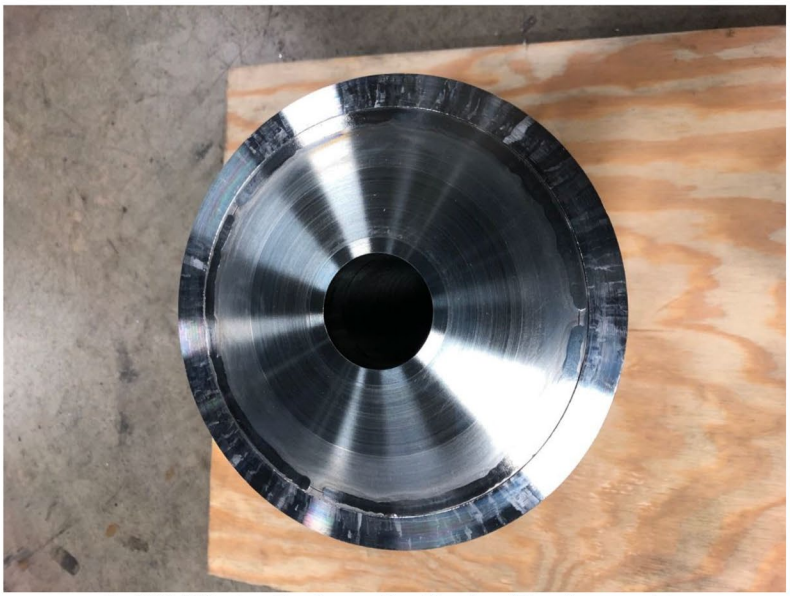

Fe12Cr2Si sheathed over the titanium/Zirc-4 assembly

ARC APPLICATIONS, INC.
AAI 21813 Multi-Metallic Composite Fuel Cladding 09-18-19

Figure 17

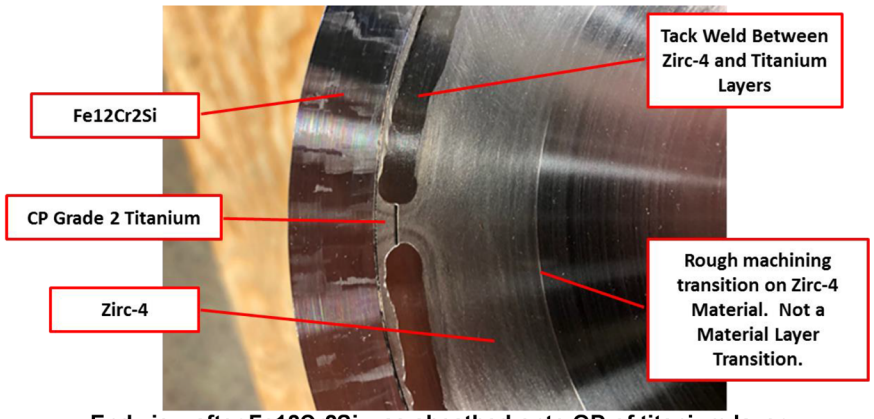

End view after Fe12Cr2Si was sheathed onto OD of titanium layer

HIP Cycle (Appendix B)

After the extrusion blank was assembled, it was shipped to Bodycote in Hanover, Massachusetts to undergo a HIP cycle in attempt to diffusion bond the layer interfaces together prior to the extrusion process. The extrusion blank was encapsulated in a carbon steel canister prior to the HIP cycle, Figure 18. MIT determined the HIP parameters, Figures 18 and 19, from previous experience:

- Temperature: 1832°F +/-25°F
- Pressure: 14750 psi +/-250 psi
- Hold Time: 4 hrs +/-15 min

Figure 18

Extrusion blank assembly encapsulated inside of carbon steel HIP canister

ARC APPLICATIONS, INC.
AAI 21813 Multi-Metallic Composite Fuel Cladding 09-18-19

Figure 19

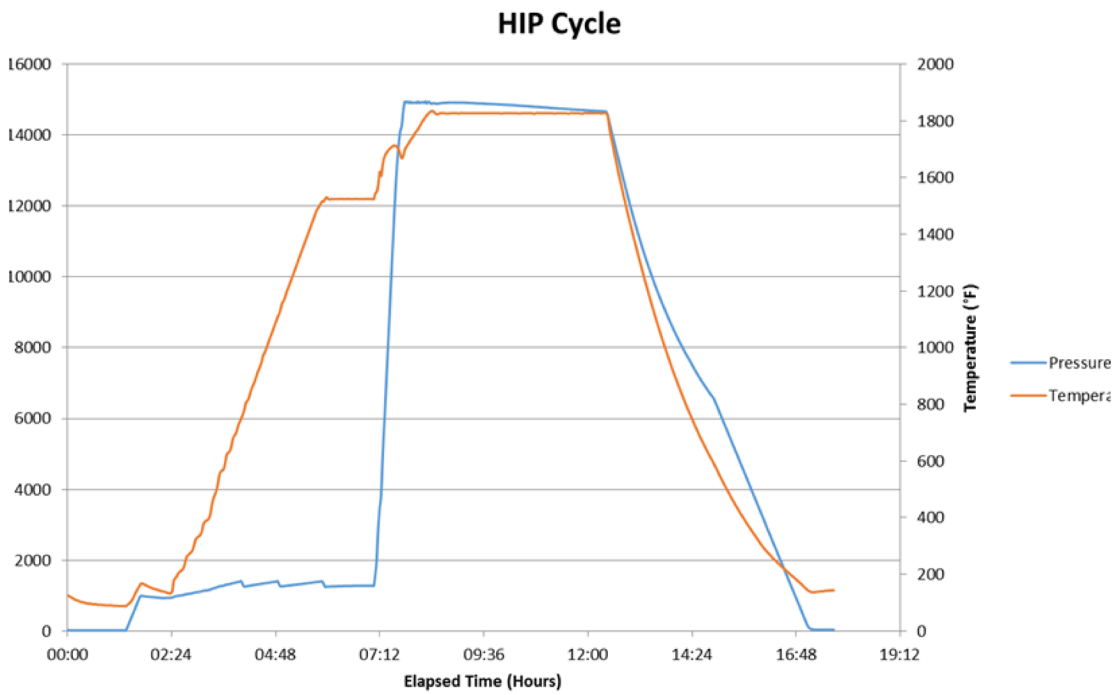

HIP cycle

Post HIP Machining and Inspection

After the HIP cycle was completed, the ends of the extrusion blank were removed by wire EDM cutting, Figure 20. Systematic cracking was visually observed on the as-cut wire EDM surface with and without the aid of penetrant testing, Figures 21 – 22. The OD and ID carbon steel HIP canister was then machined off of the extrusion blank and penetrant testing revealed similar systematic cracking around the circumference and along the entire length, Figure 23.

The interface between the Zirc-4 and the titanium appears to have diffusion bonded well as no signs of gaps or cracks were detected during penetrant testing. The interface between the titanium and the Fe12Cr2Si layer was questionable as faint lines of penetrant die could be consistently observed around the diameter of that interface.

ARC APPLICATIONS, INC.
AAI 21813 Multi-Metallic Composite Fuel Cladding 09-18-19

Figure 20

Post-HIP extrusion blank with ends removed by wire EDM cut.

Figure 21

Post-HIP extrusion as cut by wire EDM (left) and after penetrant testing (right)

ARC APPLICATIONS, INC.
AAI 21813 Multi-Metallic Composite Fuel Cladding 09-18-19

Figure 22

Visually evident systematic cracking from end view

Figure 23

Penetrant testing of systematic cracking from end view

ARC APPLICATIONS, INC.
AAI 21813 Multi-Metallic Composite Fuel Cladding 09-18-19

Figure 23

Systematic cracking observed with penetrant testing after OD HIP canister was machined away

A remnant end from the as-welded Fe12Cr2Si additive buildup was cut and machined. Penetrant testing revealed that no cracking was evident in the as-welded Fe12Cr2Si buildup, Figure 24. This observation led to the assumption that the cracking is a result of one or more variables acting upon the material during the HIP cycle.

Figure 24

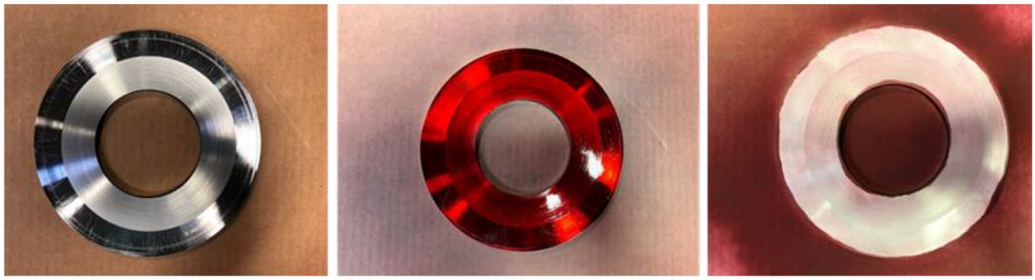

Penetrant testing sequence on as-welded Fe12Cr2Si additive buildup

ARC APPLICATIONS, INC.

AAI 21813 Multi-Metallic Composite Fuel Cladding 09-18-19

Metallography

Figure 25 shows a metallographic sample of the as-welded Fe12Cr2Si additive buildup. The grains are large and radially oriented with many single grains extending from the ID to the OD of the cylinder. No cracking was visually detected when examining the as-welded Fe12Cr2Si buildup.

Figure 26 shows a metallographic sample of the Fe12Cr2Si additive buildup after it was run through the HIP cycle. The cracking was observed to not be confined to grain boundaries but traversed grains in multiple direction and orientations.

Figure 27 shows a macro metallographic sample of the post-HIP extrusion blank showing all of the material layers including the carbon steel OD HIP canister.

Figure 25

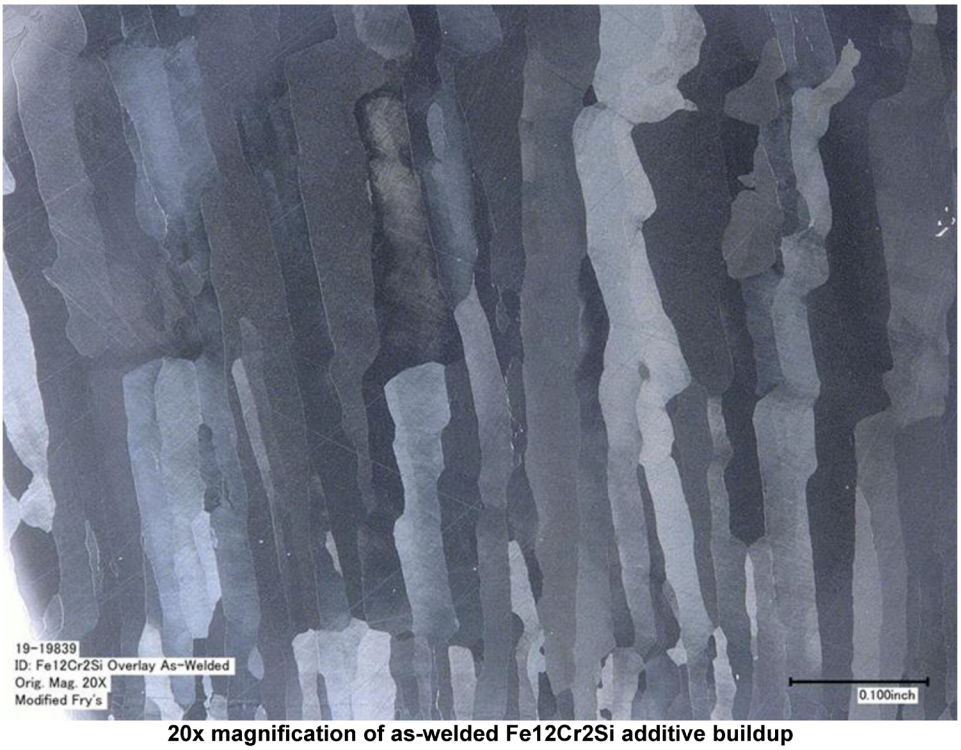

20x magnification of as-welded Fe12Cr2Si additive buildup

ARC APPLICATIONS, INC.
AAI 21813 Multi-Metallic Composite Fuel Cladding 09-18-19

Figure 26

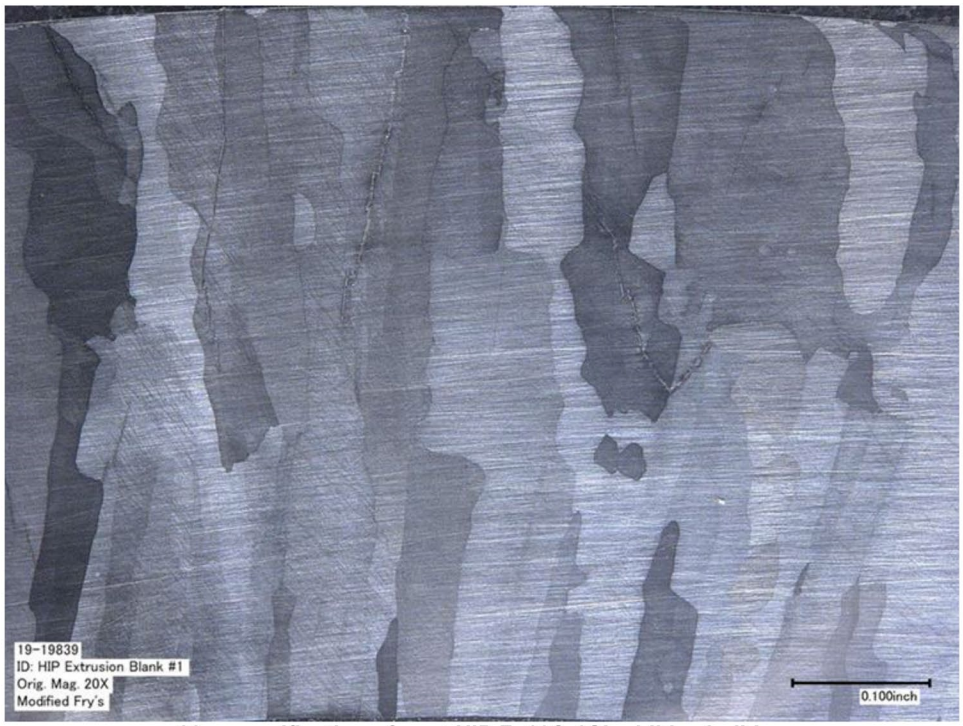

20x magnification of post-HIP Fe12Cr2Si additive buildup

Figure 27

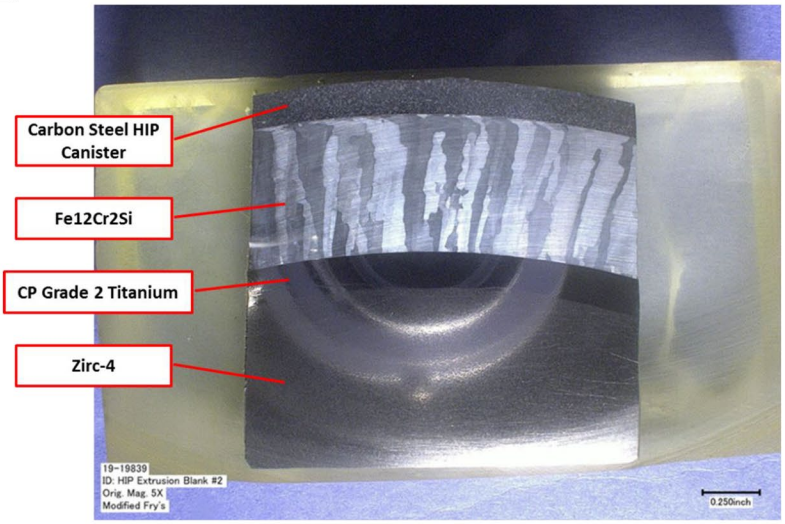

Post-HIP Fe12Cr2Si additive buildup cross section

ARC APPLICATIONS, INC.

AAI 21813 Multi-Metallic Composite Fuel Cladding 09-18-19

A cross section was removed from the upper outside corner when viewing the extrusion blank in an upright position as shown in Figures 28 and 29. This was removed prior to the carbon steel OD HIP canister being removed and prior to the carbon steel end cap HIP canister being removed. It appeared that the titanium layer partially melted due to the observed solidification structure compared next to the equiaxed grains of the titanium pipe. One potential theory was that diffusion during the HIP cycle created a lower melting eutectic composition between the titanium and Fe12Cr2Si layers. This caused a significant portion of the titanium layer to then melt and then, under the heat and pressure of the HIP cycle, was pressed out to the ends and infiltrated the gaps between the carbon steel end cap HIP canister and the Zirc-4 base billet.

Figure 28

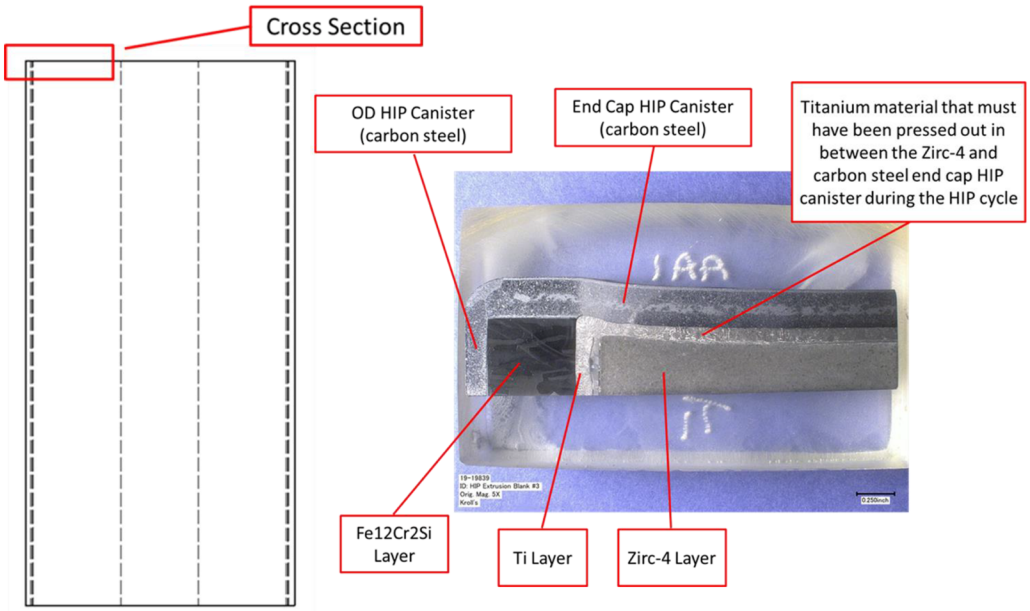

Post-HIP cross section from corner of extrusion assembly

ARC APPLICATIONS, INC.
AAI 21813 Multi-Metallic Composite Fuel Cladding 09-18-19

Figure 29

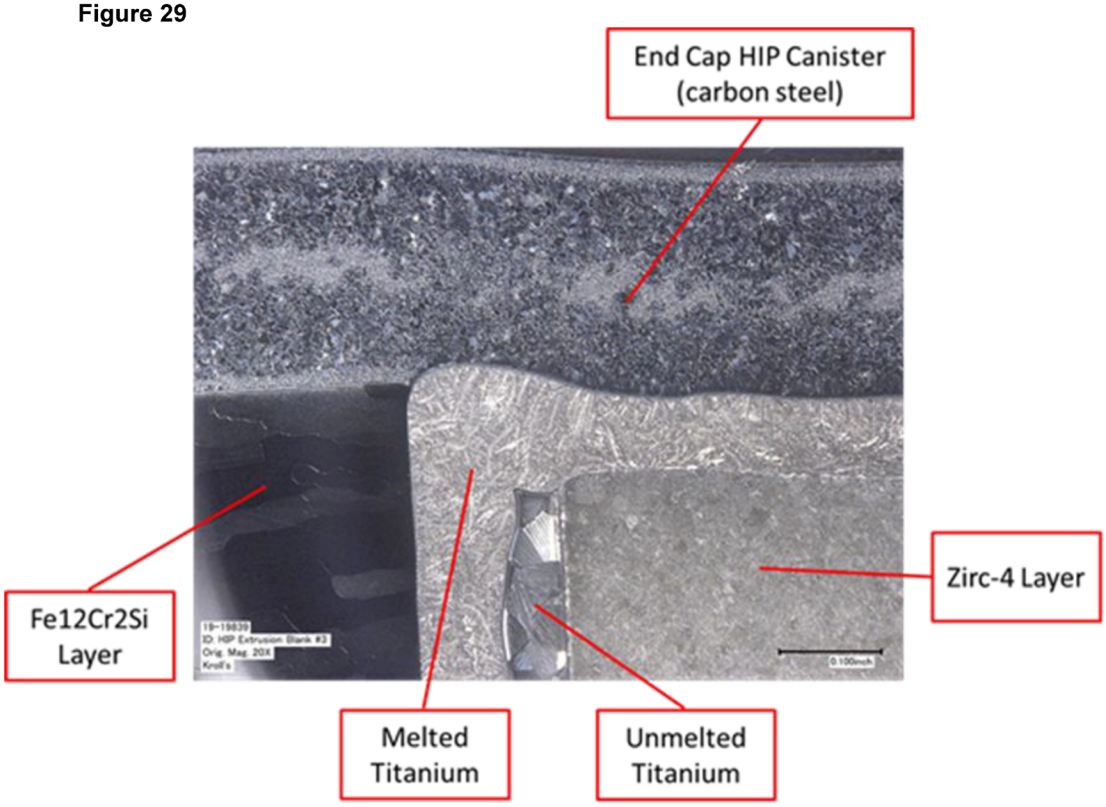

Post-HIP cross section from corner of extrusion assembly

Due to the systematic cracking observed in the Fe12Cr2Si buildup after the HIP cycle, it was readily determined that the extrusion blank was not suitable for extrusion and that indeed the planned vanadium alloy layer was necessary in order to keep the Fe212Cr2Si separated from the titanium.

ARC APPLICATIONS, INC.

AAI 21813 Multi-Metallic Composite Fuel Cladding 09-18-19

Appendix A

Setup and Parameters For Fe12Cr2Si Additive Buildup	
Test Number	21813
Groove Type	N/A
Weld type	Buildup
Position	1G
Base Material	
Type	Carbon Steel
Ht#	N/A
Filler Material	
Grade	Custom
Type	Haynes 405
Ht#	E031009-01 & -02
Dia. (in)	0.045
Tungsten	
Type	1.5% La
Dia. (in)	5/32
Ext. (in)	5/8 Max
Taper (deg)	30 included
Flat (in)	0.050
Cup Dia. (in)	3/4
Shielding Gas	
Type	50% Ar – 50% He
Flow (cfh*)	50
Trailing Gas	
Type	Argon
Flow (cfh*)	50-70
Interpass Temp (°F)	450-700
*** Flow rates based on Argon scale**	

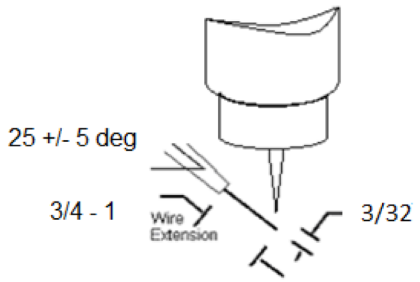

Parameters	Values
Wire Feed Speed (ipm)	65
Primary Current (amps)	225
Background Current (amps)	150
Primary Time (sec)	0.3
Background Time (sec)	0.3
Voltage (volts)	11.0
Travel Speed (ipm)	6.5
Step over (in)	0.25
Heat Input (KJ/in)	19.0
Interpass Temperature	450-645

ARC APPLICATIONS, INC.

AAI 21813 Multi-Metallic Composite Fuel Cladding 09-18-19

Appendix B

Bodycote HOT ISOSTATIC PRESSING

155 River St. Andover, MA 01810

OPF - 131 REV. "A", 1/5/2015

Assembled By: Reviewed By:

16" LOW PRESSURE Load Diagram

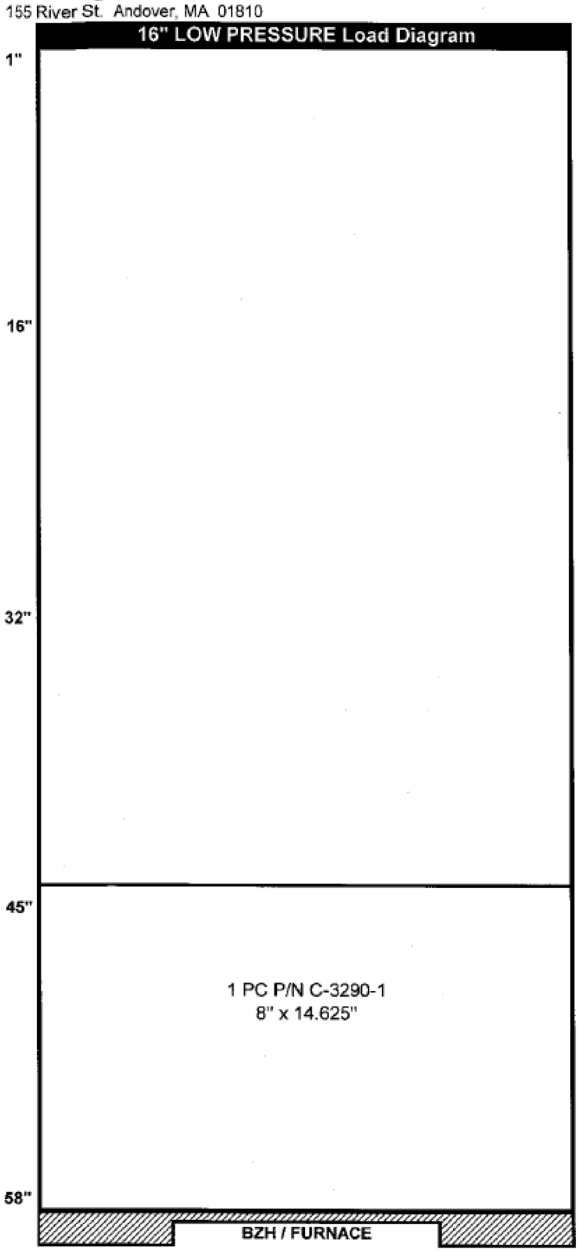

CUSTOMER:	ARC Applications
JOB NUMBER:	C-3290-1
PO NUMBER:	21813-01
PO NUMBER:	N/A
HIP NUMBER:	66380-3
DATE:	5/15/2019
TEMP:	1832°F ±25°F
PRESSURE:	14750 PSI ±250 PSI
TIME:	4 HRS +15/-0 MINS

FURNACE NUMBER: 37A

BASE NUMBER: 5

MT/C LOT NUMBER: N0176

MT/C RUN NUMBER: 2

MT/C TYPE: N

NET WEIGHT: N/A

Thermocouple Number & Locations		
MT/C#	Outside Diameter	Centerline
11	1"	
12	16"	
13	32"	
14	45"	
15	58"	
16		44"
17		44"
18		51"
19		58"
20		58"

Notes:

The recording of false, fictitious or fraudulent statements or entries on this document may be punishable as a felony under Federal statutes.

Chapter 7 – Summary and Future Work